

AL A112620

12

Bulletin 45
(Part 4 of 5 Parts)

THE SHOCK AND VIBRATION BULLETIN

Part 4
Impact, Packaging and Shipping,
Blast and Impulsive Loading

JUNE 1975

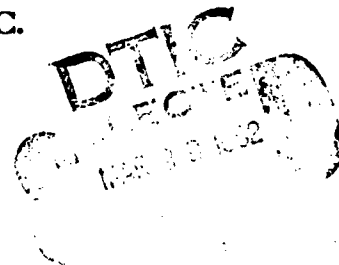
A Publication of
THE SHOCK AND VIBRATION
INFORMATION CENTER
Naval Research Laboratory, Washington, D.C.



Office of
The Director of Defense
Research and Engineering

82 03 26 074

Approved for public release; distribution unlimited.



DTIC FILE COPY

SYMPOSIUM MANAGEMENT

THE SHOCK AND VIBRATION INFORMATION CENTER

Henry C. Pusey, Director
Edward H. Schell
Rudolph H. Volin
J. Gordon Showalter

Bulletin Production

Graphic Arts Branch, Technical Information Division,
Naval Research Laboratory

Bulletin 45
(Part 4 of 5 Parts)

THE SHOCK AND VIBRATION BULLETIN

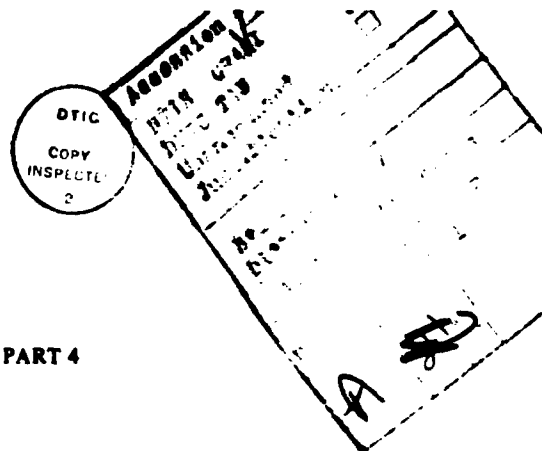
JUNE 1975

**A Publication of
THE SHOCK AND VIBRATION
INFORMATION CENTER
Naval Research Laboratory, Washington, D.C.**

The 45th Symposium on Shock and Vibration was held at the Dayton Convention Center, Dayton, Ohio on October 22-25, 1974. The Air Force Flight Dynamics Laboratory, Air Force Materials Laboratory and Aeronautical Systems Division Air Force Systems Command, Wright-Patterson AFB, Ohio were the hosts.

**Office of
The Director of Defense
Research and Engineering**

DTIC
RECEIVED
MAR 29 1982
H



CONTENTS

PAPERS APPEARING IN PART 4

Impact

- EXPLOSIVELY PROPELLED ROTATING PLATES FOR OBLIQUE IMPACT EXPERIMENTS' 1
F. H. Mathews, Sandia Laboratories, Albuquerque, New Mexico
- IMPACT TESTING USING A VARIABLE ANGLE ROCKET LAUNCHER 13
H. W. Nunez, Sandia Laboratories, Albuquerque, New Mexico
- EVALUATION OF THE SHOCK PULSE TECHNIQUE TO THE UH-1 SERIES HELICOPTER 19
J. A. George, T. C. Mayer and E. F. Covill, Parks College of St. Louis University, Cahokia, Illinois
- STRUCTURAL RESPONSE MODELING OF A FREE-FALL MINE AT WATER ENTRY' 39
R. H. Waser, G. L. Matteson and J. W. Honaker, Naval Surface Weapons Center, White Oak Laboratory, Silver Spring, Maryland
- PLASTIC DESIGN ANALYSIS OF SHIPBOARD EQUIPMENT SUBJECTED TO SHOCK MOTIONS' 47
L. T. Butt, Naval Ship Research and Development Center, Underwater Explosions Research Division, Portsmouth, Virginia

Packaging and Shipping

- HIGHWAY SHOCK INDEX (SI) PROCEDURE FOR DETERMINING SI' 53
J. H. Grier, Military Traffic Management Command, Transportation Engineering Agency, Newport News, Virginia
- THE DYNAMIC ENVIRONMENT ON FOUR INDUSTRIAL FORKLIFT TRUCKS' 59
M. B. Gens, Sandia Laboratories, Albuquerque, New Mexico
- A STATISTICALLY BASED PROCEDURE FOR TEMPERATURE SENSITIVE DYNAMIC CUSHIONING CURVE DEVELOPMENT AND VALIDATION' 69
D. McDaniel, U.S. Army Missile Command, Redstone Arsenal, Alabama, R. M. Wyskida and M. R. Wilhelm, The University of Alabama, Huntsville, Alabama
- A DAVIS GUN PENETRATOR LAUNCH SYSTEM' 81
L. O. Seamons, Sandia Laboratories, Albuquerque, New Mexico

Blast and Impulsive Loading

- X-RAY SIMULATION WITH LIGHT-INITIATED EXPLOSIVE' 87
R. A. Benham and F. H. Mathews, Sandia Laboratories, Albuquerque, New Mexico
- STRUCTURAL DYNAMIC RESPONSE TO HEIGHT OF BURST AIR BLAST LOADING' 93
H. F. Korman, N. Lipner and J. S. Chiu, TRW Systems Group, Redondo Beach, California
- RESPONSE OF FLAT PLATES SUBJECTED TO MILD IMPULSIVE LOADINGS' 105
C. A. Ross, University of Florida Graduate Engineering Center, Eglin Air Force Base, Florida and W. S. Strickland, U.S. Air Force Armament Laboratory, Eglin Air Force Base, Florida

A MATRIX STRUCTURAL DYNAMIC MODEL OF PARACHUTE THERMAL COVER EJECTION BY PYROTECHNIC DEVICES	117
A. E. Barniskis and R. A. Romanzi, General Electric Company, Philadelphia, Pennsylvania	
STRUCTUREBORNE GUN BLAST SHOCK TEST USING AN ELECTROHYDRAULIC VIBRATION EXCITER	127
N. D. Nelson, Hughes Aircraft Company, Fullerton, California and R. L. Woodfin, Naval Weapons Center, China Lake, California	
DYNAMIC PROPERTIES OF CONCRETE UNDER IMPACT LOADING	131
G. R. Griner, R. L. Sierakowski, and C. A. Ross, Department of Engineering Sciences, University of Florida, Gainesville, Florida	
PREDICTING PLATE RESPONSE TO BLAST LOADING	143
Lt. Col. Robert O. Meitz and Lt. Philip B. Atken-Cade, Air Force Institute of Technology, Wright-Patterson Air Force Base, Ohio	

PAPERS APPEARING IN PART 2

ADDRESS OF WELCOME

Dr. D. Zonars, Chief Scientist, Air Force Flight Dynamics Laboratory, Wright-Patterson Air Force Base, Ohio

ADDRESS OF WELCOME

Mr. George Peterson, Director, Air Force Materials Laboratory, Wright-Patterson Air Force Base, Ohio

KEYNOTE ADDRESS

Lt. General James L. Stewart, Commander, Aeronautical Systems Division, Wright-Patterson Air Force Base, Ohio

Invited Papers

STANDARDIZING THE DYNAMICS OF MAN

Dr. H. E. Von Gierke, Aerospace Medical Research Laboratory, Wright-Patterson Air Force Base, Ohio

THE RIVET GYRO STORY

Mr. John E. Short, Aeronautical Systems Division, Wright-Patterson Air Force Base, Ohio

AVIONICS RELIABILITY

Lt. Colonel Ben H. Swett, Headquarters, Air Force Systems Command, Andrews Air Force Base, Washington, D.C.

Panel Sessions

MIL-STD-810C

TEST OR ANALYZE?

Seismic

SEISMIC SIMULATOR FOR SILO CONSTRAINED MISSILE GUIDANCE PLATFORM

R. L. Felker, Rockwell International Corporation, Anaheim, California

EARTHQUAKE RESPONSE OF COMMUNICATIONS EQUIPMENT IN SMALL BUILDINGS

N. J. DeCapua and F. X. Prendergast, Bell Laboratories, Whippany, New Jersey

SEISMIC ANALYSIS OF MOTORS FOR NUCLEAR POWER PLANTS

L. J. Taylor, Westinghouse Electric Corporation, Buffalo, New York and N. M. Isada, State University of New York at Buffalo, New York

Special Problems

EXTENSION OF CONTROL TECHNIQUES FOR DIGITAL CONTROL OF RANDOM VIBRATION TESTS

J. D. Tebbs and D. G. Smallwood, Sandia Laboratories, Albuquerque, New Mexico

VIBRATION-INDUCED DOPPLER EFFECTS ON AN AIRBORNE SHF COMMUNICATION SYSTEM

J. Pearson and R. E. Thaller, Air Force Flight Dynamics Laboratory, Wright-Patterson Air Force Base, Ohio

FATIGUE DAMAGE EQUIVALENCE OF FIELD AND SIMULATED VIBRATIONA¹ ENVIRONMENTS

D. D. Kana and D. C. Scheidt, Southwest Research Institute, San Antonio, Texas

AN EVALUATION OF SHOCK RESPONSE TECHNIQUES FOR A SHIPBOARD GAS TURBINE

J. R. Manceau and E. Nelson, AiResearch Manufacturing Company of Arizona, Phoenix, Arizona

THE DEVELOPMENT OF A WATER PARTICLE VELOCITY METER

J. D. Gordon, Naval Ship Research and Development Center, Underwater Explosions Research Division, Portsmouth, Virginia

PAPERS APPEARING IN PART 3

Aerospace Vehicles

AN EXPERIMENTAL/ANALYTICAL DETERMINATION OF TRANSPORTER LOADS ON THE VIKING SPACECRAFT

G. Kachadourian, General Electric Company, Hampton, Virginia

DETERMINATION OF PROPELLANT EFFECTIVE MASS PROPERTIES USING MODAL TEST DATA

J. C. Chen and J. A. Garba, Jet Propulsion Laboratory, Pasadena, California

UNIQUE FLIGHT INSTRUMENTATION/DATA REDUCTION TECHNIQUES EMPLOYED ON THE VIKING DYNAMIC SIMULATOR

F. D. Day, Martin Marietta Aerospace, Denver, Colorado and B. K. Wada, The Jet Propulsion Laboratory, Pasadena, California

ANALYTICAL PREDICTION AND CORRELATION FOR THE ORBITER DURING THE VIKING SPACECRAFT SINUSOIDAL VIBRATION TEST

G. R. Brownlee and J. A. Garba, Jet Propulsion Laboratory, Pasadena, California, and F. D. Day, III, Martin Marietta Aerospace, Denver, Colorado

FAIL SAFE FORCED VIBRATION TESTING OF THE VIKING 1975 DEVELOPMENTAL SPACECRAFT

J. W. Fortenberry, Jet Propulsion Laboratory, Pasadena, California, and P. Rader, Martin Marietta Corporation, Denver, Colorado

A METHOD FOR DETERMINING TACTICAL MISSILE JOINT COMPLIANCES FROM DYNAMIC TEST DATA

J. G. Maloney and M. T. Shelton, General Dynamics Corporation, Pomona, California

Vibro-Acoustics

DYNAMIC STRAIN MEASUREMENT TECHNIQUES AT ELEVATED TEMPERATURES

R. C. Taylor, Air Force Flight Dynamics Laboratory, Wright-Patterson Air Force Base, Ohio

AN ACTIVE LINEAR BRIDGE FOR STRAIN MEASUREMENT

P. T. JaQuay, Air Force Flight Dynamics Laboratory, Wright-Patterson Air Force Base, Ohio

VIKING DYNAMIC SIMULATOR VIBRATION TESTING AND ANALYSIS METHOD

A. F. Leondis, General Dynamics Corporation, San Diego, California

ANALYSIS AND FLIGHT TEST CORRELATION OF VIBROACOUSTIC ENVIRONMENTS ON A REMOTELY PILOTED VEHICLE

S. Zurnaciyen and P. Bockemuhle, Northrop Corporation Electronics Division, Hawthorne, California

AERO-ACOUSTIC ENVIRONMENT OF RECTANGULAR CAVITIES WITH LENGTH TO DEPTH RATIOS IN THE RANGE OF FOUR TO SEVEN

L. L. Shaw and D. L. Smith, Air Force Flight Dynamics Laboratory, Wright-Patterson Air Force Base, Ohio

PREDICTION OF ACOUSTICALLY INDUCED VIBRATION IN TRANSPORT AIRCRAFT

H. W. Bartel, Lockheed-Georgia Company, Marietta, Georgia

SIMPLIFIED TECHNIQUES FOR PREDICTING VIBRO-ACOUSTIC ENVIRONMENTS

K. Y. Chang and G. C. Kao, Wyle Laboratories, Huntsville, Alabama

USE OF A SEMI-PERIODIC STRUCTURAL CONFIGURATION FOR IMPROVING THE SONIC FATIGUE LIFE OF STIFFENED STRUCTURES

G. Sengupta, Boeing Commercial Airplane Company, Seattle, Washington

PAPERS APPEARING IN PART 5

Isolation and Damping

IMPACT ON COMPLEX MECHANICAL STRUCTURES

S. F. Jan, Bechtel Power Corporation, Houston, Texas and E. A. Ripperger, The University of Texas at Austin, Austin, Texas

ENERGY ABSORPTION AND PHASE EFFECTS IN SHOCK EXCITED COUPLED SYSTEMS

C. T. Morrow, Advanced Technology Center, Inc., Dallas, Texas

HIGH PERFORMANCE VIBRATION ISOLATION SYSTEM FOR THE DD963 GEARS

P. C. Warner, Westinghouse Electric Corporation, Sunnyvale, California and D. V. Wright, Westinghouse Electric Corporation, Pittsburgh, Pennsylvania

THE DESIGN AND MEASUREMENT OF A HIGH IMPEDANCE FOUNDATION TO 20 kHz AND USE OF THE DATA IN CORRECTING NOISE MEASUREMENTS

J. R. Hupton, Westinghouse Electric Corporation, Sunnyvale, California

RESPONSE OF THICK STRUCTURES DAMPED BY VISCOELASTIC MATERIAL WITH APPLICATION TO LAYERED BEAMS AND PLATES

M. Lalanne, M. Paulard and P. Trompette, Institut National des Sciences Appliquees, Villeurbanne, France

CONTROLLING THE DYNAMIC RESPONSE OF JET ENGINE COMPONENTS

D. I. G. Jones, Air Force Materials Laboratory, Wright-Patterson Air Force Base, Ohio and C. M. Cannon, M. L. Parin, University of Dayton, Dayton, Ohio

AN INVESTIGATION OF THE RESPONSE OF A DAMPED STRUCTURE USING DIGITAL TECHNIQUES

M. L. Drake, University of Dayton Research Institute, Dayton, Ohio and J. P. Henderson, Air Force Materials Laboratory, Wright-Patterson Air Force Base, Ohio

AN ALTERNATIVE SYSTEM FOR MEASURING COMPLEX DYNAMIC MODULI OF DAMPING MATERIALS

D. I. G. Jones, Air Force Materials Laboratory, Wright-Patterson Air Force Base, Ohio

Dynamic Analysis

NONLINEAR VIBRATION OF CYLINDRICAL SHELLS UNDER RADIAL LINE LOAD

S. S. Tang, Rockwell International Corporation, Los Angeles, California

DETERMINATION OF THE ELASTIC MODES AND FREQUENCIES WHEN RIGID BODY MODES EXIST

J. W. Straight, Christian Brothers College, Memphis, Tennessee

ON THE FORCED VIBRATION OF TRIANGULAR PLATES

H. M. Negm, S. Chander, and B. K. Donaldson, Department of Aerospace Engineering, University of Maryland, College Park, Maryland

EXPERIMENTAL DETERMINATION OF MULTIDIRECTIONAL MOBILITY DATA FOR BEAMS

D. J. Ewins, Imperial College of Science and Technology, London, England and P. T. Gleeson, Middlesex Polytechnic and Imperial College, London, England

A NEW STUDY OF THE HARMONIC OSCILLATOR WITH NON-LINEAR FLUID DAMPING

R. A. Eyman, Martin Marietta Aerospace, Orlando, Florida

MECHANICAL DESIGN, ANALYSIS, AND TEST OF THE STANDARD ELECTRONICS CABINET AND CONTROL DISPLAY CONSOLE FOR THE AN/BQQ-5 SONAR SET

R. E. Denver and J. M. Menichelio, IBM Corporation, Owego, New York

SHOCK SPECTRA, RESIDUAL, INITIAL AND MAXIMAX AS CRITERIA OF SHOCK SEVERITY

C. T. Morrow, Advanced Technology Center, Inc., Dallas, Texas

IMPACT

EXPLOSIVELY PROPELLED ROTATING PLATES FOR OBLIQUE IMPACT EXPERIMENTS

**F. H. Mathews
Sandia Laboratories
Albuquerque, New Mexico 87115**

ABSTRACT

A new technique for using explosive-driven flyer plates in impact studies is described. The simulation of high-velocity impacts at predictable shallow angles is now possible. The detonation of a solid explosive is used to accelerate massive, slowly rotating plates to high velocities. The device to be impacted is positioned at a distance along the flight path sufficient to allow rotation of the flyer plate before impact. Thus, any angle between the plate's surfaces and the plate velocity vector can be obtained. Either plastic or metal plates can be used to study impact response against hard or soft materials. The technique is employed to allow evaluation of the performance of full-scale fuzing hardware at velocities from 1500 to 3500 m/sec. Procedures for designing flyer plate experiments are described. Data establishing experimental repeatability are presented.

Summary

Plastic explosive has been incorporated into an assembly that propels a rotating plate of metal or plastic into a target for impact-fuze experiments. Data verifying the technique have been obtained at velocities from 1500 to 3500 m/sec. Methods of designing experiments are presented. The repeatability of two explosive systems has been measured and the data are presented. A typical experiment is described.

It is concluded that accurately controlled high-velocity impact experiments can be conducted with the new technique, including shallow impact-angle conditions not previously possible. Future work will be directed toward applying explosive systems to fuze experiments over an extended range of velocities.

Introduction

Explosive warheads can be initiated by fuzing systems that actuate upon target impact. Fuzing must occur quickly and reliably enough that the warhead has time to function before disabling damage occurs. The requirements for the fuze, therefore, are conflicting: it must react practically instantaneously, yet must be thoroughly reliable and insensitive to prefire.

Modern ballistic-missile warheads contain impact fuzes that must function at impact velocities from 1000 to 4500 m/sec. A common tactical demand that complicates fuzing requirements is that of oblique impact. In the past, fuzing experiments have been conducted with track-guided, rocket-propelled sleds carrying target materials into stationary

fuze assemblies. Propulsion costs and sled-shoe failures have limited this technique to velocities below 1800 m/sec. In experiments at higher velocities (2000 to 4000 m/sec), explosives have been used to propel metal and plastic plates into test materials. A major deficiency of this technique has been that the only impact angles that could be simulated were those at approximately 90° from the trajectory.

In this paper is described a way to improve flyer-plate technology in this regard. The slow and predictable rotation of the flyer plate during flight allows impacts to be made at any angle, while the velocity vector and the plate's surface normal remain in the proper orientation. Impact-fuze testing with this technique can be conducted at velocities from 1500 to 4000 m/sec.

Explosive Requirements

The principles behind the rotating flyer plate experiments are illustrated in Fig. 1.

It is essential that the impulse from explosive gases vary uniformly over the plate surface, since the flyer plate must remain

intact and reasonably planar over distances approaching 20 m. This is accomplished by surrounding the flyer plate with a guard plate backed up by an explosive layer. A weak joint is provided by gluing the flyer plate into a tapered recess in the guard plate. Since explosive pressures are relieved most rapidly toward edges, the guard plate is thus free to lag during acceleration. A sufficient amount of guard plate assures that edge relief does not cause the flyer itself to bend or break up. Typical proportions for an explosive assembly are shown in Fig. 2, where h is the explosive thickness over the flyer plate's center. A triangular ramp of explosive leads to the gradually tapered section over the plate. With the geometry of Fig. 2, a large part of the explosive is used over the guard plate and does not impart velocity to the flyer. Typically, only about 10 to 50% of explosive weight actually propels the flyer plate. Relatively thick plates moving at high velocities produce the least efficient geometries and may require unacceptably large quantities of explosive.

When the explosive is initiated by line-wave initiators, a detonation wave progresses through the explosive, sweeping over the flyer-plate/guard plate assembly. Resulting high-pressure gases accelerate both plates. Acceleration is completed in a few 10^{-6} s of

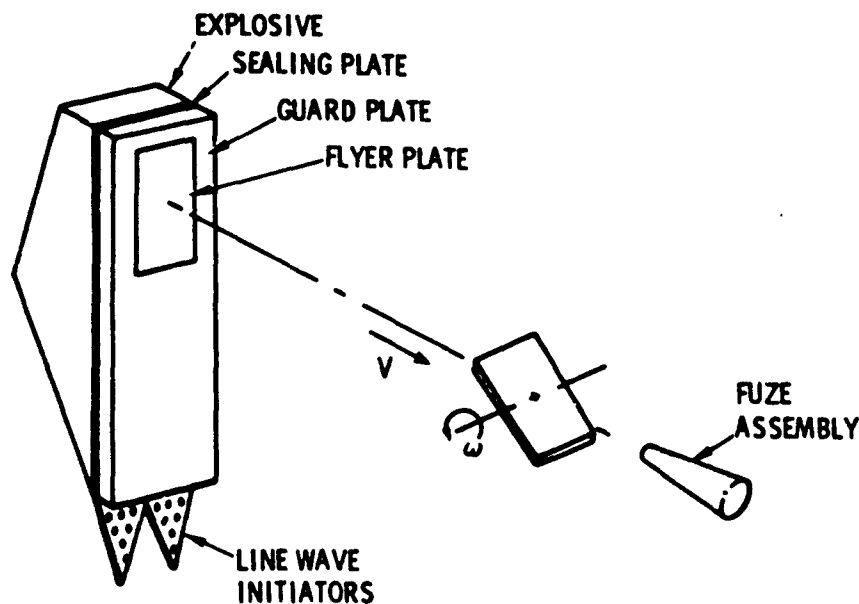


FIG. 1 ARRANGEMENT FOR ROTATING FLYER PLATE IMPACT EXPERIMENT.
PLATE VELOCITY v , ROTATION RATE ω

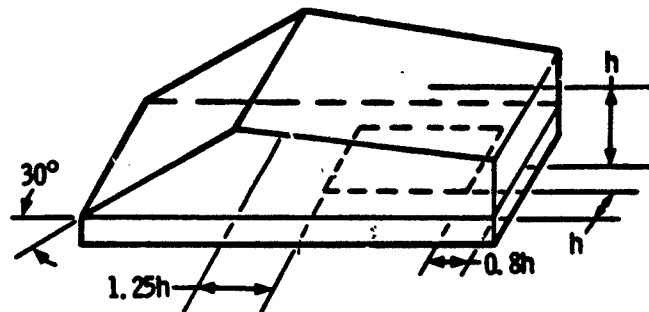


FIG. 2 PROPORTIONS OF A TYPICAL EXPLOSIVE ASSEMBLY

microseconds and requires a displacement of a few centimeters. The explosive is tapered so that the velocity imparted varies uniformly along the length of the plate, causing it to rotate slowly during flight. The fuze assembly is positioned along the flight trajectory, at a distance that will permit rotation of the flyer plate to the desired angle before impact. Velocity gradients associated with rotation are only a few percent of average velocity and have negligible effect during impact.

Shock waves from explosive pressures reflect at free surfaces and may produce sufficient tensile stresses to cause fracture, resulting in plate separation along spall planes.[1, 2] Use of side initiation and a "grazing" detonation reduces pressures and the tendency to spall when compared to the case where detonation strikes the plate at normal incidence. Spallation is more likely at low velocities and with light materials. In these experiments, aluminum was not spalled at velocities from 1.7 to 3.7 mm/ μ sec, with Comp C-4 explosive directly in contact with the metal. However, nylon that was intact at 2.3 mm/ μ sec developed spall at 1.5 mm/ μ sec and to prevent this it was necessary to place a thick sponge-rubber cushion between the explosive and the plate.

The final velocity of explosively accelerated plates may be calculated from the Gurney model [3, 4] which depends upon the experimentally determined specific energy (E , kJ/g) available from the explosive to produce the kinetic energy of gases and fragments. The "open-faced sandwich" form applies directly to the center region of the plate explosive assembly where edge relief is prevented by the surrounding guard plate.

Hence,

$$V = \frac{\sqrt{2E}}{\left(\frac{1 + 5\alpha + 4\alpha^2}{3}\right)^{1/2}}$$

where V is the plate's final velocity, $\alpha = M/C$ the ratio of plate areal density to explosive areal density, and $\sqrt{2E}$ is the Gurney velocity (a constant for a particular explosive). This equation is plotted in Fig. 3 for Comp C-4 explosive using 2.75 mm/ μ sec for $\sqrt{2E}$. Experimental points for both the plastic and aluminum plates included in this figure show good agreement over the full velocity range.

The Gurney equation may be applied along the tapered length of the explosive assembly, making allowance for downstream motion of the explosive gases after detonation. Typically observed rotation rates are from 50 to 100% of the value estimated in this way, while velocities are within a few percent. Relatively thick explosive assemblies with high rotation rates show the poorest agreement. Ordinarily, several half-scale experiments are conducted, with explosive taper being modified until the desired rotation rate is obtained. The scaled rotation rate is then reproduced in full-scale experiments.

The efficiency with which explosive energy is transmitted to the plate is given by

$$\epsilon = \frac{3\alpha}{1 + 5\alpha + 4\alpha^2}$$

where ϵ , the mechanical efficiency, is the ratio of plate kinetic energy to explosive Gurney energy. Mechanical efficiency is high over the region of interest, decreasing from

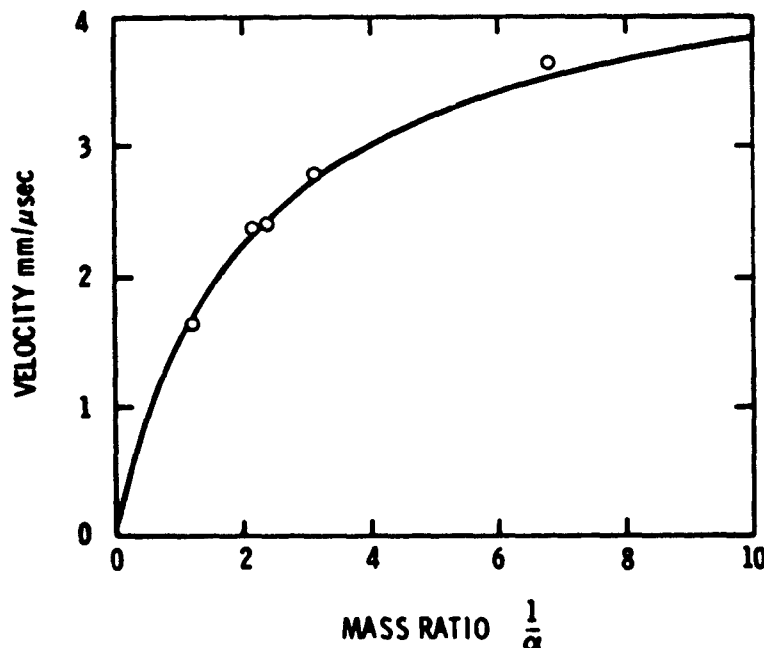


FIG. 3 COMPARISON OF CALCULATED AND OBSERVED PLATE VELOCITIES OBTAINED WITH COMP C-4 EXPLOSIVE

33 to 25% as velocity increases. Overall efficiency (the product of geometrical and mechanical efficiencies) ranges from 4 to 15%. Fortunately, energy in the form of C-4 explosive is relatively inexpensive. The principal problem associated with low overall efficiency is that large explosive quantities are necessary, making the protection of experimental apparatus difficult.

Trajectory Considerations

The plate trajectory may be considered in three segments; launch, flight, and impact. The launch segment occupies a few tens of microseconds and a motion of a few centimeters. Explosive forces are completely dominant and the plate is rotated through an angle and launched along a trajectory approximately as described by Kennedy. [4] Because of the taper of the explosive, it is necessary to empirically adjust both the rotation angle and the trajectory by a few degrees on the basis of experience gained during half-scale experiments.

The flyer edge is deformed as the detonation sweeps over it and must be tapered sufficiently that interference between the guard plate and flyer does not affect rotation. A 10° taper angle in aluminum was insufficient, causing interference and a variation in plate rotation rate. A relief angle of 20° reduced this scatter.

The flight portion of the trajectory is the interval beginning after the first few centimeters of motion and continuing to impact. After approximately the first meter of travel the plate is surrounded by the explosive fireball. Then, depending upon the quantity of explosive, the presence of barriers erected to reduce fireball size, and distance to impact, the flyer emerges from the fireball and moves through undisturbed air where appreciable aerodynamic forces retard its motion. These aerodynamic forces must be considered because of their effect on accurate timing and trajectory predictions. Hoerner [5] gives aerodynamic drag coefficients C_D that may be applied to flat plates as a function of angle at hypersonic velocities. His drag function

$$C_D = 2.1 \sin^2 \theta \quad 0 \leq \theta \leq 60.8 \text{ deg}$$

$$= 1.6 \quad 60.8 \leq \theta \leq 90 \text{ deg}$$

may be used with the assumption of constant rotation rate to compute drag forces and resulting velocity, position, angle, and time information. Since the drag force acts normal to the plate surface, a complementary lifting force may be calculated with which to estimate vertical displacements. When these equations are applied over the first quarter-turn of the plate, a velocity reduction of ~4% is indicated, with a vertical displacement of a few centimeters. Typically, actual impact times may be predicted to within $\pm 1\%$ of total flight time and trajectory angles within $\pm 0.2^\circ$ over a 10-meter trajectory, by using these techniques in conjunction with empirical observations on half-scale experiments.

Internal stresses caused by rotation act during the flight portion of the trajectory. These forces are negligible in metals but are appreciable for plastic materials in which yield strength is reduced by shock heating. Creep and stretching are observed with plastics. Polyethylene is unsuitable for this reason, but nylon is an acceptable substitute. Vibration and bending are also much more noticeable in plastic plates, contributing to a modest uncertainty about plate planarity.

It is essential that the first significant input to the fuze component be produced by plate impact. However, other mechanical inputs may precede impact, risking fuze prefire. These can include an air shock wave radiating outward from the explosion, explosive gases that may move ahead of the plate and strike the fuze, or the air shock wave associated with plate motion in undisturbed air.

Air shock waves are of sufficiently low amplitude to be neglected in our work. However, if it were found necessary, the effects of such waves could be reduced by placing the fuze in a chamber that was frangible at one end and was evacuated or filled with helium.

Explosive gases, which are relatively dense compared to air, do produce sufficient pressures to cause concern. By sealing the flyer and guard plate so that little or no explosive gas can escape, however, experiments can be conducted as close as one-half meter from the plate's initial position. Ultrahigh-speed photographs show that venting of explosive gases is retarded by using a continuous sealing plate (see Fig. 1), $1/32$ of the flyer

thickness, which would allow a half meter of plate travel before explosion gases outrun the plate. A sealing plate allows sufficient time before impact that shock waves within the flyer will have receded to an acceptably quiescent state, permitting impact angles of nearly 90° .

Later in its flight the plate outruns the explosion gases, emerging from the gas cloud after a displacement of

$$x = 1.9 M_{HE}^{1/3}$$

where x is in meters and the explosive mass (M_{HE}) is in kilograms. If a barrier equipped with an aperture slightly larger than the flyer is placed close to the flyer's initial position, the distance that it takes the flyer to emerge from the cloud can be reduced to half the above value.

If experiments must be conducted at angles still denied by the impingement of explosion gas, the target may be set up farther along the flight, so that the plate has time to rotate through half a turn and strike the target with the back of the plate. Such a test setup naturally results in correspondingly larger uncertainties in timing, position, and velocity.

Impact Requirement

Plate thickness and material are dictated by the desire to duplicate as nearly as possible the conditions of actual earth targets. Because of the high pressures generated during impact, shock Hugoniot may be compared to establish a basis for selecting suitable materials for simulation. Nylon, for example, is a reasonable material with which to simulate water impact. Aluminum has a somewhat higher impedance than granite. Thus, extreme parameters of likely earth targets are simulated by materials adaptable to explosive acceleration.

Plate thicknesses are determined in a less exact way. Since geometrical efficiency of the explosive system drops rapidly with flyer thickness, little is gained by increasing explosive weights beyond an upper bound for a particular flyer area. The flyer thickness that may be considered for any specific velocity is therefore limited. Measured fuze performance, together with computer calculations employing a two-dimensional shock-wave code, are used in judging whether a particular plate thickness is adequate. The

25-mm-thick aluminum plates propelled by 45 kg of explosive that we are using appear to be marginal or inadequate. Configurations employing 180 kg of explosive to propel 50-mm-thick plates are under development.

Experiment

Elements of an aluminum flyer plate system are shown in Figs. 4 and 5. The flyer, in this case 0.3 m by 0.25 m wide by 25-mm-thick, is epoxied into the guard plate and mounted in a wooden platform. A continuous thin aluminum sealing plate (not shown) is placed over the aluminum assembly. Wooden side and end rails provide a mold into which 45 kg of plastic Comp C-4 explosive is pressed to the desired contour. Line-wave initiators are then added.

The arrangement for an impact-fuze experiment at a velocity of 2400 m/sec is shown in Figs. 6 and 7. The explosive assembly is inclined at a slight angle, as shown in Fig. 6, to establish a nearly horizontal flight path. The sandbag walls reduce blast effects on cameras and x-ray equipment. The flyer proceeds through an aperture that restricts the passage of explosion gases, allowing optical observation of plate motion after 4 meters of travel.

Protective cassettes for x-ray film, placed beside the flight path, allow three shadowgraphs to be taken just before and after impact, providing accurate position and angle data for determination of velocity, rotation rate, and impact time. A representative shadowgraph from the middle x-ray cassette is shown in Fig. 8. Argon candles provide illumination for high-speed camera coverage (1 million frames/sec) of the impact. Information describing the fuze output signal is obtained electrically. Stress wave arrival times are determined by placing piezoelectric crystals on the assembly and observing the output signals. In this experiment, a relatively large distance between the explosive and the target allowed the plate to rotate through 151° before impact, thus providing sufficient distance so that explosion gases did not interfere with either the impact or the camera view.

Experimental repeatability has been good, as indicated by the data in Table I. In general, impact times may be predicted from previous experiments within about $20 \mu\text{sec}$, even at relatively long range. The scatter in rotation rates observed in the aluminum experiments has caused some difficulty in the accurate prediction of impact angles. This scatter was caused when explosive detonation deformed an edge of the flyer plate against the guard plate, disturbing rotation predictability.

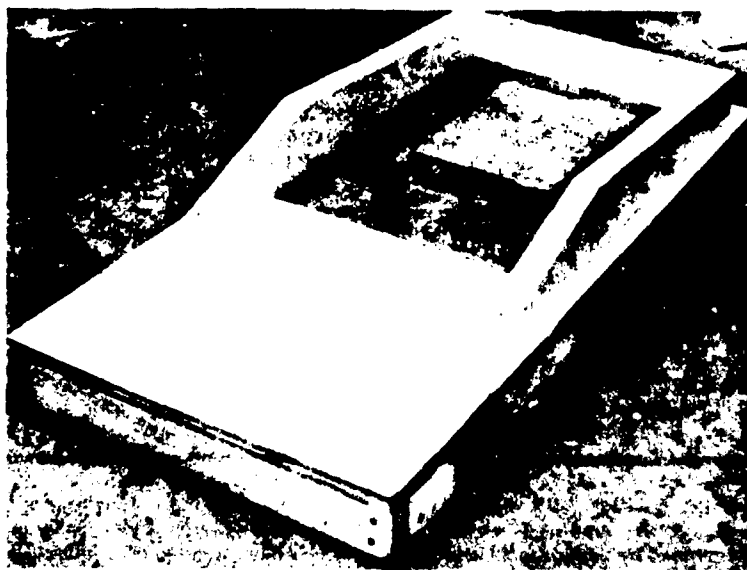


FIG. 4 ASSEMBLY BEFORE LOADING WITH EXPLOSIVE

This problem was overcome by increasing the angle of edge taper on the flyer plate. Careful alignment and a repeatable trajectory angle are critical for long-range experiments. Optical alignment coupled with excellent trajectory-angle repeatability in our test setups allow shallow-angle experiments at 10 meters and head-on impacts at 20 meters, with uncertainties of $\pm 0.2^\circ$ giving acceptably small scatter in impact locations on the plate. Lateral trajectory scatter and yaw angles have proven negligible.

Acknowledgments

The thoughtful assistance of B. W. Duggin and personnel of the Sandia Laboratories explosive firing site and the preparation of the manuscript by Mrs. B. D. Conley is gratefully acknowledged.

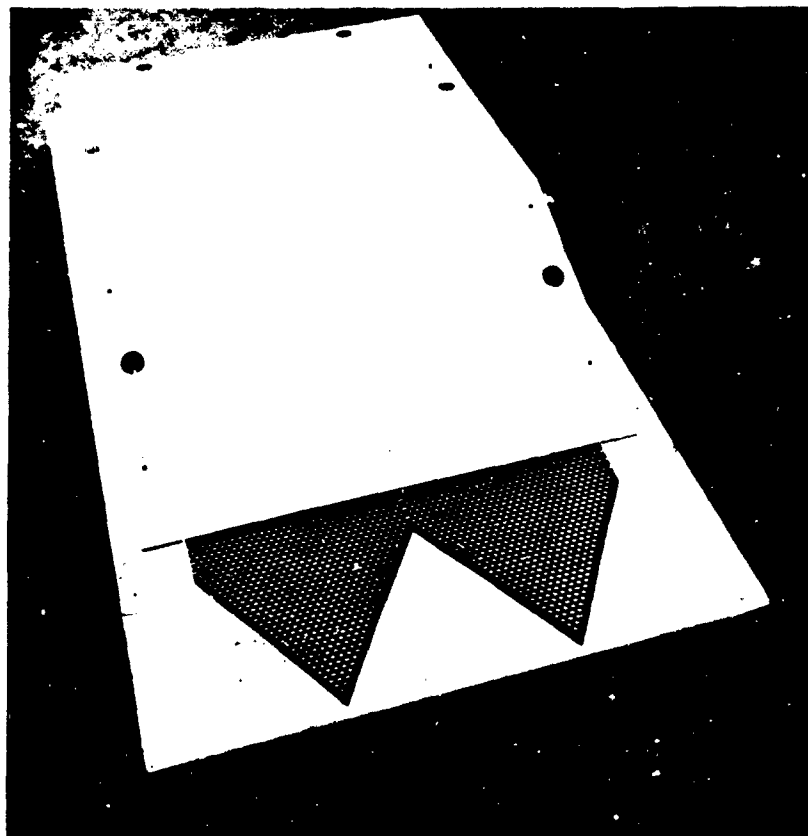


FIG. 5 ASSEMBLY AFTER EXPLOSIVE LOADING

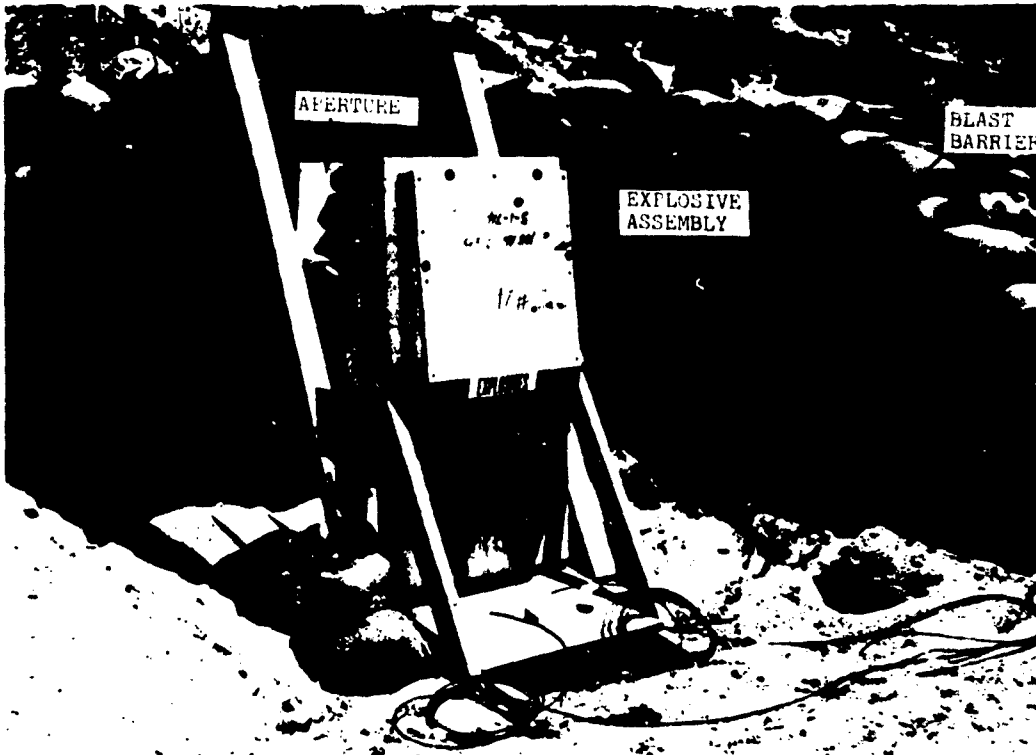


FIG. 6 EXPLOSIVE ASSEMBLY IN POSITION FOR FIRING

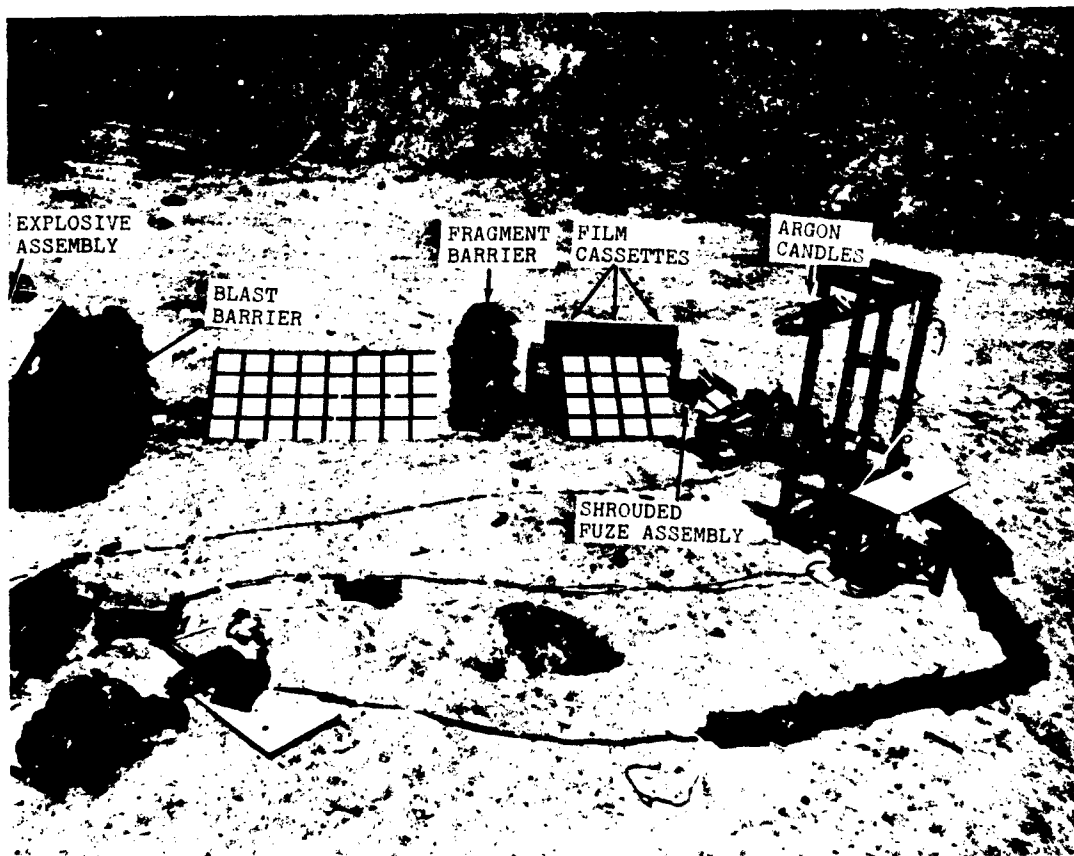


FIG. 7 EXPERIMENT ARRANGEMENT



FIG. 8 X-RAY SHADOWGRAPH OF AN ALUMINUM PLATE 0.3 M LONG, 0.25 M WIDE, AND 0.025 M THICK OBTAINED AFTER A FLIGHT OF 7 METERS. PLATE VELOCITY IS 2330 M/SEC; ROTATION RATE IS 800 RAD/SEC

TABLE I

Observed Performance⁽¹⁾ of Two Systems

Plate	Scale	Initial Velocity m/sec	Rotation Rate rad/sec	Trajectory Angle
25 mm Aluminum	Half	2400	790 (1580) ⁽²⁾	9.2
	Full	2350	1010	9.3
	Full	2350	770	(1)
	Full	2400	1000	9.4
	Full	2400	800	9.4
50 mm Nylon	Half	2380	800 (1600) ⁽²⁾	10.3
	Half	2330	890 (1780) ⁽²⁾	10.4
	Full	2370	820	10.5
	Full	2370	(3)	(3)
	Full	2380	820	10.3
	Full	2380	(3)	10.4

(1) Tolerances are approximately: velocity ± 30 m/sec, rotation ± 25 rad/sec, trajectory angle $\pm 0.1^\circ$.

(2) Higher value is observed rotation rate, table value has been adjusted by scale factor.

(3) Not determined due to short flight distance.

References

- [1] Jones, O. E., "Metal Response Under Explosive Loading," Behavior and Utilization of Explosives in Engineering Design, 12th Annual Symposium ASME. Published by The New Mexico Section ASME, March 2-3, 1972.
- [2] Hoskin, N. E., Allan, J. W. S., Bailey, W. A., Lethaby, J. W., and Skidmore, I. C., "The Motion of Plates and Cylinders Driven by Detonation Waves at Tangential Incidence," Fourth Symp. (Intl.) on Detonation, ONR ACR-126, 14-26, 1965.
- [3] Gurney, R. W., "The Initial Velocities of Fragments from Bombs, Shells, and Grenades," U.S. Army Ballistic Research Laboratory Report 405, 1943.
- [4] Kennedy, J. E., "Explosive Output for Driving Metal," Behavior and Utilization of Explosives in Engineering Design, 12th Annual Symposium ASME. Published by The New Mexico Section ASME, March 2-3, 1972.
- [5] Hoerner, S. F., "Fluid Dynamic Drag," published by author, Cambridge, MA, Library of Congress Catalog Card No. 57-13009.

IMPACT TESTING USING A VARIABLE ANGLE ROCKET LAUNCHER

M. W. Nunez
Sandia Laboratories
Albuquerque, New Mexico

This paper describes a test facility which uses a rocket powered sled to launch a test item at an impact target. The rail along which the sled is launched is capable of being elevated so that the relative angle between the line of flight and the impact target face can be varied between 90° and near 0°. A 2000 pound test unit can be accelerated to an impact velocity of approximately 200 feet per second.

INTRODUCTION

Sandia Laboratories has numerous facilities for subjecting test items, both large and small, to various types of shock, vibration or impact environments. These include such facilities as a 5000-foot rocket sled track, a 35-foot radius centrifuge, a 185-foot drop tower, various caliber guns, shock tubes, vibration tables and many others.

One such facility which has been used very successfully in the past is the Rocket Launcher Facility. This is probably a misnomer because rockets are not actually launched, but instead are used to propel a sled and test item along a guide rail until a predetermined velocity is reached at which time the test item is separated from the sled and allowed to fly free to impact with a target. This facility offers several advantages as follow:

1. Point of impact and angle of impact may be closely controlled.
2. Testing is relatively inexpensive because turnaround time is short, instrumentation is uncomplicated, temperature conditioning of a test unit is easily accomplished, and the rocket motors used cost only \$10 each. Test fixture design is also quite simple.

3. The facility provides a convenient means of testing relatively large items at fairly low impact velocities. Units weighing up to 2000 pounds can be tested at impact velocities of approximately 200 feet per second and velocities of 450 feet per second can be attained with lighter units.

LAUNCHER STRUCTURE AND TARGET CONFIGURATIONS

The main feature of the Rocket Launcher Facility is the guide or launcher rail. This rail consists of a 73 foot long, 16 inch deep wide-flange shape weighing 96 pounds per foot. One end of this beam is welded at right angles to an 8 foot long similar wide-flange shape. The ends of this short cross beam are attached to two upright frame supports by 3 inch diameter steel hinges. The free end of the long guide rail can be elevated by means of a cable passing over pulleys between upright columns on either side of the rail. Figure 1 is an overall view of the facility with the guide rail in a raised position.

Figure 2 is a closeup of the hinged end of the guide rail and the frame supports. In Figure 2, note the bolt holes on the front side of the supports. Depending on the impact angle, these holes allow the hinges to

be positioned at a location which will provide maximum unobstructed views of the impact area.

Figure 2 also shows the impact area for most test conditions. The area between the frame supports is in the form of a shallow pit 6 feet wide by 14 feet long by 15 inches deep. Normally, this pit is filled with tamped dirt to a depth of 3 to 4 inches and a reinforced concrete slab 12 inches thick is placed

on top to provide an impact surface. First impact and secondary impact or slapdown will occur on this surface.

The guide rail can be elevated to approximately 60° from the horizontal. By placing the guide rail in a horizontal position, test items can be launched against vertical or near vertical targets. Typical targets for this type testing are massive concrete blocks or soft dirt banks for soft recovery.

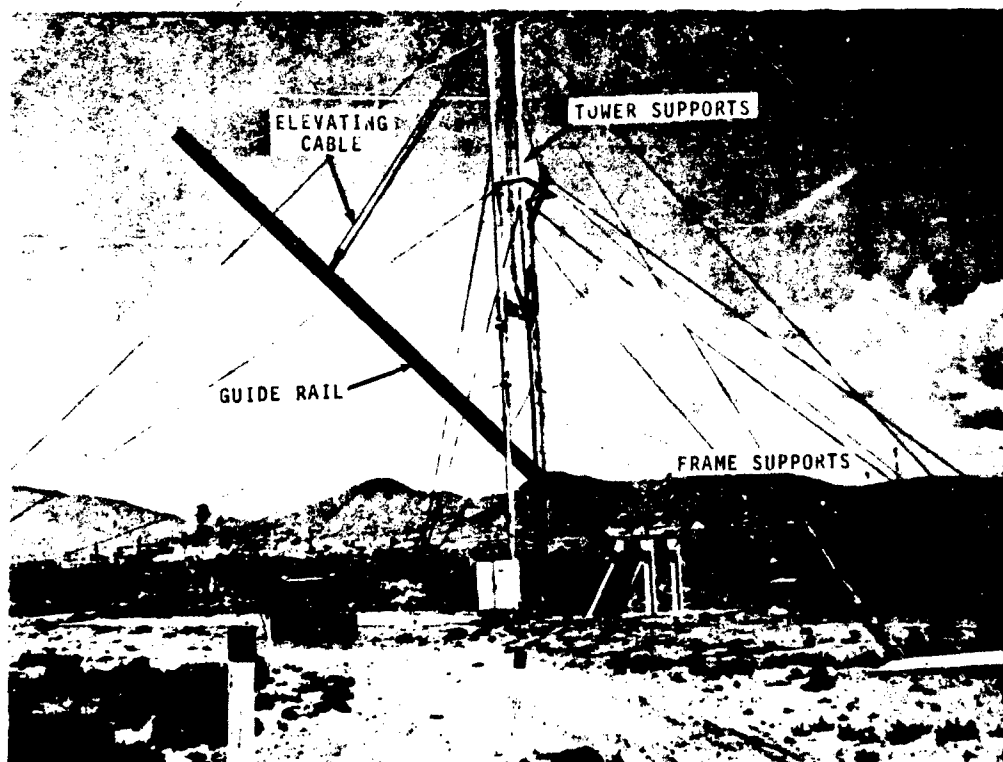


Figure 1 - Rocket Launcher Facility

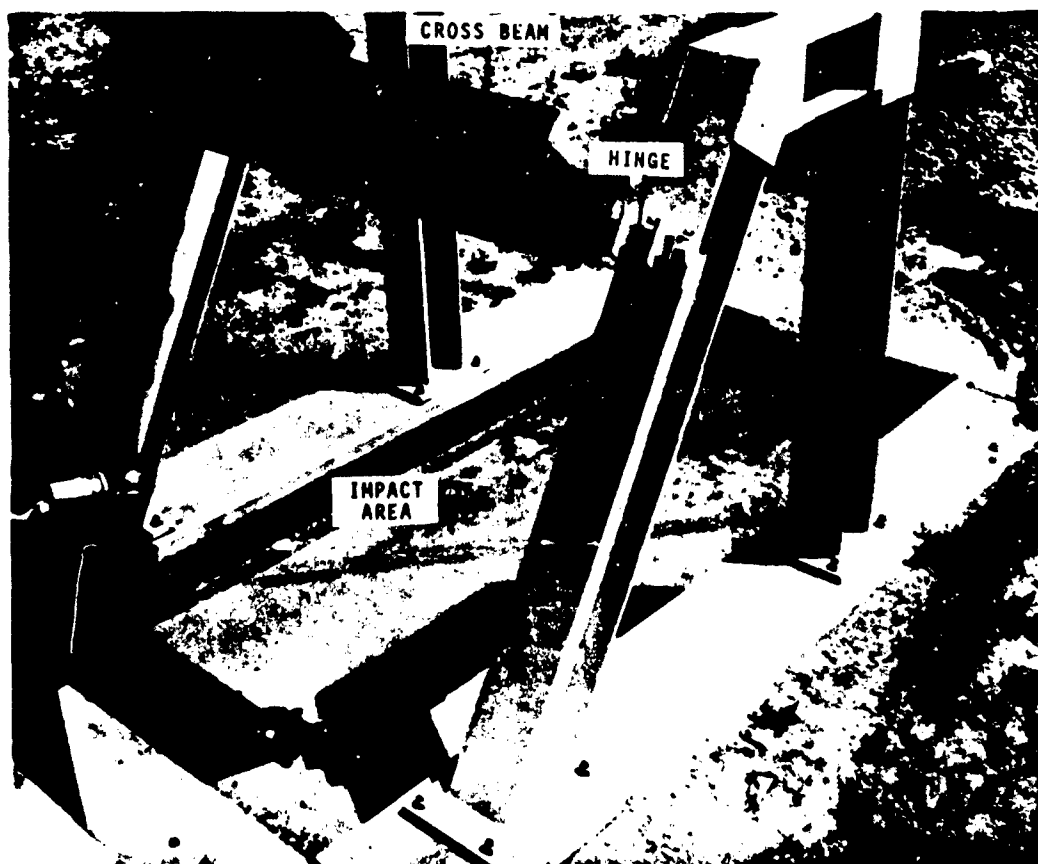


Figure 2 - Lower Support Frames and Impact Area of Rocket Launcher Facility

SLED STRUCTURE

The sled which carries the test item is a welded steel structure designed to ride on the inside surface of the lower flange of the guide rail. A typical sled is shown in Figure 3. The test item is suspended below the sled on a set of special hangers or a specially designed sub-carriage. This carriage is designed to support the test item and to push it forward during the thrusting phase of rocket burn. Figure 4 shows a unit suspended from the sled prior to installing rocket motors. For angle impact tests, a test unit is tied back to the beam with a "weak-link" which breaks when the rockets start to thrust.

At the end of a run, the sled is stopped by impacting against aluminum honeycomb. When this sled deceleration occurs, the test item slips forward off the hangers and continues in free flight to impact.

The sled has provisions for mounting rocket motors on each side of the center web and in the area between the upper and lower flanges of the guide rail.

ROCKET MOTOR CHARACTERISTICS

The rocket motor used on almost all tests is a U.S. Navy High Velocity Aircraft Rocket (HVAR). This solid propellant motor is 5 inches in diameter and 51 inches long. It weighs

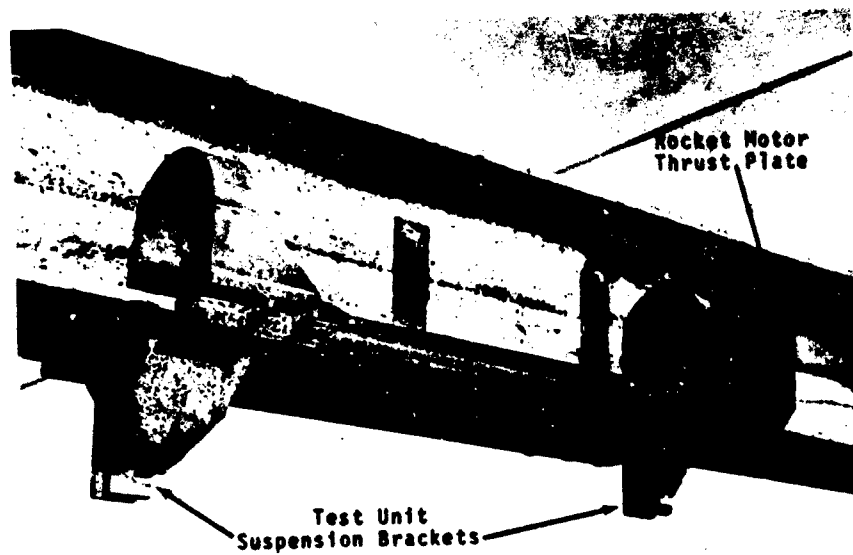


Figure 3 - A Typical Sled

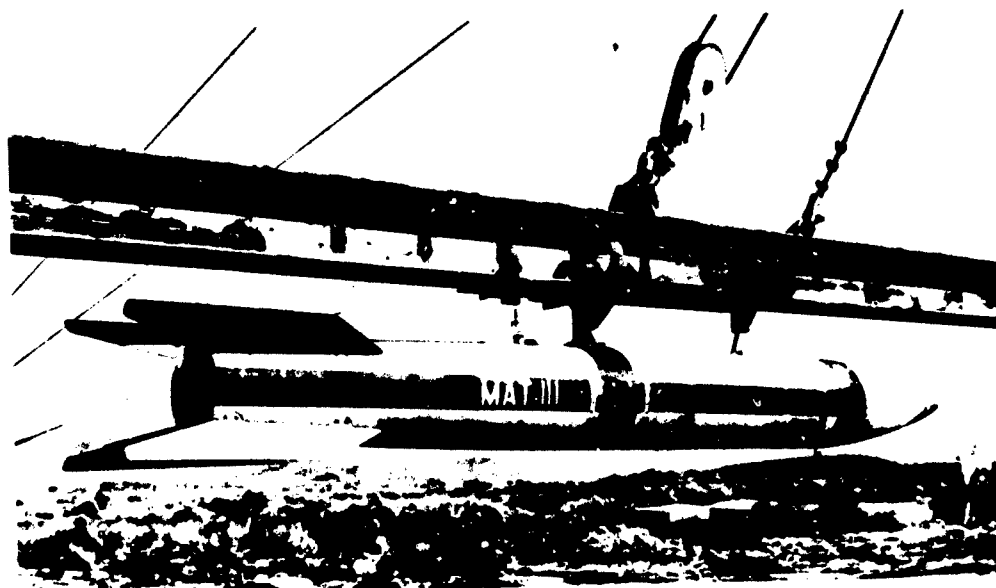


Figure 4 - Unit Suspended From Sled
Prior to Rocket Motor Installation

82 pounds and has a maximum impulse of 5150 lb-sec. The burn time of the motor is nominally 1.1 seconds and the average thrust over this period is 4740 lb.

TRAJECTORY CALCULATIONS

The basic procedure for calculating position vs time or trajectory of the rocket launcher sled is as follows:

- Step 1. Determine the number of motors required to propel the given weight to the desired velocity from:

$$n = \frac{(W) (V)}{(32.2) (T_a) (t)}$$

where: n = number of motors

W = initial launch weight, pounds

V = desired velocity, feet per second

T_a = average motor thrust, pounds

t = motor burn time, seconds

- Step 2. After determining the number of motors required - usually 2, 4 or 6 - solve Step 1 for the time required to attain the desired velocity.

- Step 3. Verify that the travel distance required is within the limits of the Rocket Launcher guide rail from:

$$\text{Distance, feet} = \frac{(\text{Velocity}) (\text{Time})}{2}$$

Example: Assume a total weight (carriage, test item and rocket motors) of 2400 lb. is to be accelerated to a velocity of 300 ft/sec.

From Step 1.

$$n = \frac{(2400) (300)}{(32.2) (4740) (1.1)} = 4.28$$

Use 6 motors

From Step 2.

$$t = \frac{(2400) (300)}{(6) (32.2) (4740)} = 0.79 \text{ sec.}$$

From Step 3.

$$\text{Distance} = 1/2 (300) (.79) = 119 \text{ ft.}$$

But the guide rail is not this long, so this velocity is unattainable with these motors.

Example: Assume a total weight of 400 lb. is to be accelerated to a velocity of 200 ft/sec.

From Step 1.

$$n = \frac{(400) (200)}{(32.2) (4740) (1.1)} = 0.5$$

Use 2 motors

From Step 2.

$$t = \frac{(400) (200)}{(2) (32.2) (4740)} = 0.26 \text{ sec.}$$

From Step 3.

$$D = 1/2 (200) (.26) = 26 \text{ feet}$$

In actual practice, a computer program is used to provide a print-out of distance, velocity and acceleration for each 0.050 second period based upon the weight of the test item and the number of motors used. This program is quite refined and considers the decreasing mass of the rocket motors as the propellant is burned as well as the thrust vs time characteristics of the rocket motor.

Typically, using six HVAR motors, a 2000 lb. test unit can be propelled to a free flight velocity of 200 feet per second or a 50 pound test unit can be propelled to approximately 450 feet per second.

INSTRUMENTATION

Almost all types of conventional transducers have been used at this facility. These included accelerometers, strain gages, thermocouples, crush switches, etc. Due to the relatively short travel distance

(80-100 feet) of the test unit, it is possible to hardwire between the transducers and an instrumentation patch panel located at the base of the tower.

High speed motion picture cameras are also used on all tests to record impact motions.

By building lightweight, expendable enclosures around a test item suspended from the sled, it is possible to temperature condition a unit prior to testing. Temperatures of -65° and + 165° F have been attained.

DISCUSSION

Voice: I just have one question. I noticed you had it hard wired for your data retrieval and I was wondering about what percentage of survival you had of the leads? Your going up about what, 400 feet/sec?

Mr. Munoz (Sandia) So far we have been running in the range of 200 ft/sec for hard wired data and the retrieval has been surprisingly good. We've tried to develop techniques to keep the cable out from underneath the slap-down and so far we've been reasonably successful. One of the problems we are facing is the everpresent problem of noise in moving cables.

Voice: Yes we've had similar problems, I just wanted to know how the other side was doing.

EVALUATION OF THE SHOCK PULSE DIAGNOSTIC
TECHNIQUE TO THE UH-1 SERIES HELICOPTER

J. A. George*, T. C. Mayer†, E. F. Covill†
Parks College of Saint Louis University
Cahokia, Illinois

The use of shock pulse techniques as a diagnostic tool for the UH-1 series helicopter was investigated. A standard off-the-shelf SKF Industries model MEPA-10A was employed to construct shock emission envelopes of shock rate versus shock level. Operational helicopters of a Reserve Army Aviation unit were available and data was collected on the hanger bearings of the tail rotor assembly as well as the 42° gearbox. Selected hanger bearings and gearboxes were removed for teardown analysis. Further data was obtained from helicopters at Fort Rucker, Alabama, with known implants in the 42° gearbox. The correlation between shock emission envelopes and degree of degradation is described. The shock pulse meter does show promise for its ability to separate those hanger bearings and 42° gearboxes with normal wear, or the onset of damage, from those with severe damage.

INTRODUCTION

The U.S. Army Aviation Systems Command (AVSCOM) has an ongoing program to develop a system which will automatically accomplish inspection, diagnostic, and prognostic maintenance functions on related subsystems of the UH-1 helicopter. This program, called AIDAPS, is intended to provide equipment which will contribute to an increase in the tactical mobility of Army aviation operations and provide an effective reduction in aircraft maintenance costs and maintenance related accidents.

Past efforts (1-3), have included the collection of vibration data with a subsequent analysis of the resulting Power Spectral Densities to determine the condition of the helicopter powertrain. Another approach, particularly in determining bearing condition, is to use shock pulse techniques. The technique and instrumentation were devel-

oped by AB SKF, Sweden and are available in the United States through SKF Industries, Inc. (4). When a bearing race or rolling element contains a discrete fault, such as a pit or spall, the rolling contact between this fault and the other rolling elements will result in repetitive impacts of short duration. As a result of these impacts, a shock wave travels through the bearing housing causing a pulse displacement input to a suitably mounted accelerometer. The output of the accelerometer is passed through a high gain amplifier tuned at the resonant frequency of the accelerometer, in this case, 38 kHz. The amplifier acts as a sharp band-pass filter. After the signal is processed, a meter on the face of the instrument gives output information. The meter registers the frequency of peaks above a preset shock pulse amplitude threshold.

PRELIMINARY EVALUATION

A preliminary evaluation (5), of the feasibility of using pulse techniques to the UH-1 series helicopter (Figure 1) was conducted by Parks College under contract to AVSCOM. A standard off-the-shelf SKF Industries

*Professor, Aerospace Engineering
Department
†Research Associate



Fig. 1 - UH-1H helicopter

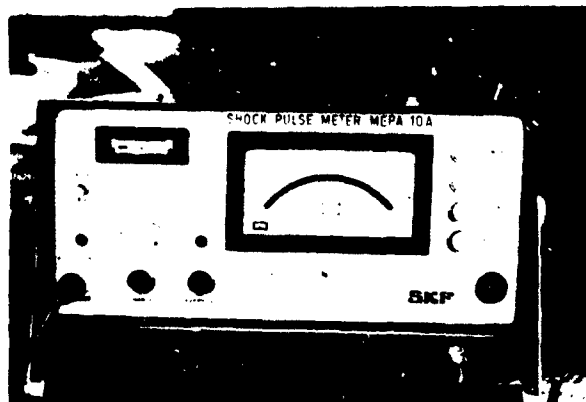


Fig. 2 - Model MEPA-10A Shock Pulse Meter

Model MEPA-10A Shock Pulse Meter (Figure 2) was employed to construct shock emission envelopes of shock rate versus shock level. The study concentrated primarily on the hanger bearings of the tail rotor assembly on the UH-1 helicopter. Shock emission data was collected from laboratory tests and ground runs on "good" and "bad" bearings.

In constructing the shock emission envelope (Figure 3), the first point plotted on the ordinate axis is the rate, in pulses per second, at an amplitude level of cne. A threshold varying dial on the MEPA-10A meter

housing ranges from a level of one to ten thousand in a logarithmic scale. As the threshold is increased, successive rates are plotted until the curve crosses the abscissa. The value at the intercept becomes the highest potentiometer level at which at least one shock pulse per second can be measured. In plotting the data points, a period of integration time is allowed to ensure accuracy. This integration time is noted in the left-hand margin of the shock emission curves. The rate is given in pulses per second and the level obtained is in relation to the potentiometer level which is a function of the accelerometer used.

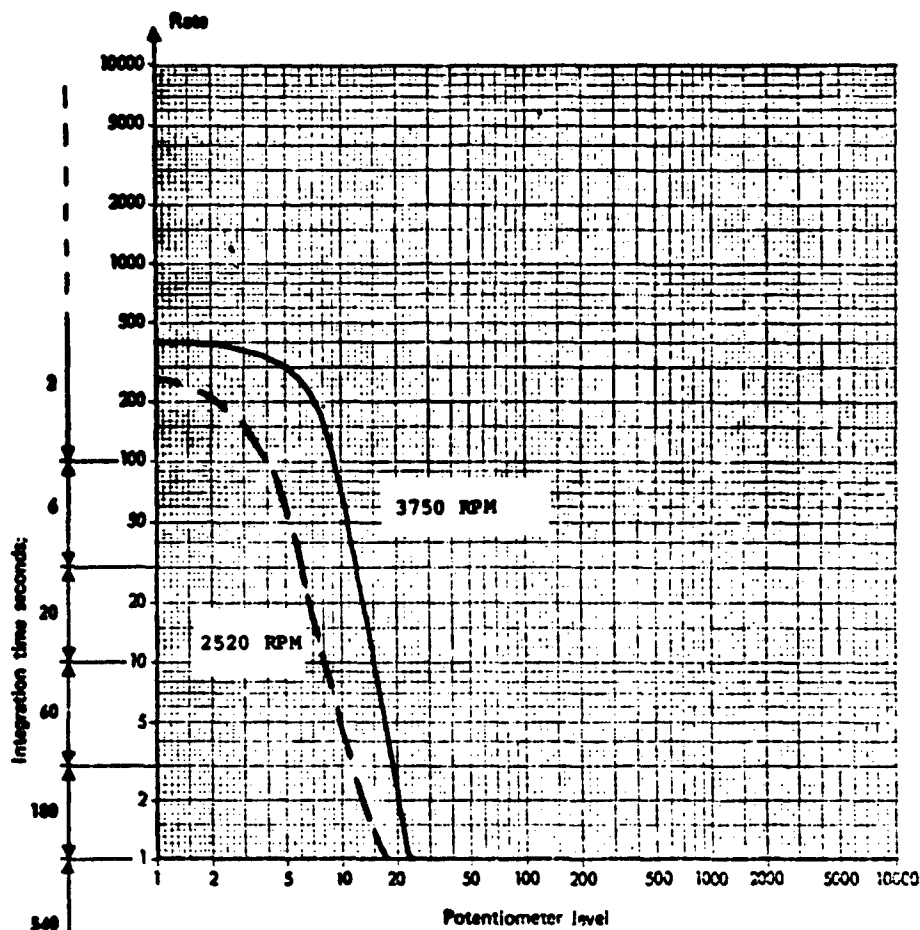


Fig. 3 - Shock emission envelope showing speed dependence

The preliminary investigation showed the technique to be promising. The laboratory findings provided the necessary experience and methodology to be utilized on the actual UH-1 aircraft. The major results were:

1. Accelerometer placement and attachment are critical. SKF provides a vice-grip on which an accelerometer is attached. Significant differences were found in readings dependent on placement and security of the vice-grip attachment. A pressure clamp has been fabricated which can be fitted to the lands of the bolts which

hold the bearing fixture in place. The accelerometer, in turn, is attached to the pressure clamp. Shock rates and levels are now easily reproducible for a given bearing assembly.

2. The shock rates and levels are speed dependent. Figure 3 shows the shock emission curve at two different rpm.
3. The general shape of the shock emission curve varies with the type and extent of damage. Figure 4 has representative curves for a new bearing, a

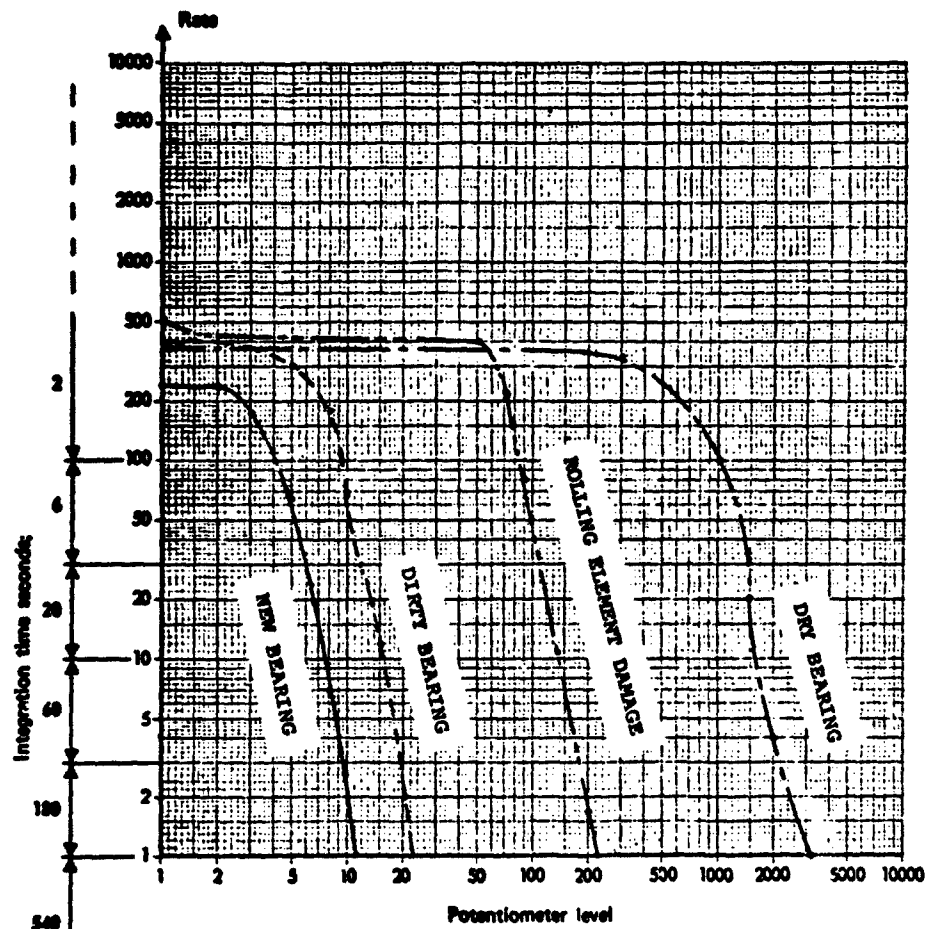


Fig. 4 - Comparison of new and damaged hanger bearings

bearing with dirty lubricant, a dry bearing, and one with rolling element damage. In each case, the damaged bearing shock emission curve exhibits increases in rate and level over that of the new bearing.

4. Although a damaged bearing could be discerned, it was not possible to localize damage as to the inner or outer race, rolling element, etc.
5. Laboratory readings of rate versus level differed from those of the same bearing assembly installed on a UH-1H helicopter (Figure 5). Thus, generalized damage assessment

curves must be generated with the bearing in the actual operating environment.

UH-1 SERIES HELICOPTER DATA COLLECTION

Upon completion of the preliminary evaluation, the College undertook to collect additional shock pulse data. Initial efforts concentrated on building up a data bank of shock emission curves of hanger bearings of the tail rotor assembly and the 42° gearbox as installed on operational helicopters (Figure 6).

UH-1 type helicopters were made available by a Reserve Army Aviation unit stationed near the College. Data was collected on three models: UH-1D, UH-1H and UH-1M. The federal stock

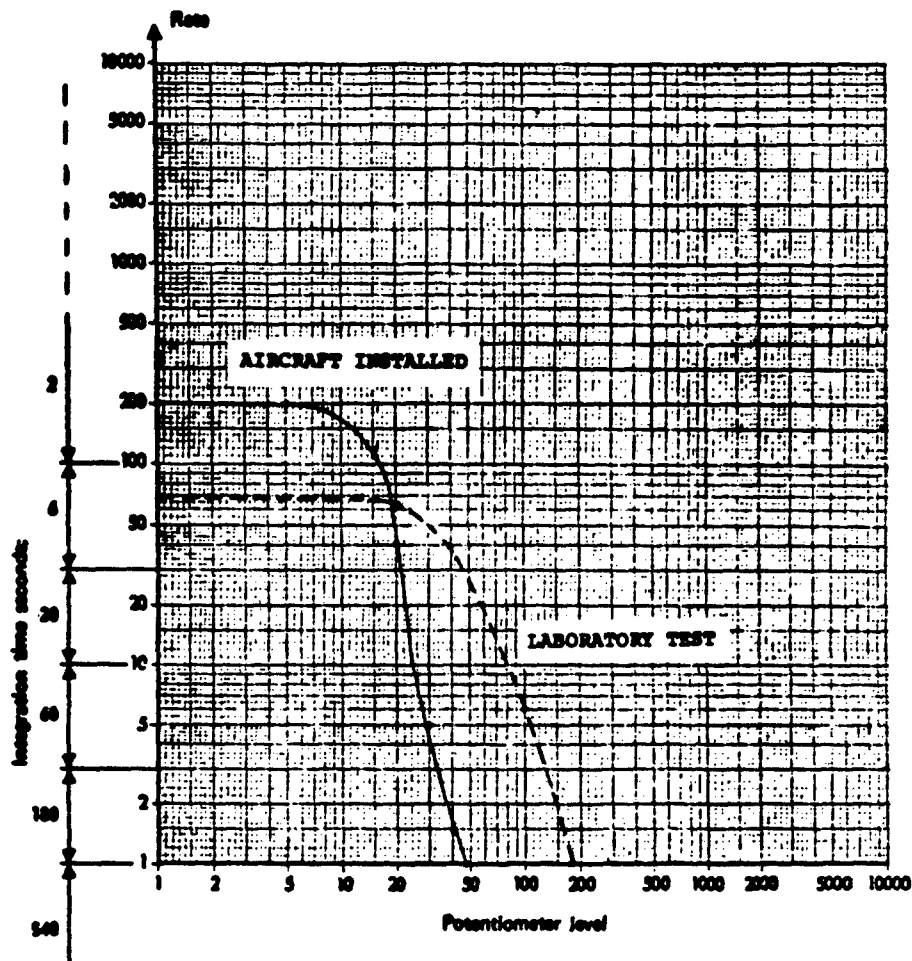


Fig. 5 - Comparison of shock emission envelopes obtained from a hanger bearing in laboratory test and as installed in aircraft.

Fig. 6 - Tailrotor drive-shaft and 42° gearbox assembly, UH-1H helicopter

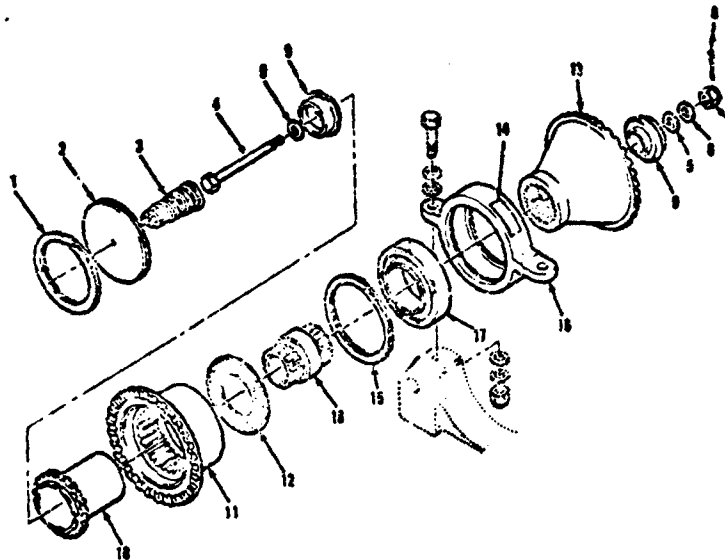


number for all hanger bearings and for those on the 42° gearboxes is the same for these series of helicopters. Differences are only in the number of hanger bearings with the UH-1D and -1H having four hanger bearings, while the UH-1M has three. The aircraft were made available on a noninterference basis. No modifications could be made which would result in the aircraft being in a nonflyable status nor any interference with the normal maintenance routine or flight operations. The pressure clamp attachment described previously greatly facilitated the rapid setup and recording of data.

teardown analysis. These were selected on the basis of shock rates, potentiometer levels, or unusual shock pulse curve characteristics. The time since overhaul for these hanger bearings ranged from zero to over five hundred hours.

The shock rates were found to vary from 55-340 pulses per second. Approximately half of the hanger bearing rates were between 100-200 pulses per second. Statistically, the sample mean rate was 184 with a standard deviation of 86. The potentiometer levels of the hanger bearings tested

Fig. 7 - Tailrotor driveshaft hanger bearing assembly, UH-1H helicopter



All tests were ground runs at a $N_2 = 6600$ rpm. This gives a tail rotor drive shaft speed of 4300 rpm. Selected hanger bearings and gearboxes were removed for teardown analysis. Pulse signatures were then correlated with the teardown analysis.

A second phase concerned data collected from the helicopters in use in the AIDAPS program being conducted at Fort Rucker, Alabama. This phase included 42° gearboxes with known implants.

HANGER BEARING ANALYSIS

Twenty-nine hanger bearing assemblies were tested, including originally installed and replacement bearings (Figure 7). Eight were removed for

varied considerably; the range of levels were from 45 to 6000 units. However, approximately two-thirds were between 45 and 200 units. The sample mean and standard deviation were found to be 558 and 1192 respectively.

Eight hanger bearings, with potentiometer levels from moderate to high, were selected for teardown analysis. This work was performed by the Bell Helicopter Company. Teardown analysis revealed that defects, if they existed, consisted primarily of pitting and corrosion varying from slight to severe. The data has been summarized in a single shock emission envelope which can be used to separate hanger bearings of normal wear (or the onset of damage) from those of severe damage (Figure 8).

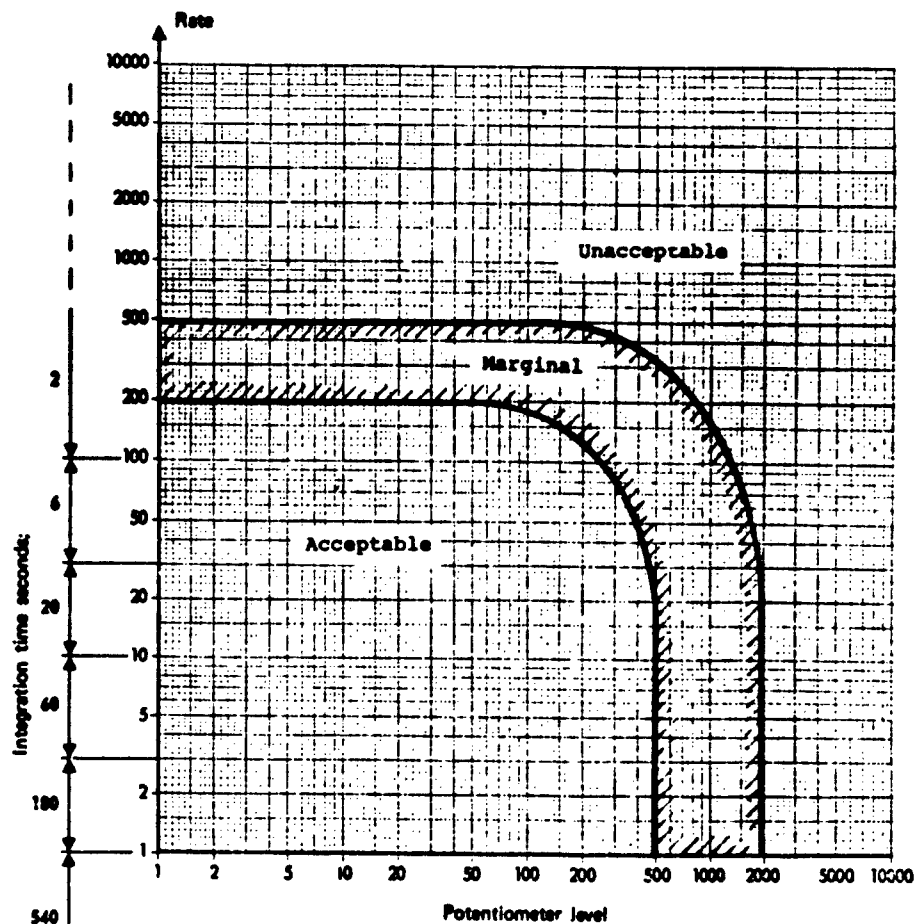


Fig. 8 - Shock emission envelope to determine hanger bearing condition

Figure 9 shows the shock pulse curves for two hanger bearings removed from UH-1H aircraft which would normally warrant their rejection at overhaul. Figures 10 and 11 are pictures of corrosion and pitting damage found on the ball bearing and outer race of hanger bearing with the lesser potentiometer level reading. Figures 12-14 show the evidence of pitting and corrosion on the ball bearings as well as both inner and outer races for the second of the two hanger bearings given in Figure 9. It was also noted that the bearing rotated roughly before teardown.

Whenever a hanger bearing was re-

moved for teardown analysis, readings were taken on the new, or rebuilt, replacement bearing. In each case, a marked reduction in potentiometer readings was noted. Figure 15 compares a damaged hanger bearing (that shown in Figures 9-11) with its zero time replacement. The potentiometer levels of the zero time hanger bearings were found to vary typically from 50 - 100 units.

Additional data was collected on hanger bearings installed on helicopters involved in the AIDAPS program at Fort Rucker. These hanger bearings were inspected and found acceptable prior to their use in that program.

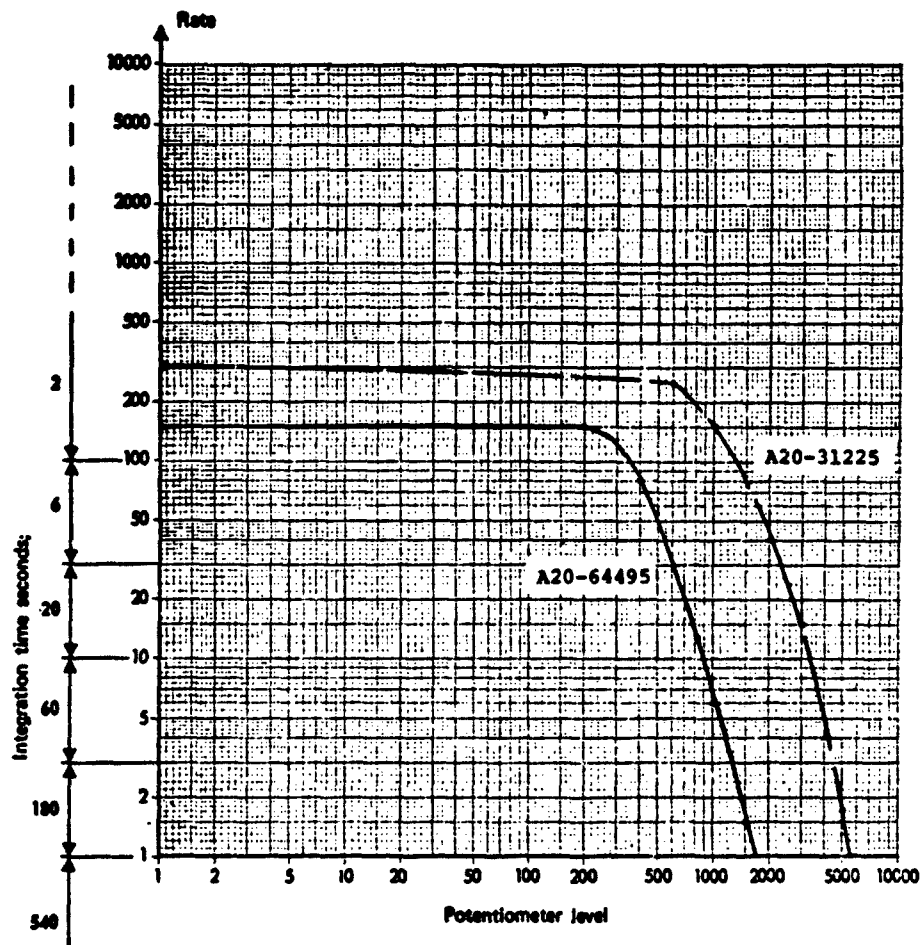


Fig. 9 - Two examples of hanger bearings which warrant replacement



Fig. 10 - A20-64495 - Corrosion
Damage on ball bearing

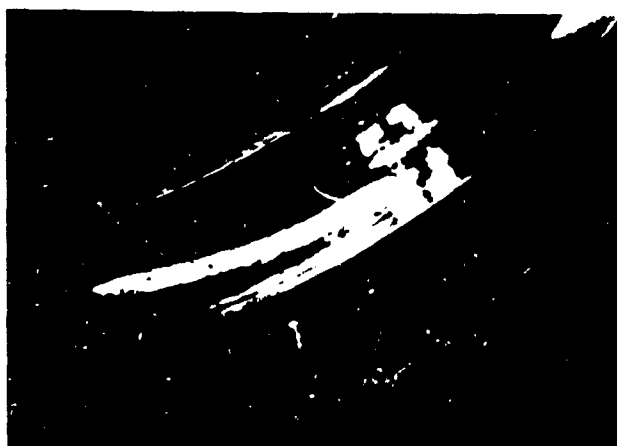


Fig. 11 - A20-64495 - Corrosion
and pitting on outer
race



Fig. 12 - A20-31225 - Corrosion
and pitting on outer race



Fig. 13 - A20-31225 - Corrosion
damage to inner race



Fig. 14 - A20-31225 - Corrosion and pitting on ball

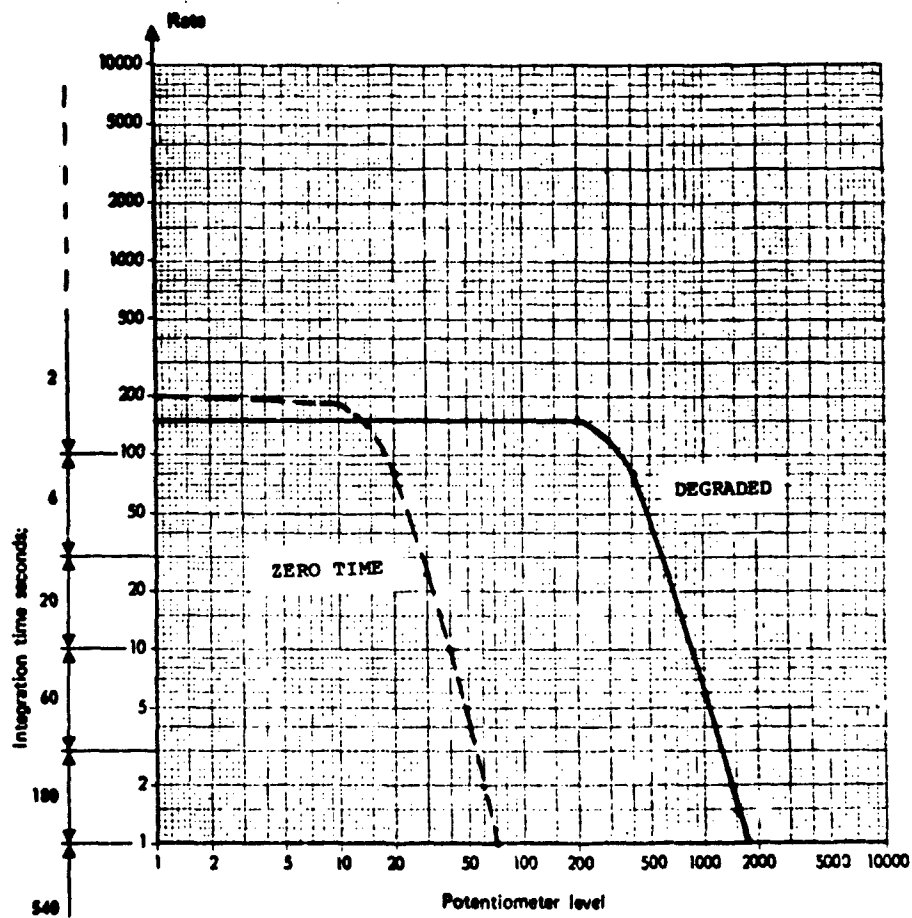


Fig. 15 - Comparison of degraded hanger bearing and its zero time replacement

Figure 16 shows the effect of engine rpm variation and anti-torque pedal (tail rotor) inputs on the number 4 hanger bearing. The difference between flight idle data and that at 6400 and 6600 is apparent. At a

given N_2 , pedal deflection gives a slight increase in the potentiometer level, generally shifting the shock pulse curve to the right. Similar results were obtained on the number 3 hanger bearing.

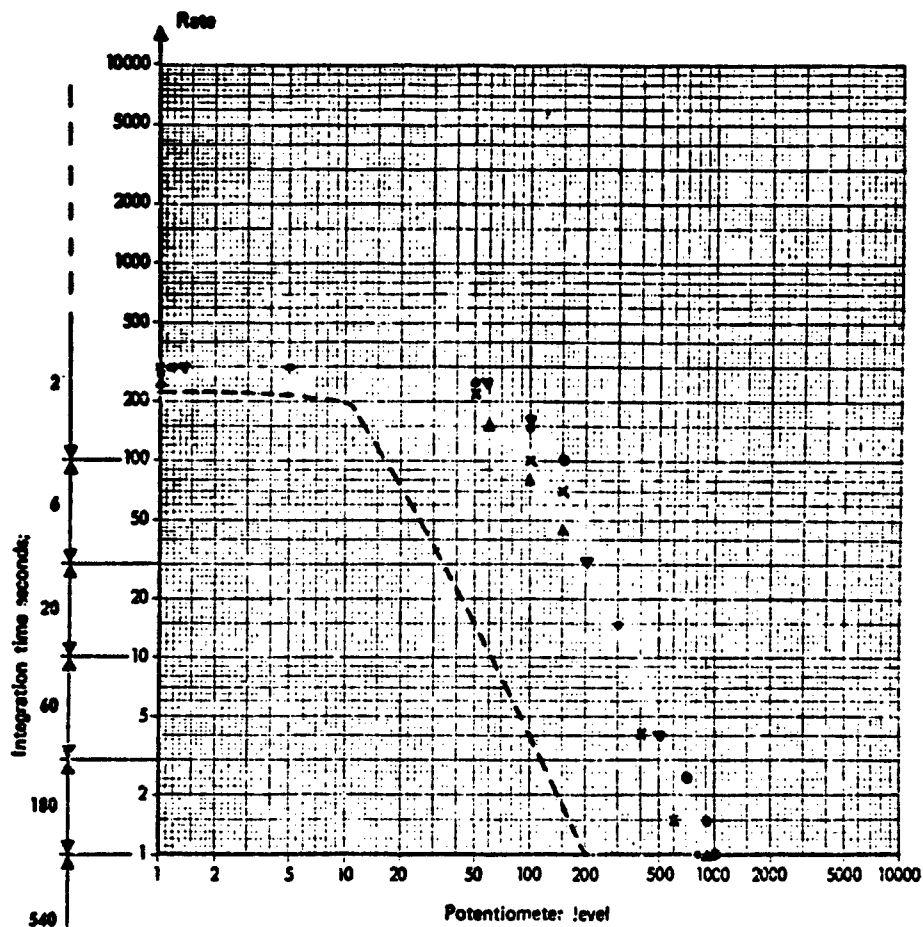


Fig. 16 - Tie-down tests, Fort Rucker, Alabama
Bearcat 14 (S/N 65-9846)

run	symbol	engine rpm	anti-torque pedal
1	----	flight idle	neutral
2	.	6400	full right
3	.Δ	6400	full left
4	x	6600	neutral
5	o	6600	full right
6	▽	6600	full left

42° GEARBOX ANALYSIS

Shock pulse data was collected on 42° gearboxes installed on nine Reserve unit helicopters. The 42° gearbox consists of two bearing packages, one used for the input drive quill and the other used on the output drive quill assembly (Figure 17). The attachment of the pressure clamps to the input and output side of the gearbox is shown in Figure 18.

The gearboxes proved to be quite consistent in their shock emission profiles and, therefore, difficult to determine a removal criteria. The shock rates for both input and output quills ranged from 75 to 600 pulses per second with the sample mean rate and standard deviation being 221 and 151 respectively. The potentiometer levels varied from 45 to 300 units with a mean of 133 and a standard deviation of 70. Nevertheless, four of the gearboxes were removed for teardown analysis, primarily due to peculiarities

in curve shape rather than excessively large shock rates or levels.

The teardown analysis did not reveal any extreme conditions of wear or damage. The various bearing elements did exhibit evidence of small pits and scratches, false brinelling, and small spalls. Some of the gears had unacceptable wear patterns. Bell did not classify the defects as to severity or flight worthiness.

As was mentioned earlier, the gearboxes were removed primarily because of an unusual shock pulse curve rather than abnormally high readings. Figure 19 shows such a curve. At a fixed potentiometer level, the rate would not stabilize at a single value but would vary between the limits shown. This swing could be due to the multiple bearing and gear assemblies present in the quills as well as accelerometer placement. Teardown analysis did indicate corrosion and pitting throughout the output inner

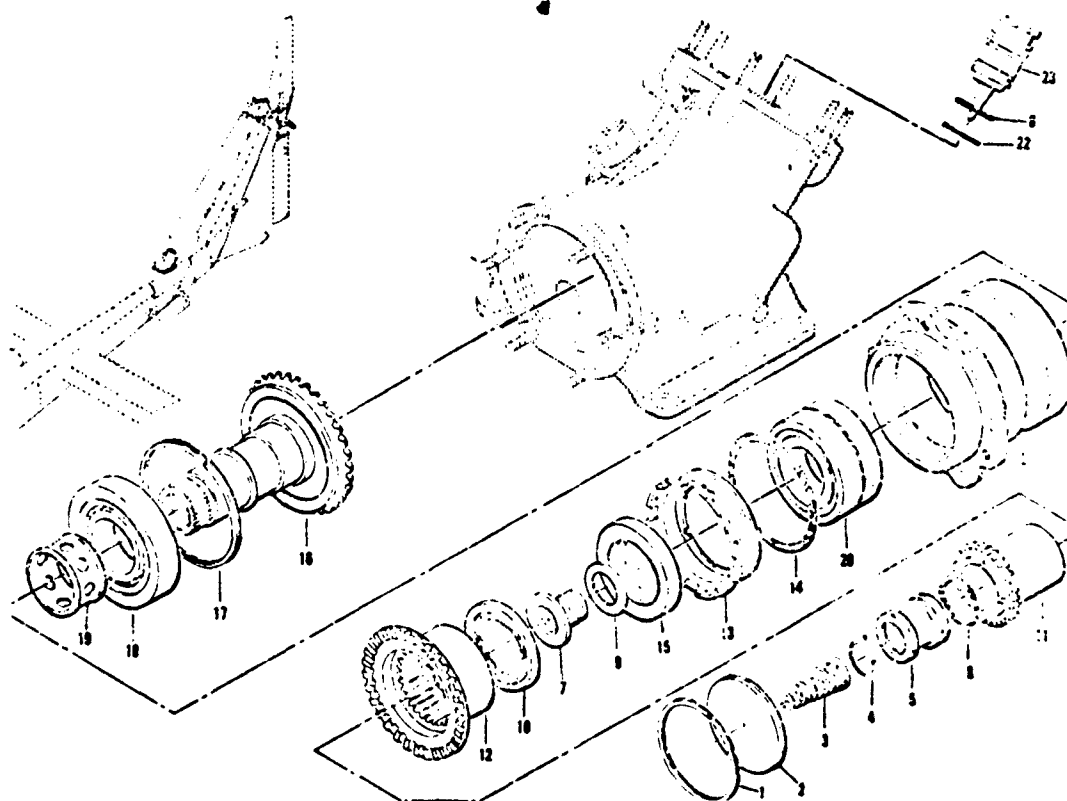


Fig. 17 - UH-1H 42° gearbox assembly

Fig. 18 - Accelerometer
attachments
to 42° gear-
box assembly

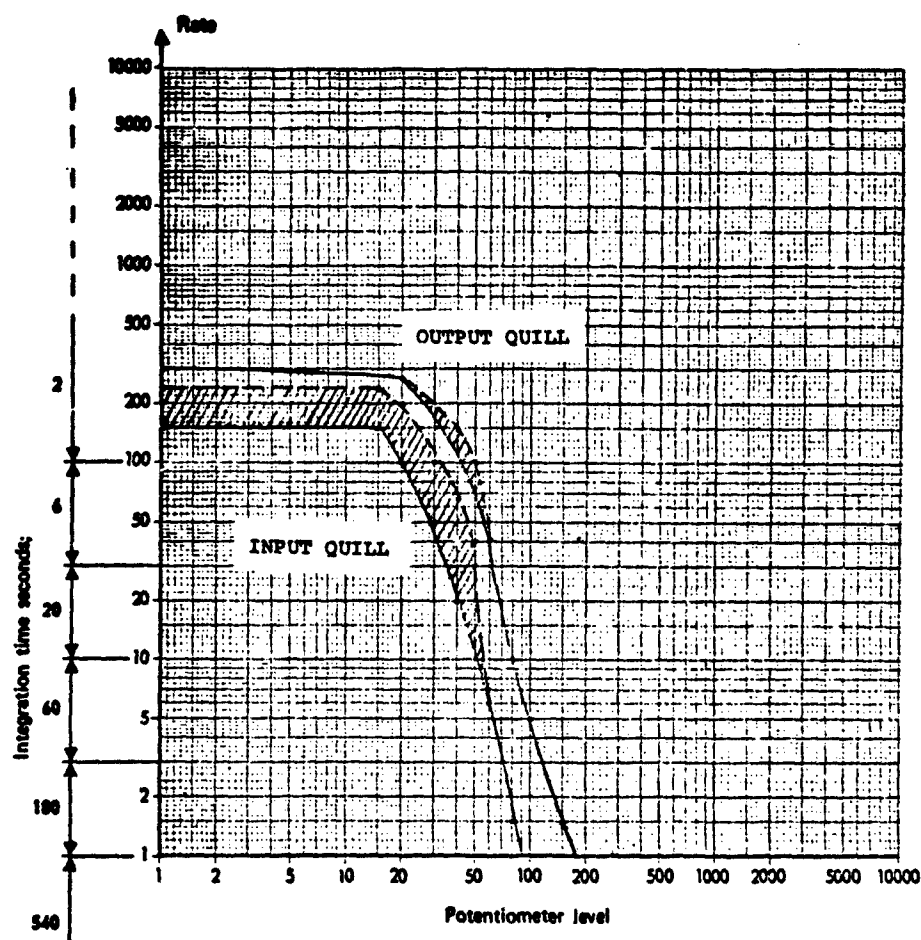
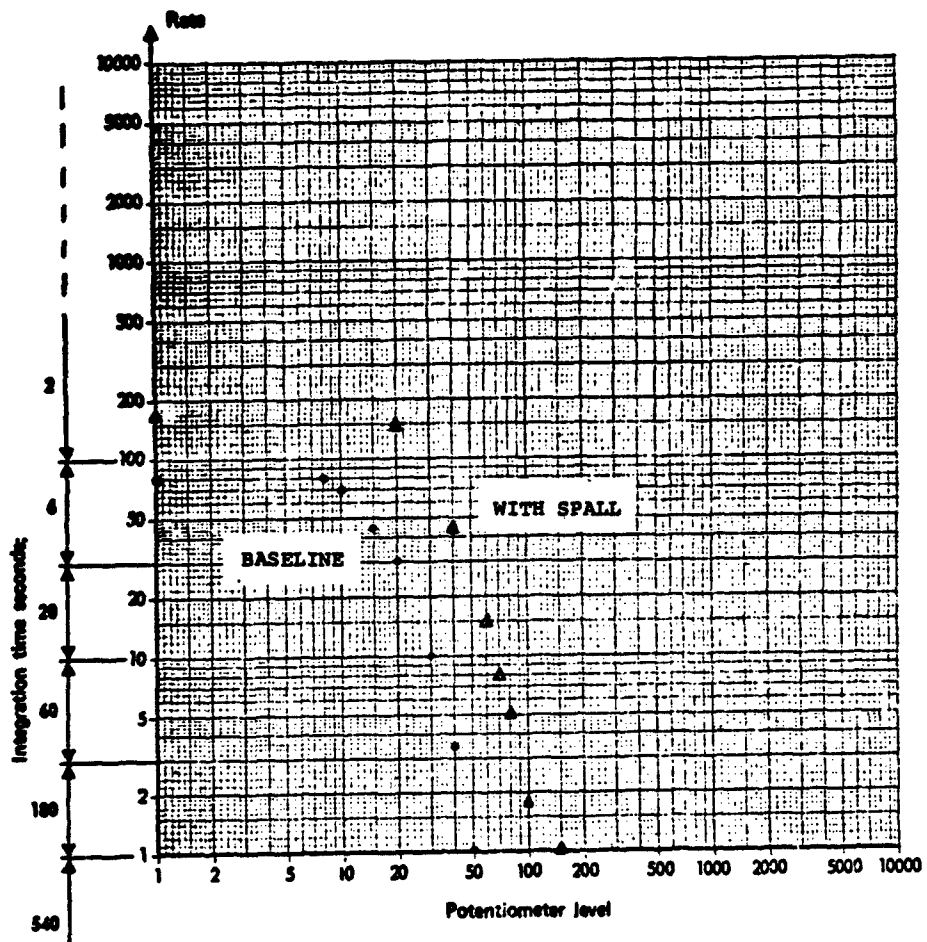


Fig. 19 - Shock pulse curve of 42° gearbox removed for
teardown analysis. Lined areas indicate
variation in output readings.



an outer ball (Figure 20-22), radial scratches in the output roller bearing, and output gear pattern too high and too far towards the toe, as well as pits on the input ball and roller bearings.



Fig. 20 - Output, inner bearing, corrosion damage on outer race



Fig. 21 - Output, inner bearing, corrosion on ball



Fig. 22 - Output, outer bearing, corrosion and pitting on outer race

The data collected on the AIDAPS helicopters was from gearboxes of known condition. Each gearbox was completely disassembled, inspected, and any necessary component replacement accomplished prior to reassembly and use in the program. The data included that from an implanted input quill duplex bearing (item 20, Figure 17) with known defects.

Figure 23 shows the shock pulse curve for the "sanitized" gearbox as well as one with an implanted duplex bearing. In this case, the outboard half of the duplex bearing had a single spall in the outer race, 0.14" x 0.14", with a definite depth; the inboard half had some corrosion caused pitting with one pit in the ball's path (Figure 24, 25). This damage was classified in category C which corresponds to moderate spalling.

A second duplex ball bearing, this one with a single shallow spall approximately 0.08" x 0.08" in the outer race, was implanted in another 42° gearbox. Of particular interest was the observation of progressive damage while the test was in progress. The shape of the shock emission curve changed continuously over a period of minutes in both rate and shock level. Figure 26 shows two curves developed on a single run. A change in slope takes place (A), a sharp increase in rate (B-C), a continual change in slope (C-D). Without shutting down the engine, the second curve (E-F-G) was

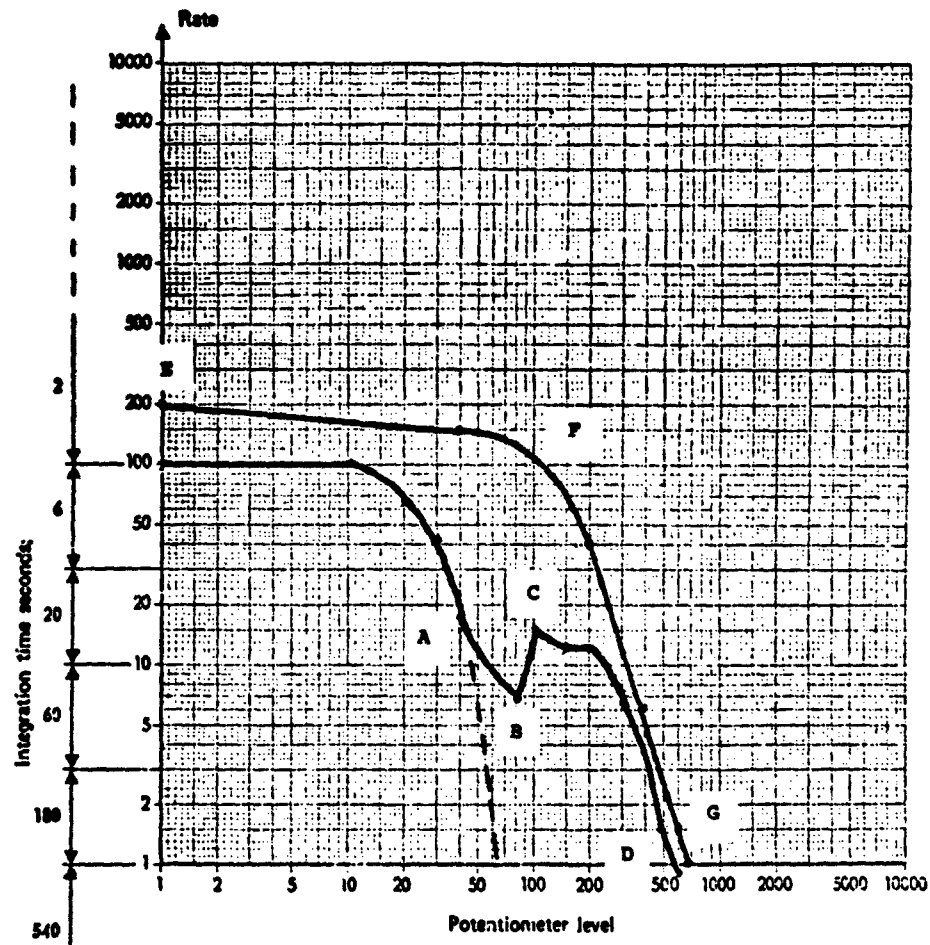


Fig. 26 - 42° Gearbox implanted with a spalled duplex ball bearing. Evidence of damage progressing.

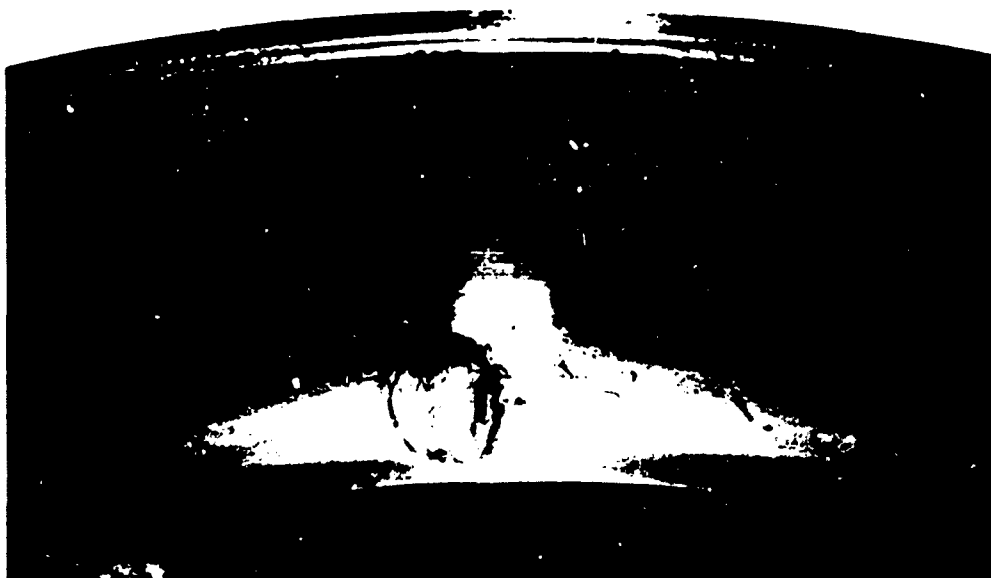


Fig. 24 - Spall in outer race of duplex bearing
implanted on 42° gearbox



Fig. 25 - Corrosion caused pitting in outer race of
duplex bearing implanted in 42° gearbox

DISCUSSION

Mr. Matteson: (NSWC) You indicated that you had some difficulty in getting consistent readings in your earlier tests. Were the inconsistencies due to the non-rigid support of the accelerometer or of the accelerometer itself?

Mr. George: The non repetitive readings were due to the fact that we used off the shelf equipment. The Army purchased it and asked the college to evaluate it. The original piece of equipment had a very large pair of vise grips and you simply clamped them on the bolt or somewhere on the structure; the accelerometer was mounted on the head of the vise grips. The problem was that two people could clamp with different degrees of severity so we could not get repetitive readings under that system. All of the data I have presented here is with the pressure clamp that was shown in the figures themselves, that is the pressure clamp would be mounted on the land of the bolt and then the accelerometer was screwed in to the mount itself. So I mention that as a problem of the off the shelf piece of equipment rather than a problem with the data. We do have some difficulty with repetition and if we make a run and find something abnormally high we try to find the cause. Usually it is very easy to find that the pressure clamp is not tight or the accelerometer is not screwed in properly, it is very evident, it is a quick check. We

have built up enough background so that if something becomes abnormal we have actually been able to classify it as either high rates or high levels of setting where I get a band of rates, or a time varying curve where damage actually progresses with time. These are the four categories which we look for. I might add that we have also had one transmission that we suspected and also a series of 90 degree gear boxes, one of which had been torn down, where damages had been found. So as we go to more complicated mechanisms we find that the technique shows promise. It is fairly easy to get the data, it takes a few minutes to fill out a curve and then it requires an interpretation. Interpretation has been built up simply to experience. We did not analyze the innards of the shock pulse meter or try to improve on it we just simply looked at its feasibility as a field tool.

developed. After engine shutdown, an oil sample analysis revealed traces of metal, although not beyond that deemed unacceptable. The dotted line is an extrapolation of the initial slope and gives an indication of the shock level stabilizing at a factor of ten higher. Two more runs were made which essentially repeated curve E-F-G. Teardown analysis showed that the original degradation had not changed noticeably but that new spalls were found on the outer race and on one ball bearing.

SUMMARY

The use of shock pulse techniques has proven successful as a diagnostic tool in the limited applications on the UH-1 to date. The MEPA-10A shock pulse meter has shown its ability to diagnose degraded hanger bearings, particularly when significant degradation exists. A single shock emission envelope has been developed which can be used to separate hanger bearings of normal wear, or the onset of damage, from those with severe damage.

Although not able to isolate the particular damaged element in a more complex unit such as the 42° gearbox, the MEPA-10A does show promise in indicating those with some level of degradation. Furthermore, in one case, it has shown its ability to respond quickly to rather small changes in degradation.

Work continues in enlarging the present data base as well as investigating the extension of the technique to other power-train components such as the 90° gearbox, transmission, and engine.

ACKNOWLEDGEMENTS

The investigation was supported by U.S. Army Aviation Systems Command under Delivery Orders DAJ01-72-A-0027-0001 and -0002.

REFERENCES

- ¹James Provenzano, John Games, Al Wyrostek, Art Ostheimer, Jack Young, "UH-1H AIDAPS Test Bed Program," Vol. I and II; USAAVSCOM Technical Report 72-18, Aug. 1972.
- ²Robert R. Butcher, Russel Kirby, Jr., John Nakakihara, T. C. Watkins, "UH-1H Test Bed Program," Vol. I and II; USAAVSCOM Technical Report 72-19, June 1972.
- ³J. A. George and R. M. Andres, "Parks College UH-1H AIDAPS Program," Parks College of Saint Louis University, Final Report, Sept. 1974.
- ⁴P. L. Howard, "Shock Pulse Instrumentation", Proceedings of the 14th Mechanical Failures Prevention Group Meeting, Los Angeles, Calif., Jan. 1971; MPPG Technical Report 2, Feb. 1971.
- ⁵E. F. Covill, T. C. Mayer, J. A. George, "Preliminary Evaluation of the Shock Pulse Technique to the UH-1 Series Helicopters," Parks College of Saint Louis University, Jan. 1974.

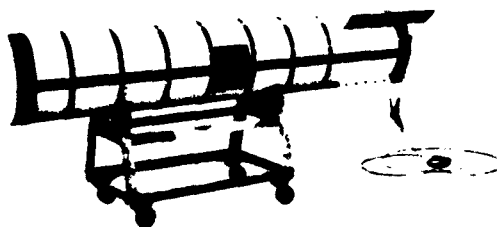


Fig. 2 - Full-scale Prototype Test Vehicle

INSTRUMENTATION

Mechanical peak shock recorders were mounted on the instrumentation plate in both the prototype and sub-scale model test vehicles. In the prototype vehicles, two types of shock recorders were used. The first type was a mechanical spring-mass oscillator which consists of a coil spring connected to a mass with a scribe which records the amplitude of vibration on a rotating cylinder (Ref. (1)). The cylinder is driven by a spring which is released by the initial shock. The speed of the cylinder is not constant, but its motion does serve to separate such events as water impact and seabed impact. For purposes of plotting a shock spectrum, the acceleration from these recorders is calculated for each natural frequency as

$$a = \frac{\omega^2 \delta}{g}$$

where a is acceleration in g's, g is the gravitational constant, ω is the natural frequency of the oscillator, and δ is the displacement of the oscillator mass from its static position. For these tests, two oscillator units each containing four spring-mass systems of different frequencies from 23.8 Hz to 228 Hz were used. These units covered the low frequency region. Measurements in the high frequency region were made with copper ball peak shock recorders (Ref. (2)). These recorders incorporate one or more copper balls, each of which is deformed by a different size mass when the unit is shocked. The size of the mass with the characteristics of the ball determines the effective natural frequency of a system. The calibrations of the units are calculated and checked experimentally against crystal-type accelerometers. Units containing a total of up to 18 copper balls, covering frequencies from 580 to 18,800 Hz, were used in the prototype vehicle.

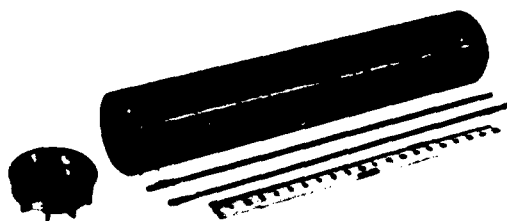


Fig. 3 - Model With Pressure Bars

The sub-scale model, like the prototype, had peak shock recorders mounted on the instrumentation plate. For the low frequency region, the coil spring oscillators were too massive for the model size, so they were replaced by some small, lightweight units manufactured by Engdahl Enterprises. These units each contain eight mechanical oscillators which use a cantilever-beam spring with a mass carrying a diamond stylus which records displacement on a gold-plated stationary hub. Two of these units were used which provided readings at a total of 16 different frequencies from 310 to 2000 Hz. For the higher frequency range, nine copper ball/mass systems housed in a single unit (NOL Mod 8 in Ref. (2)) were used to cover the frequency range from 4000 to 18,800 Hz.

The sub-scale model was also instrumented with two Hopkinson-type pressure bars for a number of tests to record pressure on the model nose at water impact (Fig. 3). These bars, which were steel rods 0.25 inch in diameter by 25 inches long, were instrumented with a pair of semiconductor-type strain gages close to the sensing end. The strain gages accurately indicate the applied pressure, while cancelling out any bending waves, until the leading pressure wave is reflected from the opposite end of the bar, where it is fastened, and again arrives at the gages. The bars are sufficiently long that this reflected wave does not arrive at the gages until after the desired measurement is completed. Wires trailing from the model were used to connect the strain gages to the recording instrumentation.

SCALING LAWS

Several different scaling laws were considered in this study. The simplest scaling is equal velocity scaling with a geometrically-scaled model constructed of the same type materials as the prototype. With this

STRUCTURAL RESPONSE MODELING OF A FREE-FALL MINE AT WATER ENTRY

R. H. Waser, G. L. Matteson, J. W. Honaker
Naval Surface Weapons Center, White Oak Laboratory
Silver Spring, Maryland

Shock levels were determined for a mine-test vehicle during water entry at near-normal angles. Experimental tests were made with a sub-scale model and full-size prototype. Scaling laws were developed which produced good data correlation. A computer analysis was made using a structural response program which produced results in agreement with the experimental data. Also, pressure measurements were made on the nose of the sub-scale model which indicated a non-uniform pressure distribution with very high localized pressure transients.

INTRODUCTION

An underwater mine is under study which can be planted by aircraft, being dropped from any altitude without a retardation device. Among the advantages of eliminating retardation devices, such as parachutes, are that the shorter descent time reduces drift and hence increases placement accuracy, the reduced air time decreases the probability of enemy observation of the planting, and the mine is mechanically simpler, more reliable, and hopefully less expensive. The resulting high-speed water impact, however, about 900 fps, results in severe structural loading and bottom burial problems. This study was directed only to the water-entry problem, specifically to defining the structural loading conditions, the structural response of the mine, and the failure modes. The analysis covers only the axial loading at water impact, and does not consider possible transverse loading produced at a later time by slap against the water-cavity wall. The approach taken was to conduct experimental tests with both sub-scale and full-scale vehicles, and to use the resulting data as input to, and verification of, a computer analysis.

TEST VEHICLE DESIGN

A test vehicle, shown schematically in Fig. 1, was designed to represent the proposed mine. The prototype characteristics are a weight of 2060 pounds, a diameter of 21 inches, and a length of 120 inches. The case and structural components are all steel. The flat disk nose shape was chosen for

its high drag to produce a minimum water-impact velocity and minimum seabed impact velocity. This shape, however, does produce a maximum water-impact shock for a given velocity.

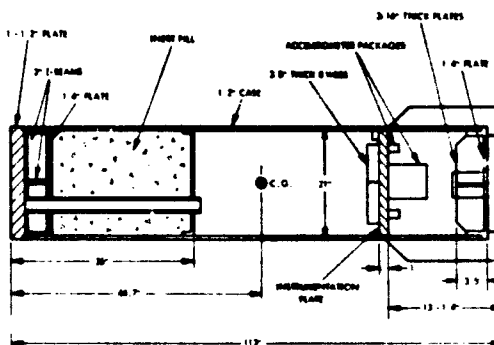


Fig. 1 - Free-Fall Mine Test Vehicle

Two vehicles were built to the full-scale dimensions, and one sub-scale model was constructed. Figs. 2 and 3 show one of the full-scale vehicles, and the model, respectively. The sub-scale model, geometrically scaled and constructed of the same type materials as the prototype, was designed to be launched from a 5-inch-bore diameter air gun into the NSWC Hydroballistics Tank. The exact model diameter was 4.855 inches, giving a scale factor

$$\lambda = \frac{4.855}{21} = 0.231$$

so that

$$\frac{(\ddot{x}_{\max})_m}{(\ddot{x}_{\max})_p} = \frac{\left(\frac{t_{\text{pulse}}}{T_N}\right)_m}{\left(\frac{t_{\text{pulse}}}{T_N}\right)_p} = \frac{1}{\sqrt{\lambda}}$$

or

$$(a_{\max})_m = \frac{1}{\sqrt{\lambda}} (a_{\max})_p$$

For the shock region where the input pulse duration is greater than the vehicle natural period, i.e., for

$$\frac{t_{\text{pulse}}}{T_N} \gg 1$$

the value of

$$\frac{\ddot{x}_{\max}}{\ddot{u}_{\max}} \approx 1$$

Since

$$\ddot{u}_m = \ddot{u}_p$$

it then follows that

$$(\ddot{x}_{\max})_m \approx (\ddot{x}_{\max})_p$$

or

$$(a_{\max})_m \approx (a_{\max})_p$$

if it can again be assumed that the vehicle responds as a simple spring mass system.

In summary, the modified Froude relationships which have been derived are as follows:

velocity $v_m = \sqrt{\lambda} v_p$

length $l_m = \lambda l_p$

pressure $p_m = \lambda p_p$

frequency $\omega_m = \omega_p / \lambda$

$$\text{acceleration} \left\{ \begin{array}{l} (a_{\max})_m = \frac{1}{\sqrt{\lambda}} (a_{\max})_p \\ \frac{t_{\text{pulse}}}{T_N} \leq 0.5 \\ (a_{\max})_m \approx (a_{\max})_p \text{ for } \\ \frac{t_{\text{pulse}}}{T_N} \gg 1 \end{array} \right.$$

PRESSURE MEASUREMENT TESTS

Knowledge of the pressures on the nose of the vehicle at water entry was desired for input to a computer for analysis. Accordingly, the sub-scale model was instrumented with two Hopkinson-type pressure bars as previously described. With this instrumentation, the model was fired into the water with a trajectory 5 degrees from vertical at velocities of 150 to 200 fps.

The pressure data obtained from the pressure bars, which is believed to be accurate, showed wide variations in amplitude and rise time from test to test. Maximum amplitudes varied by a factor of five or six, with the higher readings a factor of two above the value of ρV (where ρ and c are the density and sound speed of water, respectively, and V is the model impact velocity) which is the theoretically maximum obtainable value. It is hypothesized that the following may be occurring (See Fig. (4)): air pushed in front of the body dishes the water surface before impact so that effective impact angles less than the trajectory angle may occur. These shallow angles accelerate the water tangentially at very high velocities. Measurements of difference in time at which the two nose gages first saw pressure indicated water velocities up to about 4000 fps, or 20 times the impact velocity. Water at these velocities, when stagnated within the dish surface, would generate high erratic localized pressures such as those observed. Because these pressures are localized, it is not possible to use a limited number of readings for purposes of calculating impact forces or accelerations. The pressure measurement portion of the program was therefore terminated.

SHOCK MEASUREMENT TESTS

a. Sub-scale Model Tests. The 0.231-scale model as used for shock measurements contained the mechanical peak shock recorders described above mounted on the instrumentation plate. The recorders gave readings at 25 different frequencies. Tests were made at 150 fps with an entry angle of 85 degrees. Fig. 5 shows data from six of these tests. The relationships from which the shock spectrum grids are drawn are

$$a = \frac{\omega^2 \delta}{g} \quad \text{and} \quad v = \omega \delta$$

A few tests were made at greater velocities, with permanent deformation of the nose in the form of dishing taking place at 300 fps.

scaling, the stresses experienced by the model are exactly equal to those of the prototype and the scaling holds through gross plastic failure. The only feature of this scaling which may be undesirable is that the accelerations felt by the model are higher by the scale factor than those experienced by the prototype. Following are the scaling relationships where λ is the scale factor, and the subscripts m and p refer to the model and prototype, respectively:

velocity	$v_m = v_p$
length	$l_m = \lambda l_p$
time	$t_m = \lambda t_p$
acceleration	$a_m = a_p / \lambda$
stress	$\sigma_m = \sigma_p$
structural frequencies	$\omega_m = \omega_p / \lambda$

The other scaling law studied was Froude scaling. This scaling was chosen because Froude number governs the dynamics of free-surface flow, and the input accelerations to a rigid model and prototype are equal. The basic scaling relationships are as follows:

velocity	$v_m = \sqrt{\lambda} v_p$
length	$l_m = \lambda l_p$
time	$t_m = \sqrt{\lambda} t_p$
acceleration	$a_m = a_p$
input	$a_m = a_p$
pressure	$p_m = \lambda p_p$

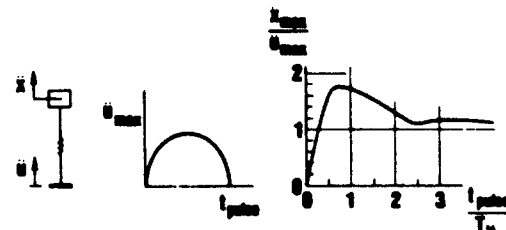
If the same type materials are used for model and prototype, the structural frequency relationship is $\omega_m = \omega_p / \lambda$. The time and frequency relationships are not reciprocals as they must be. The result is that the pressure input pulse duration is too long with respect to the model natural frequency. Further, the pressure relationship is λ rather than unity which means that incipient and subsequent plastic failure will not scale with the same materials. Thus, true Froude scaling requires the use of materials with different physical properties. The time relationships will be satisfied if materials are selected to keep the Cauchy number constant. The Cauchy number is MV^2/EL^3 , where the quantities involved are mass, velocity, modulus of elasticity, and length. Further attention to material strengths and

stiffness of sections results in correct modeling of failure modes. Ref. (3) deals with this type modeling in some detail. Applying this modeling is difficult because of the unavailability of structural materials with the desired properties, which then dictates making compromising geometric changes.

In this study a modified type of Froude scaling was used which allows use of identical materials in model and prototype and seems to work well for scaling peak shocks. This scaling involves the use of different scaling relationships in high and low frequency regions. The velocity scaling is the Froude relationship $v_m = \sqrt{\lambda} v_p$ and since the structural materials of model and prototype are the same, the frequency relationship is $\omega_m = \omega_p / \lambda$. For the low frequency region where the input pulse duration is short with respect to the vehicle natural period, i.e., for

$$\frac{t_{\text{pulse}}}{T_N} = \frac{\omega_p t_{\text{pulse}}}{2\pi} \leq 0.5$$

the following analysis can be used. Consider the dynamic load factor curve for a simple spring mass system as shown below (Ref. (4)) where u is the displacement input to the system and x is the response.



SYSTEM INPUT RESPONSE

For the region $\frac{t_{\text{pulse}}}{T_N} \leq 0.5$, $\frac{\ddot{x}_{\text{max}}}{\ddot{u}_{\text{max}}} =$

$\frac{k t_{\text{pulse}}}{T_N}$ where k is the slope of the response curve. Then,

$$\frac{\left(\frac{\ddot{x}_{\text{max}}}{\ddot{u}_{\text{max}}} \right)_m}{\left(\frac{\ddot{x}_{\text{max}}}{\ddot{u}_{\text{max}}} \right)_p} = \frac{\left(\frac{t_{\text{pulse}}}{T_N} \right)_m}{\left(\frac{t_{\text{pulse}}}{T_N} \right)_p}$$

where the subscripts refer to the model and prototype respectively. For Froude scaling

$$\ddot{u}_m = \ddot{u}_p$$

plotted for comparison with the prototype data from Fig. 7. It is seen that the agreement is good.

A study of the Free-Fall Mine data, see Fig. 7, shows that the water-entry input shock level is related to the maximum spectrum velocity change and the highest spectrum peak g in the low frequency range. Spectrum peak g for the high frequency range is a measurement of the ringing in the vehicle structure from shock. The peak g in the high frequency range followed no consistent pattern with respect to water-entry velocity.

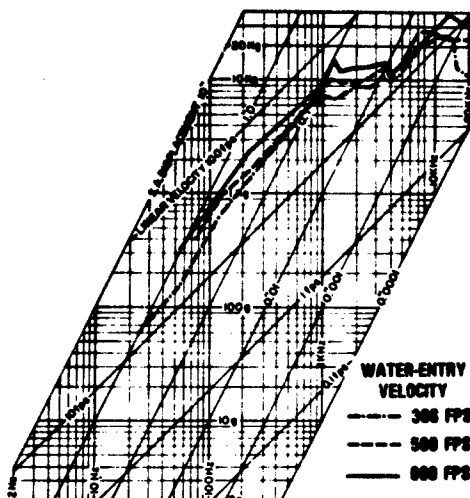


Fig. 7 - Shock Spectra for Water Impact of Prototype Vehicle

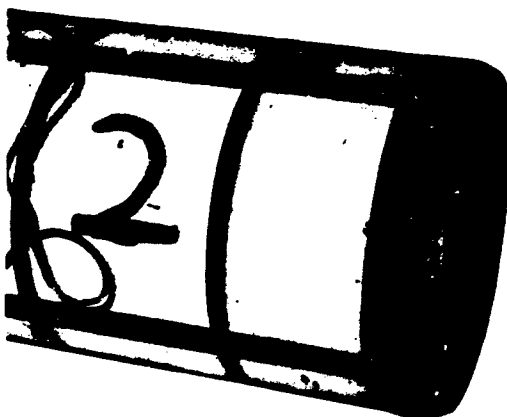


Fig. 8 - Prototype Test Vehicle Nose Damage from 600 fps Water Impact

The velocities at which failure occurred in the sub-scale model and prototype did not agree as well as might be desired. The scaling relationships indicate that stresses are equal in sub-scale model and prototype at equal velocity. Deformation of the model nose occurred at 300 fps; the prototype nose did not deform at 300 fps, but at 500 fps deformation occurred which was greater than the model deformation at 300 fps. This discrepancy is attributed to the effects of the roughness of the water surface. In the model tests, the laboratory water surface was perfectly placid; the ocean water into which the prototype vehicles were dropped, however, was somewhat rippled. It is felt that a rippled surface results in a "less solid" impact and hence, lower stresses.

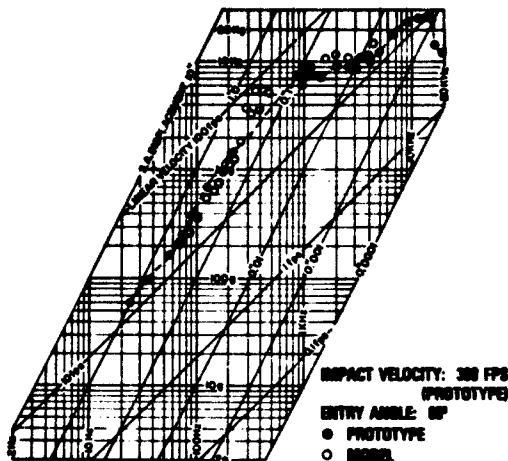


Fig. 9 - Comparison of Shock Spectra from Scaled Model Data and Experimental Prototype Data

COMPUTER SIMULATION STUDIES

The Free-Fall Mine was modeled for the NASA Structural Analysis (NASTRAN) computer program (Ref. (5)) to see if the structural response of the model and prototype could be adequately simulated. Since the materials in the model and prototype were similar, changing the computer program from one to the other involved only multiplying the physical dimensions by the scale factor.

From Ref. (6) an estimate was made of the expected input pulse to the sub-scale model at water entry. This pulse was put into the NASTRAN program and the response of the model at the peak shock recorder location was determined. This

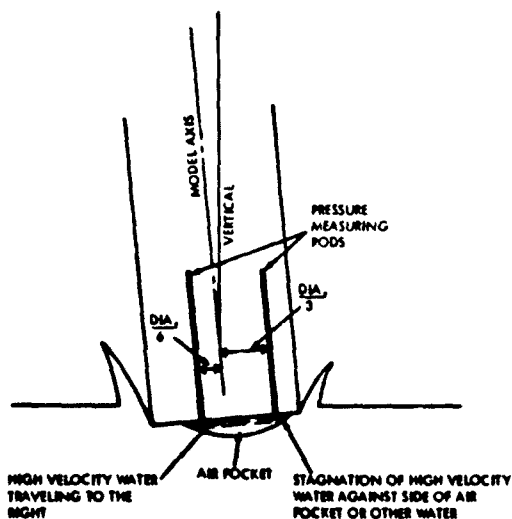


Fig. 4 - Diagram of Water Impact Showing Possible Cause of High Recorded Pressure

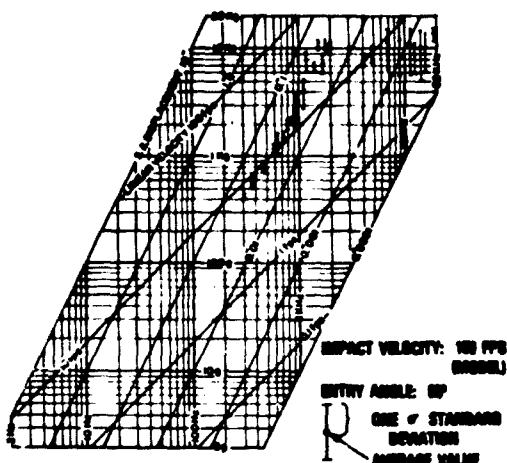


Fig. 5 - Shock Spectrum for Water Impact of Model

b. Prototype Tests. Two 21-inch-diameter prototype test vehicles were fabricated for this test series. Each had 26 peak shock recorders of different frequencies mounted on the instrumentation plate. The vehicles were dropped into the ocean from a helicopter at altitudes required to attain the desired water-entry velocities. Six tests were made. The first four tests were with water-entry velocities

of from 300 to 395 fps. At these velocities no damage to the vehicle was experienced. Fig. 6 shows mechanical oscillator traces from one of these tests. Fig. 7 shows the shock spectra from these tests at three different water-impact velocities. The last two tests were made with impact velocities of 500 and 600 fps. In both of these tests, the nose and tail covers were dished in from hydrodynamic loading and inertial response, respectively. Fig. 8 shows the nose damage for the 600 fps water impact.

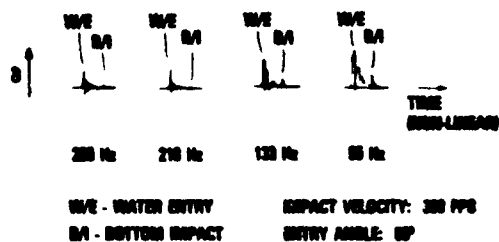
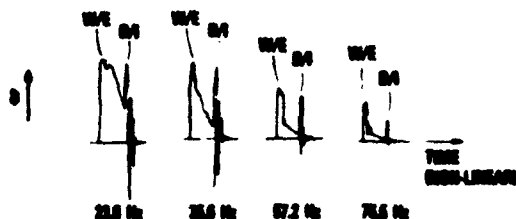


Fig. 6 - Mechanical Oscillator Traces from Prototype Vehicle

MODEL AND PROTOTYPE DATA CORRELATION

The shock data from the sub-scale model was scaled to prototype values using the modified Froude relationships derived under "Scaling Laws." These relationships were used rather than the equal velocity relationships because the greater accelerations of the model with equal velocity scaling were out of range of the low frequency peak shock recorders. Since velocity scales as the square root of the scale factor with Froude scaling, the 150 fps model tests correspond to the 300 fps prototype tests. Fig. 9 shows the sub-scale model data from Fig. 5 scaled to prototype values and

CONCLUSIONS

The following conclusions have resulted from this study:

1. Sub-scale model testing is a valid, economical technique for obtaining structural response data from a vehicle experiencing water entry.

2. The simplest applicable scaling for the structural response of a water-entry vehicle is equal velocity scaling in which the sub-scale model is geometrically scaled using the same materials as in the prototype, with model and prototype test velocities equal. The only disadvantage of this type of scaling is that the model accelerations are higher than those of the prototype by the scale factor. (This disadvantage made the use of equal velocity scaling impractical for this study because low frequency peak shock recorders with a sufficiently high acceleration capability were not available.)

3. A modified Froude scaling technique for water entry (relationships given under "Scaling Laws") is valid which does not require the scaling of model material properties as is required for exact Froude scaling.

4. Using a structural response computer code, such as NASTRAN, with experimental model data from a series of peak shock recorders, the input pulse at water entry can be inferred. Once this is done, the pulse can be scaled to the full-size prototype case and the structural response at any desired location can be obtained from the computer.

ACKNOWLEDGEMENTS

The authors would like to acknowledge Dr. J. E. Goeller for his assistance with scaling laws, J. M. Etheridge for running the NASTRAN program, and H. K. Steves and D. F. Newell for help with the experimental program

NOMENCLATURE

a = acceleration
c = sound speed of water
E = modulus of elasticity
g = gravitational constant
k = constant
l = characteristic length dimension
M = mass
p = pressure
t = time
T = period
u = input displacement

v, V = velocity
x = response displacement
 δ = displacement of oscillator mass
 λ = scale factor
 ρ = density of water
 σ = stress or standard deviation
 ω = frequency

Subscripts

m = model
N = natural
p = prototype

REFERENCES

1. V. F. DeVost, "Shock Spectra Measurements Using Multiple Mechanical Gages," Naval Surface Weapons Center, NOLTR 67-151, 20 Sep 1967
2. G. L. Matteson, "Calibration of NOL Copper Ball Accelerometers," Naval Surface Weapons Center, NOLTR 72-67, 7 Mar 1972
3. Baker, Westine, and Dodge, Similarity Methods in Engineering Dynamics, Hayden Book Co., N. J., 1973
4. Harris and Crede, Shock and Vibration Handbook, Volume 3, McGraw-Hill, New York, 1961
5. C. W. McCormick, The NASTRAN User's Manual, NASA SP-222-(01), Jun 1972
6. J. L. Baldwin, "An Experimental Investigation of Water Entry," Ph.D. Thesis, University of Maryland, 1972

SPONSOR

This program was sponsored by NAVSEA-03512, Dr. T. Peirce.

response was put into a smaller computer program to determine the responses of the peak shock recorders. The pressure pulse input to the NASTRAN program was then modified to bring the calculated peak shock recorder responses into good agreement with the experimental responses. Fig. 10 shows the input pulse to the NASTRAN program and the computed response at the location of the peak shock recorders on the instrumentation plate in the model. Fig. 11 shows the shock spectrum calculated from Fig. 10 plotted for comparison with the experimental data from Fig. 5.

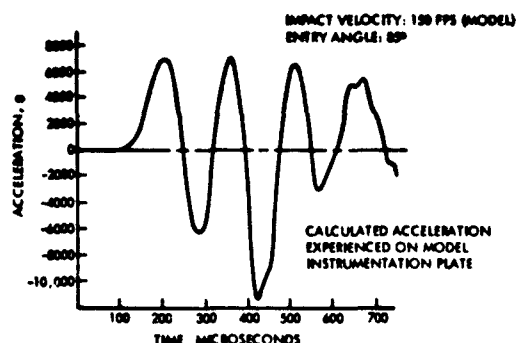


Fig. 10 - Computer Code Input and Output for Model

Having inferred the input pressure pulse to the sub-scale model by attaining agreement between the NASTRAN program and the experimental data, this input pulse pressure and duration were scaled to prototype values using the relationships

$$P_p = \left(\frac{v_p}{v_m} \right)^2 P_m$$

$$t_p = \frac{v_m}{\lambda v_p} t_m$$

This pressure relationship is felt to be valid for impact angles up to 85 degrees. The resulting pulse was input to the NASTRAN code with the prototype vehicle dimensions and the output was analyzed to obtain a peak shock spectrum. Fig. 12 shows this data compared to full-scale experimental data.

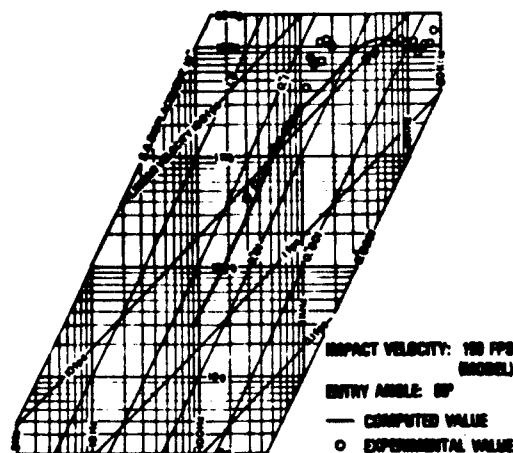


Fig. 11 - Comparison of Computed and Experimental Shock Spectra for Model

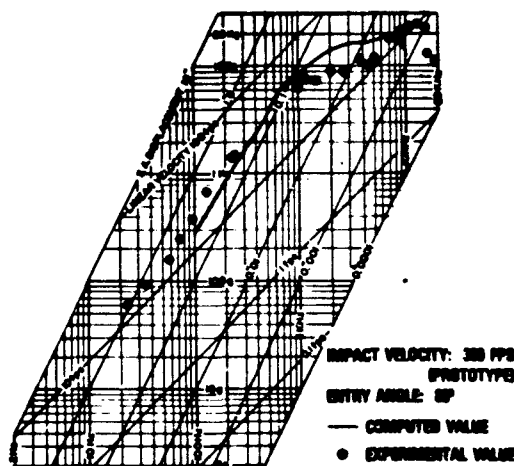


Fig. 12 - Comparison of Computed and Experimental Shock Spectra for Prototype

structures and to simplify the required analysis. In general this is accomplished by designing a structure for a collapse load greater than the working load. The resulting structure bears the working load with negligible permanent deformation. The formation of a plastic hinge in a structure does not necessarily allow collapse but merely allows a redistribution of stresses. The reserve strength beyond yield allows rotation of the plastic hinge as the load is increased. Redistribution and the increase in load will ultimately result in a collapse mechanism. The collapse mechanism in terms of a static load constitutes catastrophic failure; however, the collapse mechanism also constitutes energy dissipation greater than the elastic strain energy per unit of displacement. For example, the energy dissipated at a displacement twice the elastic limit in a simple structure may be four times that absorbed elastically. At two elastic limit displacements, deflections are not likely to be visible.

These basic principals can be readily shown by example. Consider a fixed ended beam (Fig. 1) loaded at its center; the beam thus representing a foundation and the load representing an equipment.



Fig. 1 - Simple System

A comparison of the energies at various points of displacement will demonstrate the advantages of plastic design. The loads associated with the example are as shown in Fig. 2.

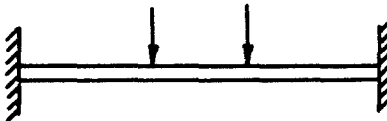


Fig. 2 - Beam Loading

The beam may have four stages of deformation:

1. Elastic limit
2. Plastic hinges have formed at the ends and the load increases towards the ultimate load.
3. Ultimate load is reached.
4. Deformation beyond the mechanism formation.

The load displacement relationship for the beam

is shown in Fig. 3.

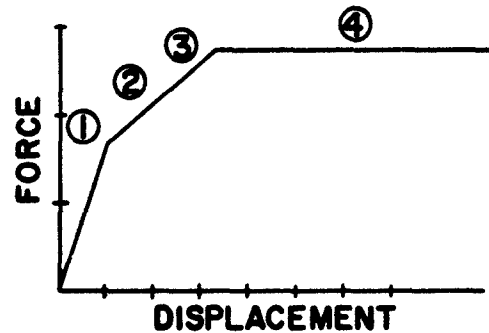


Fig. 3 - Load Displacement

The area under this curve represents the energy absorbed or dissipated. The energy at the formation of the mechanism is about 4.0 times greater than at the elastic limit. Beyond the mechanism formation the energy dissipation for each increment of displacement equal to the elastic limit is about 3.0 times greater than the energy at the elastic limit. In terms of a step velocity input of say 10 ft/sec to reach the elastic limit it would require 20 ft/sec to reach the mechanism formation. On the other hand a light structure could be substituted if the input is held at 10 ft/sec. Allowing three elastic limit displacements, a weight savings of 75 percent can be realized.

HISTORY AND STATUS

The plastic design of statically loaded steel structures was initiated nearly 50 years ago. In 1961 there were more than 2,000 structures built which had been designed using the plastic design methods. These structures have demonstrated the usefulness of plastic design as applied to static loads. It is expected that the gains to be made in structures designed for dynamic loads would be even more profitable. This can be realized since static structures deform catastrophically when the load reaches the collapse load while in a dynamic structure the collapse mechanism merely allows energy dissipation.

Early investigations carried out by the Brown University under contract to Naval Ship Research and Development Center (NSRDC) produced methods which looked promising toward application to certain classes of structures subjected to impulsive load. These methods and others developed at NSRDC were applied to some simple structures by NSRDC. Experimental investigations were carried out and correlations were made. The results showed that these methods give acceptable estimates on the plastic deformation expected. These investigations were carried out on simple structures as an initiation of the work to develop a plastic design methods. Three systems were investigated:

PLASTIC DESIGN ANALYSIS OF SHIPBOARD EQUIPMENT SUBJECTED TO SHOCK MOTIONS

Lowell T. Butt
Naval Ship Research and Development Center
Underwater Explosions Research Division
Portsmouth, Virginia

The application of plastic design techniques in shipboard use is discussed. Emphasis is placed on applications in the shock design of equipment and structures. Approximate design methods are discussed and results of simplified model tests are given and compared with these methods. These comparisons show that these simplified methods give results which are acceptable as good first estimates of shock damage. The accuracy indicates that these methods can be applied in the design of structures where small set displacements are allowable.

INTRODUCTION

The complexity of modern naval ships and submarines requires constant updating of design methods and procedures. This is particularly true of light high-speed advanced designs. New design methods and design criteria which will result in weight and space savings are essential. In current naval vessels there exist structures which are obviously overdesigned and would allow significant savings in weight and space; foundations in particular.

Shipboard equipment can be divided into three categories of design: One category can be classified as those equipments which always require a close alignment. For these equipments it is necessary that response to operating and shock loads be confined to the elastic range. Equipments such as SINS, turbines, reduction gears, shafting, turbogenerators and similar items fall in this category. A second category which includes a large majority of shipboard structures and equipment may be classified as those items which do not require alignment and can allow small deformations. Piping, resiliently-mounted equipments and many foundations for example can be considered for this category. The enormity of this category in particular warrants a careful consideration of new methods which may lessen costs, weight and space requirements. A third category may be classified as those items which can tolerate large deformations (deformations greater than four elastic limit displacements). Foundations for electronic cabinets, weapon cradles and dollies, decks, stanchions and other support structures can be considered for this category. Methods which result in significant shock protection are advantageous and necessary for many

items in this category.

Little attention has been given to the efficiency of design. Over-designed foundations for example can be improved significantly by taking advantage of the reserve strength in the material above its yield point. This reserve strength combined with the redundancy generally encountered in foundation design can serve to optimize foundation efficiency. To make use of the reserve strength requires plastic design procedures. Currently, plastic design procedures are practically nonexistent for dynamic loads.

Simple one degree-of-freedom beam structures are plastically designed using the limit load procedure (see DDS 9110-7). More complex structures may be designed using an elastic analysis procedure (DDAM) but using reduced inputs. This procedure results in a structure which will deform plastically at the unreduced shock level. The resulting deformation or response of the structure is of course unknown. This limited usage of the plastic design concept does not allow optimization of design efficiency.

Purpose

The purpose of this paper is to delineate the plastic design method for shipboard application and the expected gains.

Plastic Design Methodology

Plastic design is the art of utilizing the reserve strength of ductile materials to optimize the efficiency of

the load required to form a mechanism is unchanged, only the available energy has changed slightly. Initially, the energy available up to the point of strain hardening ϵ_{st} , is about 25 times that at the elastic limit. At four elastic limits, less than 15 percent of this energy has been dissipated. And even at that, the energy and load-carrying capacity above the point of strain hardening has not been considered. This is pointed out to show that fracture is well above the highest strain considered in plastic design. Therefore predictions within three or four elastic limits should be acceptable for plastic design of beams in the second category previously mentioned. The experience this far has shown that methods are available for the plastic design of simple structures.

SPIN OFFS

It has been pointed out that small plastic deformations do not decrease the load-carrying capacity of a structure. In addition, the energy available above the elastic limit for most structural steels is many times greater than that at the elastic limit. For shipboard equipments not required to maintain alignment, foundations could be designed to dissipate shock energy by taking advantage of the strain energy above the elastic limit. The simple foundation of Ref. (3) was investigated to determine the shock mitigation afforded through large plastic deformations. The acceleration response of the simulated equipment is given in Fig. 5. The corresponding set

displacement was 6.5 times the elastic limit. It is seen that the accelerations were limited to about 25 g's which may be compared to a 100 g input. This limit was maintained during a subsequent test at a higher severity.

The torsion tube mount, Ref. (4), is another instance where advantage of plastic deformation has been utilized. The tubes of the mount dissipate energy through torsional plastic deformation. The load-carrying capacity of the mount is constant throughout deformation.

Other spin offs of plastic design could be its application to bulkheads, decks, and stanchions; possibly even the hull structure for explosion resistance and seaway loads.

CONCLUSION

The inherent reserve strength in structural steels will allow an optimization of the structural efficiency of shipboard structure. It is expected that foundation weights can be reduced from that required for elastic design if maximum set displacements are allowed to reach three elastic limit displacements. Similar weight reductions can be expected in structures other than foundations where plastic design is applicable. The weight savings depend on the trade off allowances for all the factors involved. Considerations for noise, vibration, and maximum set deformations must enter the trade off allowances.

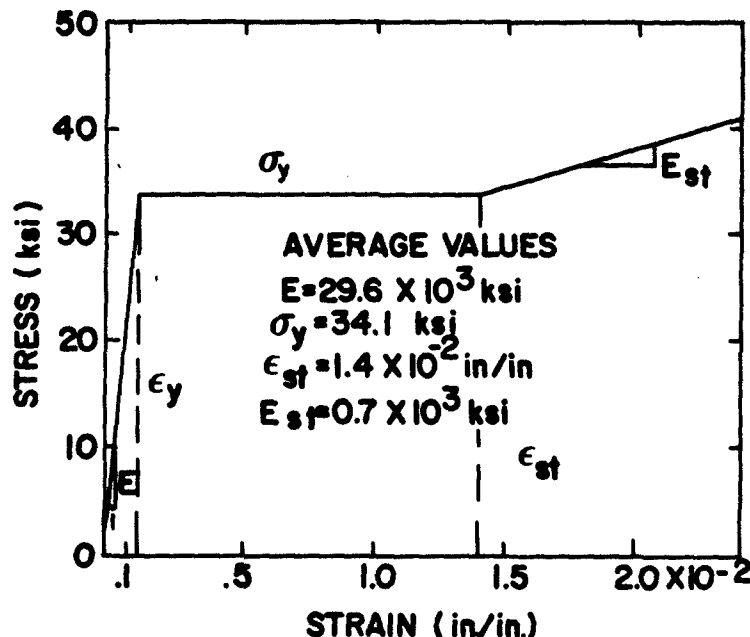


Fig. 4 - Idealized Stress-Strain Relationship for a Medium Steel

1. Tip loaded cantilever beams
2. Three-span beam
3. Simple foundation

Each of these systems was installed on the Floating Shock Platform (FSP). Simulated underwater weapon attacks were conducted. Analytical predictions on the set displacements were compared to the experimental results. These investigations are reported in Ref. (1), (2) and (3) respectively. A summary of comparisons in Ref. (1) and (2) is given in Tables 1 and 2. The abbreviations given in Table 1 indicate the various methods which were evaluated in the study. Details of the methods are given in the references.

In all cases shown, the predicted and the experimental deformation are within four elastic limit displacements. It should be noted that even at four elastic limit displacements the deformations are too small to be seen. The peak displacement of the three-span beam for example, was on the order of 1/4-inch in a span length of 78 inches. The warp in many welded structures amounts to this much and are readily acceptable. Even though these structures deformed plastically it should be pointed out that their load-carrying capacity was unaltered. Referring to Fig. 4, strains up to 3 or 4 times that at the elastic limit represent only a small portion of the available energy represented by the area under the stress-strain curve. Upon reloading from a set of four elastic limits

TABLE 1
Cantilever Beam Comparison of Theoretical and Experimental Plastic Deformations *

Beam	Initial Plastic Deformation $\frac{\delta}{Y_0}$						Final Set $\frac{\delta}{Y_0}$
	Measured	EPMR	EPB	RPB	EPMA	RPMA	Beam Measurement
A	-2.99	-2.38	-2.66	-3.31	-2.75	-3.25	-2.445
A	-2.47	-2.49	-2.45	-3.08	-2.53	-3.03	-2.095
B	-0.91	-0.97	-1.13	-1.69	-1.12	-1.62	-0.258
B	-1.06	-1.23	-1.29	-1.85	-1.28	-1.78	-0.452
C	-0.58	-0.75	-0.89	-1.42	-0.87	-1.36	-0.081
C	-0.72	-0.97	-1.02	-1.55	-0.99	-1.49	-0.199
D	-0.244	-0.49	-0.59	-1.12	-0.55	-1.06	-0.000
D	-0.47	-0.76	-0.80	-1.32	-0.76	-1.26	-0.045

* Abbreviations

- EPMR - Elastic-Perfectly-Plastic Mode Response
- EPB - Elastic-Perfectly-Plastic Bound
- RPB - Rigid-Perfectly-Plastic Bound
- EPMA - Elastic-Perfectly-Plastic Mode Approximation
- RPMA - Rigid-Perfectly-Plastic Mode Approximation
- δ - Deformation
- Y_0 - Elastic Limit Displacement

TABLE 2
Three-Span Beam Comparison of Analytical and Experimental Predictions

Method	Peak Displacement (in.)
Finite Difference	0.34
Rigid-Plastic Bound	0.45
Approx. Rigid-Plastic Mode	0.34
Experimental	0.220

A complete list of references is given on page 6.

In addition to the savings in weight which relates to costs, there is also an expected cost reduction due to the simplicity of plastic design analysis methods.

The lighter structures resulting from plastic design tend to reduce the hard spots usually associated with foundations and deep frames. The lighter structures require less attachment weld which minimizes weld stresses.

Additional gains are possible employing plastic deformation concepts in shock mitigation.

REFERENCES

- (1) Butt, L. T. et al., "Shock Damage Mechanism of a Simple Structure," Naval Ship Research and Development Center Report 2191 (Mar 1967).

DISCUSSION

Mr. Warner: (Westinghouse Electric Corp) Did you check for any available data on the effect of strain rate on yield stress? I think there are a number of curves around, one by Manjoine, and it was around from the year one. Or did you just guess at it and see how well it matched?

Mr. Butt: Not prior to the test. Prior to the tests it was common knowledge that the strain rate would not affect motions at these rates; but after finding this difficulty we did go back and look through the literature and the strain rates that we had for this steel agreed with the data in the literature. The doubling of the yield stress was in accordance with the data that had been found for steels similar to this; but there is a very limited amount of data for the strain rate effects on the new steels such as HY 80 and HY 100 and so on.

Mr. Waser: (Naval Surface Weapons Center) You talked about plastic design, isn't that really a misnomer, aren't you really in the elastic region? Have you taken fatigue problems into account?

Mr. Butt: We are actually in the plastic design region using this method; we assume a rigid plastic deformation which means that we are going into the plastic range immediately and also the problem is shock which is really not affected by fatigue type deformations. The structure is assumed to be unfatigued and capable of taking some shock load.

Mr. Matheson: (Naval Surface Weapons Center) You deal with the plastic region in your analysis which most designers stay away from because it is a one way street. You do not plan to reuse the structure in the same manner after you have gone through this region. Are those your design considerations?

ment Center Report 2191 (Mar 1967).

- (2) Butt, L. T., "Shock Damage Analysis of a Three-Span Beam," Naval Ship Research and Development Center Report 3259 (Aug 1972).
- (3) Butt, L. T., "Inelastic Analysis of a Simple Machinery Foundation Subjected to Underwater Explosion Attack," Naval Ship Research and Development Center Report E SD 177-120.
- (4) Butt, L. T., "The Use of Torsion Tubes to Approach the Ideal Constant Force Maintenance-Free Restorable Shock Mount," Naval Ship Research and Development Center Report 2545 (Dec 1969).

Mr. Butt: No not exactly. The design considerations are to choose structures in which a small plastic deformation does not affect the function of the equipment or the structure, and to limit the displacement to some allowable value that you can tolerate.

Mr. Furkois: (Naval Research Laboratory) Years ago I worked on bolts and you have a problem; there is a shock fatigue concept and every time you get into the plastic range it is an irreversible process. You can't bring the material back to its original condition so even in bolts there are a certain number of shocks to failure. You might have an initial set of .25, later on you will get another shock and you add another .25, and you get an accumulative deformation until the material breaks. So you are going into another area and as the gentlemen before me said it is not a reversible process and that is why we like to stay in the elastic range. You should determine how many shocks a particular structure can take before failure and I think it is a serious problem.

Mr. Butt: That is true but there are plenty of applications of a plastic design in which you can take advantage of this tremendous amount of available strain energy without harm.

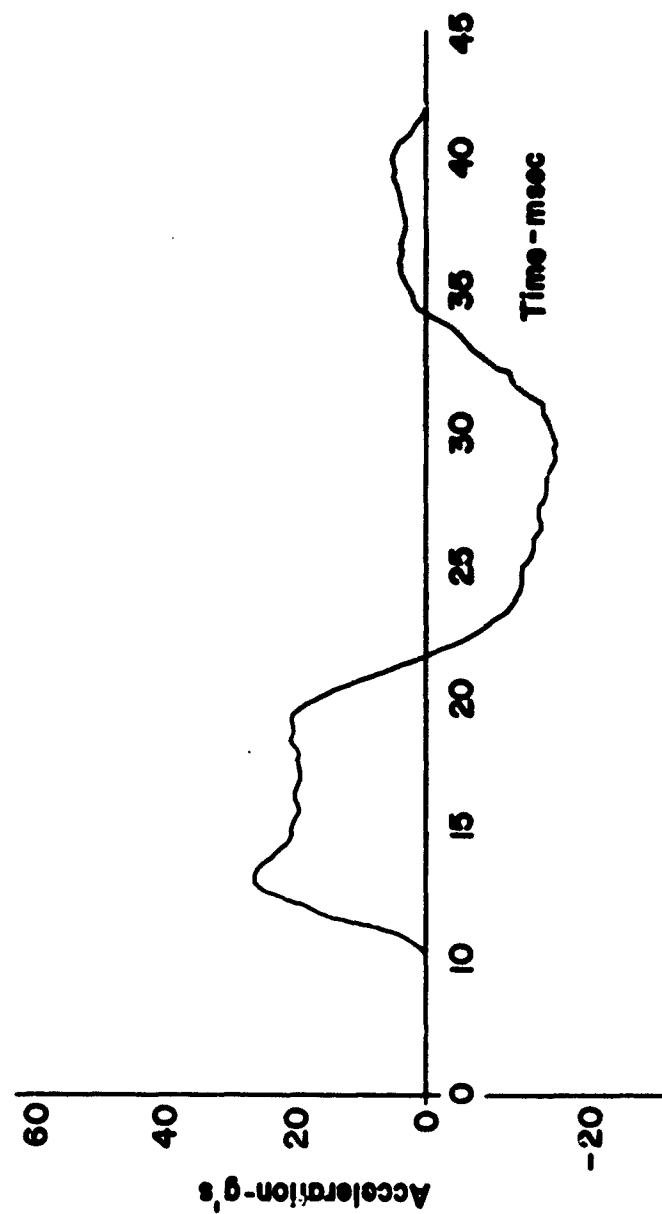


Fig. 5 - Simple Foundation Acceleration History

tractor, in combination with a 12-ton M127 tandem trailer, was used for this phase of the test program. Using military personnel and equipment considerably reduced research costs and assured technical control of the field work. As a result of these tests a procedure for testing commercial cargo trucks was developed.

During July 1973, limited field tests were initiated on the first of three leased commercial cargo trucks; all field work was completed by April 1974. Support for these tests was provided by the US Army Transportation Center and Fort Eustis. Planning, supervision of tests, analyses, and development of concepts and application were performed by MTMCTEA engineers.

The detailed procedure on how to determine the shock index for a typical highway cargo truck is contained in this report.

GENERAL

The purpose of the highway shock index (SI) is to provide a means for selecting highway cargo vehicles on the basis of their "rough" riding characteristics. The selection is based not on the vehicle configuration but on the combined payload spring rate (K) of the springs and tires on an axle. SI makes it possible to select a relatively "soft" riding vehicle for fragile cargo and thus minimize the possibility of damage to the cargo. The shock index rating system applies to restrained cargo only.

The shock index for a cargo vehicle should be representative of the roughest ride area on the truck cargo bed. Previous tests have shown, and recent tests have confirmed, that for normal operating conditions the roughest ride on a truck cargo bed is found over the rear axle for a two-axle cargo truck; or, for a truck-tractor semitrailer combination, either near the rear axle of the trailer or over the fifth wheel of the truck-tractor depending on which axle has the higher payload spring rate.

Under normal operating conditions maximum shocks on the cargo bed will occur in the vertical direction; and, based on extensive tests by MTMCTEA and other organizations, a maximum shock of 10g's is considered reasonable for a very rough road surface. Consequently, the highway shock index is based on a scale of 0 to 10g's. The numerical values of shock index vary from 5 to 0, with 5 corresponding to 0g, representing the softest "ride."

The deadweight of the vehicle is not involved in the determination of shock index; the un-

loaded weight of the vehicle is already in place and therefore is not involved in the determination of the payload spring rate. The tests have shown that of the three major variables: percent maximum payload, tire pressure, and speed, percent maximum payload has a major effect on shock index whereas tire pressure in the practical range and speed causes relatively minor changes.

Since percent maximum payload has the most effect on the "ride" on the truck cargo bed, a graph relating the payload axle spring rate, axle payload, and shock index was developed (Fig. 1). In order to develop the graph, tests were conducted on a range of cargo vehicles. The payload capability of these vehicles varied from 13,000 pounds on a two-axle truck; to 24,000 pounds on a two-axle truck-tractor, single-axle trailer combination; to 40,000 pounds on a three-axle truck-tractor, two-axle semitrailer combination.

The vehicles were instrumented to measure shock on the cargo bed and were driven over fixed, unyielding bumps at various speeds at different tire pressures, and with different payloads.

The repeatability of data measurements recorded on the test course was satisfactory in spite of the many variables that affect a dynamic test of this type. Approximately 80 percent of all data recorded over the axles of the trucks were used in the preparation of the graph and table.

SHOCK INDEX GRAPH

When shock to the cargo is of concern the following conclusions can be drawn, based on the graph (see Fig. 1).

As axle payload is increased from zero the shock index increased, providing a softer ride, to some optimum load for the vehicle. The dashed lines on the graph indicate a trend reversal, where increasing the axle payload causes a decrease in shock index, providing a progressively rougher ride. There is an optimum payload for all vehicles that will provide the softest ride for the cargo. This optimum load can be readily selected from the graph when the combined axle payload spring rates for the vehicle are known.

High, erratic shock values are most likely to occur with very light or maximum payloads since at light loads the vehicle springs are relatively stiff and at very heavy loads "bottoming out" of the springs may occur. The

PACKAGING AND SHIPPING

HIGHWAY SHOCK INDEX (SI) PROCEDURE FOR DETERMINING SI

John H. Grier
Military Traffic Management Command
Transportation Engineering Agency
Newport News, Virginia 23606

The Army, Navy, Air Force, and Marine Corps have jointly sponsored and participated in the development of a Shock Index (SI) for highway transportation. A numerical SI, associated with a particular vehicle-load combination, can now be determined at a low cost by application of simple static field measurements. The SI provides classification for vehicle-load combination as regards probability of shocks transmitted to the cargo during highway shipments.

INTRODUCTION

In 1967 representatives of the United States Army, Navy, Air Force, and Marine Corps agreed that it should be possible to establish shock indices that would be representative of the cargo environment for the various transport modes. The Services formed a Steering Committee to initiate and guide the development of a highway shock index. The highway mode was selected because of the relative ease in controlling the environment and related variables.

As an initial step the Steering and Advisory Committee let a \$53,000 contract to General Testing, Inc., Springfield, Virginia, to determine and develop a shock index equation that could be used to classify highway cargo vehicles in terms of vehicle shock to the cargo. In addition, and in conjunction with the General Testing, Inc., contract, a second \$13,000 contract was let by the joint services committee to J. A. Johnson, Inc., Short Hills, New Jersey, an independent testing organization, to check and verify the General Testing, Inc., project objective. General Testing, Inc., ran a comprehensive group of static and dynamic shock evaluation tests using five classes of cargo trucks.

General Testing, Inc., laboratories released their final report, Development of a Shock Index Classification for Highway Cargo Vehicles, dated 16 April 1971. As described

in the report "a set of semiempirical relationships have been developed to equate the performance of the vehicle/cargo with the significant variables affecting the ride." Conclusions, as presented by General Testing, Inc., are that "the SI equation developed under this contract is the result of an approach to a complex problem. In short, this work is not the ultimate answer to the problem of cargo ride; instead, it represents a foundation on which to build a firm set of requirements for the safe transportability of all cargo."

The bulk of General Testing, Inc., work concerned a controlled laboratory test arrangement. J. A. Johnson, Inc., was tasked to validate the feasibility of the General Testing classification procedure and test on public roads to establish the accuracy of method in a practical over-the-road environment. Johnson's work concluded that a shock index classification is both feasible and needed by the military community, but that more engineering expertise is required to improve accuracy prior to adoption of the classification procedure.

Accordingly, Military Traffic Management Command Transportation Engineering Agency (MTMCTEA) initiated a comprehensive shock index field test program using Fort Eustis facilities, military equipment, and personnel to assist in obtaining program objectives by developing a practical test to obtain usable impact data. A military 5-ton M52 tandem

most erratic results will occur over the fifth wheel area due to the concentration of load at the kingpin.

The graph indicates that for a relatively soft ride the vehicle payload axle spring rate should be about 7,000 pounds per inch. For this condition for an axle payload of 3,000 pounds, the cargo would most likely not be subjected to a shock of over 2g's, and the shock index rating for the vehicle would be about 4.1.

For a vehicle payload axle spring rate of 10,000 pounds per inch the maximum expected shock to the cargo should not exceed about 4g's, for axle payloads of 3,000 to 9,000 pounds. This vehicle would have a shock index of about 3.

For a vehicle payload axle spring rate of 13,000 pounds per inch the maximum expected shock to the cargo should not exceed about 6g's for axle payloads of 3,000 to 9,000 pounds. This vehicle would have a shock index of about 2.4.

For all ranges of payload, due to the many variables, dynamic behavior, and variable environment associated with the vehicle-road relationship, some radical, inexplicable shock values will occur. In the test leading to the development of the graph approximately 20 percent of the recorded values fall within this category and were accordingly discarded.

PROCEDURE FOR DETERMINING SHOCK INDEX

The procedure for estimating SI for a specific cargo truck involves two steps. First, it involves loading and unloading the truck and taking measurements on how much the cargo bed deflects under one-half and full payload. Secondly, it is necessary to know the payload axle load. This can be determined on a set of portable scales or by calculation. It is necessary that this information be obtained by physical measurements because of the high variable internal friction in leaf springs, variable stiffness in tire sidewalls, and general construction of the overall suspension system of the vehicle. Also, correlation between the manufacturer's spring rate for a leaf spring of a vehicle cannot be made with the installed spring, because in the manufacturer's test procedure, the test is performed without center clamps and shackles, and the spring ends are mounted on rollers so that they are free to move. (Reference SAE Standard Leaf Springs for Motor Vehicle Suspension, SAE J5102.) When the SI for a specific make and model of truck has been determined, it should apply to others of the same make and model, with the

same type springs and tires.

1. Required Information:

a. Vertical deflection at one-half and full payload of truck bed at rear axle(s) and/or at rear axle(s) of truck-tractor if the vehicle is a truck-tractor semitrailer combination.

b. Payload axle load causing the vertical deflections.

2. Determination of combined (springs and tires) vertical deflection at an axle(s).

a. Check tire air pressure, adjust to operating pressure.

b. Position axle(s) on scales; or, if scales not available, on a uniformly smooth, level, unyielding surface. Vehicle unloaded.

c. Accurately measure the height of the cargo bed on each side of the truck at the axle(s). If vehicle is on scales, note unloaded axle(s) load.

d. Use dummy concentrated weights, if available, to simulate axle(s) payload. Load with center of gravity directly over axle for single-axle vehicles or midway between tandem axles. If concentrated weights are not available, use available homogeneous weights and uniformly load truck bed. Accurately measure the height of the cargo bed on each side of the truck at the axle(s) (Fig. 2). The truck should

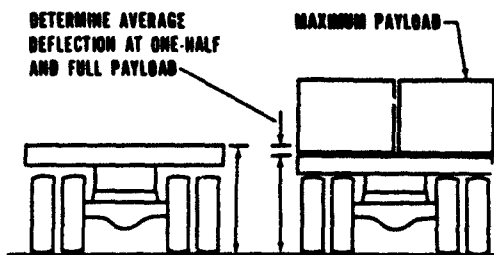


Fig. 2 - Rear View of Truck

be loaded and unloaded several times and an average deflection determined, both at one-half and full payload.

e. In order to obtain accurate average deflections proceed as follows:

(1) Fully load the truck; measure truck bed height at full load.

(2) Unload to one-half full load; measure

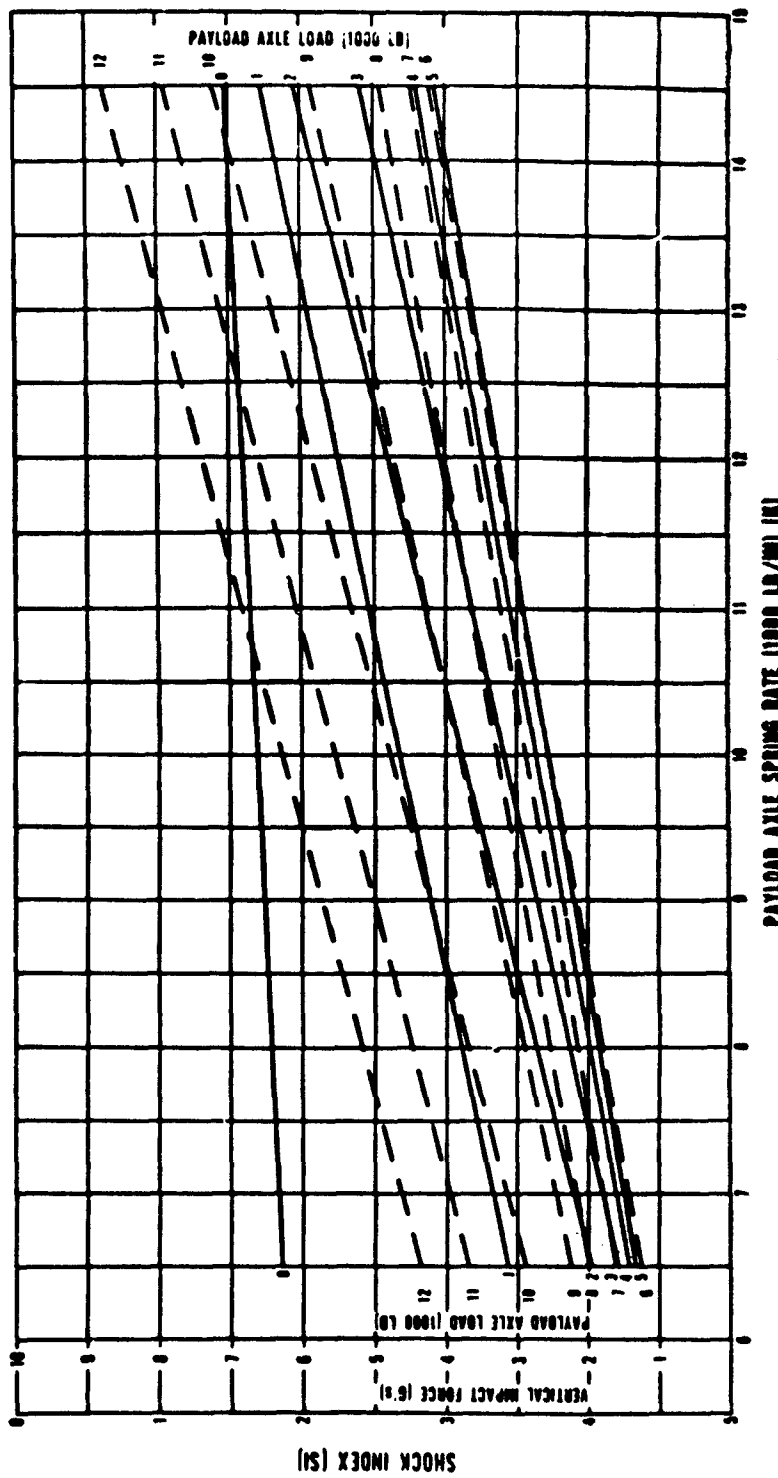


Fig. 1 - Shock Index Graph

Payload Axle Load, 1,000 lb.		TABLE 1 SHOCK INDEX PAYLOAD AXLE SPRING RATE, 1,000 lb/in.																		Payload Axle Load, 1,000 lb.	
		6.5	7	7.5	8	8.5	9	9.5	10	10.5	11	11.5	12	12.5	13	13.5	14	14.5			
0	1.85	1.85	1.80	1.80	1.75	1.75	1.70	1.70	1.65	1.65	1.60	1.60	1.55	1.55	1.50	1.50	1.45	0	0		
1	3.40	3.30	3.20	3.10	3.00	2.90	2.75	2.65	2.55	2.45	2.35	2.25	2.15	2.05	1.95	1.80	1.70	1	1		
2	4.00	3.85	3.75	3.60	3.50	3.35	3.20	3.10	2.95	2.85	2.70	2.60	2.45	2.35	2.25	2.10	1.95	2	2		
3	4.20	4.05	3.95	3.85	3.75	3.60	3.50	3.40	3.30	3.15	3.05	2.95	2.85	2.70	2.60	2.50	2.40	3	3		
4	4.25	4.15	4.05	3.95	3.90	3.80	3.70	3.50	3.50	3.40	3.35	3.25	3.15	3.05	2.95	2.85	2.75	4	4		
5	4.30	4.20	4.10	4.05	3.95	3.85	3.75	3.70	3.60	3.55	3.45	3.35	3.25	3.15	3.10	3.00	2.90	5	5		
6	4.35	4.25	4.15	4.05	3.95	3.85	3.75	3.70	3.60	3.50	3.40	3.30	3.25	3.15	3.05	2.95	2.85	6	6		
7	4.15	4.05	3.95	3.90	3.80	3.70	3.65	3.55	3.45	3.35	3.30	3.20	3.10	3.00	2.90	2.85	2.75	7	7		
8	4.00	3.90	3.80	3.70	3.60	3.55	3.45	3.35	3.25	3.15	3.05	2.95	2.90	2.80	2.70	2.60	2.50	8	8		
9	3.90	3.75	3.65	3.55	3.40	3.30	3.20	3.10	2.95	2.85	2.75	2.60	2.50	2.40	2.30	2.15	1.95	9	9		
10	3.55	3.40	3.25	3.10	3.00	2.85	2.75	2.60	2.45	2.30	2.20	2.05	1.90	1.80	1.65	1.50	1.40	10	10		
11	3.15	3.00	2.90	2.75	2.60	2.50	2.35	2.25	2.10	2.05	1.85	1.70	1.55	1.45	1.30	1.15	1.05	11	11		
12	2.80	2.65	2.55	2.40	2.25	2.10	2.00	1.85	1.70	1.60	1.45	1.30	1.20	1.05	0.90	0.75	0.65	12	12		

the roughest expected ride on the cargo bed. The shock index can be obtained, at the same time, for all axle payloads from 0 to 12,000 pounds. It need be determined only once for vehicles of the same make and model, with the same type springs and tires.

To use Table 1, use the K in the table that most nearly corresponds numerically to the K determined by physical measurement. The maximum error in SI due to using the table will be 0.625; in most cases, the error will be considerably less. The SI for each axle (if the vehicle is a truck-tractor, semitrailer combination) should be checked and lower of the numerical values should be used for SI.

6. For example, determine the SI for a two-axle truck-tractor single-axle semitrailer combination. Payload axle loads for the rear axle of the tractor and trailer axle are to be 10,000 pounds each.

The truck was loaded to one-half and full payload and deflections were measured. Scales were used to determine the payload axle load on each axle. The following data were obtained on the trailer axle:

Full payload axle load	-	12,288 lb
One-half payload axle load	-	6,123 lb
Average deflection at full payload	-	1.127 in.
Average deflection at one-half payload	-	0.687 in.

$$K = \frac{12,288 - 6,123}{1.127 - 0.687} = 14,000 \text{ lb/in.}$$

Enter Fig. 1 with K; go vertically to payload axle load that truck is to transport (10,000 pounds); horizontally to read shock index, which is 1.52 for a K of 14,000 pounds and payload axle load of 10,000 pounds. SI from Table 1 is 1.50.

This procedure should be used also on the rear axle of the truck-tractor and the lower of the two SI's used as the SI for that truck (with 10,000-pound payload axle loads). The SI for all other payload axle loads can be determined directly from the graph or table using the value of K for the truck, since K is independent of the payload.

truck bed height.

(3) Unload truck; measure truck bed height.

(4) Place one-half full load on truck; measure truck bed height.

(5) Place full load on truck; measure truck bed height.

(6) Repeat above cycle 5 times for a total of 10 measurements.

(7) Accuracy of measurements should be within one-thirty-second of an inch.

3. Determination on payload per axle at one-half and full payload.

a. If vehicle is on scales, read recorded weight, subtract axle(s) unloaded weight; and, if tandem axles, divide by 2.

b. If scales are not available, use one of the following equations to determine the single axle payload at one-half and full payload (Fig. 3).

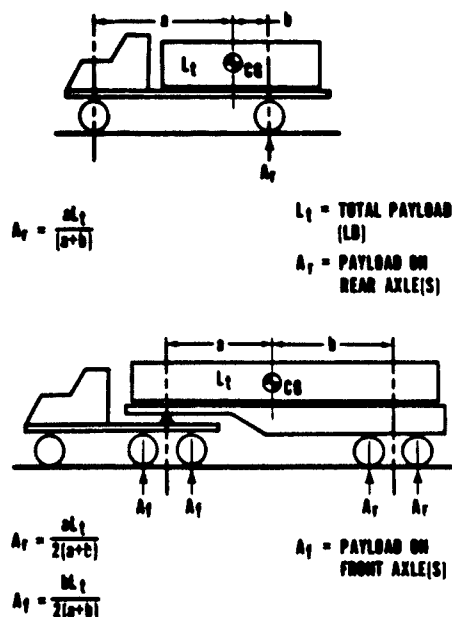


Fig. 3 - Axle Payloads

4. Determination of combined payload spring rate (K) for axle(s).

K = combined payload spring rate (lb/in.)

P_f = full payload axle load (lb)

$P_{1/2}$ = one-half payload axle load (lb)

D_f = average deflection at full payload (in.)

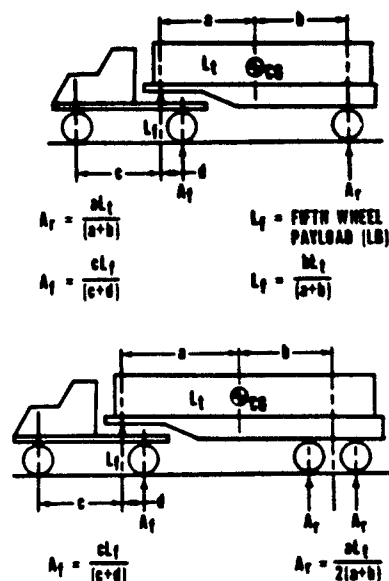
$D_{1/2}$ = average deflection at one-half payload (in.)

$$K = \frac{P_f - P_{1/2}}{D_f - D_{1/2}}$$

5. Determination of Shock Index.

Now that K has been determined for the axle(s) the SI can be read directly from the graph (Fig. 1) or Table 1. The most accurate reading can be obtained by using the graph since a table must be made up based on some arbitrary interval of K. An interval of 500 pounds per inch is used for Table 1.

To use graph, enter the graph with K on horizontal scale, go vertically to axle payload for trip, horizontally to read shock index. The shock index for each axle should be checked



and the lower of the numerical values should be used for shock index; this will represent

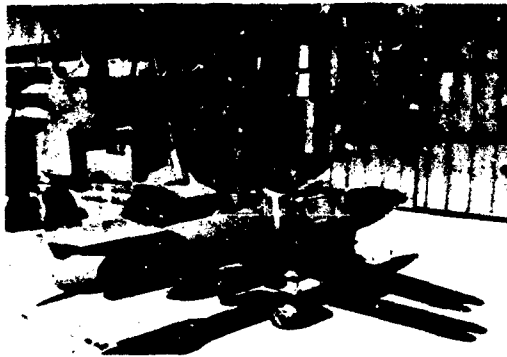


Fig. 1 - Typical Test Configuration

Forklift trucks: Four types of forklift trucks were utilized. They differed in capacity, motive power, and tire type. The four vehicles are pictured, from left to right, in Figure 2 in the order given in Table I.

TABLE I
Types of Forklift Trucks Employed

Capacity (lb)	Power	Tires
7000	Gasoline	Pneumatic
4000	Gasoline	Pneumatic
3000	Gasoline	Solid
2000	Electric	Solid



Fig. 2 - The Forklift Trucks

Two characteristics of the forklift truck should be borne in mind during examination of the results of the work. The engine or motor is rear mounted and is surrounded by a massive shield which acts as a counterbalance for the load on the forks. In the higher capacity lifts, the shield is a heavy casting; in the smaller models, steel plate is used for the same purpose. The second noteworthy characteristic is found in the forks themselves. They are attached loosely to their supports to permit adjustment to fit the load. The fork supports, in turn, fit loosely on the vertical channel to permit them to move freely. Thus, the load is supported by a loosely coupled system. The load also is coupled to the forks loosely.

Load: A simulated bomb shape was used as the load throughout the program. The shape was mounted on a storage and handling fixture. The assembly is shown in Figure 3. The load assembly weighed 900 pounds.



Fig. 3 - The Assembled Load

Instrumentation: Preliminary work had shown that during passage over very smooth pavement the excitation from the forks was low in amplitude, but when the surface being traversed was rough, amplitudes were high. In order to measure both levels, it was necessary to use two sets of accelerometers. One set was of Endevco 2220 types calibrated at 50g peak to peak; the other set was of Endevco 2223MSA types calibrated at 10g peak to peak. The accelerometers were mounted on opposite faces of the aft bulkhead of the handling fixture. Two sets of accelerometers are shown in Figure 4. Data from the upper set, mounted on the skin of the bomb shape, are not considered in this paper since they are peculiar to the shape. Only the data measured by the set on the

THE DYNAMIC ENVIRONMENT ON FOUR INDUSTRIAL FORKLIFT TRUCKS*

Mark B. Gens
Sandia Laboratories
Albuquerque, New Mexico 87115

The purpose of this study was to determine the dynamic input to cargo during carriage on various types of forklift trucks. Among the variations examined were trucks with capacities of 2000, 3000, 4000, and 7000 pounds; trucks with pneumatic and with solid tires; and trucks powered by gasoline engines and by electric motors.

The cargo used as a simulated bomb shape mounted on a cradle-like rack which is used to transport and handle weapons. It was found that there was little steady-state continuous excitation transmitted through the forks to the load. Many discrete excitations were present. Data reduction in the form of shock response spectra showed responses up to 10g in amplitude below 20 Hz and up to 40g at 100 Hz.

INTRODUCTION

The transportation of components, assemblies, and packages by forklift truck is inherent in almost all phases of manufacture, transport, handling, and storage. The forklift truck is employed in: (1) moving material and equipment during manufacture, (2) removing completed assemblies and packages to transportation points, (3) loading cargo into rail cars, trucks, or aircraft, (4) unloading cargo at destination, (5) warehousing cargo, and (6) moving cargo to point of use. The environment produced by such transport has not been defined. It was the purpose of this study to sample the dynamic environment experienced by cargo during transport by forklift truck and, by analyses of the data, develop a definition of the environment. Since this was pioneering work, the resulting definition is preliminary in nature and is subject to future modification.

The program was funded and conducted jointly by the Air Force Weapons Laboratory, Kirtland Air Force Base, New Mexico, and by Sandia Laboratories,

Albuquerque, New Mexico. It is one phase of a larger program which will provide definition of the environment experienced by cargo during handling by a variety of mechanical equipment. Program management is by the Environmental Criteria Group, Sandia Laboratories. Air Force participation in this phase was limited to funding.

The phase of the program to be reported here considers only the types of forklift trucks in general use throughout industry. It is limited to four specific trucks during outdoor use.

TEST CONFIGURATION

The test configuration consisted of a forklift truck, a load, and the necessary instrumentation. A typical assembly is shown in Figure 1.

*This work was supported in part by the Air Force Weapons Laboratory through Contract PD73-246 with the AEC, and in part by the AEC.

Test Configuration:		Forklift with Bomb Shape												
Test Maneuver:		Along 9th Street												
Instrument Number and Range:		Channel 9												
Instrument Location and Axis:		On Bulkhead, Axis V												
Acceleration Amplitude 0 to Peak G		Peak Distribution in Percent, Discrete												
		Wideband RMS = .23												
7.200														
5.200														
3.700														
2.700														
1.900														
1.400														
1.000														
.720														
.520														
.370														
.270														
.190														
.140														
.100														
.072														
Frequency Band--Hz	0	20	40	80	120	180	240	350	500	700	1000	1400	1900	
	20	40	80	120	180	240	350	500	700	1000	1400	1900	2500	
RMS Level		.21	.04	.06	.04	.02	.02	.03	.01	.02	.02	.01	.01	
Total Peaks		54	71	237	156	61	38	219	11	68	238	83	42	

Fig. 7 - Typical Peak Distribution Record, 3000 lb Capacity Forklift

bulkhead were considered as input from the forks and, therefore, of general interest.

The recording equipment consisted of an Ampex CP100 tape recorder and Endevco 2640MS charge amplifiers. Power was supplied by a portable motor generator. These were placed in a two-wheel trailer which was towed by the lift truck. The operator also rode the trailer to monitor and to record events on the voice track. Figure 5 shows the trailer and contents.

The instrumentation system was validated in the laboratory. The bomb shape in its handling cradle, less casters, was mounted on a shaker with a capacity of 17,500 lb (Figure 6). In addition to the accelerometers mounted on the test load, laboratory instruments were mounted to measure essentially the same excitation. The laboratory accelerometers were monitored by the test instruments. The data obtained were plotted on an X-Y plotter. The results were similar enough to lead to the conclusion that the test instrumentation was providing valid data [1].

TEST PLAN

A test course was laid out which included paved and unpaved areas as well as a set of railroad tracks. The paved areas included asphalt streets with manhole covers and metal utility trench covers, and concrete aprons and driveways. Some of the paving was relatively new and smooth, while some was older and deteriorated. The unpaved area was not maintained as a driving surface. It included some concrete sidewalks which were elevated about an inch above the surface.

The forklift operators were experienced. They were instructed to drive at the highest speed consistent with retaining the load on the forks. In general, the speeds chosen were less than 10 miles per hour. Much of the time it was 5 miles per hour or less.

DATA REDUCTION

The first step in data reduction was to produce an oscillograph record from the magnetic tape. From this record, specific time frames were chosen to be treated further. The excitation which appeared to be continuous in nature was reduced as a peak density distribution display. The excitation which appeared to be discrete and intermittent was reduced in the form of response spectra.



Fig. 4 - Accelerometer Position

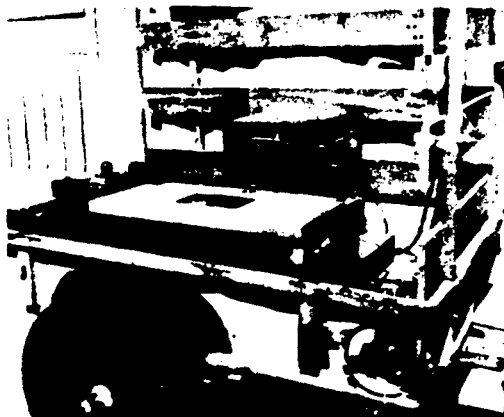


Fig. 5 - The Instrumentation Trailer

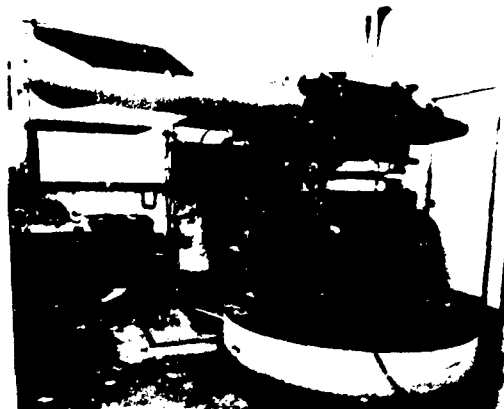


Fig. 6 - Instrumentation Test

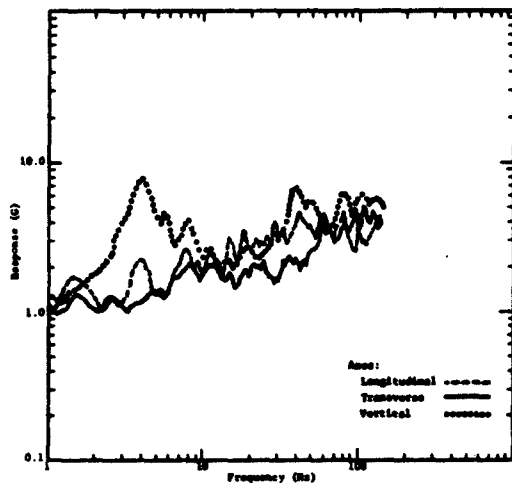


Fig. 9a
2000 lb Capacity Forklift Truck

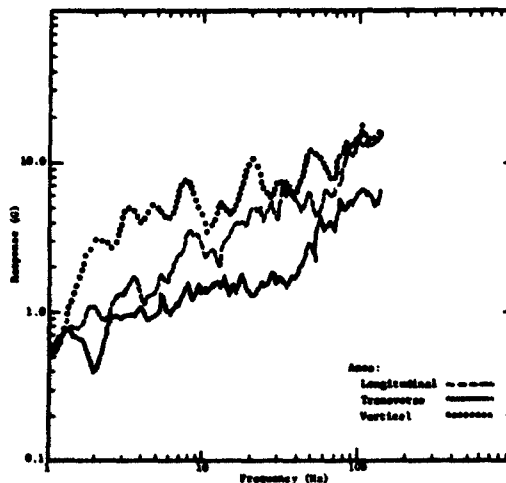


Fig. 9b
7000 lb Capacity Forklift Truck

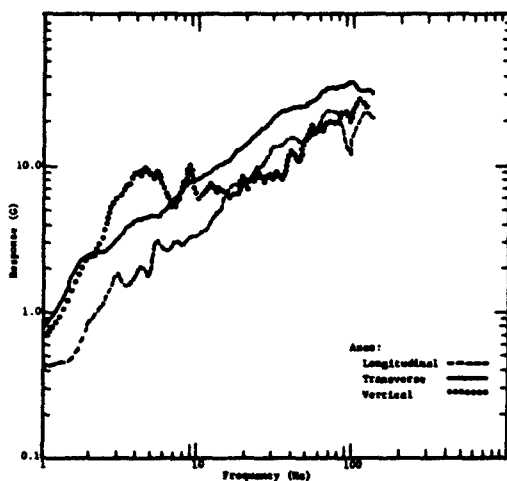


Fig. 9c
3000 lb Capacity Forklift Truck

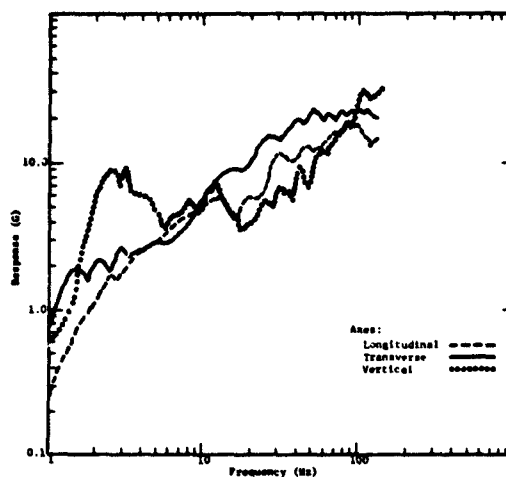


Fig. 9d
4000 lb Capacity Forklift Truck

Fig. 9 - Envelopes of Forklift Response of High Amplitude Discrete Excitation Measured at the Base of the Handling Cradle (Damping = .03)

RESULTS

General: The axis designations used in the data displays are relative to the axes of the forklift truck.

Continuous Excitation: Peak density distribution reductions were made of records which appeared to show continuous excitation [2]. Figure 7 shows a typical example of such a record. It represents the data taken when the load was carried on the 3000 lb capacity forklift truck along a good asphalt surface at approximately 5 miles per hour.

At first glance, the peak density distribution record appears to be a normal one of low amplitude excitation. However, a closer examination reveals some anomalies. In continuous excitation, the number of peaks counted increases in proportion to frequency. Since time remains constant, there will be approximately 10 times as many peaks at 100 Hz as at 10 Hz. The smallest peak count will appear in the left hand column (0-20 Hz) and the largest peak count in the right hand column (1900-2500 Hz), with a progression between the two. Here, that is not true. Several frequency bands have a lower peak count than found in the band of lowest frequency. The peak count increases until 80 Hz is reached, then diminishes, rises again in the 240-350 Hz band, and continues to rise and fall throughout the spectrum.

In looking at a specific frequency band, one would expect, were the excitation continuous, that the relationship of peak count to frequency might be expressed as:

$$N_p = (2f)(t)$$

where

N_p = number of peaks

$2f$ = number of peaks per cycle

t = time of record in seconds

When this relationship is applied to the 500-700 Hz frequency band, using 600 Hz as the mean frequency, $N_p = 2(600)(5) = 6000$. In our example, we find 68 peaks in the frequency band. These two examples indicate the absence of continuous excitation.

As further analysis to determine the true nature of the excitation which appeared to be continuous on the oscillograph record, a 5 second record

of the same event shown in Figure 7 was submitted to bandpass analysis. A typical display of the results of this effort is given in Figure 8. This display shows that the excitation is largely low amplitude pulses which are discrete in nature. Examination of other frequency bands shows that some pulses have peaks as high as 0.7g in frequencies below 15 Hz. In the higher frequencies, peaks rarely exceed 0.1g and usually are below 0.05g.

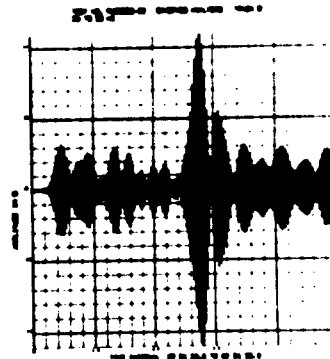


Fig. 8 - Typical Bandpass Display, 3000 lb Capacity Forklift

The absence of an incremental progression in the number of peaks across the spectrum, the few number of peaks in some of the higher frequency bands, the pulse-like character of the excitation, and the very low amplitudes indicate the absence of any significant continuous broad band random excitation in the forklift environment, regardless of the type of motive power.

Discrete Excitation: The presence of discrete excitation in the forklift environment is very apparent. Examination of the oscillograph records show frequency high amplitude bursts superimposed on the low amplitude background. These data were reduced in the form of response spectra. These spectra were summarized in two ways to show the maximum accelerations for each type of forklift truck and to show a summary of all spectra as an indication of the environment which may be encountered by cargo.

Figure 9 shows envelopes of response spectra in each axis for each of the forklifts used. These spectra reveal one common characteristic: In the frequencies below 10 Hz, the vertical axis is dominant and has high amplitudes ranging from 8 to 10g. In three cases, there is a prominent "hump" in the 3 to 5 Hz region. In the fourth record (Figure 9b), the "hump"

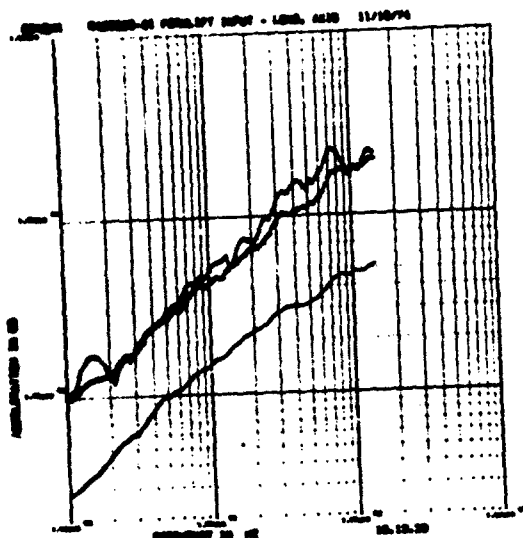


Fig. 10a - Longitudinal Axis

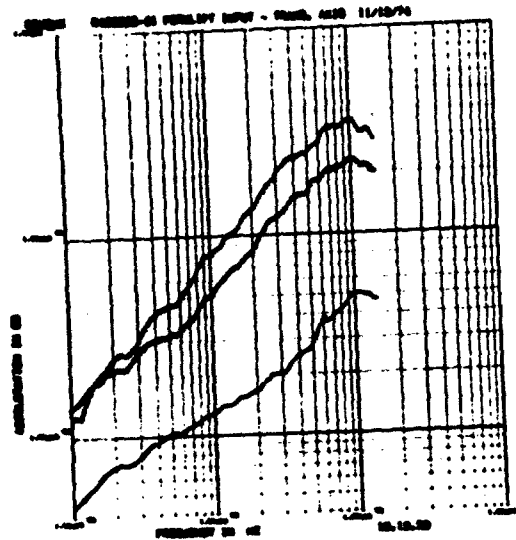


Fig. 10b - Transverse Axis

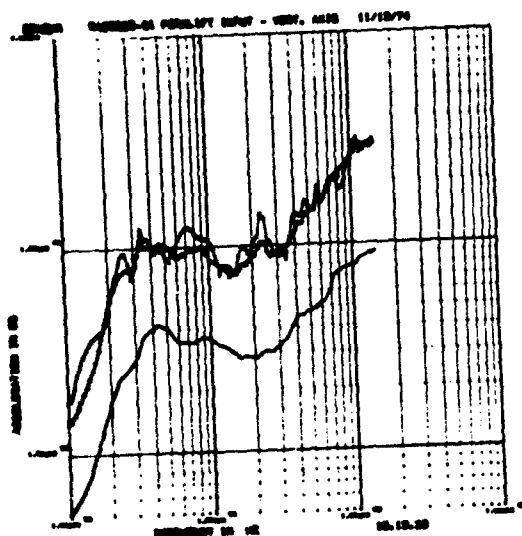


Fig. 10c - Vertical Axis

Key:

Mean —————
 Mean + 3 S.D. - - - - -
 Envelope * * * * *

Fig. 10 - Summaries of Response of Four Forklifts to a Range of Amplitudes of Discrete Excitation Measured at the Base of the Handling Cardle (Damping = .03)

is present but is overshadowed by a higher amplitude prominence at 7 to 8 Hz. Above 10 Hz, axis domination varies. Measurements made on the 3000 lb and 4000 lb forklift trucks (Figures 9c and 9d) show the transverse axis to be dominant, while in the other two cases, the vertical axis dominates throughout the spectrum. The highest response amplitude found was 37g in the transverse axis on the 3000 lb capacity truck at 100 Hz.

Comparison between these envelopes indicates that of the physical variables, between the four vehicles, the one which appears to have the greatest influence on the smoothness of ride is the ratio between the capacity of the vehicle and the weight of the load. The truck which was loaded most heavily (2000 lb capacity, Figure 9a) had the smoothest ride. No response amplitudes were higher than 8g. The truck which was loaded most lightly (7000 lb capacity, Figure 9b) had response amplitudes that were higher than 10g in only a few frequencies. Conversely, the vehicles which were loaded at 25 to 30 percent of capacity (3000 and 4000 lb capacity, Figures 9c and 9d) had response amplitudes above 10g in all frequencies above 15 Hz.

There was no evidence that the type of tire involved had any influence on the dynamic environment. The 2000 and 3000 lb capacity trucks both had solid tires, yet the response spectra were very different in shape and amplitude (Figures 9a and 9c). On the other hand, the 3000 and 4000 lb capacity trucks exhibited response spectra which were very similar, and the latter had pneumatic tires (Figures 9c and 9d).

Forty-eight response spectra were produced for the purpose of analysis of the forklift environment. In order to provide a single representation of the environment, these were combined by computer. The program operates with the coordinates from which the individual spectra are plotted. It calculates the mean, standard deviation, and highest value for each frequency of the 200 points used to produce response spectra. It then plots in mean, mean plus 3 standard deviation, and the highest value for each point. Figure 10 shows the results of this manipulation.

The summarized response spectra in Figure 10 are shown by axis. The longitudinal and vertical records show a close correspondence between the maximum values and the mean plus 3 standard deviation (3 S.D.) values. In the transverse axis, however, the curve of

maximum values lies above that of the 3 S.D. level. At 100 Hz, the difference is 15g. This may be interpreted to mean that while most of the responses in the transverse direction lie at or below the 3 S.D. level, the lurching of the forklift truck when traversing uneven surfaces can cause responses above that level often enough to be significant.

These summaries show once again that the highest amplitudes in the frequencies lower than 10 Hz are in the vertical axis. In the transverse and vertical axes, the 3 S.D. level reaches or exceeds 20g in the 80 to 100 Hz range, while the highest level of the 3 S.D. is 18 Hz in the longitudinal axis at similar frequencies. Responses above 20g were recorded in all three axes at these higher frequencies.

CONCLUSIONS

1. This work encompassed measurement of the dynamic environment of four industrial forklift trucks. It is not yet clear whether these data are typical, since little other such work has been done.
2. No continuous excitation with Gaussian-like distribution was found. There is a background of pulsating continuous excitation of very low amplitude, usually less than 0.1g.
3. Discrete excitation is frequent.
4. The lift truck which was loaded to approximately 50 percent of capacity showed the least variation in response level. The high capacity lift truck loaded to approximately 13 percent of its capacity showed relatively low levels of response below 20 Hz.
5. Responses in the longitudinal and transverse axes were higher when the lift truck was loaded to 20 to 30 percent of capacity.
6. Responses in the vertical axis were consistently the highest in frequencies below 10 Hz, but the other axes showed higher amplitude responses at frequencies above 10 Hz.
7. Examination of the distribution of the responses showed that most maximum amplitudes were at or above the mean plus 3 standard deviation levels. In the longitudinal and vertical axes, the highest responses were at approximately the same amplitude as the 3 S.D.; however, in

**A STATISTICALLY BASED PROCEDURE FOR TEMPERATURE SENSITIVE
DYNAMIC CUSHIONING CURVE DEVELOPMENT AND VALIDATION**

Don McDaniel
Ground Equipment and Materials Directorate
Research, Development, Engineering and Missile Systems Laboratory
U. S. Army Missile Command
Redstone Arsenal, Alabama 35809

Richard M. Wyskida
Industrial and Systems Engineering Department
The University of Alabama in Huntsville
Huntsville, Alabama 35807

and

Mickey R. Wilhelm
Industrial and Systems Engineering Department
The University of Alabama in Huntsville
Huntsville, Alabama 35807

The experimental results presented herein clearly indicate that a statistically significant temperature effect on the cushioning performance of a foamed thermoplastic material does, in fact, exist and should thus be explicitly considered by designers of container cushioning systems.

Drop test data were collected for Hercules Minicel material and analyzed by: 1) the development of an outlier test based on the variance associated with the three replications of each experimental condition; 2) the development of design curves for the various temperatures, drop heights, and material thicknesses based upon a second order polynomial regression of the logarithm of stress versus deceleration at impact; 3) conducting an analysis of variance for each drop height to determine the effect of temperature differences.

INTRODUCTION

Foamed thermoplastic materials are particularly attractive for use as lightweight, low-cost, easily fabricated cushioning systems in shipping containers. However, foamed materials have been used in military containers with reservations, due primarily to the difficulty the container designer encounters in attempting to predict the dynamic response of the packaged item when a container is exposed to the rigors of worldwide distribution. Military containers encounter widely varying temperature extremes in worldwide distribution. However, current design practice utilizing available dynamic cushioning curves does not account for the

effect of temperature other than the stipulation of "safe" temperature values, due to the absence of temperature sensitive dynamic cushioning design curves.

A study which was published as MICOM Report No. RL-TR-71-2 entitled "A Study of Impact Test Effects Upon Foamed Plastic Containers," [1], indicates that temperature has a significant effect upon the G level response of an item that is packaged utilizing a foam plastic cushioning system. The above referenced study was based upon a comprehensive literature search performed by the Defense Documentation Center on container drop tests conducted within the last 15 years. Many of

the transverse axis, responses as much as 15g higher than 3 S.D. were found.

8. Further work must be done using different loads, different forklift trucks, and different terrain before conclusive statements can be made about the environment experienced by cargo during forklift transport.

ACKNOWLEDGEMENTS

The author wishes to express appreciation to the Air Force Weapons Laboratory, Kirtland Air Force Base, New Mexico, for participation in the funding of this work. Special thanks are extended to Mr. A. J. Tucker, Sandia Laboratories, who supplied most of the technical expertise and ingenuity which made it possible to obtain the data upon which this document is based.

REFERENCES

- [1] A. J. Tucker, "Certification of Portable Instrumentation System," unpublished Sandia Report R423326, July 1973.
- [2] J. T. Foley, et al., "Current Predictive Models of the Dynamic Environment of Transportation," SLA 73-0456, Sandia Laboratories, Albuquerque, June 1973 (also published in the Journal of Environmental Sciences, January/February 1973).

Mr. Gertel: (Kinetic Systems) I wasn't clear as to the purpose of the shock spectrum were these analyzed as shocks or was this a steady vibration or a transient vibration and if it was a shock spectrum did you select out a particular bump out of the time history record that was analyzed in a shock spectrum method and if so what about the Q involved in this particular analysis?

Mr. Gens: These were picked from the oscillograph record as looking like shocks and were analyzed as shock with a time history and shock response spectrum type of analysis. In general they were particular bumps. There is one bump on the southside of Bldg. 894 that was in all of them. Which means nothing to you, but I started looking for it in the records because it was so characteristic. So they were reduced as shock spectra and some day there will be a report out which has all of that in it. There was another part to your question.

Mr. Gertel: It was about the Q in the shock spectrum analysis. If there is any further work being done along this area by other people or any projected analysis that would be an important standardization key to the data you are presenting.

Mr. Gens: What we presented here was 3% damping.

Mr. Gertel: Did you try to analyze by shock spectrum the bumps that might arise from lowering the equipment off the forks? It seems like usually this is the situation of most concern, that the actual handling of lifting and sitting it down some place because depending on the care and skill of the operators these could be hazardous times for delicate equipment.

Mr. Gens: They were enclosed in the envelopes but they didn't contribute very much to them and I mentioned that we had skilled operators and I don't think that we got what we might have gotten from some others. That's a guess.

Voice: You mentioned somewhere that you brought in the engine from the vehicle itself, how did the engine dynamic components compare with the actual dynamics of riding over the surfaces you were traveling on? Was the engine any significant factor in the vibration environment that you were seeing?

Mr. Gens: No, the engine didn't seem to have any particular contribution. We always started out with what we called a quiet run where everything was running but the vehicle was not moving. I didn't reduce any of that. That which I did reduce which shows the pulses higher in amplitude at least on the oscillograph record but we couldn't find any evidence of steady state vibration at all of the type which you would expect from an engine.

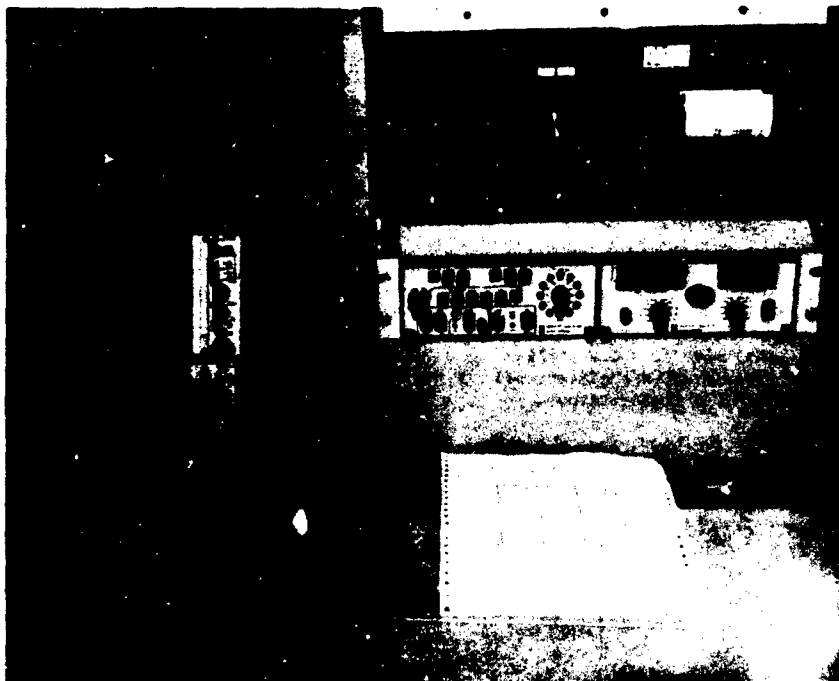


Fig. 2 - Data recording instrumentation



Fig. 3 - Temperature controlled chambers for material samples

these drop test programs were conducted only at ambient temperature, many were one-shot tests with no repetition or duplication within the test, and others did not provide a quantitative measure of container response. Consequently, the results of the literature search provided only fifteen candidate containers utilizing foamed plastic cushioning that had undergone adequately documented drop testing.

In an attempt to develop statistically significant design curves which consider temperatures in addition to the classical ambient value (70°F), an experiment was designed to investigate the change in cushion impact absorption characteristics at the specified extreme temperature values of -65°F and 160°F . The basic concept of the experiment was the premise that an actual drop test program was required to establish the validity of a temperature effect hypothesis.

PRELIMINARY CONSIDERATIONS

Prior to the design of any experiment, the pertinent influencing factors upon an experimental outcome must be identified and enumerated. Consequently, the identified factors in this research are as follows: material type, material density, drop height, material thickness, static stress, and material temperature. The findings published in this paper are concerned only with the experimental drop test results on 2 lbs/ft³ density Hercules Minicel, L-200, a closed cell, cross-linked, polyethylene foam. Drop heights considered were 12", 18", 24", and 30". Sample material thicknesses utilized were 1", 2", and 3". Static stress levels, defined as the weight of the drop test platen divided by its footprint in square inches on the material sample, were selected for each drop height based upon the expected location of the developed design curve for the specific characteristics under consideration. Consequently, static stress levels are not necessarily common for all drop heights. Based upon the extreme conditions defined in Army Regulation AR70-38, dated July 1, 1969, three material temperature levels were investigated: -65°F , 70°F (ambient), and 160°F .

The MICOM, Redstone Arsenal, Alabama drop test facility has been certified by The Air Force Packaging Evaluation Agency per specification MIL-C-26861. All data was acquired at this facility utilizing the equipment shown in Figures 1 - 3. Figure 1 shows the MTS Wide Range Cushion Tester utilized in the drop test program. The machine consists of a guided drop platen of adjustable weight which impacts on the cushion sample at controlled impact velocities. Deceleration of the platen during impact on the cushion is measured with an accelerometer and recorded on the instrumentation shown in Figure 2. Figure 3 shows the experimentation actually in process. Attention is specifically directed to the temperature controlled chambers in this Figure. The framework of the data collection process was

commensurate with the experimental design concept which follows.



Fig. 1 - MTS wide range cushion tester

EXPERIMENTAL DESIGN CONCEPT

In many experiments where a factorial arrangement is desired, it may not be possible to completely randomize the order of experimentation. Such is the case in this research effort.

It is a relatively time consuming process to vary the stress levels during experiments in that for each stress level, the drop test platen must be changed. Consequently, predetermined stress levels were set for each material type, density, and drop height, and then three replications at three thicknesses and three temperatures were performed at each of the levels.

With the restrictions on randomization indicated above, a split-split plot experimental design was determined to be superior for use in testing whether temperature does, in fact, significantly affect the performance of the various types and densities of cushioning material currently employed.

The split-split plot design is a specialized form of a nested design in which a sub-treatment factor B is nested within a main treatment A and sub-sub-treatment C is crossed with A and B [2]. The double-splitting refers to splitting the analysis into three sub-analyses:

TABLE 1

Analysis of Variance on Data for a 12" Drop Height *

SOURCE OF VARIATION	SUMS OF SQUARES	DF	MEAN SQUARES	F-STATISTIC	PROB. > F
Stress Level	303165.00	14	21654.60	753.53	0.00
Replicates	69.79	2	34.90	--	--
Error (Stress)	804.65	28	28.74	--	--
Material Thickness	136578.00	2	68289.10	2223.06	0.00
Stress x Thickness	31334.50	28	1119.09	364.30	0.00
Error (Thickness)	1843.11	60	30.72	--	--
Temperature	2038.77	2	1019.39	27.73	0.00
Stress x Temperature	127240.00	28	4544.29	123.63	0.00
Thickness x Temperature	6321.84	4	1580.46	42.99	0.00
Stress x Thickness x Temperature	3772.83	56	67.37	1.83	0.00
Error (Temperature)	6616.44	180	36.76	--	--
TOTAL	619784.00	404	--	--	--

TABLE 2

Analysis of Variance on Data for a 18" Drop Height *

SOURCE OF VARIATION	SUMS OF SQUARES	DF	MEAN SQUARES	F-STATISTIC	PROB. > F
Stress Level	365539.00	11	33230.80	302.87	0.00
Replicates	109.26	2	54.63	--	--
Error (Stress)	2413.85	22	109.72	--	--
Material Thickness	270231.00	2	135115.00	1624.72	0.00
Stress x Thickness	85727.10	22	3896.69	46.86	0.00
Error (Thickness)	3991.78	48	83.16	--	--
Temperature	1278.82	2	639.41	7.57	0.00
Stress x Temperature	203606.00	22	9254.82	109.52	0.00
Thickness x Temperature	12512.60	4	3128.15	37.02	0.00
Stress x Thickness x Temperature	7576.06	44	172.18	2.04	0.00
Error (Temperature)	12168.40	144	84.50	--	--
TOTAL	965153.00	323	--	--	--

* The values in this table may not sum due to rounding

1. An analysis consisting of the main treatment A, the replications, and an interaction which is called error of A x replications;
2. An analysis of sub-treatment B, the interaction of A x B, and the error composed of the interactions (B x replications) plus (A x B x replications); and
3. The analysis of sub-sub-treatment C, the interactions A x C, B x C, and A x B x C, and the error composed of the interactions (C x replications) plus (B x C x replications) plus (A x C x replications) plus (A x B x C x replications).

Under this design configuration, the mathematical model for each experimental observation may be written as

$$\begin{aligned}
 y_{ijkt} &= \mu + S_i + R_t + SR_{it} && \left\{ \text{WHOLE PLOT} \right. \\
 &+ Th_j + STh_{ij} + ThR_{jt} + && \left\{ \text{SPLIT-PLOT} \right. \\
 &SThR_{ijt} && \\
 &+ T_k + ST_{ik} + ThT_{jk} + && \left\{ \text{SPLIT-SPLIT} \right. \\
 &SThT_{ijk} + TR_{kt} + ThTR_{jkt} + && \left\{ \text{PLOT} \right. \\
 &STR_{ikt} + SThR_{ijkt} &&
 \end{aligned}$$

where μ = the general mean
 S_i = i^{th} static stress level
 Th_j = j^{th} material thickness
 T_k = k^{th} temperature level
 R_t = t^{th} replication
 SR_{it} = whole plot error
 $ThR_{jt} + SThR_{ijt}$ = split-plot error
 $TR_{kt} + ThTR_{jkt} + STR_{ikt} + SThTR_{ijkt}$ = split-split plot error.

DATA ACQUISITION AND ANALYSIS

Before the drop test study could proceed, provisions had to be made for collecting the resulting drop test data which would be completely compatible with the split-split plot experimental design for the determination of a

temperature effect on cushion performance. Consequently, a data form was designed and computerized which included a randomization scheme for identifying the order of experimentation in which the temperature-thickness experimental combinations should be performed.

Analysis of Variance

In order to test the significance of the temperature effect on cushioning material properties, the data set corresponding to each drop height was subjected to an Analysis of Variance to detect the significance of a temperature effect before going any further. The results were that all drop heights exhibited a temperature effect as shown in Tables 1 through 4.

Outlier Detection

In most experimental situations, cognizance must be taken that a set of observations, purportedly obtained under the same conditions, may be widely different from other observations, or an outlier from the rest.

Thus, the decision confronting the experimenter is whether to keep the suspect observation(s) in computation, or whether it should be discarded as a faulty measurement. It should be pointed out, however, that the word reject as used here means reject in computation, since every observation must be recorded.

With these concepts in mind, the data was checked for outliers, and any outliers found were removed before the design curves were generated. Further, the outlier test was only conducted on the three replications of each set of experimental conditions for each drop height, temperature, and material thickness.

Although many criteria have been proposed for guiding the rejection of outliers, none were found in the literature which were applicable to this case. Consequently, an extension of the extreme studentized deviate from the sample mean (Nair Criterion) was developed.

The first step in the outlier detection procedure is to compute the sample variances for each set of three replications of G levels for each static stress considered, to find which set has the maximum sample variance. For the set of observations having the largest variance, each observation of the set is then tested individually as a candidate for rejection as an outlier by utilizing the statistic

$$t = \frac{|x_e - \bar{x}|}{s_v}$$

where x_e = an individual observation in a set of three replications

\bar{x} = the sample mean of the three observations

s_v = an independent external estimate of the standard deviation from concurrent data.

To acquire s_v , the set of replications of G's having the maximum sample variance, as indicated above, corresponding to a particular stress level, is eliminated from the calculation. From the remaining sets of replications of G's, s_v is calculated with the expression

$$s_v = \sqrt{\frac{\sum_{i=1}^{n-1} s_i^2}{n-1}}$$

where s_i^2 = sample variance of the i^{th} set of replications of G's

n = number of stress levels.

The values of the t statistic for each observation in the set of replicates being tested are compared with the appropriate value from a table of percentage points of the extreme studentized deviate from the sample mean [3], and a point is rejected as an outlier if $t(\text{calculated}) > t(\text{table value})$.

If an observation is rejected in the first iteration of the outlier test, the set of replicates to which it belonged is no longer considered in further calculations, but the procedure then moves to the set of replicates with the next highest sample variance to check for outliers. Iteration is continued until a set of replications is checked and no points are rejected.

Safeguards are built into the outlier test procedure which restrict the number of data points that can be rejected in a set of replicates. For instance, only one point can be rejected in a set of three replications. Also, if two of the three values of t are the same, and are greater than the test criterion value of t , then neither of the observations is rejected. This is essentially a tie rule for a relatively rare but possible eventuality.

Regression Curve Development

With the outlying observations removed from the data, many different polynomial regression models were utilized in an effort to describe the theoretical dynamic cushioning curve from this data. However, none of these models were sufficient on the basis of analysis of regression variance and sample correlation coefficients of static stress (x) versus deceleration at impact in G's (y). It was not until a polynomial regression of the logarithm of

static stress (x) versus deceleration at impact (y) was attempted that significant results were obtained. The general form of the p -order polynomial regression equation was determined to be:

$$y_i = b_0 + b_1 \ln x_i + b_2 (\ln x_i)^2 + \dots + b_p (\ln x_i)^p,$$

which represents the deceleration y_i values from the logarithm of static stress level x_i values.

A fairly rigorous method for determining the degree of the polynomial to be fitted to a given set of data consists of first fitting a straight line to a set of data, i.e., $y = b_0 + b_1 x$ and testing the hypothesis $\beta_1 = 0$. Then, fit a second degree polynomial and test the null hypothesis $\beta_2 = 0$, namely, that nothing is gained by including the quadratic term. If this hypothesis can be rejected, a third-degree polynomial is fitted and the hypotheses $\beta_3 = 0$ is tested, etc. This procedure is continued until the null hypothesis $\beta_p = 0$ cannot be rejected in two successive steps and, consequently, there is no apparent advantage to carrying the extra terms [4]. However, in order to perform these tests it is necessary to impose the assumptions of normality, independence, and homoscedasticity of errors of the regression estimates.

After fitting the straight line, a second-degree polynomial is fitted and tested to see whether it is worthwhile to carry the quadratic term by comparing σ_1^2 , the residual variance after fitting the straight line, with σ_2^2 , the residual variance after fitting the second-degree polynomial. Each of these variances is given by

$$\frac{\sum_{i=1}^n (y_i - y_i')^2}{\text{degrees of freedom}}$$

with y_i' computed, respectively, from the equation of the line:

$$y_i' = b_0 + b_1 x_i$$

and the equation of the second degree polynomial:

$$y_i' = b_0 + b_1 x_i + b_2 x_i^2$$

where in this research effort $x_i = \ln(100 x_i)$

The term "degrees of freedom" in the denominator of the equation for the residual variances is $n - 2$ for σ_1^2 , because two degrees of freedom are lost in the computation of x and b_1 , and it is $n - 3$ for σ_2^2 , because three degrees of freedom are lost in the computation of x , b_1 , and b_2 .

TABLE 3

Analysis of Variance on Data for a 24" Drop Height *

SOURCE OF VARIATION	SUMS OF SQUARES	DF	MEAN SQUARES	F-STATISTIC	PROB. > F
Stress Level	475736.00	10	47573.60	150.18	0.00
Replicates	41.88	2	20.94	--	--
Error (Stress)	6335.53	20	316.78	--	--
Material Thickness	221067.00	2	110534.00	694.83	0.00
Stress x Thickness	61112.60	20	3055.63	19.21	0.00
Error (Thickness)	6999.48	44	159.08	--	--
Temperature	46759.00	2	23379.50	158.27	0.00
Stress x Temperature	310374.00	20	15518.70	105.05	0.00
Thickness x Temperature	16648.20	4	4162.04	28.17	0.00
Stress x Thickness x Temperature	12536.00	40	313.40	2.12	0.00
Error (Temperature)	19499.10	132	147.72	--	--
TOTAL	1177110.00	296	--	--	--

TABLE 4

Analysis of Variance on Data for a 30" Drop Height *

SOURCE OF VARIATION	SUMS OF SQUARES	DF	MEAN SQUARES	F-STATISTIC	PROB. > F
Stress Level	644785.00	15	42985.70	599.97	0.00
Replicates	565.57	2	282.79	--	--
Error (Stress)	2149.39	30	71.65	--	--
Material Thickness	787921.00	2	393960.00	6479.41	0.00
Stress x Thickness	283931.00	30	9464.37	155.64	0.00
Error (Thickness)	3891.92	64	60.81	--	--
Temperature	10016.50	2	5008.24	77.69	0.00
Stress x Temperature	674500.00	30	22483.30	348.79	0.00
Thickness x Temperature	97072.90	4	24268.20	376.48	0.00
Stress x Thickness x Temperature	28641.70	60	477.36	7.41	0.00
Error (Temperature)	12376.40	192	64.46	--	--
TOTAL	2545850.00	431	--	--	--

* The values in this table may not sum due to rounding

TABLE 6

Typical Regression Equations

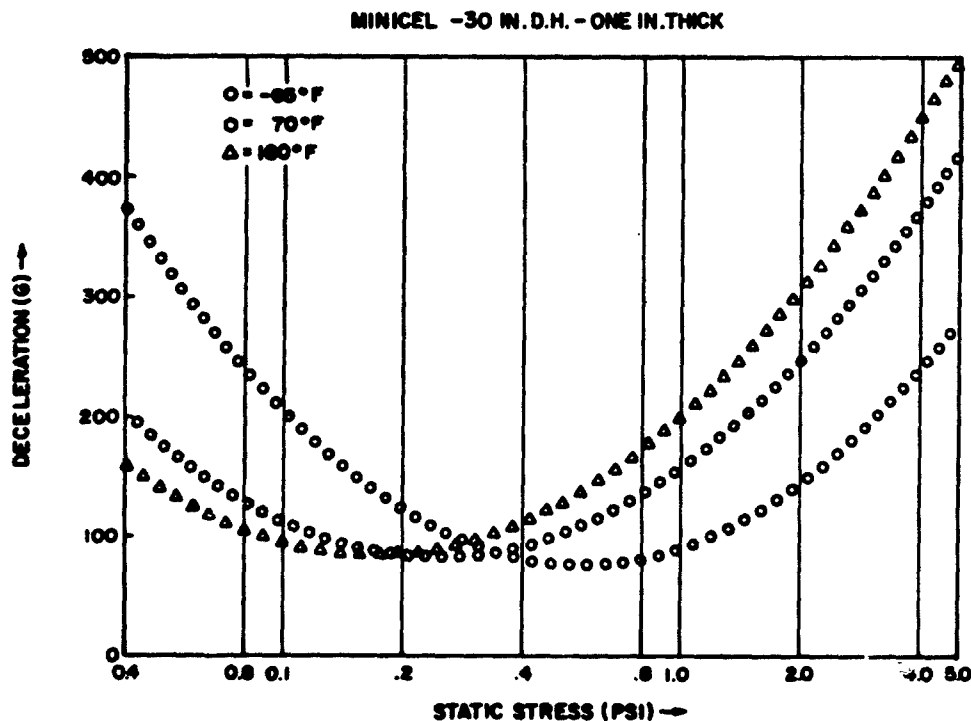
THICKNESS	TEMPERATURE	30" DROP HEIGHT REGRESSION EQUATIONS
1"	-65°	$791.96 - 341.36 \ln x + 42.40 (\ln x)^2$
	70°	$451.82 - 233.31 \ln x + 36.71 (\ln x)^2$
	160°	$368.93 - 202.81 \ln x + 36.04 (\ln x)^2$

and superimposes upon it, the -65°F and +160°F curves. When the data is presented in this manner, it is possible for a container designer to assess the effect of temperature upon cushion performance and trade-off between static stress levels for the temperatures anticipated for a particular design. From Figure 4, it can be seen that there are serious deficiencies in trying to design a container cushioning system that will experience temperature changes by utilizing only ambient cushioning curves. For example, the optimum G-level on the ambient curve is 82 G's at 0.26 psi static stress. But if this static stress level were selected and the container were dropped 30" at -65°F, a G-level of 101 G's would be anticipated which is considerably above the 70°F G-level.

However, with the presentation of cushioning data in the form of superimposed dynamic cushioning curves, this pitfall can be avoided and the designer can address the significant effect of temperature upon cushioning performance.

CONCLUSIONS AND RECOMMENDATIONS

This research shows that temperature sensitive dynamic cushioning curves are feasible to develop, and are necessary for the cushioning designer attempting to protect valuable merchandise against damage over wide temperature extremes [5].



The decision whether to carry the quadratic term is based on the statistic

$$F = \frac{\hat{\sigma}_1^2 - \hat{\sigma}_2^2}{\hat{\sigma}_2^2}$$

which is the value of a random variable having an approximate F distribution with 1 and n - 3 degrees of freedom. The hypothesis $\beta_2 = 0$ is rejected for values of F (calculated above) $> F_{\alpha}(1, n-3)$ where $\alpha = 0.05$ for this test.

Continuing with this line of reasoning, the decision whether to carry the cubic term is based on the statistical test

$$F = \frac{\hat{\sigma}_2^2 - \hat{\sigma}_3^2}{\hat{\sigma}_3^2} > F_{\alpha}(1, n-4)$$

$$\text{where } \hat{\sigma}_3^2 = \frac{\sum_{i=1}^n (y_i - [b_0 + b_1x_1 + b_2x_1^2 + b_3x_1^3])^2}{(n-4)}$$

and the decision whether to carry the quartic term is based on the test

$$F = \frac{\hat{\sigma}_3^2 - \hat{\sigma}_4^2}{\hat{\sigma}_4^2} > F_{\alpha}(1, n-5)$$

where

$$\hat{\sigma}_4^2 = \frac{\sum_{i=1}^n (y_i - [b_0 + b_1x_1 + b_2x_1^2 + b_3x_1^3 + b_4x_1^4])^2}{(n-5)}$$

As can be seen in Table 5, quadratic fits are statistically significant in all experimental conditions except three. Further, we see that absolutely nothing is gained by carrying the third and fourth degree terms, i.e., we can never reject the null hypotheses $\beta_3 = 0$ and $\beta_4 = 0$ at the 5% level of significance.

Table 6 presents the regression equations for 30" drop height and 1" thick Minicel. By substituting any selected static stress level into the regression equation for a particular temperature, the predicted G-level will be computed with excellent statistical accuracy for that particular static stress and temperature condition.

In addition to the regression equations that model G-level response mathematically, the analysis procedure also provides a graphical presentation of the design curves. Figure 4 is an example of a superimposed dynamic cushioning curve that can be generated by these equations. As can be readily seen, Figure 4 displays the ambient dynamic cushioning curve

TABLE 5

F-Statistics

$$F_{\text{CRITICAL}} = 4.10$$

$$\alpha = 0.05$$

TEMP.	THICKNESS	DROP HEIGHT = 12"		
		QUADRATIC	CUBIC*	QUARTIC*
-65°	1"	8.68	0.99	0.99
	2"	19.46	0.99	0.99
	3"	7.19	0.99	0.99
70°	1"	24.53	0.99	0.99
	2"	12.02	0.99	0.99
	3"	5.25	0.99	0.99
160°	1"	23.09	0.99	0.99
	2"	13.15	0.99	0.99
	3"	2.21*	0.99	0.99
TEMP.	THICKNESS	DROP HEIGHT = 18"		
		QUADRATIC	CUBIC*	QUARTIC*
-65°	1"	12.76	0.99	0.99
	2"	35.24	0.99	0.99
	3"	3.91*	0.96	0.99
70°	1"	39.78	0.99	0.99
	2"	10.06	0.99	0.99
	3"	9.70	0.99	0.99
160°	1"	12.71	0.99	0.99
	2"	13.77	0.99	0.99
	3"	18.17	0.99	0.99
TEMP.	THICKNESS	DROP HEIGHT = 24"		
		QUADRATIC	CUBIC*	QUARTIC*
-65°	1"	8.19	0.99	0.99
	2"	3.63*	0.99	0.99
	3"	8.31	0.99	0.99
70°	1"	15.70	0.99	0.99
	2"	16.43	0.97	0.99
	3"	8.85	0.99	0.99
160°	1"	7.18	0.99	0.99
	2"	7.67	0.99	0.86
	3"	11.15	0.99	0.99
TEMP.	THICKNESS	DROP HEIGHT = 30"		
		QUADRATIC	CUBIC*	QUARTIC*
-65°	1"	8.87	0.99	0.99
	2"	50.14	0.99	0.99
	3"	6.17	0.99	0.99
70°	1"	19.04	0.95	0.99
	2"	26.15	0.99	0.99
	3"	11.57	0.99	0.99
160°	1"	8.75	0.99	0.99
	2"	10.59	0.99	0.99
	3"	18.14	0.99	0.99

* Not significant at $\alpha = .05$

Mr. McDaniel: That's true! That is one of the problem areas with using dynamic cushioning curves generated in the manner that we generated them today. A report asked Woody Hayes do you have any problems with these football teams, he said no we haven't. We have gone as much as 7 years without fouling up the snap from center and this year we've messed it up twice and there's 14 years shot to hell! So yes that is a problem. There is no doubt about it and yes dynamic cushioning curves are a first guess that a designer uses to elbow his way in to a container design and there are all kinds of things like side constraints and the shape of the cushion and things like that. A flat cushion is not necessarily representative of exactly what you find in containers but it's the best thing we've got that I know about and I think most people will agree that dynamic cushioning curves are the best we've got today and they can be a reliable means of designing on a preliminary basis and then putting into the prototype the shape, size, statistics and wall cushioning that can be expected such that the final design should perform the way you want it to. There still are those problems of preloading that you mentioned that are not accounted for.

Experimental results on Hercules Minicel clearly indicate that a temperature effect does, in fact, exist, and should be taken into account by the container cushioning system designer. It is recommended that temperature sensitive dynamic cushioning curves be incorporated in MIL-HDBK-304, Package Cushioning Design, which will facilitate maximum distribution of the information to container designers.

The regression equations provided through the analysis procedure are a significant contribution to the study of cushioning material theory. It may be possible with the mathematical models of cushion response developed herein to formulate the mathematical relationships that represent the viscoelastic properties of cushioning materials. However, it is not expected that all cushioning materials will behave in the same pattern as the Minicel material. Consequently, each material should be tested individually, in a manner similar to the Minicel tests. It is recognized that extrapolation to other cushioning materials is not possible from one isolated material.

Based upon the encouraging results presented herein, research is continuing on additional material types and densities as well as the development of confidence intervals on generated design curves.

REFERENCES

1. McDaniel, Don, "A Study of Impact Test Effects Upon Foamed Plastic Containers," MICON Report No. RL-TR-71-2, 1971
2. UNIVAC Large Scale Systems STAT-PACK, Programmers Reference, UP7502, Sperry Rand Corp., Rev. 1, 1970
3. Matrella, Mary, Experimental Statistics, National Bureau of Standards Handbook 91, Aug. 1963
4. Miller, Irwin, and John E. Freund, Probability and Statistics for Engineers, Prentice-Hall, Englewood Cliffs, N.J., 1965
5. Wykida, Richard M. and Mickey R. Wilhelm, "Temperature Sensitive Dynamic Cushioning Function Development and Validation For Hercules Minicel Thermoplastic Foam," UAN Research Report No. 159, Sept. 1974

DISCUSSION

Mr. Cortel: (Kinetic Systems) The thing that was interesting to me in your plot was the little triangle where the three optimum curves or where the three cushioning curves sort of came together near their optimums. The question is how big does this triangle vary from material to material. If the triangle is very small it would seem that is an ideal spot to design cushioning independent of temperature effects.

Mr. McDaniel: (USAMC) That is the key as far as how big the triangle you get and not only does it vary from material to material but they also can vary from thickness or drop height of any one particular material and so in this case the triangle is rather small and in other cases if you move up on the g level spectrum the triangle gets bigger you see. So yes that is right and of course that is important and sometimes if you are high enough on the g level and for instance you have an allowable 125-150 g's then it wouldn't bother you that there is a substantial difference here in these things because you are alright at all three temperatures anyway. That's right there is that point to be concerned with, namely how big that triangle is and sometimes you just fall outside of that triangle and aren't really aware of it with the current information on the involved cushioning material.

Mr. Wasser: (Supheps, Croton) I noticed this material has the phenomena of creep when you use it in containers. Does the g factor change with reference to time when there is temperature variance or does the curve vary with time?

Mr. McDaniel: We didn't address the problem of creep we just recognized that there is that problem with any of these things and even Lord might admit that their shear mount might creep a little and yes that does happen and its one of these things that you have in a viscoelastic material. We looked at the dynamic cushioning curves just like MIL Handbook 304 suggested that it should be looked at using that same set of test parameters and inputs with the exception that we did have one slight disagreement with the handbook. I really think that kind of thing would be a very useful thing to put in MIL Handbook 304. If we can ever convince the Air Force of that maybe we can get them in.

Mr. Forkois: (NRL) I was wondering what the effect of preload would be on that? It seems to me that could make significant changes in your acceleration levels particularly when you have plus and minus loading on an item and it wasn't clear to me exactly how your test was performed. You didn't have the 1 g loading when you impacted the specimen, if I saw your drop testing arrangement properly?

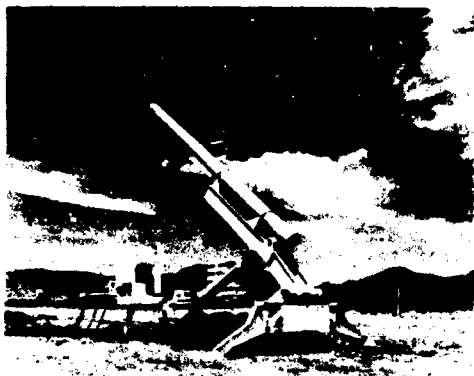


Figure 1 - Launch System in Shallow Angle Launch Configuration



Figure 3 - Launch System in Vertical Launch Configuration

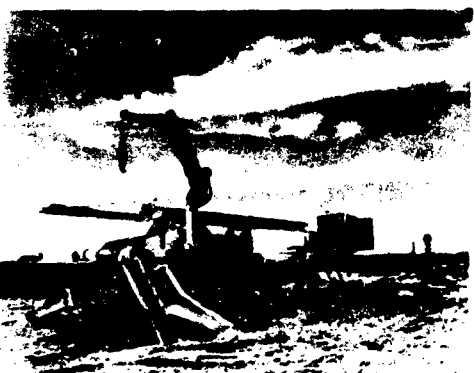


Figure 2 - Launch System in Projectile Loading Configuration

compatible with commercial tractors. In the traveling configuration, the launch system is 40 feet long, is a maximum of 10 feet wide, and is

approximately 55,000 pounds gross weight. The system is equipped with aft end stabilizing outriggers, a crane, and two winches. All this equipment, plus the main gun elevation cylinder, is powered by a 2000 psi by 15GPM hydraulic unit located at the front end. The hydraulic unit, plus an adjacent 4000-pound steel ballast, help counterweigh the gun when the launch system is in a vertical launch configuration.

The gun design was chosen from three final candidates, all powered by solid propellant. The candidates were a normal, breech loading, closed-breech gun and associated recoil system, a conventional recoilless gun, and a Davis Gun recoilless. Since no riflings or other torque-inducing features are required, all candidates were smooth bores.

The closed-breech gun was rejected primarily because the recoil system could not maintain low enough recoil forces over an acceptably small recoil distance. Low recoil forces were needed to prevent lifting the launch system during gun firing and to keep the structural loads within reason.

The Davis Gun and conventional recoilless guns were compared, and the Davis Gun was chosen. These two types

A DAVIS GUN PENETRATOR LAUNCH SYSTEM

L. O. Seamons
Sandia Laboratories
Albuquerque, New Mexico

(U) Interest in experimenting with large high velocity vehicle penetration of in situ undisturbed earth targets has culminated with a new test facility, the Davis Gun Penetrator Launch System. The launch system is a trailer mounted gun. The trailer provides mobility and doubles as a gun mount and gun elevation mechanism. The Davis Gun is a special type of recoilless gun and fires test vehicles downwards into earth targets only a few feet away. The Davis Gun advantages over other candidate guns resulted in its selection for the facility but also gave experimenters an extra projectile to worry about.

INTRODUCTION

Earth penetration research, or terradynamics, is a 12-year old study area at Sandia Laboratories. The primary object of these studies has been to understand the dynamics of the interaction between free-flying missiles, or penetrometers, and undisturbed earth targets. Maximizing penetration has been a major secondary goal.

Since the targets must be au naturel, the experiment must go to the target. Targets generally are either small, or require precision impact location, and the experimenter must deliver the penetrator with a low circular error probable (CEP). These constraints, plus available facilities, have limited study to small penetrators and low velocity phenomena.

New potential applications of penetrator technology have stimulated interest in experimenting with large diameter, high velocity penetrometers. In response, a unique facility has been designed and built to meet these goals. The new facility is named, "The Davis Gun Penetrator Launch System".

DESIGN PHILOSOPHY

The new facility was originally defined by rather general criteria:

1. The facility must be roadable, with a moderate crosscountry

capability.

2. A gun, with the maximum practical bore diameter, must be used to accelerate the payload.

3. An experimental payload of no less than 300 pounds must be delivered at velocities to 3000 ft/sec.

4. The payload must be delivered in a downward direction at angles ranging from 30 degrees off horizontal to vertical.

5. The payload impact CEP can be no more than a couple feet.

The contradiction between a roadable facility and a maximum size gun determines the nominal size and weight of the launch system. The payload-velocity-direction needs dictate the minimum gun size and general structural geometry. The resultant launch system was a trailer-mounted gun. The trailer provides mobility and doubles as gun mount and elevation mechanism at the target site. The gun fires the payload downwards automatically satisfying the low CEP requirement by limiting free flight to a few feet. The facility is shown in different configurations in Figures 1, 2 and 3.

As the photographs show, the gun rotates in a vertical plane about a pivot at the aft end of the trailer. The trailer is a fifth-wheel type and is

V_2 after the projectiles have traveled distances S_1 and S_2 . A few reasonable assumptions and the conservation of momentum principle lead to the conclusion that the same propellant charge reacting in the same initial propellant chamber volume would result in the following closed breech gun launch: A projectile weighing

$$\frac{W_1 W_2}{W_1 + W_2} \text{ after traveling } (S_1 + S_2)$$

would exit with a velocity of $(V_1 + V_2)$.

Furthermore, $\frac{W_1}{W_2} = \frac{S_2}{S_1} = \frac{V_2}{V_1}$ and the

time from first motion to gun barrel exit is the same for both projectiles. These simplified but reasonably accurate relationships enable the less familiar Davis Gun behavior to be transformed to a closed breech gun framework.

The Davis Gun has one disadvantage: a piece of hardware exits the aft end of the gun instead of a stream of gas. This makes certain range safety and gun operations more awkward, but the many advantages of the Davis Gun were felt to more than compensate. These advantages were:

1. A simpler design and significantly lower cost resulted.
2. No initial nozzle sizing was required.
3. There would be no objectionable erosion problem to be monitored and evaluated.
4. Inherent flexibility--the propellant chamber volume may be varied by merely changing the projectile spacing, and the launch point may be anywhere.
5. The internal ballistics are more predictable. This is especially important when an experiment requires large extrapolations from known behavior ranges.
6. Less propellant is required for a given propulsive task.

The specific Davis Gun designed and built for the launch system is a 12 inch inside diameter, 19.2 inch outside diameter, 35 foot long, 21000 pound tube. The gun was built from an alloy steel forging heat treated to 175000 psi tensile yield strength, and the tube was 50% autofrettaged before final machining (i.e. the plastic-

elastic interface was taken one half way through the wall thickness). The tube will have a minimum life of 500 firings of 50000 psi peak pressure.

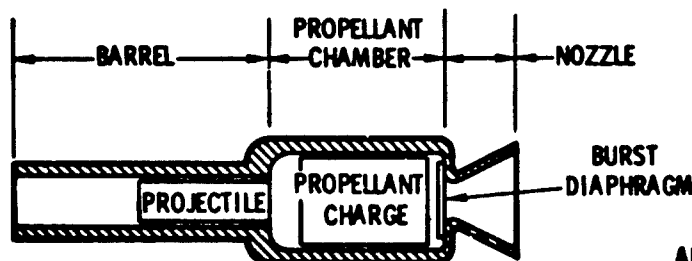
LAUNCH SYSTEM PARTICULARS

The two projectiles fired from the Davis Gun are the penetrator experiment and what is dubbed the reaction mass. Typical maximum capabilities for a tube of this size are a 380 pound penetrator to 3000 ft/sec or a 750 pound penetrator to 2000 ft/sec. In both of these cases, a reaction mass weight around 1500 pounds would be used. The mass ratio of the two projectiles is optional as is the launch point location.

A typical ready for launch hardware setup inside the tube is shown in Figure 5. In general, a penetrator experiment consists of a subcaliber (i.e. less than 12 inches) penetrator adapted to the bore diameter by a rigid foam ring in front and an aluminum/steel piston in back. Penetrators are planned to carry on-board telemetry systems capable of real time in-target data transmission. Techniques for recovering stored data without recovering the penetrator are also planned. Data recovery is vital since experiment recovery from depths in the order of 200 feet is an expensive lengthy procedure, and in some types of targets with shallow water tables, recovery is virtually impossible.

The propellant charges are modular. Each contains 50 pounds of propellant and 8 ounces of black powder igniter material. Explosive packaging is done with heavy cloth and a cardboard tube provides an axial passageway through the module for the launch positioning cable. The cloth propellant container has a laced seam for easy propellant removal when less than 50 pounds is needed. As many as four modules will be used for a given test.

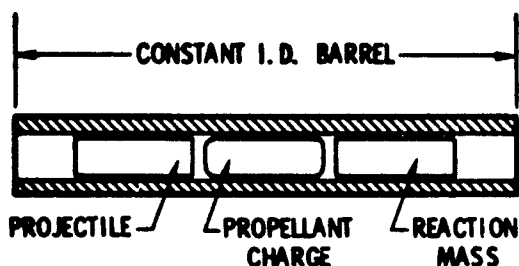
The reaction masses are also modular with an axial passageway for the launch positioning cable. The modules are sheet aluminum skins attached to wood end caps and are filled with metallic shot. Other reaction mass designs were considered and many were evaluated in scale model tests utilizing an 8-1/2 inch smooth bore gun. Liquid reaction masses were rejected because of low density. Other designs which were tried and worked were stacks of thin, 60 mil, steel plates with transverse or longitudinal lamination orientations. Solid reaction mass modules would also work, but they would require almost



CONVENTIONAL RECOILLESS GUN

ADVANTAGES

1. GAS REACTION MASS.



DAVIS GUN RECOILLESS

Figure 4 - A Conceptual Comparison of the Conventional and Davis Gun Recoilless Guns

of recoilless guns are conceptually compared in Figure 4.

As can be seen, the conventional recoilless basically consists of a barrel, a propellant chamber and a nozzle. In large caliber guns, these different parts are, of necessity, separate pieces of hardware and require joint designs for assembly. Normally, there is a burst diaphragm in the throat of the nozzle section to enhance initial pressure buildup in the propellant chamber.

In the conventional recoilless gun, the propellant charge is ignited and the pressure simultaneously accelerates the projectile and causes gas to flow through the nozzle. Proper nozzle design results in a pressure distribution which integrates out to zero net force on the gun. Typically, however, a recoilless gun must undergo a series of gun firings in a pendulum mount to size the nozzle. Either the nozzle throat or exit diameter are

machined to adjust the net recoil force. Nozzle throat erosion and changing recoil forces are experienced after the gun goes into service.

In contrast, the Davis Gun recoilless consists only of a constant inside diameter tube open at both ends. A propellant charge resides between two projectiles and, at ignition, simultaneously drives them in opposite directions. The recoil forces automatically net out to zero with the exception of negligibly small differential friction forces. Note that the zero axial force condition remains true even if projectile exit times differ. The second projectile only constrains the propellant gas enough for proper pressure to develop.

An interesting equivalence exists between the internal ballistics of a Davis Gun and a closed breech gun. Assume a Davis Gun launches projectiles weighing W_1 and W_2 at velocities V_1 and

BLAST AND IMPULSIVE LOADING

X-RAY SIMULATION WITH LIGHT-INITIATED EXPLOSIVE

**R. A. Benham
F. H. Mathews
Simulation Division 9321
Sandia Laboratories
Albuquerque, New Mexico 87115**

ABSTRACT

X-ray blowoff effects are simulated by the detonation of a sprayed coating of explosive initiated by intense light.

PROCESSED PAGE BLANK-NOT FILMED

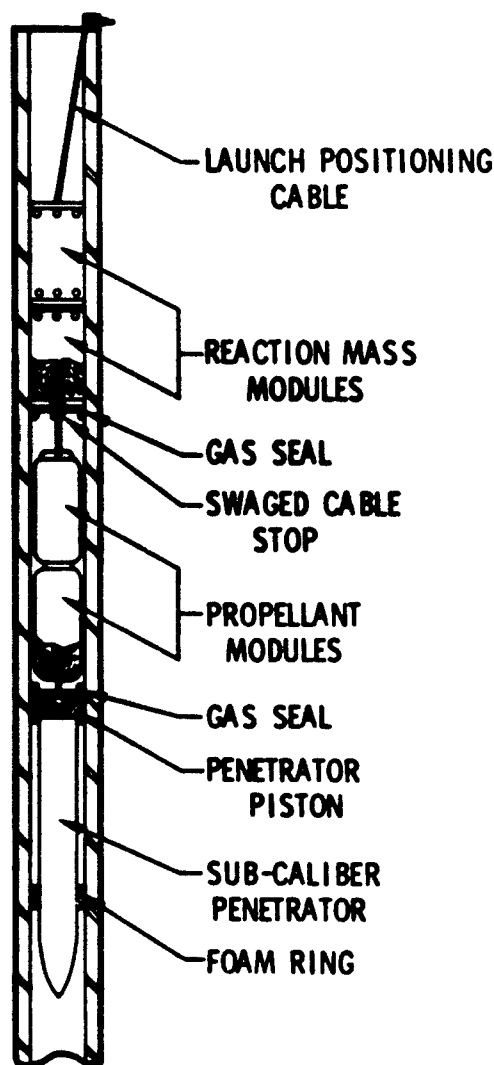


Figure 5 - Typical Davis Gun Penetrator Experiment Setup, Launch Position

unrestricted overhead air space and/or large downrange restricted areas.

The launch positioning cable is a length of 1/4 inch aircraft cable that is initially used to tow the entire launch assemblage into position and at tube elevation suspends everything in position until the propellant charge is ignited. The launch positioning cable ties into the penetrator piston at one end, passes through the axis of the propellant charge, passes through the axis of the reaction mass and ties to

the end of the gun barrel at the other end. An intermediate swage-on cable stop holds the weight of the reaction mass and keeps it off the propellant charge. The propellant charge ignition cable is attached to the positioning cable from the aft end of the propellant charge to the end of the gun barrel.

When the propellant charge is ignited, the launch positioning cable pulls out from the penetrator piston at a 60 psi pressure level. The penetrator is accelerated out the gun barrel and into the target where the foam ring and piston are stripped off. The reaction mass exits the other end of the gun barrel, and the containment skin, having been cut by knives mounted on the end of the barrel, immediately bursts and frees the metallic shot. The positioning cable is cut as the reaction mass exits by a knife blade feature built into the tie-down hardware at the end of the gun barrel. The projectile mass ratio is set for a reaction mass exit velocity less than 1000 ft/sec. This velocity and the high air drag configuration after burst limit the reaction mass range to less than 1000 feet in the initial velocity direction.

CONCLUSION

A versatile tool for conducting on site earth penetration experiments is now available at Sandia Laboratories. Present plans include testing of earth penetration devices ranging in diameter from four to six inches, in weight from 400 to 1000 pounds and in impact velocity from 1000 to 3000 ft/sec. Shake down tests will be conducted in the Albuquerque, New Mexico area and initial testing will be done at Tonopah Test Range in Nevada.

This work was supported by the United States Atomic Energy Commission.

subsequent spray operation, since explosive wet with acetone will not detonate. Erythrosin-B dye is added to increase the light absorptiveness of the SASN, thus improving its initiation properties.

The SASN-acetone supply is stirred continuously to maintain a homogeneous suspension. A peristaltic pump, employing a squeezing action on flexible rubber tubing, provides continuous circulation of SASN to the valve of the spray nozzle. The spray gun is mounted on a reciprocating carriage that can be traversed at uniform speed across the surface to be painted. By the careful control of spray parameters (i.e., position, speed, pressure, and mixture) a uniform layer of explosive is deposited during each spray pass. Since all these operations must be conducted remotely, trials with inert materials and simulated test shapes are frequently necessary to establish control of deposition.

Control and Verification

One of the techniques used to control explosive deposition is illustrated in Fig. 2. This setup was used to obtain an impulse varying as a cosine over half the surface of a stainless-steel ring. A mask restricts explosive deposition to a narrow arc of the ring surface. By rotating the ring and making repeated spray passes, the desired contour is built up in increments of explosive, each corresponding to an impulse load of 25 taps.* Initially, phenolic weighing coupons are mounted on both the ring and adjacent surfaces to assure that identical quantities of explosive are deposited in both locations. During the actual spray application, the coupons are only placed at intervals adjacent to the ring. Periodically, in the spraying sequence, the coupons are removed and weighed to determine the local areal density of the applied explosive, and adjustments in the spraying sequence are made if necessary. The impulse imparted to the test object is directly related to the areal density of deposited explosive as shown in Fig. 3. This relationship has been determined experimentally, with individual impulse measurements generally falling within 5 to 10 percent of the empirical relationship. The impulse measurements are obtained by observing, with a pulsed x-ray shadowgraph, the velocity imparted to the coupon from the detonation of the explosive on the phenolic coupon.

* 1 tap = dyne-sec/cm²



Figure 2. Spray arrangement for an axially symmetric structure

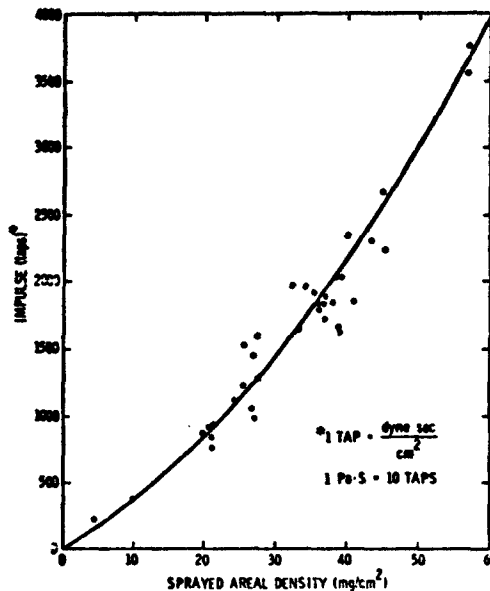


Figure 3. Impulse vs areal density for $\text{Ag}_2\text{C}_2 \cdot \text{AgNO}_3$

An example of the way the explosive distribution over half of the ring surface is checked for accuracy is shown in Fig. 4. Impulse values anticipated from coupon weights and measured from coupon firings were compared to the values desired. As an additional check, the rigid-body velocity imparted to the ring structure was measured and found to be consistent with the desired cosine distribution of impulse.

X-RAY SIMULATION WITH LIGHT-INITIATED EXPLOSIVE

Introduction

When a weapon structure is exposed to x-rays, the energy deposited in the surface material may result in its vaporization and subsequent blowoff. This blowoff imparts an impulse to the structure within a few microseconds. To furnish information about structural behavior caused by this loading, previous laboratory experiments have employed electron-beam machines, magnetically accelerated flyer plates, and strip explosives to simulate blow-off impulse. In the method described here, the weapon structure is spray-painted with a coating of silver acetylide-silver nitrate (SASN), a light-sensitive explosive. This explosive combines initiation sensitivity and loading simultaneity with the ability to detonate in thin layers. When detonated by an intense flash of light, the explosive delivers a pressure load that simulates x-ray impulse effects on a test structure. This technique is particularly useful for structures with irregular surfaces and is employed with other simulation techniques and with underground experiments to study weapon vulnerability.

This technique was first developed at Southwest Research Institute in 1965 [1, 2]. Early work involved spraying the explosive, by hand, onto relatively small and simple structures.

Facility

A facility suitable for the handling of primary* explosives is required for spray-painting SASN. The facility (Fig. 1) is designed so that all operations involving significant quantities of explosive are performed remotely. The operator is protected by an explosion-proof window and has access to the temperature-controlled spray chamber by a pair of master-slave manipulators. An exhaust system draws over-spray of the explosive into a disposable filter that can be transported to an incinerator by a remotely controlled monorail. A similar monorail is used to transport the test object into firing position. Here the light source, an array of tungsten wires powered by the discharge of a capacitor bank, initiates the explosive. Instrumentation is available for measuring strain, acceleration, pressure, and displacement, and for obtaining both high-speed photographic and pulse x-ray pictures of test events.

tungsten wires powered by the discharge of a capacitor bank, initiates the explosive. Instrumentation is available for measuring strain, acceleration, pressure, and displacement, and for obtaining both high-speed photographic and pulse x-ray pictures of test events.

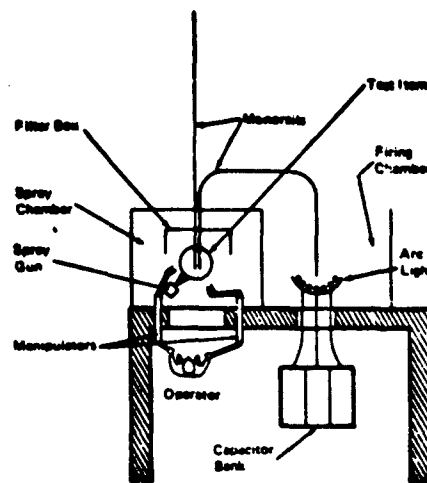
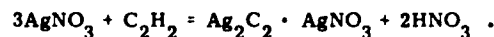


Figure 1. Plan view of facility

Spray Application of Explosive

The SASN explosive is manufactured in the spray chamber by remote control as the first step in each spray operation. A precipitation process is employed in which acetylene gas is dispersed through a solution of silver nitrate and methyl cyanide. The silver nitrate reacts with the acetylene gas as follows:



The SASN ($\text{Ag}_2\text{C}_2 \cdot \text{AgNO}_3$) settles out as a white precipitate and the supernatant fluid (nitric acid) is decanted into a waste beaker. The explosive is then washed with acetone to remove excess nitric acid and other impurities. Acetone is used as a carrier in the

*Primary explosives can be detonated easily by heat or shock.

subsequent spray operation, since explosive wet with acetone will not detonate. Erythrosin-B dye is added to increase the light absorptiveness of the SASN, thus improving its initiation properties.

The SASN-acetone supply is stirred continuously to maintain a homogeneous suspension. A peristaltic pump, employing a squeezing action on flexible rubber tubing, provides continuous circulation of SASN to the valve of the spray nozzle. The spray gun is mounted on a reciprocating carriage that can be traversed at uniform speed across the surface to be painted. By the careful control of spray parameters (i.e., position, speed, pressure, and mixture) a uniform layer of explosive is deposited during each spray pass. Since all these operations must be conducted remotely, trials with inert materials and simulated test shapes are frequently necessary to establish control of deposition.

Control and Verification

One of the techniques used to control explosive deposition is illustrated in Fig. 2. This setup was used to obtain an impulse varying as a cosine over half the surface of a stainless-steel ring. A mask restricts explosive deposition to a narrow arc of the ring surface. By rotating the ring and making repeated spray passes, the desired contour is built up in increments of explosive, each corresponding to an impulse load of 25 taps.* Initially, phenolic weighing coupons are mounted on both the ring and adjacent surfaces to assure that identical quantities of explosive are deposited in both locations. During the actual spray application, the coupons are only placed at intervals adjacent to the ring. Periodically, in the spraying sequence, the coupons are removed and weighed to determine the local areal density of the applied explosive, and adjustments in the spraying sequence are made if necessary. The impulse imparted to the test object is directly related to the areal density of deposited explosive as shown in Fig. 3. This relationship has been determined experimentally, with individual impulse measurements generally falling within 5 to 10 percent of the empirical relationship. The impulse measurements are obtained by observing, with a pulsed x-ray shadowgraph, the velocity imparted to the coupon from the detonation of the explosive on the phenolic coupon.

* 1 tap = dyne-sec/cm²



Figure 2. Spray arrangement for an axially symmetric structure

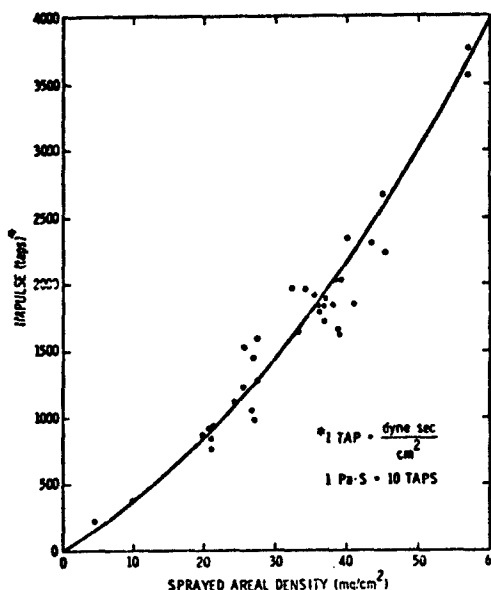


Figure 3. Impulse vs areal density for $\text{Ag}_2\text{C}_2 \cdot \text{AgNO}_3$

An example of the way the explosive distribution over half of the ring surface is checked for accuracy is shown in Fig. 4. Impulse values anticipated from coupon weights and measured from coupon firings were compared to the values desired. As an additional check, the rigid-body velocity imparted to the ring structure was measured and found to be consistent with the desired cosine distribution of impulse.

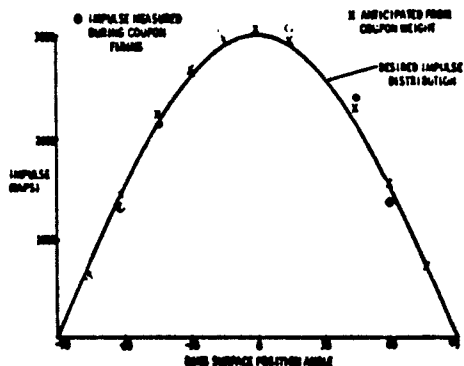


Figure 4. Comparison of impulse from coupon measurements to desired impulse

Explosive Behavior

The explosive is initiated through heating caused by an intense flash of light. Light radiating from an arc formed around each wire provides a power input to the explosive surface of several hundred kilowatts per square centimeter, causing explosive initiation 5 to 6 μsec after arc formation. A 100-kJ capacitor system provides sufficient energy to initiate one square meter of explosive surface.

Initiation occurs independently at many discrete points on the explosive, with initiation densities ranging from 20 to 300 per square centimeter. A detonation wave propagates from each point until a similar wave radiating from an adjacent initiation point is encountered. The resulting intersections generate high-pressure regions that leave a visible pattern on the surface of the test item, as shown in Fig. 5. The dimensions of these patterns and the detonation rate of the explosive (1.2 mm/ μsec) may be used to determine the time needed to detonate the explosive surface in a particular region. About 0.4 μsec would be required for the area in Fig. 5, where there are about 150 initiation points for each square centimeter of surface. Simultaneity measurements indicate that even widely separated points of a large surface initiate within 1 μsec of each other.

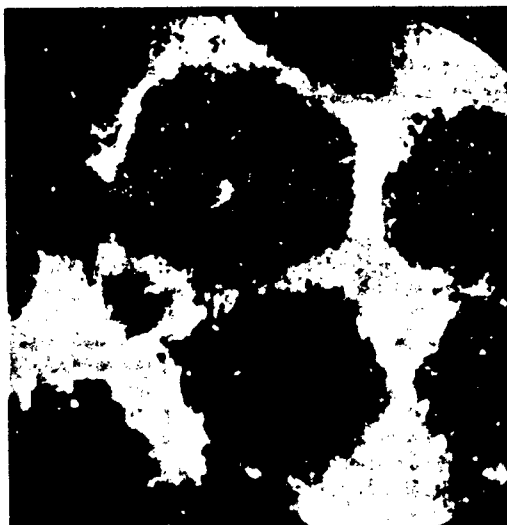


Figure 5. Magnified view of markings left by explosive detonation

The detonation wave striking the surface is not planar and retains a shape imposed by the discrete detonation points. However, the detonation wave strikes the entire surface within 1 μsec , which is much shorter than the rise time of the structural response. Quartz and tourmaline gauges that average pressure over several initiation points indicate that average pressures up to 4 kilobars may be obtained at the structure surface.

Experimental Verification

The test on the stainless-steel ring (Fig. 2) was performed to establish the validity of the photo-explosive method for simulating impulse loading. This was done by demonstrating a measured response from the explosive test that duplicated or closely followed the response predicted by elastic ring theory. A comparison of predicted and measured responses is shown in Fig. 6. The theory curve comes from the modified Humprey-Winter Modal solution to the problem of elastic response of a thin ring to a pure impulse load. The ring material had minimal strain rate and strain hardening effects (3). Strain is shown during a relatively early time when

it is dominated by a high-frequency membrane wave. Similar comparisons at other locations and at later times, when bending strains dominate, are equally close. This demonstration justifies the use of the photo-explosive process for simulating impulse loading so that applications may now include structures where unknown material properties [4] or geometrical complexity prevent complete analysis.

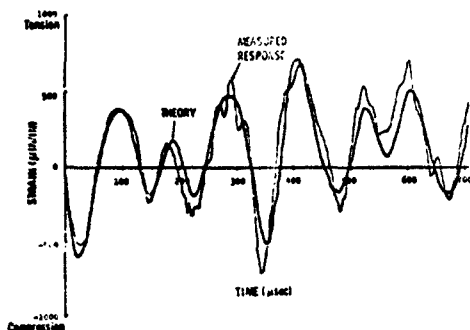


Figure 6. Comparison of predicted and measured strain for a steel ring; explosive detonation occurred at $T = 0$

Experiments on more complex structures have included lateral loading of nose segments [5] and aft loadings of full vehicles. A toroidal aft cover is the most difficult geometry yet attempted [6].

DISCUSSION

Mr. O'Hearne: (Martin Marietta) I was a little unclear as to how you located the light sources relative to the target?

Mr. Benham: We have a positioning indicator on the trolley of the monorail system which remotely stops the carriage when it gets in the proper position in front of the light source so this is set up prior to starting the spray operation.

Mr. O'Hearne: What I am thinking of is when you initiate the explosion with your lights impulse, how are the sources arrayed? What I was thinking of was the problem you have when you have a complex shape and you place the layers on there according to the charge you want, how do you get them initiated uniformly? How are the sources arrayed relative to the target?

List of References

1. G. E. Nevill, Jr., and F. O. Hoese, "Impulse Loading Using Sprayed Silver Acetylide-Silver Nitrate," Experimental Mechanics, September 1965, pp. 294-298.
2. F. O. Hoese, C. G. Langner, and W. E. Baker, "Simultaneous Initiation Over Large Areas of a Spray-Deposited Explosive," Experimental Mechanics, September 1968.
3. M. J. Forrestal, M. J. Sagartz, and H. C. Walling, "Response of a Cylindrical Shell to a Cosine Distributed Impulse over Half its Circumference," AIAA Journal, Vol. 11, No. 9, September 1973, pp. 1355-56.
4. R. A. Benham, "Impulse Tests of Graphitized CVD Carbon Felt Rings," Sandia Laboratories Report SLA 73-0941, January 1974.
5. R. A. Benham, "Nose Tip Impulse Tests Using Light Sensitive Explosive," Sandia Laboratories Report, SAND74-0211, November 1974.
6. R. A. Benham, "Impulse Tests of the SAMAST-02 Aft Cover," Sandia Laboratories Report, SLA 74-0293, August 1974.

Mr. Benham: The positioning of the light source with respect to the explosive is not very critical. We have to be within 4 to 6 inches from the surface of the explosive so we have some flexibility. The test object is taken around on the monorail and positioned in front of the light array where these circles indicate the light array itself. We have a position indicator on the monorail system which stops the carriage that's supporting the test object in front of the monorail system at the proper position.

STRUCTURAL DYNAMIC RESPONSE
TO HEIGHT-OF-BURST AIR BLAST LOADING

H. F. Korman, N. Lipner, J. S. Chiu
TRW Systems Group
Redondo Beach, California

The traditional technique for designing or assessing the hardness of protective structures to air blast loads uses equivalent triangular pressure histories to represent the blast. This introduces a degree of approximation which can result in hardness overestimates or underestimates, depending on the method for determining the load duration time. This paper describes the development of structural dynamic response factors for air blast loading which considers the complete pressure history. The loading is based on the most recent advances in air blast phenomenology which provides a calculational procedure for the determination of the waveform shape as a function of weapon yield, peak pressure and detonation height-of-burst.

The analysis modeled the structure as a single degree of freedom system with an elastic-perfectly plastic spring and no viscous damping. For structure frequencies of interest, code calculation results essentially collapsed into one set of parametric curves which relate the following key variables: structure frequency, weapon yield, pressure decay time parameter, allowable ductility ratio, and dynamic load factor. These curves provide a technique for design or evaluation of structure components which is no more complex than using the dynamic load chart for triangular pulses.

INTRODUCTION

With advances in the design of nuclear hardened weapon systems, it has become increasingly more important to accurately assess the hardness of protective structures to air blast loads. The traditional technique for design or assessment [1] uses equivalent triangular pressure histories to represent the air blast. This introduces a degree of approximation which can result in hardness overestimates or underestimates, depending on the method for determining the effective load duration time. This paper describes the development of structural dynamic response factors for air blast loading which considers the complete pressure history. The loading is based on the most recent advances in air blast phenomenology [2] which provides a calculation procedure for determining the waveform shape as a function of weapon yield W , peak pressure p_m , and detonation height-of-burst HOB .

DYNAMIC RESPONSE ANALYSIS

In this study the structure was considered to be a surface flush target (Figure 1) which could be modeled as a single degree-of-freedom system with an elastic-perfectly plastic spring and no viscous damping. The spring resistance $q(x)$ is linear with deflection x until the yield deflection x_y is reached [where $q(x_y) = q_y$] and then is constant until the peak deflection $u x_y$ is attained. Thus, the ductility u is defined as the ratio of peak deflection to yield deflection. The elastic frequency f is related to q_y , x_y and m as shown in the Figure. Structure dynamic response was determined for two analytical fits (termed simple and direct) to the airblast loading as defined in Reference 2.*

* These analytic fits produce essentially the same pressure histories for a surface burst as the earlier Brode triple exponential pulses [3].

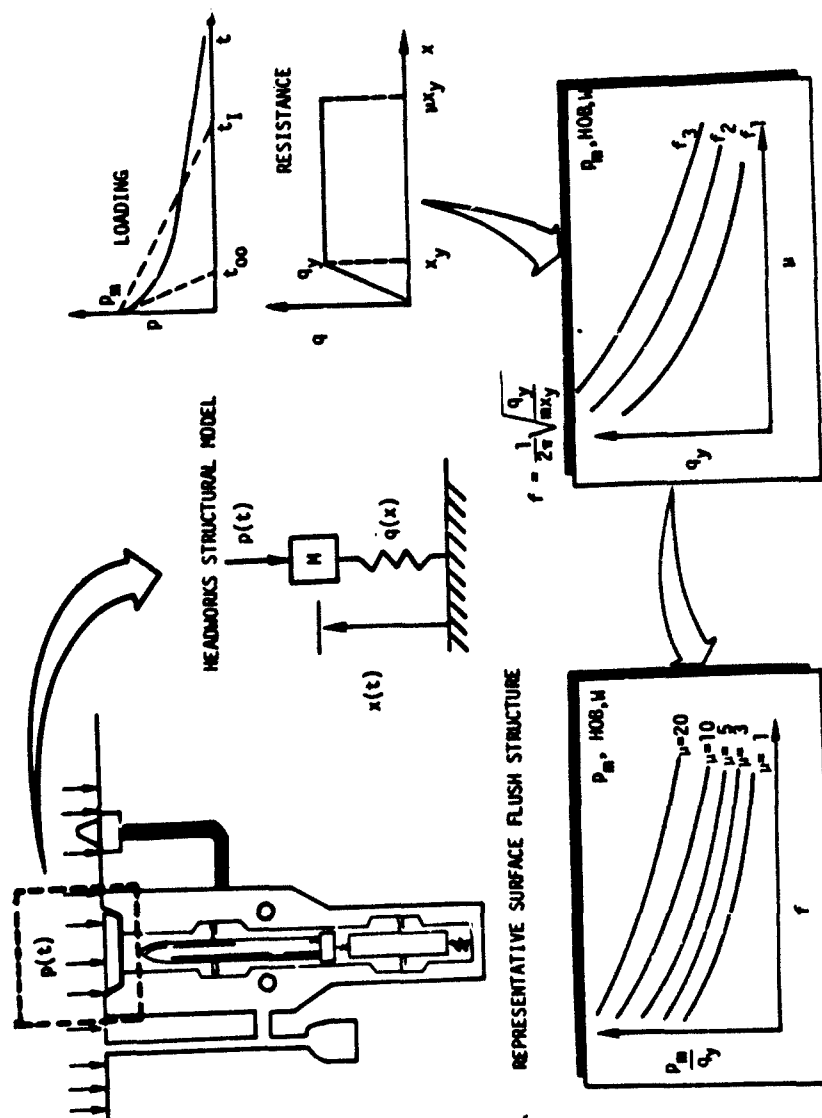


FIGURE 1. STRUCTURAL DYNAMIC RESPONSE ANALYSIS - SURFACE PRESSURE AND HEIGHT-OF-BURST.

Figure 1 summarizes the calculational procedure for determining dynamic response factors (p_m/q_y) for a specified p_m and HOB. A series of computer calculations generate $u(q_y)$ curves for several values of the frequency for the pressure waveform associated with p_m , HOB and W . Details of structural dynamic

response analysis are given in many textbooks such as [4]. Crossplotting the curves produces the dynamic response factors as a function of f with u as a parameter.

If similar dynamic response charts were required for each p_m and HOB which might be of interest, this approach would be too cumbersome to be of value. Fortunately there is a technique for generalizing the chart shown in Figure 1 to apply to a significant range of p_m and HOB. In this manner at most only a few charts would be required for the total range of p_m and HOB which might be of interest.

Consider the initial slope intercept t_{oo} of the Brode pulse shown in Figure 1. This parameter is an approximate measure of the time scale of pressure decay for various p_m . In the same manner that $W^{1/3}$ is an exact measure of this time scale for a given p_m and HOB. Thus a natural approach for attempting to generalize the dynamic response was through the parameter ft_{oo} or alternatively the parameter

$$ft_{oo}' \left[\frac{W}{W_o} \right]^{1/3}$$

where t_{oo}' is the value of t_{oo} for a 1MT burst and $W_o = 1$ MT. As will be seen in the next section, this approach was quite successful.

The variation of t_{oo}' with p_m for several HOB is shown in Figure 2. The figure is based on [5] which contains data for additional HOB. Also shown in Figure 2 is total impulse intercept t_i which is the intercept of a linearly decaying pulse with the same impulse per unit area as the pressure waveform.

Brode pulse results will be compared to zero rise time triangular pulse results which appear in the literature in the form of dynamic load charts (e.g., [1]). Two intercepts will be considered, t_{oo} (initial slope related) and t_i (impulse related).

RESULTS AND DISCUSSION

Since Brode presents two approximations for air blast pulses, it is of interest to compare structural response results for each approximation. Figures 3 and 4 present such results for two sets of parameters. Each comparison shows little difference between the two approximations. The essential difference between the two figures

is that in Figure 4 the parameters (HOB = 1000 ft, $p_m = 3000$ psi) correspond approximately to the optimal HOB condition (largest ground range for achieving the p_m value), while in Figure 3 the conditions are below optimal HOB (HOB = 1000 ft, $p_m = 1000$ psi). It should be noted that HOB = 1500 ft is the approximate optimal condition for 1000 psi. Thus, from a structural response viewpoint, it makes little difference whether the simple or direct fit is used. Brode pulse results in Figures 5-7 discussed below were generated using the direct fit.

Structural response analyses were conducted for 1MT and peak pressures ranging from 300 to 3000 psi. Both surface and air bursts with HOB's as high as 3000 ft were considered. When the response ratio p_m/q_y was displayed as a function of ft_{oo} with u as a parameter, the curves essentially collapsed upon each other for $ft_{oo} > 0.6$.

Figure 5 shows, for three values of u , the band within which the results collapsed. The deviation as ft_{oo} becomes small are to be expected because the response becomes more sensitive to ft_i as f is reduced. It should be noted that for most hardened targets of interest, ft_{oo} will be large enough to permit the use of a single set of curves. For this region a hardness evaluation technique based on these Brode pulses is no more complex than the dynamic load chart for triangular pulses.

A comparison of the Brode pulse results (for a surface burst at $p_m = 1000$ psi) with the two types of triangular pulses is presented in Figure 6. It is seen that at high frequency the t_{oo} triangle approximation is adequate. However, in the lower frequency region the initial slope response ratios increase faster as ft_{oo} is decreased than do the Brode pulse curves. For example, given a 1MT surface burst at 1000 psi, a structure frequency of 60 cps ($ft_{oo} = 1$), and ductility of 5, the t_{oo} triangle approximation will yield a response 17% lower than that of the Brode pulse. Whether or not a hardness evaluation using t_{oo} triangles will be significantly unconservative can be determined from Figure 5. On the other hand, the impulse triangle pulse curves fall off much more slowly than Brode pulse curves as ft_{oo} is decreased. Preserving total impulse with triangular pulses thus produces results which are too conservative for the ft_{oo} range shown in the Figure. For very small ft_{oo} , the curves must begin to converge again because the response is impulse sensitive. The advantage in using Brode pulse results instead of

*Heights of Burst discussed in this section are referenced to 1MT conditions.

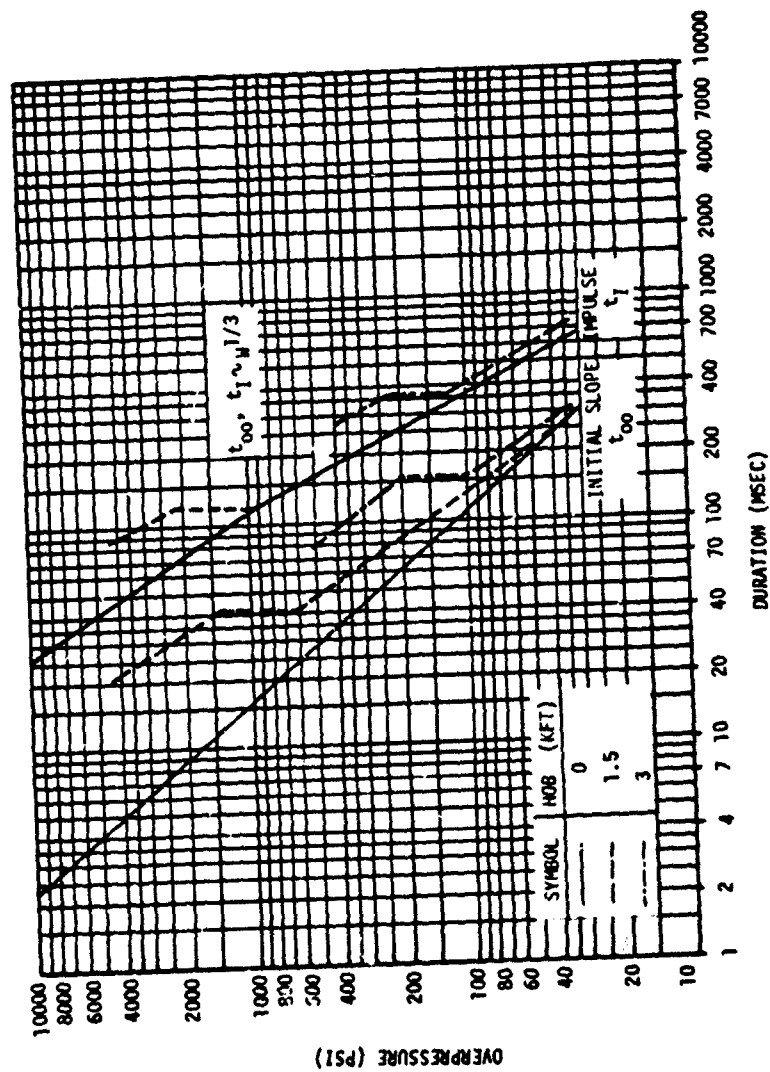


FIGURE 2. COMPARISON OF DURATION TIMES AS A FUNCTION OF OVERPRESSURE FOR INT AND SEVERAL HEIGHTS OF BURST (REFERENCE 2).

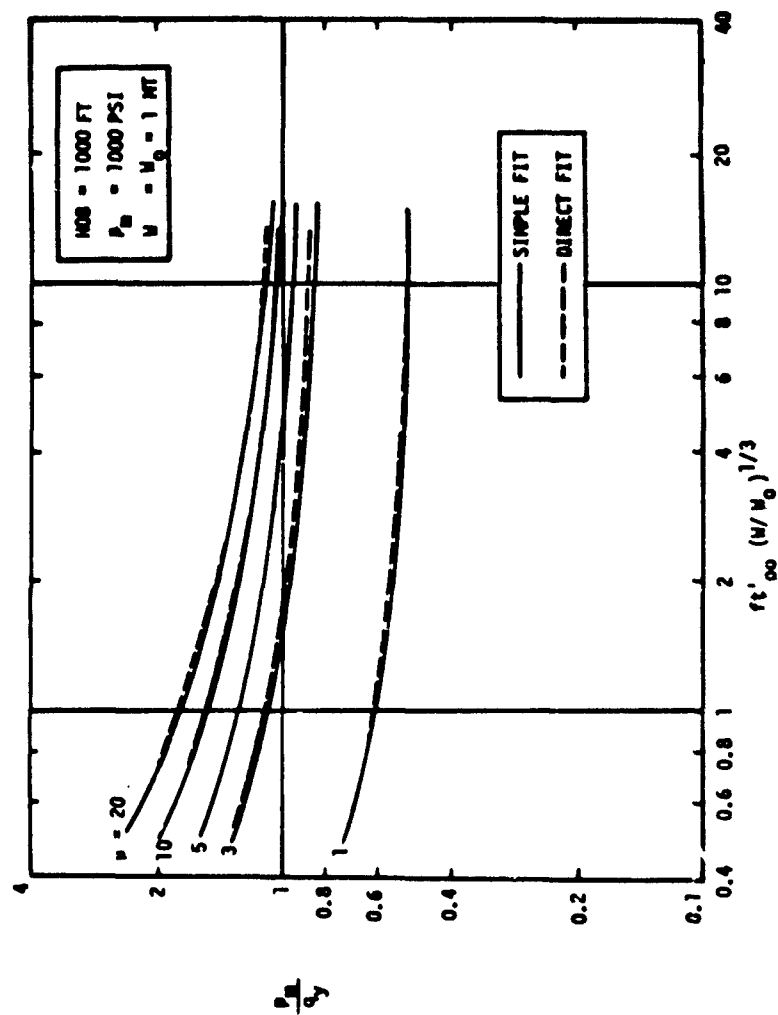


FIGURE 3. STRUCTURAL RESPONSE COMPARISON FOR SIMPLE AND DIRECT FIT BRODE PULSES. SUB-OPTIMAL HOB.

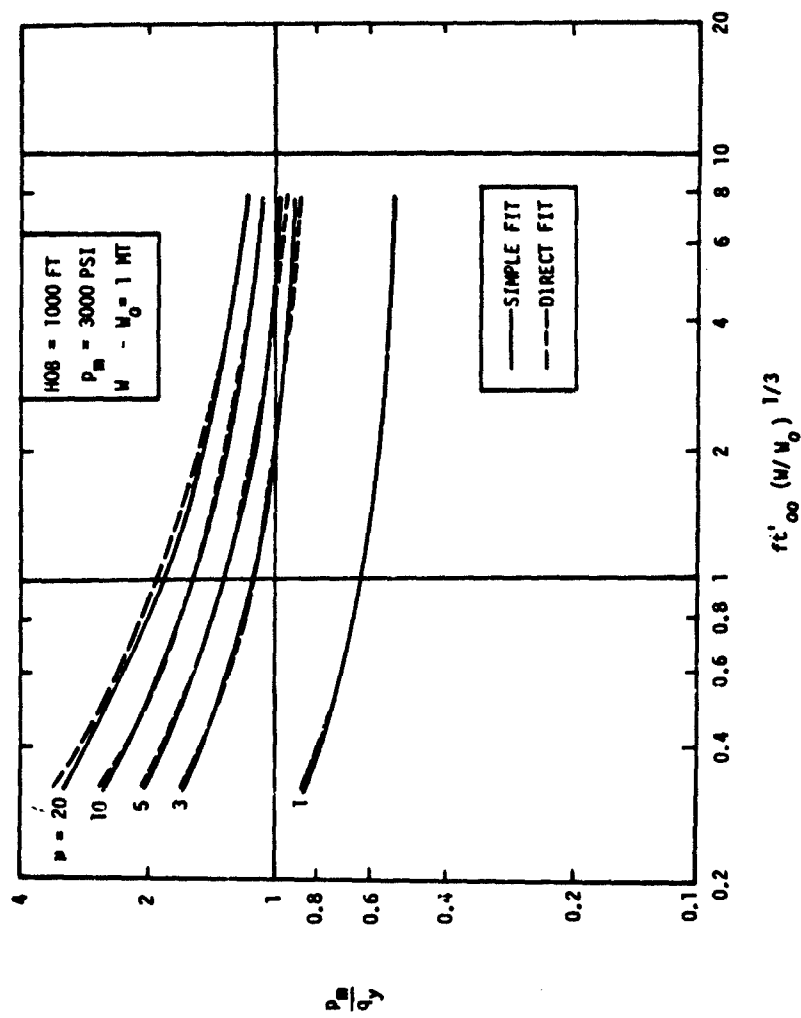


FIGURE 4. STRUCTURAL RESPONSE COMPARISON FOR SIMPLE AND DIRECT FIT BRODE PULSES, OPTIMAL HOB.

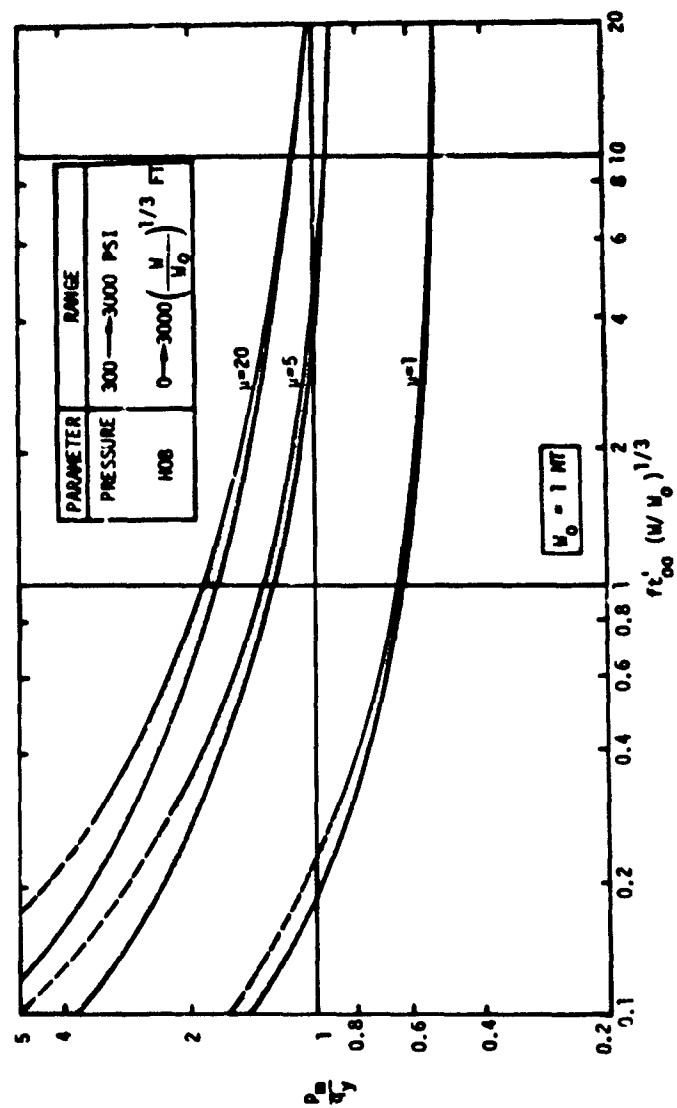


FIGURE 5. BRODE RESPONSE RESULTS FOR A RANGE OF PEAK PRESSURES AND HOB'S.

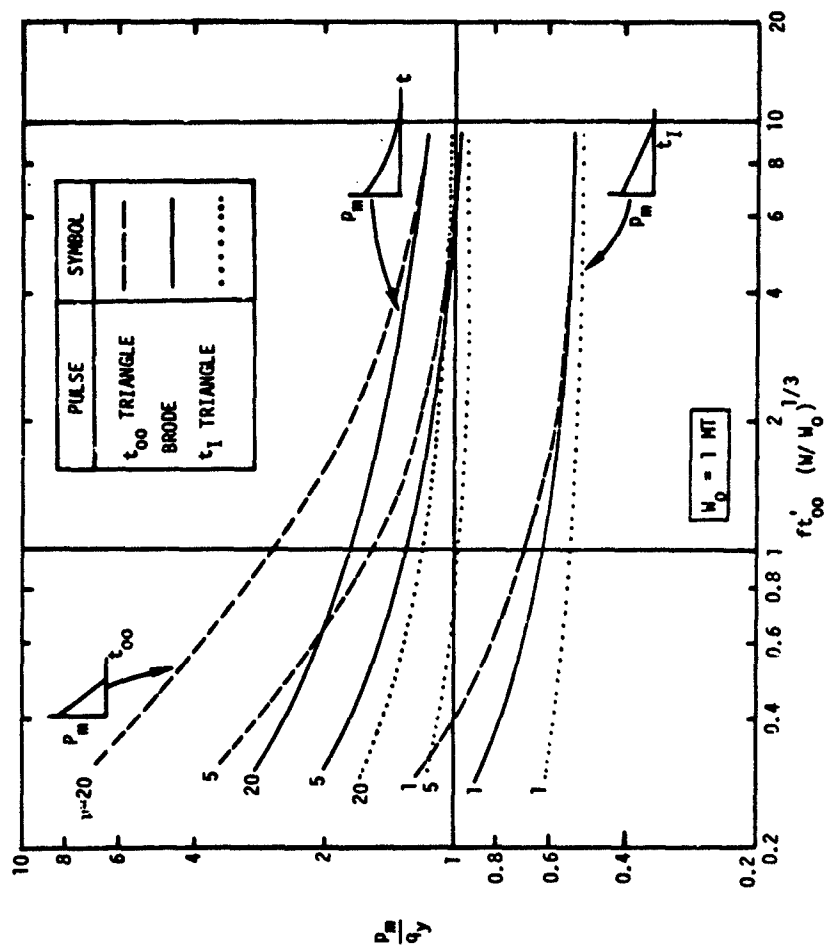


FIGURE 6. COMPARISON OF STRUCTURAL RESPONSE FOR INITIAL SLOPE TRIANGLES, BRODE PULSES, AND IMPULSE TRIANGLES.

those for the equivalent triangles is clearly demonstrated, especially for low yield conditions.

CONCLUSIONS

The above discussion has shown that the Brode pulse results can be simply and accurately used for structural dynamic response to air blast loading. Hence, it is recommended that Figure 7 (generated using the direct fit Brode pulse with $P_m = 1000$ psi and surface burst conditions) be used for design and hardness assessment of protective structures for a pressure range from 200 to 6000 psi and HOB range up to $3000 (W/W_0)^{1/3}$ ft ($W_0 = 1$ MT). Results are only shown for $ft_{\infty} \geq 0.3$ to preclude any significant errors with the collapse technique. The accuracy of the curves outside this region has not been investigated; other pressure levels are of limited interest.

ACKNOWLEDGEMENT

This work was performed through the support of the United States Air Force SAMS0 Contract No. F04701-74-C-0088. The authors wish to express their appreciation to M. R. Brady for her computer programming efforts.

REFERENCES

1. Newmark, N. M., et. al., "Air Force Design Manual," AFSMC-TDR-62-138, December 1962.
2. Brode, H. L., "Height-of-Burst Effects at High Overpressures," DASA 2506, July 1970.
3. Brode, H. L., "A Review of Nuclear Explosion Phenomena Pertinent to Protective Construction," Rand Report R-425-PR, May 1964.
4. Biggs, J. M., Introduction to Structural Dynamics, McGraw Hill, 1964.
5. Newmark, N. M., "Effect of Height-of-Burst on Horizontal Yielding Targets," DNA-3252F, March 1974.

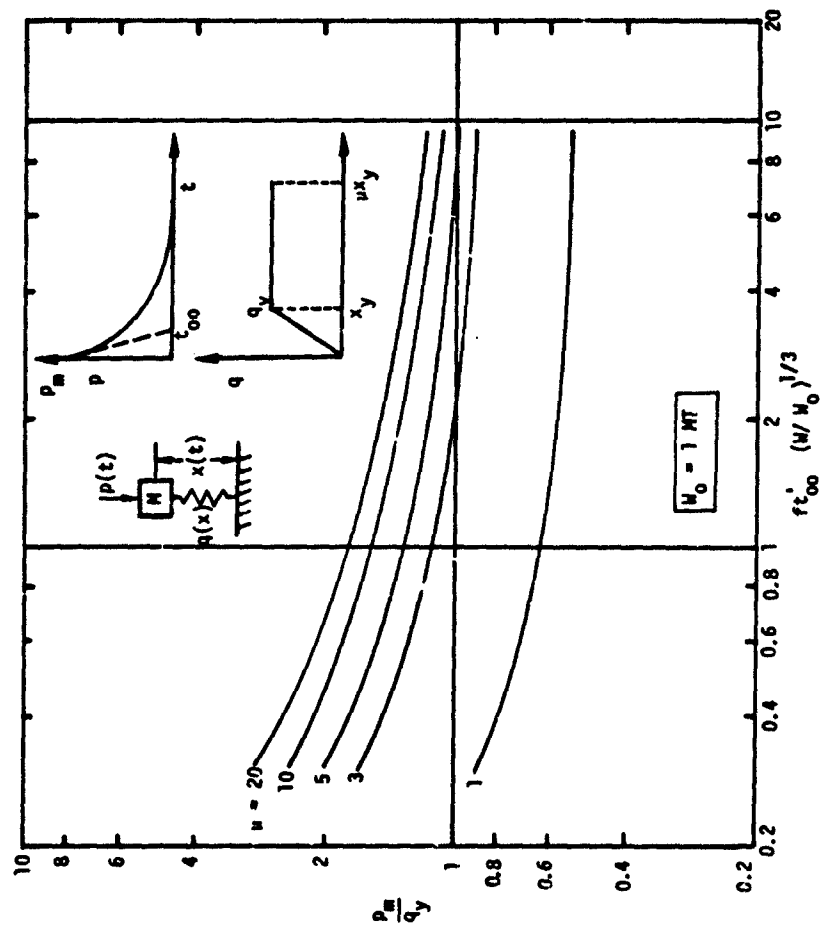


FIGURE 7. STRUCTURAL DYNAMIC RESPONSE CHART FOR AIR BLAST LOADING.

DISCUSSION

Mr. O'Hearne: (Martin Marietta) You just remarked that the curves are quite applicable and my personal feeling of insecurity is in the modeling of this head structure and similar structures as single degree of freedom elastic/plastic systems perhaps you could comment on that?

Mr. Korman: (TRW Systems) Yes, I said that our work takes out just one element of the art in this activity. You are quite correct in pointing out the other element that is exceedingly important which is the choice of your system parameters. That is really something which is based on a lot of civil engineering experience, but in some of our applications we have test data which demonstrates what the fundamental mode is and then we can pick out the frequency. One can use standard civil engineering practice, where static calculations are used to determine these resistance forces. We've also done structural response analysis with finite element codes to pin down what the primary modes are and again it is a modal analysis that counts and guessing the right resistance force is a key factor which is still an art or something based on one's engineering judgment and experiences.

RESPONSE OF FLAT PLATES SUBJECTED TO MILD IMPULSIVE LOADINGS

C. A. Ross
University of Florida Graduate Engineering Center
Eglin Air Force Base, Florida 32542

W. S. Strickland
U. S. Air Force Armament Laboratory
Eglin Air Force Base, Florida 32542

This paper presents the results of an effort to determine failure of flat plates subjected to mild impulsive loadings generated by a fuel air explosive. A membrane model based on a total plastic strain energy function, a rigid strain hardening constitutive relation and an assumed final deformed shape was used to derive an equation of motion for the plate centerpoint deflection. Controlled fuel air explosions, contained in a gas bag, were used to produce blast loadings on square aluminum plates with fixed edges. A dynamic shadow Moire technique was used to observe plate deformation modes. Plate failure occurred as a result of gross deformation.

INTRODUCTION

Response of plates to impulsive loads is usually described in terms of two rather distinct mechanisms, i.e., a static mode in which the plate deforms under a rather continuous pattern throughout the deflection process and a plastic hinge mode in which the initial deformation is by a traveling plastic hinge associated with stress wave propagation. The demarcation between the two mechanisms has been defined in one case [1] in terms of the characteristic period of elastic vibration and the positive pressure phase of the impulsive load. In this case if the positive pressure phase of the loading exceeds one quarter of the characteristic period of the plate then the plate will respond in a vibratory manner. If the positive pressure phase of the loading is less than a quarter of the elastic characteristic period of the plate then a plastic hinge will form at the boundaries and will move toward the central portion of the plate.

Abrahamson, et al, [2] assumed only bending in circular plates and describe the dividing region between the static and traveling plastic hinges mechanisms in terms of the static collapse load based on the plastic moment required to produce a plastic hinge. In this case if the maximum overpressure of the loading is less than twice the static collapse pressure the static mechanism is operative and if the maximum overpressure is greater than twice the static collapse load then the traveling hinge mechanism is assumed to operate. Results of reference [2] indicate that bending alone is not sufficient to predict large plate deformation and membrane forces must be taken into account in the analysis. Cox and Morland [3] using the same general assumption of reference [2] determined the total central deflection of simply supported square plates subjected to mild impulsive loads. Hudson [4] was probably the first to observe the hinge mechanism in thin circular diaphragms subjected to blast loadings and developed a

simplified theory in which both radial and circumferential stresses were considered. Figure 1 shows the deformation process for both the static and traveling hinge cases. A general discussion of the response of circular plates subjected to impulsive loads is given by Cristescu [5]. The response of rectangular plates is a much more complicated phenomena and several computer studies such as those by Kay [6] and Huffington [7] are available.

flat plates to loadings associated with fuel air explosions. The impulsive loadings associated with fuel air explosion are mild in comparison to near field loads of a high energy explosion. Pressure-time curves of a reflected fuel air explosion are characterized by low peak over pressures up to approximately 1000 psi and a positive pressure phase durations of one to twenty milliseconds. The peak reflected overpressure is a constant for a given fuel

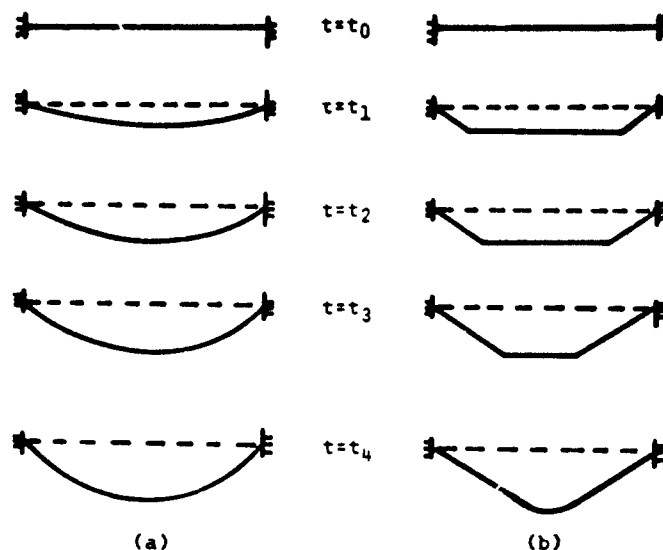


Fig. 1. DEFORMATION MECHANISM FOR (a) THE STATIC CASE AND (b) FOR THE TRAVELING PLASTIC HINGE CASE.

Dynamic response as described in previous paragraphs is concerned with deformation of the plate and plate failure or rupture occurs as a result of large stresses or strains due to gross deformations or stress wave interaction. As the impulsive load becomes more severe failure occurs at boundaries without appreciable deformation of the central portion of the plate. This phenomenon is described by Sewell and Kinney [1] and the failure is assumed to occur when the initial velocity of the plate exceeds the critical particle velocity [8] of the plate material. This phenomenon is very similar to a shear failure mechanism observed by Menkes and Opot [9] in aluminum beams subjected to intense impulsive loads.

The fundamental purpose of this study is to determine the response of

air mixture [10] and the positive pressure phase duration is dependent on the cloud size. This type loading is termed a mild impulsive load for this study and its effect on ductile rectangular metal panels of sizes found in metal buildings, aircraft, radar vans, etc. is the major subject of this paper. The positive pressure phase duration of the fuel air explosion is approximately equal to a quarter of the characteristic period of many panels found in the above mentioned items. This then places the response of these panels in a region roughly between the static and traveling plastic mechanisms discussed previously. The final deformed shape of a plate obtained by either mechanism, as shown in Figure 1, is characterized by gross deflection due to plastic deformation. Therefore, it could be assumed that plate failure is more dependent on

this gross deflection than the manner in which the deflection was obtained. Using this assumption the following analysis is given.

ANALYSIS

The basic assumption as stated before is that the plate deflection at failure is more important than the manner in which that deflection took place. It is further assumed that only membrane forces are acting and that the plastic strain and associated plastic energy is much larger than the elastic energy. The latter assumption leads to the use of a rigid-strain-hardening constitutive relation as shown in Figure 2.

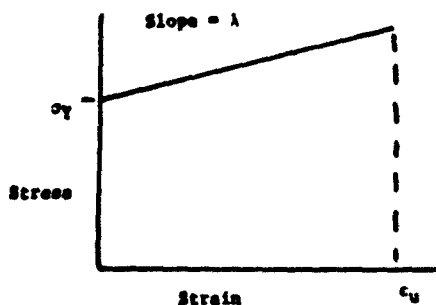


Fig. 2. ASSUMED STRESS STRAIN CURVE FOR ANALYSIS OF FLAT PLATES (MEMBRANES).

The basic approach used in this analysis is to 1) assume some deformed mode shape in terms of the undeformed dimensions of Figure 3, 2) calculate the kinetic energy, the dissipative functions (plastic energy) and generalized forcing function in terms of the undeformed plate dimensions, 3) apply a Lagrangian formulation to obtain the equation of motion, and 4) apply a maximum allowable strain to determine plate failure in terms of the plate center point deflection.

The assumed deflections are given as,

$$\begin{aligned} u &= u_0 \sin \frac{\pi x}{a} \cos \frac{\pi y}{2b} \\ v &= v_0 \sin \frac{\pi y}{b} \cos \frac{\pi x}{2a} \\ w &= w_0 \cos \frac{\pi x}{2a} \cos \frac{\pi y}{2b} \end{aligned} \quad (1)$$

where u , v , and w are the deflections in

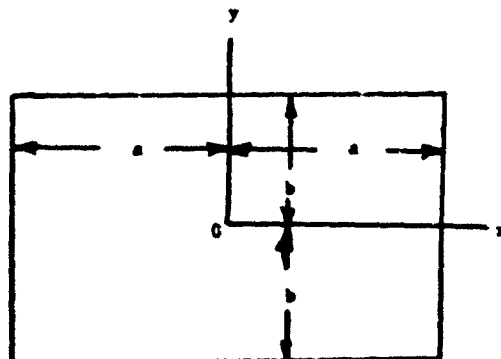


Fig. 3. COORDINATE SYSTEM FOR RECTANGULAR PLATES.

the x , y , and z directions respectively, u_0 and v_0 are the maximum deflections in the x and y directions respectively, and w_0 the plate center point deflection in the z direction. The assumed deflection equations satisfy the boundary conditions of a membrane with no translation at the boundaries. Under the assumption of no bending, rotation may occur at a so called fixed boundary. Assuming a plane stress case the stresses are written as

$$\sigma_x = \sigma_Y + \frac{\lambda}{1-\mu}(\epsilon_x + \mu \epsilon_y)$$

$$\sigma_y = \sigma_Y + \frac{\lambda}{1-\mu}(\epsilon_y + \mu \epsilon_x) \quad (2)$$

$$\tau_{xy} = (\sigma_Y + \lambda^1 \tau_{xy})$$

where:

σ	normal stress
τ	shear stress
σ_Y, τ_Y	yield stresses
ϵ	strain
γ	shear strain
λ	work hardening slope for normal stresses
λ^1	work hardening slope for shear stresses = $\lambda/2(1+\mu)$
μ	Poisson's ratio

Neglecting all the second order terms except the squares and products of the terms $\frac{\partial w}{\partial x}$, $\frac{\partial w}{\partial y}$, the strain equations become

$$\epsilon_x = \frac{\partial u}{\partial x} + \frac{1}{2} \left(\frac{\partial w}{\partial x} \right)^2,$$

$$\epsilon_y = \frac{\partial v}{\partial y} + \frac{1}{2} \left(\frac{\partial w}{\partial y} \right)^2, \quad (3)$$

$$\gamma_{xy} = \frac{\partial u}{\partial y} + \frac{\partial v}{\partial x} + \left(\frac{\partial w}{\partial x} \right) \left(\frac{\partial w}{\partial y} \right).$$

Defining the dissipative function or plastic energy per unit volume as the area under the stress strain curve the total plastic energy PE is expressed as

$$\begin{aligned} PE = h \int_{-a}^a \int_{-b}^b & \left[\sigma_Y (\epsilon_x + \epsilon_y) \right. \\ & + \frac{\lambda}{2(1-\nu^2)} (\epsilon_x^2 + \epsilon_y^2 + 2\nu\epsilon_x\epsilon_y) \\ & \left. + \sigma_Y \gamma_{xy} + \frac{\lambda^2 \gamma_{xy}^2}{2} \right] dx dy, \quad (4) \end{aligned}$$

and the kinetic energy KE can be determined from

$$KE = \frac{mh}{2} \int_{-a}^a \int_{-b}^b (\dot{w}^2 + \dot{u}^2 + \dot{v}^2) dx dy, \quad (5)$$

where m is the mass density per unit volume and h is the plate thickness. Substituting Equations (3) into Equation (4), Equation (1) into Equation (5) and integrating both results gives expressions for PE and KE in terms of the displacements u_0 , v_0 , and w_0 and their time derivatives.

The blast pressure $p(t)$ is assumed to act as a uniformly distributed load over the area of the plate and the generalized force is determined from the virtual work δW of the pressure force moving through a virtual displacement δw . In that the pressure force is assumed to act only in the z direction the generalized force is associated with only the generalized coordinate w_0 and is found from the expression,

$$F_{w_0} \delta w_0 = \int_{-a}^a \int_{-b}^b \left[p(t) \frac{\partial w}{\partial w_0} \right] dx dy. \quad (6)$$

The other generalized forces associated with u_0 and v_0 are zero due to zero forces in the direction of the virtual displacements δu_0 and δv_0 .

Defining the Lagrangian L as $L = KE - PE$ and the Lagrangian equation of motion as

$$\frac{d}{dt} \left(\frac{\partial L}{\partial \dot{q}_i} \right) - \left(\frac{\partial L}{\partial q_i} \right) = F_{q_i} \quad (7)$$

where q_i represents the generalized coordinates u_0 , v_0 , and w_0 , the equations of motion for the plate may be determined. Performing the proper steps as called for in Equation (7) leads to three coupled nonlinear differential equations prescribing the deflections of the membrane. These equations are omitted here and the assumption that u and v are small in comparison to w is imposed. Applying this assumption to all the preceding Equations (1) to (6) and substituting the results into Equation (7) the equation of motion for a rectangular plate (membrane) of size $2ax2bxh$ subjected to a pressure-time load of $p(t)$ becomes,

$$\begin{aligned} \ddot{w}_0 + \frac{g\tau^2}{\lambda ab} \left\{ \frac{\sigma_Y}{4} \left[\frac{b}{a} + \frac{a}{b} \right] \right. \\ + \left[\frac{2\lambda\tau^2}{(4)^2(1-\nu^2)} \left(\frac{9b}{a^3} + \frac{2\mu}{ab} + \frac{9a}{b^3} \right) \right. \\ \left. \left. + \frac{2\lambda^2\tau^2}{(4)^2 ab} \right] w_0^2 \right\} w_0 = \frac{16gp(t)}{\tau^2 \rho h}, \quad (8) \end{aligned}$$

where ρ is the specific density in weight per unit volume and g is the gravitational constant. The integral involving the shear yield stress σ_Y is zero when integrated over the entire plate area.

Previous tests indicate that the reflected pressure for a controlled fuel air explosion closely approximates an exponential decay function of the following form.

$$p(t) = P_{max}(1-t/\tau)e^{-at/\tau}, \quad (9)$$

when

- P_{max} = peak reflected over pressure
- t = time
- τ = duration of the positive pressure phase
- a = decay term.

A schematic of a typical pressure-time function used in this analysis is shown in Figure 4.

A failure criteria based on an ultimate material elongation (strain) ϵ_u for a uniaxial stress-strain diagram may be determined from Equations (1) and (3). Using the assumed deflection equations (1) the strains are largest at the

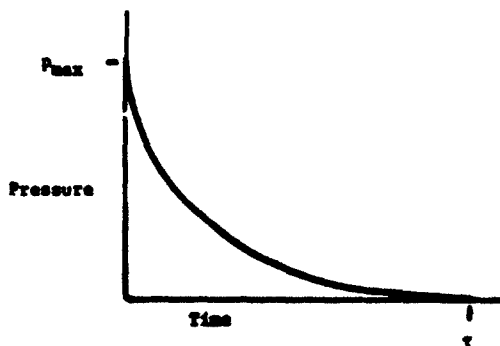


Fig. 4. TYPICAL PRESSURE-TIME CURVE USED IN PLATE ANALYSIS.

midpoints of the sides. For a square plate the strain would reach a maximum at the midpoints of all four sides. In terms of the center point displacement w_0 the strains at the midpoints of the sides become

$$\epsilon_x = \frac{\pi^2 w_0^2}{8a^2}$$

and

$$\epsilon_y = \frac{\pi^2 w_0^2}{8b^2}$$

(10)

Using the ultimate strain ϵ_u the maximum center point deflection w_{ou} corresponding to ultimate strain or failure may be determined. For example if b is the smaller side dimension ϵ_y would approach ϵ_u before ϵ_x and the center-point deflection for this condition becomes

$$w_{ou} = \frac{2b}{\pi} \sqrt{2\epsilon_u} \quad (11)$$

As is typical of a membrane analysis the maximum deflection of Equation (11) is independent of the plate thickness.

Equation (8) above holds for time of $0 < t < \tau$ and a similar equation with the right hand side equal to zero would hold for $t > \tau$ but due to the long duration τ the deflection of the plates tested reached a maximum before the end of the pressure loading. For this reason the equation of motion for $t > \tau$ is omitted.

EXPERIMENTAL PROCEDURE

Controlled explosions contained in a gas bag used previously in development of fuel air explosive devices [11], were used to produce blast loadings on square 2024-T3 aluminum plates with fixed edges. A metal tube framework 4'x4'20' covered with sheet plastic for each test was used as the fuel-air container. The test panel was mounted on a stand made of one inch thick steel plate and bolted to a thick concrete pad. As shown in Figure 5 the upright part of the test stand was designed to accommodate an 18"x18" square panel. The panel was bolted on all four edges by one half inch diameter bolts passing through the test panel and test stand to prevent slippage. A friction device was also used on the edges of the plates and a specified torque was applied to the retaining bolts.

After the container or bag was in place the following procedure was used:

- 1) place one hundred grams of red data sheet and a primer cap at the end of the bag opposite the test panel,
- 2) charge the bag with two pounds of MAPP gas,
- 3) allow ten minutes for mixing using an electric fan sealed in the bag during fabrication,
- 4) clear the area and detonate data sheet from remote control in block house.

Upon detonation of the data sheet (initiator) a detonation wave in the fuel air mixture was established and moved down the gas bag as a planar wave impinging on the test stand and test panel at the opposite end. Both side on and reflected pressures were recorded using piezoelectric pressure gages and associated recorders. Pressure measurements were made at the stations indicated in Figure 5.

A dynamic shadow Moire technique similar to that of Beynet and Plunkett [12] was used in an effort to determine a deflection time relation for the test panels. A search light, a high speed camera and a Moire grid arranged in the manner shown in Figure 6 was used for this test. The tests were performed during the day and scattered light and reflections from the plexiglass, used to hold the grid, caused some problems. Due to the light problems only qualitative data was obtained.

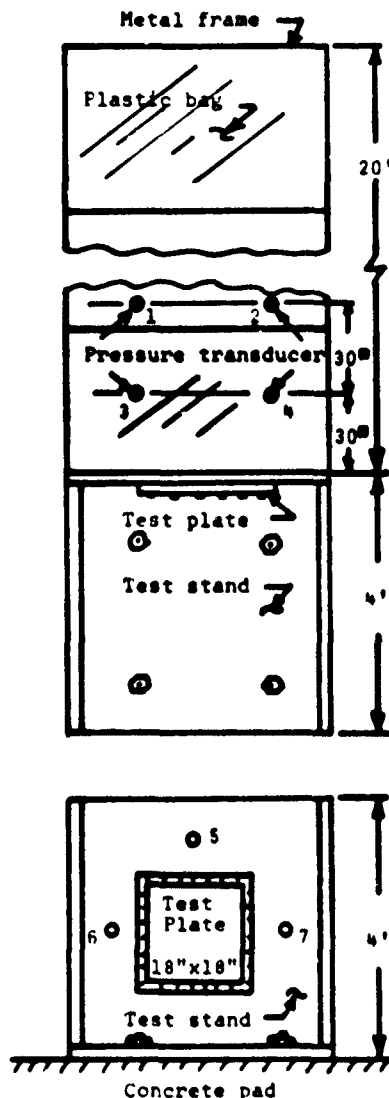


Fig. 5. TEST EQUIPMENT FOR CONTROLLED FUEL AIR EXPLOSION. PRESSURE TRANSDUCERS 1, 2, 3, 4 MEASURE STATIC PRESSURE ON GROUND. PRESSURE TRANSDUCERS 5, 6, 7 MEASURE REFLECTED PRESSURE.

DISCUSSION OF RESULTS

A typical experimental pressure time curve for the reflected pressure of a controlled fuel air explosion is shown in Figure 7. The average reflected peak overpressure for the detonation wave of all the gas bag experiments flush with the test stand was 800 psi. This agrees very well with predicted values obtained by Nicholls [13] and also reported in Reference 10. The pressure-time curve of Figure 7 is representative of the reflected pressure when the bag is positioned immediately adjacent to the test panel. The magnitudes of the peak overpressure P_{max} were varied by moving the bag to specified distances away from the panel. The effect of this change on the decay term s was quite small and the decrease in the peak overpressure resulted in a reduction of the maximum impulse as shown in Table I.

Solutions of Equation 8 were obtained for 18"x18" 2024-T3 square aluminum panels of variable thickness using the material properties obtained from Reference 14. These properties are listed with tabulated results in Table 1. Experimentally determined values of P_{max} , t , s were used in the pressure time function of Equation 9. Due to the large amount of plastic deformation a Poisson's ratio of 0.5 was used in the calculations. An analog simulation program using a fourth order Runge-Kutta technique [15] was used in the solution of Equation 9. Reasonable agreement between the analytical predictions and experimental results was obtained and is shown in Figure 8.

The ultimate center point deflection w_{ou} corresponding to a strain of ϵ_u at the edge of the plate was calculated using Equation 10 and an ultimate strain of 0.12 to 0.17. The range of strain produces a band of $(w_o)_{max}$ shown also in Figure 8, above which failure is assumed to occur. The solid symbols of Figure 8 indicate plate failure, however they are plotted at the deflection point calculated using Equation 9.

Plate failure started as a crack at the edge of one of the sides of the plate and progressed around the edges and curving around the corners of the panel as shown in photograph of Figure 9. Any crack formation was considered a failure in Table 1. The failed surfaces at the initial crack opening were typical of a uniaxial tensile failure of flat sheet.

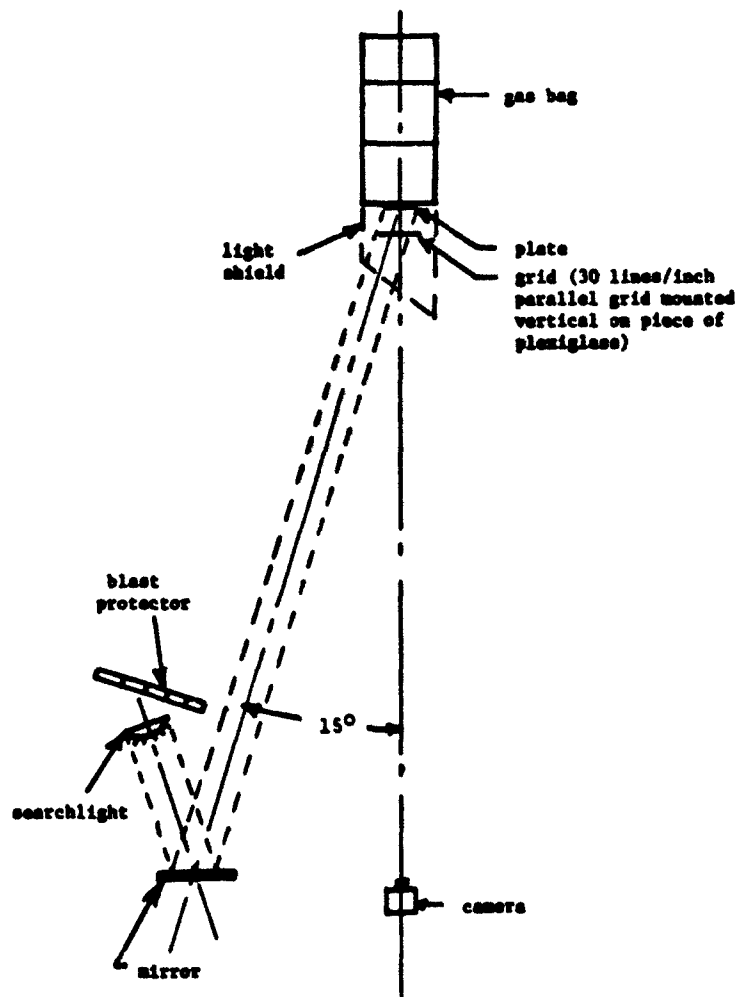


Fig. 6. SCHEMATIC OF EQUIPMENT FOR MOIRE PATTERN EXPERIMENT.

Using the Moire technique discussed previously it was determined that the initial deflection was a traveling hinge mechanism as that shown in Figure 1b. Using a high speed camera running at approximately 40,000 frames per second a sequence of Moire fringes were photographed and several frames of this high speed film are shown in Figure 10. Due to the poor resolution of the film the innermost fringe has been highlighted by hand. The absence of fringes in the central portion of the plate indicates an area of uniform deflection whereas the fringes on the sides of the plate

show a rather uniform linear deflection distribution. Each frame in Figure 10 represents approximately half of the plate area.

The solution of Equation 9 shows that the maximum deflection w_{max} occurs at about half the positive pressure phase duration. This was verified experimentally by observing the number of frames in the high speed film required for the total deflection process.

Strain rate effects were neglected in this analysis, however the strain

rate is in the order of $10^2/\text{sec}$ and for materials other than aluminum the changes in the yield stress σ_y and the ultimate strain ϵ_u may be significant.

CONCLUSIONS

The deflection mechanism mode for thin plates or membranes subjected to a fuel air explosion is initially one of a traveling plastic hinge with uniform bulging in the center portion of the plate at the latter stages of the deformation process. An equation of motion based on a static mechanism gave very good predictions of maximum center point deflection and plate failure for the square aluminum plates tested. Deflection and failure for large thin plates (membranes) are very dependent on blast peak overpressure and decay rate for mild impulsive loads. Increased peak overpressure may cause other deformation mechanisms to be operative but the peak overpressure causing failure predicted by the membrane model will be the lower bound for plate failure.

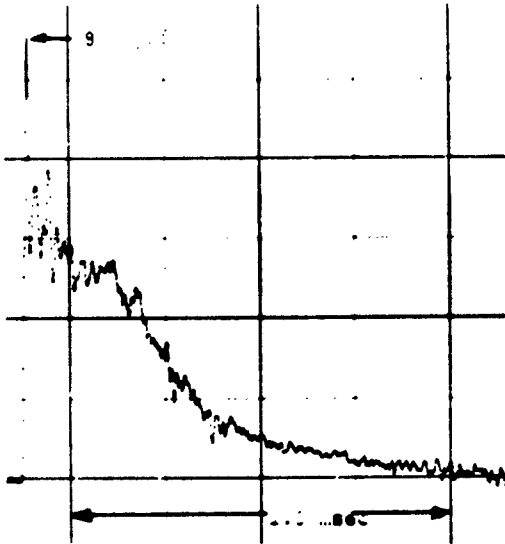


Fig. 7. EXPERIMENTALLY DETERMINED PRESSURE TIME CURVE FOR A CONTROLLED FUEL AIR EXPLOSION.

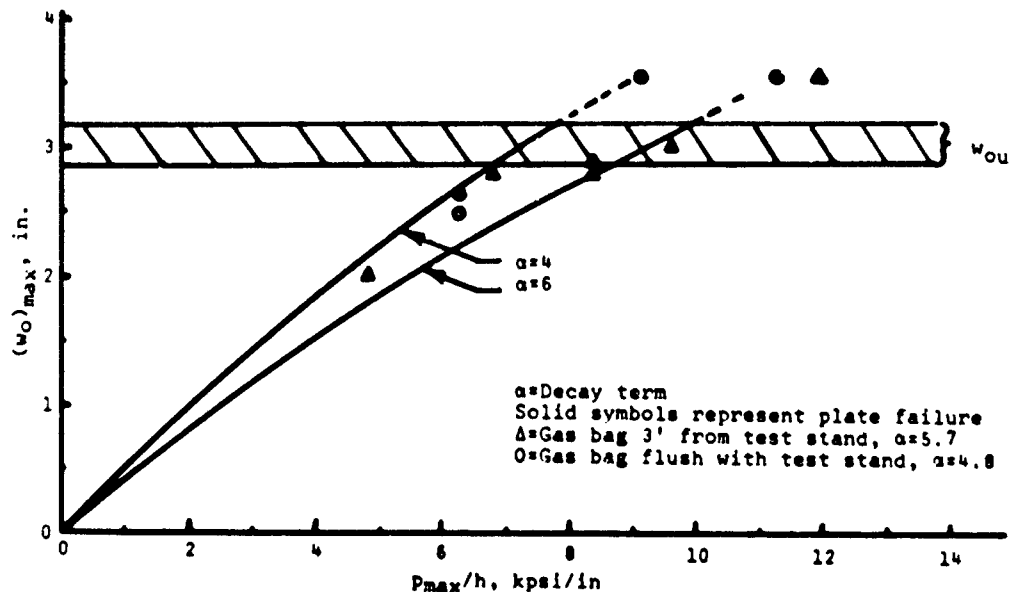


Fig. 8. MAXIMUM PLATE DEFLECTION AS A FUNCTION OF PRESSURE/THICKNESS RATIO.

TABLE I. EXPERIMENTAL DATA FOR 2024-T3 ALUMINUM PLATES

h (IN)	w _{max} (IN)	PLATE FAILURE	P _{max} psi	$\frac{P_m}{h} \times 10^{-3}$	I _{max} psi-msec	D FT.
.071	N/A	YES	800	11.30	220	0
.090	N/A	YES	800	8.90	220	0
.125	2.45	NO	800	6.40	220	0
.125	2.60	NO	800	6.40	220	0
.071	2.80	NO	600	8.45	130	3
.090	2.75	NO	600	6.67	130	3
.063	3.00	NO	600	9.52	130	3
.071	2.70	NO	600	8.45	130	3
.050	N/A	YES	600	12.00	130	3
.125	1.98	NO	600	4.80	130	3

h = plate thickness (inches) τ = approximately 1.5 msec for all tests
 w_{max} = maximum plate deflection (inches) λ = 147,000 psi
 I_m = total reflected impulse (psi-msec) σ_y = 43,000 psi
 D = distance from plate to gas bag (ft) ρ = 0.1 lb/in³
 P_{max} = peak reflected over pressure (psi) $\lambda^1 = \lambda / 2(1 + \mu)$
 a = 9 in (18" square plate) for all tests

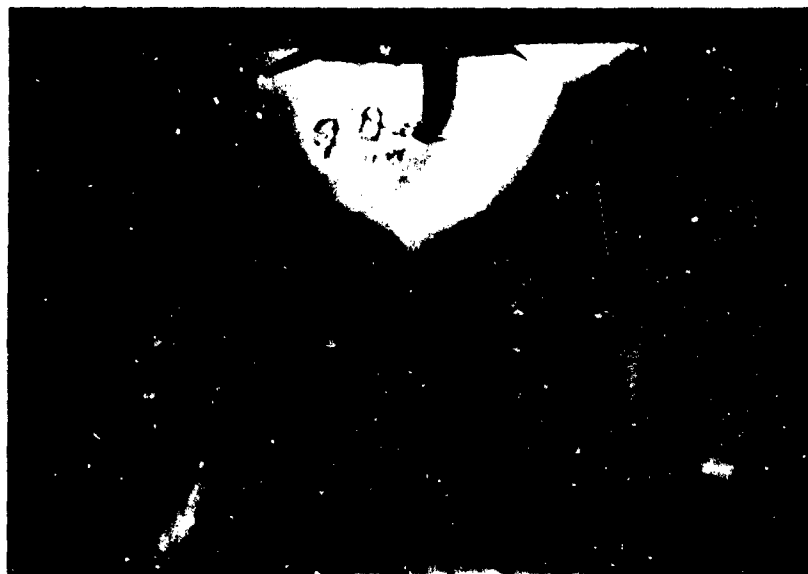


Fig. 9. TYPICAL PLATE FAILURE.



Fig. 10. DYNAMIC MOIRE FRINGE PATTERNS FOR DEFLECTING PLATE. EACH NUMBERED FRAME REPRESENTS APPROXIMATELY HALF OF THE DEFORMED PLATE. NUMBERING SEQUENCE REPRESENTS INCREASING TIME. THE FIGURE IS INTENDED FOR QUALITATIVE OBSERVATIONS ONLY, HOWEVER APPROXIMATE TIME BETWEEN FRAMES IS 0.025 MILLISECONDS AND THE FRINGE CONSTANT IS APPROXIMATELY 0.125 IN.

REFERENCES

- [1] Sewell, R. G. S., and Kinney, G. F., "Response of Structures to Blast: A New Criterion," Naval Weapons Center Report No. 4422, June 1968.
- [2] Abrahamson, G. R., Florence, A. L., and Lindberg, H. E., "Radiation Damage Studies (RADS), Vol. XIII Dynamic Response of Beams Plates and Shells to Pulse Loads," BSD-TR-66-372 Vol. XIII. September 1966.
- [3] Cox, A. D., and Morland, L. W., "Dynamic Plastic Deformation of Simply Support Square Plates," J. Mech. Phys. Solids, 7, No. 4 229-241 (1959).
- [4] Hudson, G. E., "A Theory of the Dynamic Plastic Deformation of a Thin Diaphragm," J. Appl. Phys. 221 (1951).
- [5] Cristescu, N., Dynamic Plasticity, North-Holland Publishing Co., Amsterdam, 1967, pp. 292-334.
- [6] Kay, F. J., and Whitehouse, G. D., "The Plastic Deformation of Clamped Rectangular Membranes Subjected to Impulsive Type Loading," Proceedings of the IASS Symposium, Hawaii, 1971.
- [7] Huffington, N. J., Jr., "Blast Response of Panels," BRL TN 1702, August 1972.
- [8] Rinehart, J. S., and Pearson, J., Behavior of Metals Under Impulsive Loads, Dover Publ. Co., New York, 1955.
- [9] Menkes, S. B., and Opat, H. J., "Broken Beams," Experimental Mechanics, Vol. 13, No. 11, November 1973, pp. 480-486.
- [10] Strickland, W. S., and Ross, C. A., US Air Force Armament Lab. AFATL TR-74-181.
- [11] Collins, D. M., "Critical Energy Threshold for Detonation Initiation in MAPP-Air Mixtures," AFATL-TR-72-192 (1972).
- [12] Baynet, P., and Plunkett, R., "Plate Impact and Plastic Deformation by Projectiles," Experimental Mechanics, Vol. 11, No. 2, February 1971, pp. 64-70.
- [13] Nicholls, J. A., University of Michigan, private communication.
- [14] MIL-HDBK-5, "Metallic Materials and Elements for Flight Vehicle Structures."
- [15] Hildebrand, F. B., Advanced Calculus for Engineers, Prentice Hall, Inc., New York, N. Y., 1953.

DISCUSSION

Mr. Korman: (TRW Systems) What was the incident pressure that goes along with your Figure 7?

Mr. Ross: (University of Florida Grad. Eng. Ctr. Eglin AFB) Roughly about 300 psi. In a shock wave in air the reflected pressure should be around 2000 psi, right?

Mr. Korman: Right!

Mr. Ross: So it's quite different.

Mr. Korman: How many pounds of explosive were you using?

Mr. Ross: It's a fuel/air mixture and we only used about 20 grams of data sheet as initiator and I think there is only 3 lbs. of map gas in a bag.

Mr. Korman: I was wondering whether in fact your instrumentation wasn't picking up the peak pressure as opposed to not getting the appropriate reflection factor because I would guess that you had a sufficiently small gas to air ratio such that you should get a reasonably close shock wave in air and should in fact get that factor of 6.

Mr. Ross: No, we've gone through this with Nickels at University of Michigan. He seems to be our expert and we finally convinced him that we would not get that high order pressure reflected.

Mr. Korman: Did you do any calculations with a gamma of 1.2 which is representative of explosive gases to see what kind of reflected pressure you would predict?

Mr. Ross: Well, if you would go to Stan Ukovich in his translation you will find that he has an equation for the reflected pressure, and it doesn't matter what the gamma ratio is it is about 2 1/2 even for condensed explosives.

Mr. Korman: The reason why I am bringing it up is because in Brodes, height of burst report he has done some calculations for reflected pressure ratios, a function of specific heat ratios.

Mr. Ross: For shock wave and air?

Mr. Korman: Yes, for air or any gamma. For example, he has a gamma for 1.2 that would be appropriate to combusted gas. Ok, I am talking about a Chapman-Jouget system in which we have a detonation moving through an explosive. Was that whole air bag filled with explosive gases?

Mr. Ross: It's a mixture of gas and air. There is a fan in there circulating it around, and it's at the right volumetric-stoichiometric values to give us an explosion. If you were off to the right or left either way of that ratio you won't get one, you would just get a deflagration.

Mr. Korman: So you feel then that your instrumentation was adequate enough to pick up the peak pressure?

Mr. Ross: Yes sir. We've gone through, see this is the reason we really bet this thing to death, but nobody would believe us. That's the problem, so we have really searched it out and gone to various instrumentations and we finally wind up some big gas men believing us. So Michael's in Michigan has given this answer.

Mr. Gary Fox: (Barry Division) Can you tell from the experiment at what point in time the plate failed, was it during the final part of the explosion or did it fail just when the stress wave started at the edge?

Mr. Ross: About half of the pressure time curve had elapsed. It occurred at $3/4$ of a millisecond and we found that our pressure time curve lasted about $1\frac{1}{2}$ milliseconds so about half way through it failed and our film shows this and our calculations indicate this, namely, that the maximum deflection will occur about half way through the pressure time curve. And also our film showed this.

Mr. Fox: So that's before it gets to the hemispherical shape?

Mr. Ross: I am not absolutely sure about that now. Let me say that if we calculate the maximum deflection of the center point, which we can do and look at it experimentally it occurs at about half way through the pressure time curve and if it is going to fail it occurs at about that time.

A MATRIX STRUCTURAL DYNAMIC MODEL OF PARACHUTE THERMAL COVER EJECTION BY PYROTECHNIC DEVICES

A. E. Barniskis and R. A. Romanzi
General Electric Co.
Re-entry and Environmental Systems Division
3198 Chestnut Street
Philadelphia, Pa. 19101

This paper presents a method developed at General Electric (RESO Division - Philadelphia, Pa.) for predicting separation velocities of a flexible thermal cover ejected by four cartridge type pyrotechnic devices. The method developed consisted of a structural dynamic model of the cover driven by four ejector pistons using a three-dimensional table of piston pressure, displacement and time as the forcing function.

The structure was modeled as an assembly of beam elements with stiffnesses and masses adjusted so that the mathematical model characterized the dynamic response of the cover observed in vibration tests. All first and second order physical parameters affecting performance of the separation system were included in the model.

The dynamic model has demonstrated excellent accuracy simulating system performance and predicting ejection velocities of several designs as corroborated by ground tests, and has been used effectively as a tool for guiding design optimizations.

1. INTRODUCTION

The energy transfer of a pyrotechnic ejector device is strongly dependent on the displacement time history of the ejected mass. A typical series of pressure time histories for several rigid masses ejected by a pyrotechnic ejector is shown in Figure 1.

The piston pressure for the heavier masses, which have corresponding lower accelerations, are higher throughout most of the ejection cycle. It would therefore be extremely difficult to obtain accurate predictions of the ejected velocities for a wide range of inertia loads by using an "average" pressure time history and integrating it to obtain a corresponding velocity time history. The problem is further complicated when the ejected body is an elastic system, as idealized in the two-degree-of-freedom system shown in Figure 2.

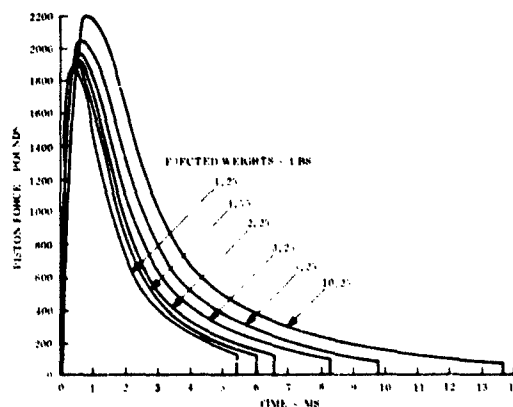


Figure 1. Pyrotechnic Ejector Force Time History

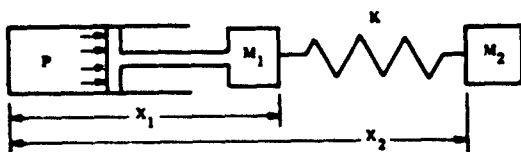


Figure 2. Idealized Elastic Ejection System

Initially, when the system is undeformed, the only force on mass m_1 will be the instantaneous pressure P acting on piston area A , and the accelerating force is simply PA . As m_1 moves to the right and spring K compresses, the accelerating force becomes $PA - K(X_2 - X_1)$. Thus, as the system compresses, the apparent mass inertia "seen" by the ejector piston increases, and the pressure time history produced by such an ejection would cross the traces of the rigid body ejected weights, moving from a lighter to a heavier time history curve.

The practical significance of this became apparent when the first attempts were made to predict the velocity of a parachute thermal cover ejected by four pyrotechnic ejectors. It was observed during ground test firings of an 8.0 lb cover that the highest ejected velocity obtained was approximately 20% below the velocity obtained during ejection of an 8.0 lb. rigid mass. Velocity losses as great as 40% were measured when the ejectors were fired non-simultaneously.

At first, it was hypothesized that the velocity losses were attributable to energy lost to structural deformation and friction. Attempts to assign percentage values to the velocity losses attributed to each of these parameters by empirical methods failed.

The failure of a thermal cover design to give the required velocity performance and the subsequent redesign effort provided the incentive for a more complete investigation of how ejection system parameters affected performance. This investigation began with a review of the data recorded for single piston rigid body firings of one charge adapter lot, which (Table 1) revealed that while the momentum of the ejected mass increases as weight increased, as indicated by the areas under the curves in Figure 1, the kinetic energy of the ejected mass decreased as weight increased. From this it was determined that the energy transmitted by a pressurized piston was not a fixed quantity but was a function of the displacement time history of the ejected mass. To verify

these conclusions, a method was developed describing the physical system as a mathematical model. The requirements for this model were:

- that it incorporate a structural model of the thermal cover which would accurately characterize the dynamic response during ejection and provide means of predicting structural loading during firing.
- that the forcing function used to simulate the pyrotechnic ejectors include the effect of the piston displacement.
- that the model be readily modifiable for purposes of revision, correction, or updating, as the physical system became more clearly understood.

The model described in the following sections has evolved in several stages since December 1973. While each version has been somewhat more sophisticated than its predecessor, the concept has remained unchanged.

2. DYNAMIC MODEL - GENERAL

A typical thermal cover is shown in Figure 3. Covers usually consist of a sheet aluminum box portion covered with an elastomeric thermal protection material, fastened to stainless steel "Z" rails joined at the corners by aluminum or titanium fittings which also serve as the attachments for the ejector pistons.

For simulation of thermal cover ejection, a matrix structural dynamic model of this assembly was developed. A schematic drawing of the physical simulation of the thermal cover separation system dynamics is shown in Figure 4.

In the present version the dynamic model may be represented by a variable number of degrees-of-freedom from a minimum of 6 to a maximum of 20. Of N degrees-of-freedom, the first $N-1$ are related to the structural model of the cover and the N th is related to a lumped forebody mass. Of the $N-1$ thermal cover degrees-of-freedom, the first four are assigned to axial degrees-of-freedom at each piston location, and the remaining $(N-5)$ are assigned to the top of the thermal cover box structure. Each of the four corners is driven by the pyrotechnic forcing function after ignition of the charge. The pyrotechnic forcing function (described in Section 2.2) is defined so that it is

TABLE 1
Piston Performance Test Data

Test No.	Peak Press. (psi)	Velocity (ft/sec)	Calculated Impulse (lb-sec)	Energy (ft-lbs)	Ejected Weight (lbs)
1.	10,000	55.6	5.61	157.5	3.0
2.	10,200	55.6	5.61	157.5	3.0
3.	10,400	53.4	5.39	145.5	3.0
4.	10,400	54.8	5.53	153.0	3.0
5.	10,400	53.4	5.39	145.5	3.0
6.	10,200	40.1	6.54	129.0	5.0
7.	9,400	39.3	6.40	128.5	5.0
8.	9,400	37.2	6.06	113.4	5.0
9.	10,800	42.9	7.00	150.5	5.0
10.	10,600	41.2	6.70	139.1	5.0
11.	11,200	40.8	6.67	136.8	5.0
12.	11,200	50.2	5.06	130.5	3.0
13.	10,000	78.6	4.24	166.6	1.5
14.	10,000	78.6	4.24	166.6	1.5
15.	9,800	92.6	3.61	167.2	1.0
16.	9,600	90.6	3.53	160.0	1.0
17.	9,500	85.1	3.32	141.2	1.0
18.	10,800	80.1	4.33	173.2	1.5
19.	11,500	27.0	8.58	115.9	10.0
20.	11,400	27.9	8.97	123.9	10.0
21.	11,200	27.0	8.58	115.9	10.0
22.	10,000	90.6	3.53	160.0	1.0
23.	9,200	92.6	3.61	167.2	1.0
24.	9,800	86.8	3.38	147.0	1.0

NOTES

1. Piston performance tests conducted 9/18/70 to 9/25/70
2. Energy and impulse calculations based on piston weight of 0.25 lb
3. Weight listed in "Ejected Weight" column does not include weight of piston
4. Pistons all modified to install instrumentation except where noted (Dwg. No. 47D173285)
5. Instrumentation for all pressure readings was a KISTLER 607L Pressure Transducer
6. SVA testing accomplished in accordance with Charge Adapter Specification No. 1375-02-0001
7. Firing altitude in all tests 100,000 feet

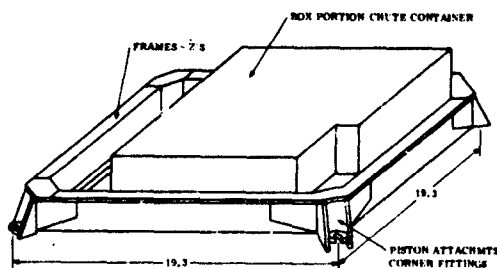


Figure 3. Aluminum/ESM Parachute Thermal Cover

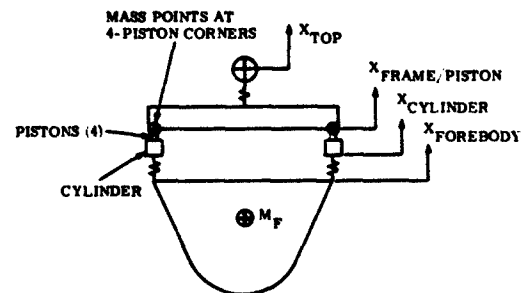


Figure 4. Schematic of Thermal Cover Dynamic Model

a function of displacement at each corner and the time since firing of that corner. With this simulation non-simultaneous firing events are accommodated by specifying individually the firing times of each piston.

Program input parameters are stiffness, mass, and damping matrices, ejector firing times, and the ejector forcing function expressed as a table of piston force versus time and displacement. Logic related to each force contributor is contained in a separate subroutine to facilitate logic changes without major reprogramming. The equations of motion, described in the following section, are integrated numerically using a fourth-order Runge-Kutta technique [1] through which the accelerations of the N mass points are integrated to obtain the velocities, which are integrated to obtain the displacements.

2.1 Equations of Motion

The equations of motion of the physical system are:

$$[M] \ddot{X} = \{F(X_s, t_f)\} - [K] X - [C] \dot{X} \quad (1)$$

$$X_s = X_p - X_f + F(X_s, t_f)/K_f \quad (2)$$

$$V_{me} = (1/M_{total}) [1] [M] \dot{X} \quad (3)$$

where,

- $\{X\}$ = Vector of displacements
- \dot{X} = Vector of velocities
- \ddot{X} = Vector of accelerations
- X_p = Piston displacement
- X_f = Forebody displacement
- X_s = Piston stroke
- t_f = time since piston firing
- $\{F(x_s, t_f)\}$ = piston force as function of stroke and time since firing
- $[M]$ = System mass matrix
- $[K]$ = System stiffness matrix
- $[C]$ = System damping matrix
- K_f = Charge adapter to forebody local stiffness.
- V_{me} = momentum equivalent velocity
- M_{total} = total mass of thermal cover

Equation 1 lists the inertial force on the thermal cover and forebody due to forces generated by the ejector pistons, structural stiffness, and system damping effects. The thermal cover corners are modeled as being rigidly coupled to the forebody before ignition. At ignition, a corner is uncoupled from the forebody; after all four ejectors have fired, the forebody is completely uncoupled from the thermal cover and is acted on only by the sum of the pressure of all four ejectors. Equation 2 defines the piston stroke which is the displacement of the piston relative to the charge adapter cylindrical housing. The piston stroke during firing is the difference between the corner displacement and forebody displacement, plus the deflection of the mount. Equation 3 defines the momentum equivalent velocity of the thermal cover mass points at time of the last piston clearing the ejector.

2.2 Pyrotechnic Ejector Forcing Function

The pyrotechnic forcing function is represented by a three-dimensional function of piston force, displacement, and time. Table 2 shows the three-dimensional forcing function for a typical charge adapter.

The method used to derive a table of this type was to obtain a series of oscillograph traces of pressure time histories for firings of 1-, 2-, 3-, 5- and 10-lb rigid weights and then numerically integrate each curve twice to obtain a displacement time history for that test. The velocities and displacements from this numerical integration were then checked against test results for each case, and the displacements for the various weights paired with their corresponding pressures through the time histories. For chosen increments of time, a "best fit" interpolating polynomial [1] is used to express pressure as a function of displacement.

After the table was assembled some data smoothing was required, using engineering judgement. In the routine, a table look-up and bilinear interpolation scheme is used to compute the pressures at times and displacements falling in regions between rows and columns.

2.3 Thermal Cover Structural Model

The dynamic analysis for the thermal cover was performed using a finite element model obtained by the direct stiffness method [2] to

TABLE 2
Piston Force Versus Time and Deflection

Time (ms)	Deflection Y (Inches)																		
	0	.02	.04	.06	.08	.10	.15	.20	.30	.40	.60	.80	1.0	1.5	2.0	2.5	3.0	3.7	4.0
0	0	0	0	0	0	0	0	0	0	0	0	0	0	0	0	0	0	0	0
.4	0	1.00	1.00	1.00	1.04	1.22	1.74	1.70	1.60	1.30	1.35	1.20	1.00	.85	.70	.60	.50	.47	0
.8	0	2.17	1.99	1.92	1.88	1.86	1.73	1.69	1.58	1.40	1.30	1.15	.90	.75	.65	.56	.46	.46	0
1.2	0	2.40	2.17	2.05	1.95	1.86	1.73	1.64	1.41	1.34	1.20	.96	.80	.70	.60	.50	.46	.40	0
1.6	0	2.00	2.00	1.95	1.89	1.80	1.72	1.55	1.37	1.21	.96	.84	.75	.66	.55	.43	.45	.35	0
2.0	0	1.80	1.87	1.86	1.82	1.77	1.67	1.55	1.30	1.10	.92	.77	.69	.59	.46	.46	.37	.30	0
2.5	0	1.80	1.86	1.81	1.87	1.84	1.64	1.57	1.21	1.05	.84	.72	.62	.52	.47	.39	.30	.20	0
3.0	0	1.70	1.87	1.85	1.83	1.81	1.64	1.52	1.21	1.05	.80	.66	.56	.46	.40	.37	.30	.20	0
3.5	0	1.60	1.80	1.80	.90	.90	.90	.90	.90	.90	.74	.63	.53	.41	.34	.31	.20	.27	0
4.0	0	1.50	1.15	.95	.83	.82	.80	.70	.74	.72	.60	.60	.52	.39	.32	.27	.25	.22	0
5.0	0	1.40	1.05	.90	.75	.70	.58	.57	.66	.64	.53	.51	.40	.30	.26	.20	.20	.18	0
6.0	0	1.30	1.00	.85	.70	.65	.50	.47	.44	.40	.42	.41	.40	.34	.26	.20	.17	.15	0
7.0	0	1.20	.95	.80	.65	.60	.47	.46	.30	.37	.35	.34	.33	.29	.20	.10	.15	.13	0
8.0	0	1.15	.90	.75	.60	.55	.44	.46	.26	.31	.30	.29	.28	.25	.20	.10	.12	.10	0
11.0	0	1.00	.80	.70	.55	.50	.40	.37	.29	.20	.27	.26	.25	.22	.15	.13	.11	.09	0
15.0	0	.90	.80	.65	.50	.45	.35	.33	.20	.27	.26	.25	.24	.20	.10	.12	.09	.07	0
19.0	0	.80	.75	.60	.45	.40	.32	.30	.27	.20	.25	.24	.23	.20	.10	.11	.08	.06	0

represent the structure. The model consisted of a finite number of rigid masses connected by massless elastic links. The mass degrees-of-freedom are shown as solid dots in Figure 5.

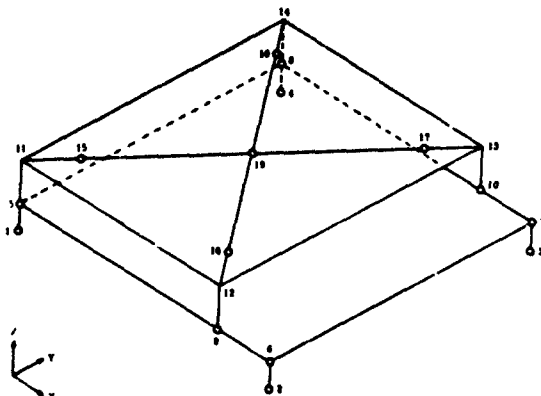
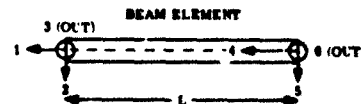


Figure 5. Thermal Cover Structural Model - Mass Points

A total of 19 joints were used to describe the thermal cover, resulting in 114 static DOF (6 DOF/joint). The stiffness matrices for the 19 joint models were assembled using an elemental beam stiffness matrix shown in Figure 6.



F_1	$\frac{AE}{L}$					$\frac{AE}{L}$													
F_2		$2S_3$				$-LS_3$													
F_3			$2S_2$			LS_2													
M_1				$\frac{GL}{L}$															
M_2					N_2														
M_3						N_3													
F_4	$\frac{AE}{L}$										$\frac{AE}{L}$								
F_5		$-2S_3$				LS_3													
F_6			$2S_2$			LS_2													
M_4				$\frac{GL}{L}$															
M_5					N_2														
M_6						N_3													

$$\begin{aligned}
 S_2 &= 6EI_2(1 - C_2)L^3 & S_3 &= 6EI_3(1 - C_3)L^3 \\
 C_2 &= 12EI_2(KA)_2GL^2 & C_3 &= 12EI_3(KA)_3GL^2 \\
 N_2 &= 2S_2L^2(1 - C_2/4)^3 & N_3 &= 2S_3L^2(1 - C_3/4)^3 \\
 N_2 &= S_2L^2(1 - C_2/2)^3 & N_3 &= S_3L^2(1 - C_3/2)^3
 \end{aligned}$$

Figure 6. Beam Stiffness Matrix

The parameters used in defining the elements for this stiffness matrix were given by:

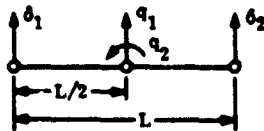
A	Cross-section area
E	Modulus of elasticity
F	Force
G	Shear Modulus of elasticity
J	Moment of inertia about Axis 1
I_2	Moment of inertia about Axis 2
I_3	Moment of inertia about Axis 3
L	Length of beam
M	Moment
KA	Effective shear area

For boundary conditions, the model was pinned in the X & Y directions at joints 1, 2, 3, and 4. The stiffness matrix for the original cover design was correlated with static test data and showed reasonable agreement. With the corners pinned, the stiffness of the basic rail structure is due to both twisting of the rails, and, because of the offset of the pinned bottom joint, side bending of the rails. It was found that the side bending of the rails is significant and that the predicted values of the stiffness were within the range of values determined from static load tests at each of the frame corners. For the thin aluminum cover, the box structure does not significantly stiffen the rails. The 114 DOF stiffness matrix was then reduced to 15 dynamic DOF's corresponding to the 15 lumped masses moving in the Z-direction using the static stiffness reduction technique, i.e., reduced stiffness is

$$K_{11} - K_{12} K_{22}^{-1} K_{21}$$

In the "released" condition, each corner of the cover is free to move in the Z direction. Due to the rigid characteristics of the rails, a generalized mass matrix can be written which transforms the lumped masses and inertias from the center of the rails to the four corners.

For a single rail with mass concentrated at its center (as in sketch below) the transformation equations from the center to the ends of the rail are



$$\{q\} = [\beta] \{\delta\} \quad (4)$$

where the transformation matrix is

$$[\beta] = \begin{bmatrix} 1/2 & 1/2 \\ 1/L & -1/L \end{bmatrix} \quad (5)$$

The mass matrix in the q coordinate system is

$$[M]_q = \begin{bmatrix} m & 0 \\ 0 & I \end{bmatrix} \quad (6)$$

Therefore since Kinetic Energy is invariant under coordinate transformations, the mass matrix in the δ coordinate system is

$$[M]_\delta = [\beta]^T [M]_q [\beta] = \begin{bmatrix} \left(\frac{m}{4} + \frac{I}{L^2}\right) & \left(\frac{m}{4} - \frac{I}{L^2}\right) \\ \left(\frac{m}{4} - \frac{I}{L^2}\right) & \left(\frac{m}{4} + \frac{I}{L^2}\right) \end{bmatrix} \quad (7)$$

Now for the 4 beams together the generalized mass matrix is obtained.

$$[M]_\delta = \begin{bmatrix} \left(\frac{m}{4} + \frac{I}{L^2}\right) & \left(\frac{m}{4} - \frac{I}{L^2}\right) & 0 & \left(\frac{m}{4} - \frac{I}{L^2}\right) \\ \left(\frac{m}{4} - \frac{I}{L^2}\right) & \left(\frac{m}{4} + \frac{I}{L^2}\right) & 0 & 0 \\ \text{SYMMETRIC} & \left(\frac{m}{4} - \frac{I}{L^2}\right) & \left(\frac{m}{4} + \frac{I}{L^2}\right) & \left(\frac{m}{4} - \frac{I}{L^2}\right) \\ 0 & 0 & \left(\frac{m}{4} - \frac{I}{L^2}\right) & \left(\frac{m}{4} + \frac{I}{L^2}\right) \end{bmatrix} \quad (8)$$

This coupled 4 x 4 generalized mass matrix was used for the model to represent the rail masses at joints 5, 6, 7 and 8.

The generalized equation of motion is given by

$$[M] \{\ddot{X}\} + [K] \{X\} = \{F(t)\} \quad (9)$$

where,

- $[M]$ = mass matrix
- $[K]$ = stiffness matrix
- $\{X\}$ = displacement vector
- $\{\ddot{X}\}$ = acceleration vector
- $\{F(t)\}$ = force vector

This equation was then reduced to a 15 DOF problem by applying the matrix reduction transformation. The 15 DOF's remaining correspond to the masses located at firing points of the 4 pistons and the masses at the center of the panel.

The matrix reduction is a static transformation that reduces the size of the eigenvalue problem while retaining the inertial effects in the mass matrix. For the static case, the force-deflection relationship can be expressed in partitioned form as

$$\begin{Bmatrix} F_1 \\ -F_2 \end{Bmatrix} = \begin{bmatrix} K_{11} & K_{12} \\ K_{21} & K_{22} \end{bmatrix} \begin{Bmatrix} X_1 \\ X_2 \end{Bmatrix} \quad (10)$$

where,

$$\begin{aligned} [F] &= \text{force} \\ [K] &= \text{stiffness matrix} \\ [X] &= \text{static deflection} \end{aligned}$$

If F_1 are the only external forces acting on the structure, (i.e., $F_2 = 0$), then the equations in partitioned form may be written as

$$\begin{aligned} F_1 &= [K_{11}] X_1 + [K_{12}] X_2 \\ 0 &= [K_{21}] X_1 + [K_{22}] X_2 \end{aligned} \quad (11)$$

and X_2 may be expressed as

$$X_2 = -[K_{22}]^{-1} [K_{21}] X_1 \quad (12)$$

By substituting the solution for X_2 into the first equation, the familiar reduced stiffness matrix, K^* , is obtained:

$$K^* = K_{11} - K_{12} K_{22}^{-1} K_{21} \quad (13)$$

and the reduced equation for the static case may be written as

$$F_1 = [K^*] X_1 \quad (14)$$

Using the expression for X_2 in terms of X_1 , one can define a coordinate transformation given by

$$\begin{Bmatrix} X_1 \\ -X_2 \end{Bmatrix} = [T] X_1 \quad (15)$$

where,

$$[T] = \begin{bmatrix} - & - & - & - & 1 & - & - & - & - \\ & & & & -I & & & \\ & & & & -K_{22} & & & \\ & & & & & & & K_{21} \end{bmatrix}$$

By substituting the coordinate transformation into the equation of motion and pre-multiplying by $[T]^T$, the reduced equation of motion will be given by

$$[M^*] \ddot{X}_1 + [K^*] X_1 = [F^*(t)] \quad (16)$$

where,

$$\begin{aligned} [M^*] &= [T]^T [M] [T] \\ [K^*] &= [T]^T [K] [T] \\ [F^*(t)] &= [T]^T [F(t)] \end{aligned}$$

Note that the triple product $[T]^T [K] [T]$ will result in a K^* matrix that is identical to the K^* derived from the static case. Motions for the $\{X_2\}$ coordinates can be obtained by applying the coordinate transform used to obtain the reduced equation of motion.

Because the equations of motion during cover ejection were to be solved with numerical integration, it was considered desirable to reduce the number of DOF's to 15 in order to reduce the complexity of the integration program.

3.4 Charge Adapter Stiffness

Charge adapter stiffness is included to simulate the structural response of the mounting in determining the effects on energy transfer produced by the pistons. This effect is accounted for in the equations of motion by Equation (3) which defines the piston stroke and is included as a displacement term approximating the charge adapter deflection due to firing forces. The stiffness value used for this simulation is 40,000 lb/in. for each adapter. Measurements of local stiffness were obtained from impedance vibration tests. Results were on the order of 1.0 to 1.5×10^5 lb/in. for a 10-lb maximum input from the shaker. Due to this low input force, compared to the high levels obtained during thermal cover ejection (about 2000 lbs) the 40,000 lb/in. value was used pending static tests at higher load levels.

2.5 Moving Forebody

The moving forebody was included to simulate the loss of energy and piston stroke due to forebody motion and to determine its effects on the total TC velocity produced by the piston. The forebody was modeled as a 76-lb lumped mass, free to move in the axial direction in response to the piston forces.

2.6 Damping Effects

Damping includes all forces which are a function of mass point velocities. Included are thermal cover structural damping, and a drag coefficient simulating all frictional losses. The drag coefficient simulates frictional losses by applying a retarding force to the corner mass points proportional to velocity. It was derived empirically from previous test results. The elements of the structural damping matrix are proportional to the stiffness matrix and are computed as the structural damping coefficient multiplied by the ratio of the corresponding cover stiffness matrix element to the stiffness of the center relative to the corners. Structural damping was assumed in phase with velocity.

3. VIBRATION TESTS

The objective of the vibration tests was to obtain dynamic characteristics of the thermal cover used in refinement of the stiffness and mass matrices incorporated in the ejection model. From test results it was observed that the box portion was highly flexible and nonlinear. Tests performed at three vibration levels showed that the cover became stiffer at high force levels as indicated by an increase in resonant frequency. When the T/C was driven at the first modal frequency, large lateral displacements were measured with 80 to 80% of the mass effective. In addition, the deflection of the top caused large lateral motions of the unsupported sides.

In the second mode, the motion of the top of the cover indicated that the center moved out of phase with the sides, i.e., there was a modal circle between the center and the other accelerometer location on the cover top. In the frequency range between 5 and 200 Hz, the frame showed no significant dynamic motion in the vertical direction.

Using the vibration test data described above, the stiffness and mass matrices of the 114-degrees-of-freedom structural model were adjusted until the predicted frequencies and

and mode shapes obtained from an eigenvalue-eigenvector solution closely agreed with measured dynamic behavior of the thermal cover. It was this refined structural model which was used in the velocity prediction model.

4. THERMAL COVER EJECTION PERFORMANCE

This section is devoted to a discussion of performance predictions obtained with the use of the dynamic model. Contained herein is a comparison of predicted ejection velocities with ejection test data for several thermal covers, an empirical derivation of the drag coefficient cited in Section 2.3, and an identification of velocity losses incurred during thermal cover ejection.

A comparison of dynamic model predictions and ejection test velocities, for three different thermal cover models, is shown in Table 3. The drag coefficient used in the dynamic model for all three covers was 0.27 lbf-sec/in. The good agreement with test results indicates that this method of representing the unidentified frictional losses was sufficiently accurate. Discussion of the derivation of this value follows in Section 4.2.

4.1 Empirical Derivation of Drag Coefficient

As stated in Section 2.1, the drag coefficient was attributed to non-accountable effects such as parachute, baffle, and piston friction, and, for ground test firings, the pressure differential aerodynamic drag. Parametric studies were performed to determine the effect of this drag coefficient on predicted velocity. From the results, values of 0.27 and 0.165 lbf-sec/in. were chosen as the values to predict ground test and flight ejection velocities, respectively.

4.2 Thermal Cover Velocity Loss Identification

To guide the redesign of heavier thermal covers it was envisioned that knowing the various loss coefficients, modifications to the redesign could be made. The production thermal cover ejected was chosen as the baseline design for analysis of the contribution of various physical parameters to the energy balance.

The velocity losses associated with each of the physical parameters simulated in the dynamic model are shown in Table 4. It was observed that a total velocity loss in ground test of 15.2 ft/sec is obtained when all physical

TABLE 3
Comparison of Predicted Cover Nominal Velocity With Test Values

Cover Jettison Weight (lb)	Corrected Test Value Velocity (ft/sec)	Predicted Velocity (ft/sec)
12.3 Weighted Production Model	38.5 39.3 39.3 Average 40.2	40.7
11.8 Production Model	42.3	42.3
11.8 Stiffened Production Model	45.3	44.7

TABLE 4
T/C Velocity Loss Identification.

Physical Parameters	Velocity Loss (fps)	Predicted Eject Vel With Individual Effects (fps)
Single Piston - Rigid Body	0	57.5
T/C Stiff and Structural Damping	5.3	49.7
Forebody Mass	2.0	46.4
Charge Adaptor to Forebody Local Stiffness	.3	44.7
Piston Loss Damping Attributed to Parachute and Piston Friction	7.6	49.8
Dynamic Model Which Includes All Above Effects	15.2	42.3

effects are included. The velocity losses identified in Table 4 were calculated by deleting the physical parameters one at a time from the dynamic model and noting the velocity gained. For example, the effect of the moving forebody was determined by running a trial case with infinite forebody weight; cover flexibility loss was determined by running a case including all effects, but ejecting a rigid lumped mass equal to the mass of the cover. The remaining velocity loss required to bring the predicted velocity down to test velocity after all other effects were accounted for, was assigned to frictional or drag effects, as discussed previously.

5. CONCLUSIONS

Presented in this section are conclusions arrived at regarding the particular ejection system that has been cited as an example, modeling techniques applied to pyrotechnic ejection simulations, and some general conclusions regarding pyrotechnic ejection of elastic systems.

5.1 Basic Aluminum/ESM Thermal Cover Design

The production thermal cover that was the object of this investigation was designed to

withstand a high load re-entry environment. Using the ejection dynamic model as a design tool, ejections of many proposed designs were simulated. From these simulations it was concluded that the design separation velocity could not be achieved using the original pyrotechnic charges. As a result, a new higher energy pyrotechnic device was developed. For this charge, the dynamic model made accurate pre-test predictions of separation velocities without applying additional empirical adjustments, i.e., using the previously defined system parameters with a new three-dimensional pyrotechnic forcing function, immediately yielded predictions that agreed with ground test results.

5.2 Conclusions Regarding the Method of Modeling a Pyrotechnic Ejector

Since the methods used to express and integrate the equations of motion of the structure are relatively conventional and have been applied previously to problems of structural dynamics, it is the opinion of the authors that the most unique and valuable aspect of this investigation, beyond the immediate benefit of providing a useful design tool for the particular problem, was the derivation and validation of a method for representing the highly non-linear pyrotechnic forcing function. The method described in Section 2.2 appears to be valid when the displacement of the ejector piston is a monotonically increasing function of time, and the displacement time histories to be modeled fall within the range of the test displacement time histories from which the forcing function table is derived. It is anticipated that this technique can be of great benefit in modeling pyrotechnic actuation devices as well as ejection devices.

It is also concluded that the excellent accuracy achieved in velocity predictions was due to a large extent to the accurate characterization of the dynamics of the structure achieved by refining the mathematical model using vibration test results.

5.3 Effect of Structural Elasticity

In general, it was concluded that for a given weight, the more closely a structure approaches a rigid body, the higher the ejected velocity. The reason for this is that this condition will maximize the average pressure over the time of piston stroke, thus maximizing system momentum. This approach of rigidizing the structure also minimizes structural deformation and thus non-recoverable energy losses. While it is conceivable that a structure could

be designed that was "tuned" to optimize the pressure time history produced by a given pyrotechnic device, it is believed that for design purposes the rigidizing approach is most practical.

6. FURTHER INVESTIGATION

While the method of describing the pyrotechnic forcing function developed for this investigation has proven entirely adequate for analyzing the present system, it would be worthwhile to investigate other methods not subject to the restrictions cited in Section 4.2. For example, it would be worthwhile to attempt modeling the physical process of pyrotechnic propellant burning and pressure generation. This investigation could add significantly to the knowledge of pyrotechnic/structural systems in particular, and response of structures to highly non-linear forcing functions in general.

REFERENCES

1. Carnahan, B., Luther, H., and Wilkes, J., Applied Numerical Methods P. 363, P. 573, John Wiley and Sons, Inc., 1969.
2. Rubinstein, M., Matrix Computer Analysis of Structures, P. 178, Prentice-Hall Inc., 1966.

STRUCTUREBORNE GUN BLAST SHOCK TEST USING AN ELECTROHYDRAULIC VIBRATION EXCITER

Mr. N. D. Nelson
Hughes Aircraft Company
Ground Systems Group
Fullerton, California

Dr. R. L. Woodfin
Naval Weapons Center
China Lake, California

A test method for simulating the effects of structureborne gun blast is described in this paper. The test levels were defined in terms of the shock response spectra and the number of shocks to simulate the repetitive nature of gun firing sequences. Results of tests on typical electronic assemblies are presented and discussed briefly.

INTRODUCTION

After determining that MIL-S-901 levels were too high to demonstrate compliance with the gun shock of a ship-board target acquisition system, a test method was developed using an electrohydraulic vibration exciter to simulate the proper levels. A point defense target acquisition system being developed at Hughes Aircraft Company, Ground Systems Group had a specification requirement for uninterrupted operation during and after application of shock levels expected in the ship structure as a result of blasts from guns coupled to the structure. Initial efforts were made to relate the shock response of the system to the MIL-S-901C shock tests for the same equipment. The MIL-S-901 test results were unsatisfactory for this purpose, since a) the system's shock levels are approximately an order of magnitude higher than those specified for structureborne gun blasts and b) an interruption of operation is permitted for MIL-S-901C shock.

The equipments involved in the system are complex electronic assemblies ranging from a computer to a high power transmitter. These assemblies were known to be susceptible to the effects of shock and vibration. The "fragility level" for uninterrupted operation was unknown and could not be derived from the effects of other environmental tests.

The shock levels were analyzed to be within the capability of available electrohydraulic vibration exciters. Therefore a decision was made to derive a shock response spectra controlled test specification and to conduct the test using the vibration exciter. The rationale for using the electrohydraulic vibration exciter, which proved in practice to be valid, was threefold: 1) the technique was the most economical available (it required much less setup and operation time than, say, low-level drops on a MIL-S-901C shock machine); 2) the shock pulses were repeatable to a high degree and always under control; and 3) the shock pulses could be shaped to give a spectrum which characterizes the structureborne gun blast shock to conform to the best available measured data.

TEST SPECIFICATION

Since there are no known military test specifications nor measured data to analyze the shock effects of structureborne gun blasts during repetitive firing, a specification was generated that defined the shock input in terms of its response spectra rather than an arbitrary waveform. The system specification defined the design requirement in terms of velocity and peak acceleration values. These values are shown as the nominal values in Figure 1. The velocity and acceleration values were treated as the asymptotes of a response spectra to yield a break-point frequency of 80 Hz. The waveform of the input shock was not specified, but was defined as the structureborne component of an air blast coupled to the structure. The measured waveform then would be expected to be a complex noise pulse containing a relatively wide range of frequencies. It was considered unrealistic to define the shock in terms of an arbitrary waveform, since a) there was no way of relating a shock pulse, such as a one-half sine wave, to the existing situation and b) the actual waveform would be too complex to synthesize.

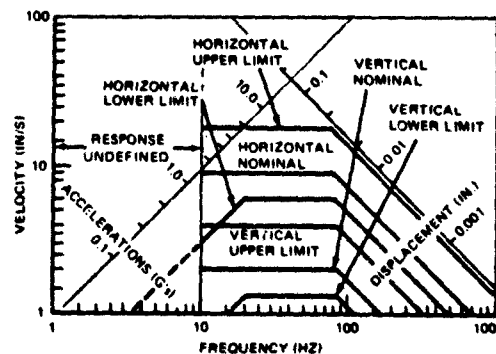


Figure 1. Input Shock Response Spectra for a Structureborne Gun Blast (Velocity vs Frequency)

It was decided to define the shock input in terms of its response spectra over the frequency range from 10 Hz to 500 Hz and to set tolerance limits on the test. The specified tolerance limits were set at reasonable values of +6 dB and -3 dB relative to the nominal acceleration as shown in Figure 1. Figure 1 is plotted with velocity and frequency as the coordinates. The velocity versus frequency plot is shown because it is easy to visualize the parameters of displacement and acceleration.

The data shown in Figures 1 and 2 was derived from the system specification requirements, and the source of the data used for preparation of the system specification is unknown. Upper and lower tolerance limits were assigned according to test procedures and were chosen to exercise reasonable control without being unnecessarily restrictive.

Figure 2 includes the same data plotted as acceleration versus frequency which are the coordinates plotted by the available shock response spectrum analyzer. It should be noted that the intention was to control the shock input to the nominal values. The upper and lower tolerance limits are specified primarily to impose limits on the type of waveforms that will yield acceptable response spectra. As illustrated in Figure 2 the lower tolerance limit plots break, with a horizontal displacement of 0.050 inches and a vertical displacement of 0.011 inches, at 20 Hz in order to permit the use of a waveform having zero total velocity change. The response spectra is undefined in the frequency range of less than 10 Hz and greater than 500 Hz. The lack of definition at frequencies less than 10 Hz was justified on the basis that none of the test specimens would have resonant frequencies in that frequency range. This turned out to be not true for some specimens, and in all cases the response spectrum was plotted to less than 5 Hz.

The number of shocks to be applied consecutively in the same direction was the subject of considerable discussion. The type of failures expected to be detected, if they were present, included nonlinear responses such as circuit cards which tended to "walk" progressively

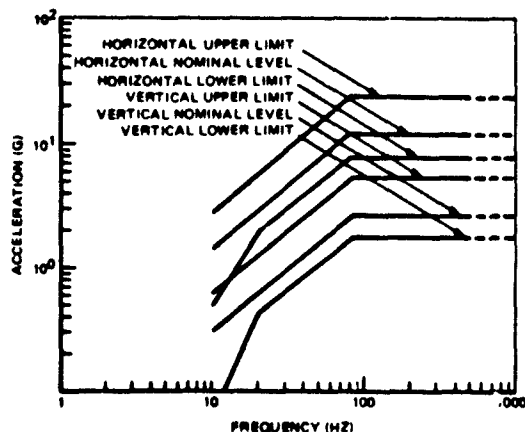


Figure 2. Input Shock Response Spectra for Structureborne Gun Blast (Acceleration vs Frequency)

out of the mating connector. The cumulative effect then would be a function of the number of shock pulses and the direction of each. The total effect of a number of pulses in alternating directions would not be the same as that for a number of pulses which are all applied in the same direction. The final test plan specified 10 shock pulses in each direction along each of 3 mutually perpendicular directions for a total of 60. In addition, 5 pulses were allowed in each axis for adjustment of the shock pulse level, if required. The time spacing of the shock pulses was approximately 10 seconds, which was long enough to allow the response transients to decay between pulses.

TEST PROCEDURE

The specified shock pulse was generated by a vibration exciter with a peak force of 50,000 lbs and an Exact Electronics Waveform Generator monitored by a response spectra analyzer. The instrumentation for generating, controlling, and recording a shock pulse is shown in Figure 3. This instrumentation complies with the requirements of Figure 1. The shock pulse was synthesized with an Exact Electronics Waveform Generator and was adjusted to yield the specified shock response spectra. A wide range of waveforms could have been used to generate an acceptable response spectrum. The first trial waveform used was a simple approximate one-half sine wave with reverse "tails" to give zero velocity.

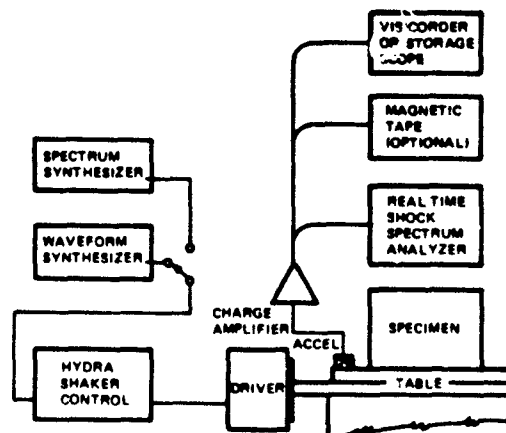


Figure 3. Instrumentation Setup for Generating and Controlling the Shock Response Spectrum

The vibration exciter that was used has parameters of:

Peak Force	50,000 lbs
Peak Velocity	17 in./sec
Stroke	1 in.
Response	dc to 250 Hz minimum

and was demonstrated to have sufficient capacity to generate the specified shock pulse as a single (non-

repetitive) pulse. Figure 4 is a photograph of the test setup for an electronic cabinet in the horizontal axis.

A typical shock response spectrum plot is shown in Figure 5. The waveform and response spectrum varies somewhat with the dynamic characteristics of the sample and fixture. There was no attempt to optimize the response spectrum for each test specimen. Figure 6 shows the response spectrum and waveform for a horizontal y-axis shock pulse on a top-supported electronic cabinet. The peak acceleration was controlled to the nominal value, and it was not necessary to adjust the waveform for the samples tested.



Figure 4. Setup for a Structureborne Gun Shock Test

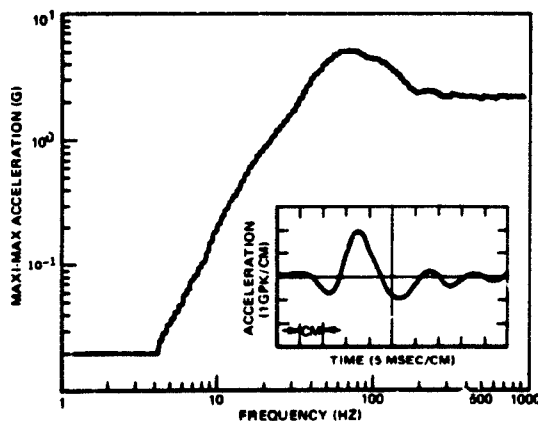


Figure 5. Input Shock Response Spectrum and Input Waveform for a Typical Test in the Vertical (Z) Axis ($C/C_0 = 0.1$)

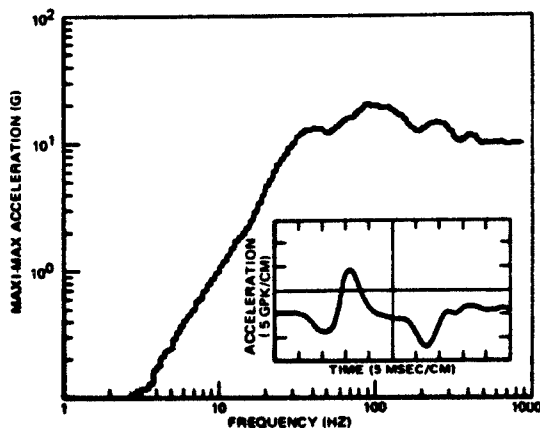


Figure 6. Input Shock Response Spectrum and Input Waveform for a Typical Test in the Horizontal (Y) Axis ($C/C_0 = 0.1$)

TEST RESULTS

The results of the shock tests revealed much more response than was expected; the primary indication of anomaly was system interrupts in a number of different units. These shock tests were conducted to detect conditions which could cause problems in the system during sea trials. Some of the results are described briefly in the following paragraphs.

Figure 7 shows the shock response spectra at the input and output of the shock isolators of a cabinet. The transmissibility of the isolator was plotted and the plot showed that the isolators were tuned to 18 Hz instead of 10 Hz as expected. The isolators then transmitted an appreciably higher shock level than the design condition. The isolator design was subsequently modified to provide the designed isolation frequency of 10 Hz.

An electronic cabinet was found to have a panel circuit breaker which tripped under the shock input. Examination and accelerometer data indicated that the panel was resonant at a relatively low frequency which approximately matched the peak of the input shock spectrum. The panel was stiffened and the circuit breaker no longer tripped at the specified shock level. The same unit had an intermittent connection in a circuit card. Substitution of another card removed the intermittent condition and the unit was capable of operating through the shock pulse.

A digital card rack having a high density machine-wired back plane was shown to have conductive debris trapped in the wire bundles. The shock pulses caused migration of the particles and several short circuits within the wiring. The unit had previously been vibrated until the release of particles had dropped to essentially zero. The vibration level was approximately 1 gravity to a maximum frequency of 33 Hz. The shock input was 10 to 25 times higher than the vibration acceleration and excited the entire frequency spectrum. The test unit operated through 10 consecutive shocks in each direction in each of 3 axes after approximately 120 shocks.

No physical damage was expected, and none was observed during the tests, since all of the units tested were designed for MIL-S-901C shock which has shock inputs 10 to 50 times higher than those specified for structureborne gun shock.

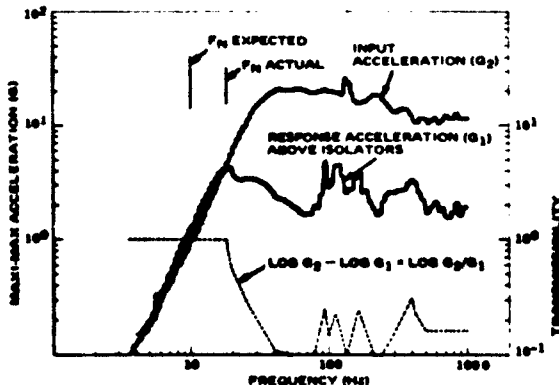


Figure 7. Shock Transmissibility. The plots show the measured shock response spectra at the input and output of isolators and the derived transmissibility at damping ratio (C/C_0) of 0.10.

DISCUSSION

Mr. Forkoie: (NRL) You can do the same thing on the medium weight shock machine by reducing the height of the hammer drop!

Mr. Foley: (Hughes Aircraft Co.) I think the reason we chose this was because we could hit 60 to 120 shock impulses and have them fall right on the line, I don't think I could do that with the medium weight shock machine, we have tried to do it with the medium weight shock machine but we were not successful. Right now we are using a soft deck, I don't know if you are familiar with that or not, and we are trying to get some repeatability but at that time we couldn't get it on medium weight shock machine.

Mr. Donohue: (Naval Weapon Center) And also as a matter of cost this test has worked right in with the Mil Std 167.

Mr. Foley: Yes, that's right, it was on the same machine we could complete our vibration set up and do the shock. There was no additional fixture required.

Mr. Forkoie: My only concern is this is a low level shock input and by no stretch of the imagination should this be considered a substitute for the MIL-STD 901C test.

Mr. Donohue: No, it isn't.

CONCLUSION

The test method described herein is useful for detecting nuisance malfunctions in hard-mounted complex electronic assemblies which are required to operate without interruption and are subjected to structureborne shocks at levels characteristic of gun firing. The shock levels are at levels of approximately 1/20 of the level of MIL-S-901C and consequently give a measure of circuit fragility at levels roughly equivalent to the response to vibration. Vibration per MIL-STD-167 extends through the frequency range of 4 to 33 Hz and does not yield data relative to the response in the 33- to 500-Hz region of the spectrum, which is strongly excited by structureborne gun shock of the type specified.

This test method was included with the vibration test and was spectrum controlled. If the equipment is available, the test is relatively inexpensive and can be applied for qualification or acceptance testing of complex shipboard electronic equipments.

BIBLIOGRAPHY

- (1) Shock and Vibration Handbook, McGraw-Hill Book Co., edited by C. M. Harris and C. E. Crede, vol 1 (1961)
- (2) Instruction Book, Model 330, Shock Response Spectrum Analyzer; Spectral Dynamics Corp.

Mr. Forkoie: I have used the medium weight shock machine with inclined bulk head which allowed me to get shock components in three directions simultaneously down to levels as low as 3 1/2 g's and 5 Hz frequency by the simple expedient of using isolating mounts between the structures and the table itself. It's a very versatile machine and you can do that. The only difficulty that I think can happen here is that you may not be able to drop the hammer repeatedly in 20 seconds it might take you 30 seconds to drop it and instead of dropping it 2 1/2 feet you may drop it 6 inches and get the same effect with all the frequency components that exist in the standard mounting for the standard test if this is what you are looking for.

DYNAMIC PROPERTIES OF CONCRETE UNDER IMPACT LOADING

G. R. Griner, R. L. Sierakowski, and C. A. Ross
Department of Engineering Sciences, University of Florida
Gainesville, Florida

Experimental studies were conducted to determine the dynamic impact behavior of concrete bar specimens at stress levels near or below the tensile failure strength of the material. Strain pulse propagation characteristics were monitored with pulse shape change, pulse propagation speed, and amplitude attenuation catalogued for bars of varying diameter and particle aggregate. Dynamic impacts were introduced into long bar specimens by the use of an air gun with impact velocities in the range of 100 to 800 in/sec. Three steel impactors (ball, 1" cylinder with hemispherical nose, 2" cylinder with hemispherical nose) were used to obtain varying pulse lengths. The effects on pulse shape and length were recorded for bars with a protective steel cap 0.25" thick and the results compared with the data for uncapped bars. In addition, dynamic threshold impact velocity measurements were made to determine initial fractures for each type of impactor.

INTRODUCTION

As a structural material, concrete is often used as a protective and/or containment medium for impact and blast loadings. For such applications, an assessment of material degradation and damage are important failure criteria to establish. In general, three fracture regions are readily apparent and may be identified as 1.) a pulverized or crater region, 2.) a region of crushed aggregate, and 3.) a region of numerous microcracks in which elastic waves can be considered important (Figure 1). Since

concrete is inherently weak in tension, wave propagation through this latter region can produce microcracks, scabbing, or corner fractures when the dynamic tensile strength of the concrete is exceeded.

Currently, only a limited amount of data is available in the open literature on the dynamic behavior of concrete. This lack of information makes it difficult to establish criteria for use in designing protective and containment structures. A currently used design criteria is to select the dynamic tensile strength as twice the static ultimate tensile strength, [1]. Studies on the dynamic compressive strength of concrete have also been reported in [2]. Results from these studies show that (a) the compressive strength increased with the rate of loading and was twice the static value for intermediate loading rates (10 in/in/sec), (b) the dynamic elastic modulus was found to be 1.5 times the static value, and (c) that the impact resistance of the material was found to increase with the rate of loading. Additional investigations of the dynamic properties of impacted concrete bar specimens [3,4] have shown that the wave propagation velocity is similar to that in igneous rocks, that the dynamic elastic modulus is greater than the static value and that pulses of short duration and high rise time propagate with little dispersion and some

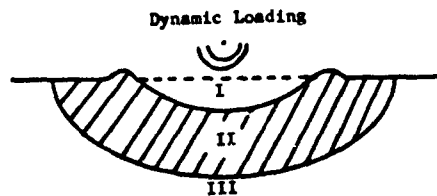


Figure 1. Effects of Dynamic Loading on a Rock Medium (I, Crater Region; II, Crushed Aggregate; III, Elastic Region)

Table 1. Summary of grain size properties and mix proportions for aggregates A-3 and A-4.

Bar Diameter inches	Aggregate	D ₅₀ (mm)	C _u	s/c	w/c
3/4	A-3	0.425	1.64	2.0	0.56
1-1/2	A-3	0.425	1.64	2.0	0.56
1-1/2	A-4	1.30	1.49	2.0	0.50

attenuation, the latter dependent upon the specific strain level. Most recent studies [1] indicate that a strain energy fracture criterion may provide a meaningful guide for design against spall and corner fractures. Also, some current results obtained for brittle material other than concrete [5] indicate that a statistical correlation between static tensile fracture and corresponding wave propagation failure in long bar specimens may be possible.

In the present investigation, information relative to the microcrack region has been experimentally obtained on instrumented long bar specimens. These specimens have been impulsively loaded using impactors of different length and shape, with the specimens being of variable diameter and concrete aggregates. The bars have been impacted at stress levels well below the compressive strength of the material in order to investigate the extent and nature of the tensile fracture phenomenon occurring within the specimens. Surface strain gages have been used to measure the strain pulse propagation characteristics including pulse shape change, pulse speed and amplitude attenuation. In addition, changes in particle aggregate sizes along with bar geometry changes have been studied for potential scaling purposes.

SPECIMEN PREPARATION

The concrete specimens were fabricated from high early strength cement, Portland Type III and an aggregate with a low uniformity coefficient, (i.e. the grain diameters are homogeneous in size). Selection of aggregate was made such that scaling between bars of varying diameter and aggregate size could be investigated. Table 1 summarizes the gradation and grain size data which include the mean diameter (D₅₀), the uniformity coefficient (C_u), the soil/cement ratio (s/c) and the water/cement ratio (w/c). The aggregates used were 99.5% SiO₂.*

The test specimens were fabricated for two

geometrical diameters, 0.75 inches and 1.50 inches. Molds for the specimens were constructed from PVC tubes split on two sides 180° apart for easy removal after setting of the concrete had occurred. Then ends of the molds were sealed by rubber stoppers; a number 3 stopper was used for the 0.75" mold and a number 9 for the 1.50" mold. An elaborate taping procedure was developed to prevent leaking of the water/cement mixture from the mold. Duct tape was used to seal the longitudinal seams and masking tape was wrapped around the mold to keep it from expanding laterally. Electrical tape was used to seal the rubber stoppers to the mold. An oil base mold release agent was coated on the inside surface of the mold before casting to prevent adhesion of the cement to the mold.

The mix proportions were adjusted for the combination that resulted in a bar with the best (smooth) surface for strain gage application. The parameters involved in the mix proportions were the soil/cement (s/c) ratio and the water/cement (w/c) ratio. The s/c ratio was selected to be 2 to 1 for high strength properties and the w/c was adjusted in a range of .50 to .65. Values of .56 for the A-3 aggregate and .50 for the A-4 aggregate resulted in bars with minimal surface air pockets, good consolidation, and little or no water leakage through the seams and ends of the mold.

Concrete was mixed in quantities sufficient to prepare three specimens. The mix was added to a prepared mold in a vertical position in two inch layers, consolidated by tamping with a flat ended 5/8 inch fiber glass rod, and sealed with the upper stopper and electrical tape. The sealed concrete filled mold was then laid horizontally for three days to allow for setting of the concrete after which the mold was then removed and the bar immersed in water at room temperature (76°F) for a period of 4 days. After the 7 day cure time the bar was allowed to air dry for a minimum of 3 days before testing. For the case of the 28 day cure specimens the procedure was the same except the cure in water was increased from 4 days to 25 days.

Examples of typical concrete bar specimens are shown in Figure 2. The bars take the shape

*Private conversation, Al Fiori, NL Industries Edgar, Fla., 8 July, 1974

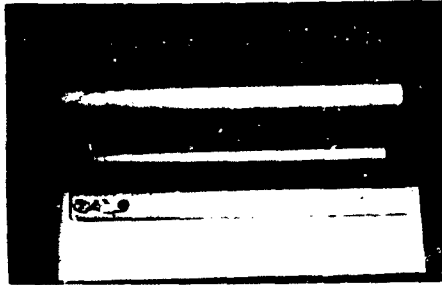


Figure 2. Typical Concrete Bar Specimens

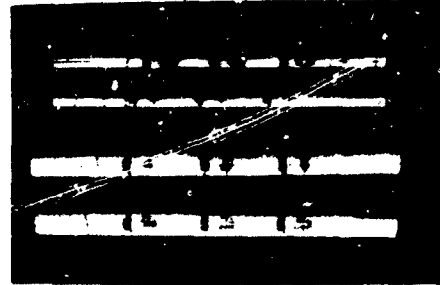


Figure 3. Instrumented Test Specimens

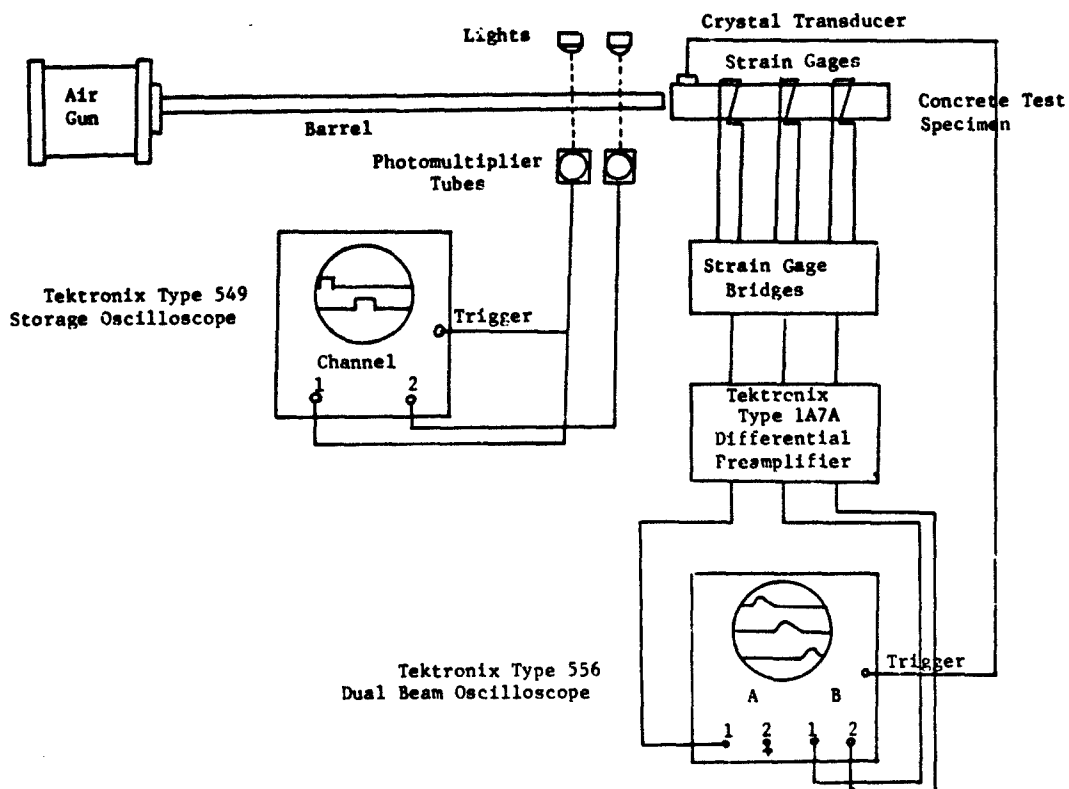


Figure 4. Air Gun and Instrumentation

of the molds which are not perfectly round and have some inside surface irregularities. However, the resulting nominal diameters are 0.75 and 1.50 inches respectively and are well suited for purposes of experimental investigation.

EXPERIMENTAL APPARATUS

Strain pulses were measured by strain gages bonded to the surface of the specimens using Eastman 910 cement. MLH, SR-4 paper back strain gages of lengths 0.13 inches (FAP-12-1286) and 0.50 inches (FAP-50-1286) were used to measure the strain. The gages were diametrically placed on the bars and connected in series in order to eliminate any bending components present in the strain pulse. Each bar was instrumented at three stations (see Figure 3).

Strain measurements were obtained using a strain gage bridge, a Tektronix Type 1A7A differential preamplifier and a Tektronix Type 556 dual beam oscilloscope. The strain pulses were recorded photographically using Polaroid Type 127 film from the oscilloscope trace while in a single sweep trigger mode. A crystal transducer mounted on the specimen at the impact end was used to trigger the oscilloscope. The strain gage leads were shielded to eliminate noise.

Dynamic impacts on the concrete specimens were produced by an air gun as shown in Figure 4 and described in detail in [6]. The impact velocities were determined by measuring the time increment the projectile required to interrupt two light beams passing through drilled holes 4 inches apart at the end of the gun barrel. As the projectile passed through each light beam the output of the photocell was changed causing a step in the output signal. The output of each photocell was displayed on a Tektronix Type 549 storage oscilloscope and the time increment between the voltage steps of each trace were recorded. Oscilloscope triggering was initiated by the change in output of the first photocell.

The concrete specimens were supported by semi-circular teflon supports which could be adjusted both laterally and vertically, (see Figure 5). The teflon supports reduced friction and allowed free suspension of the specimen. The specimen was aligned to the bore of the gun barrel for concentric impacts, with the specimen and support assembly enclosed in a protective plywood box to contain spallation and projectile ricochet.

STATIC TESTS

Static tensile and compressive tests were conducted on the concrete specimens, with test data reported in Table 2. The density of the concrete composed of aggregate A-3 was found to be 130 lb/ft³ and for the concrete composed of

A-4 aggregate 140 lb/ft³. Specimens for the static compressive tests (see Figure 6) were cut from long bar specimens such that the length to diameter ratio was 2. The end surfaces were ground flat and teflon sheeting was used at the ends of the specimen to reduce friction effects. The 0.75 inch diameter specimens were tested in a Tinius-Olson testing machine at a crosshead speed of 0.01 in/min and at a load range setting of 6,000 lb. A deflectionometer was used to detect the crosshead motion and in turn was recorded on an oscillograph. Compression was continued until fracture of the specimen occurred.

A second testing machine with a greater load capacity was required to obtain the ultimate strength of the 1.50 inch diameter specimens. Thus, modulus of elasticity was determined from the Tinius-Olson testing machine and ultimate strengths determined from the second machine. The resulting fractures were generally of the observed cone shape as shown in Figure 7.

Compressive tests were also conducted on specimens 3 inches in diameter and 6 inches long so that comparison with the results for the smaller diameter specimens could be made. Concrete has been shown to exhibit a strength effect as a function of specimen size and has been discussed in reference [7]. However, size effects are less significant as the homogeneity of the concrete is increased. All of the large cylinders tested were capped with a sulfur compound called "fly ash" to insure uniform loading. Good agreement of the ultimate strength data resulted.

Two types of tension tests were conducted. The first consisted of specimens 3 inches in length and 0.75 inches in diameter cut from the long bar specimens. Special steel pulling ends were fabricated and glued to the ends of the specimen using Devcon "5 minute" epoxy. The pulling ends consisted of steel disks 0.25 inches thick, with eyebolts threaded into the disks. The eyebolts were then attached to the loading machine as shown in Figure 8. This method of tension testing has been used previously with some success, [3,7] however, introduction of bending stresses unavoidably develops, and lower values of ultimate strength were recorded in this series of tests as compared with the results of the "Briquet Tests" subsequently described.

Tension tests were also conducted on specimens 1.50 inches in diameter and 6 inches in length. Pulling ends similar to the ones described previously were constructed for the larger size specimens. Fractures invariably resulted at the epoxy joint, however, within the concrete itself. This indicates bending stress build up and substantiates the previously drawn conclusion. Hence, tension test data for large diameter cylinders appears questionable.



Figure 5. Specimen Support Mechanism

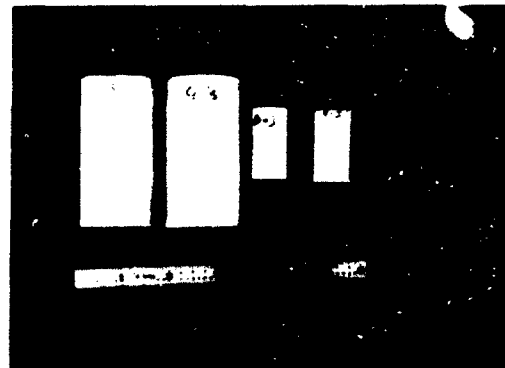


Figure 6. Specimens for Static Compressive Tests

Table 2. Static Properties

Shape	Diameter (in)	Cross Sectional Area (in ²)	Aggregate	Cure time (days)	Compression		Tension	
					Ult. Strength (psi)	Young's Modulus (x10 ⁻⁶ psi)	Ult. Strength (psi)	Young's Modulus (x10 ⁻⁶ psi)
Cylinder	3/4	0.4418	A-3	7	5540	3.33	394	3.63
				28	8819	4.47		5.53
	1 1/2	1.7671	A-3	7	5538	3.02		3.87
	1 1/2	1.7671	A-4	7	6340	3.01		3.95
Bricquet		1"	A-3	7			585	
			A-4	7			541	



Figure 7. Typical Static Compression Fractures

The second method of tension testing involved the casting of the concrete into especially designed molds. The shape is shown in Figure 9 and was designed such that concentration of the load occurs at the narrow portion of the briquet. The load is determined from a proving ring calibration chart. Ultimate strengths in tension were substantially higher from this test series and greater confidence is placed upon these values because of uniformity of specimen failure.

FRACTURE THRESHOLD IMPACT VELOCITY MEASUREMENTS

Dynamic impact tests were conducted on non-instrumented concrete bars in order to determine the minimum velocity required to cause a single tensile fracture. The effects of the addition of a protective steel cap to the impact end were also investigated. Bar diameters of 0.75 and 1.50 inches were used with the A-3 aggregate and a diameter of 1.50 inches was used for the A-4 aggregate. Some typical fractures are shown in Figure 10. A range of impact velocities were used in order to establish the lower threshold velocity limit for a single fracture. For cases where the bar was not fractured, repeated tests were conducted at the same or higher impact velocities to determine if the dynamic characteristics changed due to the previous passage of a tensile wave through the specimen. Also, for some bars the fractured specimens were rebonded using Devcon "3 minute" epoxy and repeated dynamic testing conducted. A summary of the threshold limits are given in Table 3.

ULTRASONIC TESTS

Ultrasonic test specimens 0.25 inches and 0.50 inches were cut from both unshocked (virgin) bars and previously shocked (one or more prior impacts) bars. Both ends of the specimens were ground flat and 0.13 inch diameter transducers were mounted to produce axial motion. These tests were conducted as a



Figure 8. Static Tension Test Fixture

separate investigation and served as a comparison for the data obtained from the dynamic instrumented impact tests.

A Mavetek Model 144 wave generator provided the input signal frequency of 800,000 hertz. The output signal was read directly by a Tektronix Type 545B oscilloscope and the input and output signals were then simultaneously displayed on the oscilloscope trace. The time required for the first wave to traverse the thickness of the specimen was observed and wave speed calculated. The dynamic modulus was then determined by using the elastic wave speed equation ($E = \rho c^2$).

Some typical wave patterns for the 0.25 inch and 0.50 inch specimens have been shown in Figures 11 and 12 and the resulting ultrasonic test data have been given in Table 4.

DYNAMIC IMPACT TESTS

A total of twelve bars were instrumented with strain gages for dynamic impact testing. Repeated impacts were conducted on the bars using the following impactors: sphere, 1" cylinder with hemispherical nose, 2" cylinder with hemispherical nose. Fast sweep speeds (200 μ sec/cm) on the oscilloscope were used to obtain data for calculating pulse speed and determining pulse shapes for each type of impactor. Slow sweep speeds (200 μ sec/cm) were used to observe pulse attenuation. Some typical pulse shapes have been included in Figures

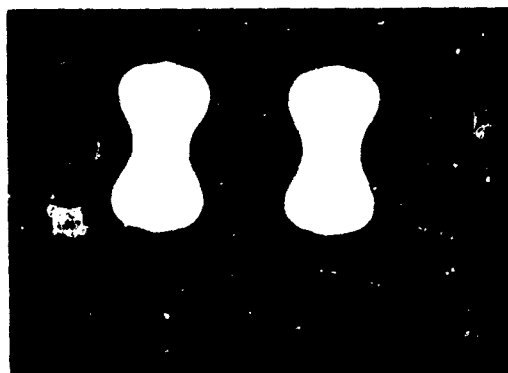


Figure 9. Briquet Specimens Used in Static Tension Tests

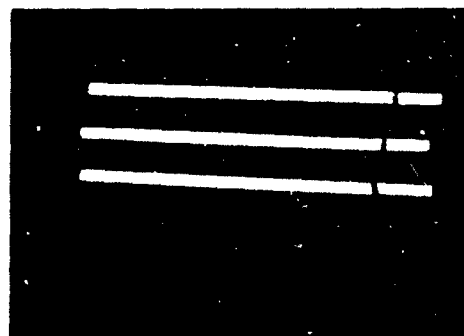


Figure 10. Typical Dynamic Tensile Fractures for 0.75 inch Diameter Bars

Table 3. Average Tensile Fracture Impact Velocity Threshold Limits

Bar Diameter (inches)	Aggregate	Cure (days)	Impactor (inches)	End Condition (C-capped U-uncapped)	Average Velocity Threshold Limit (in/sec)
0.75	A-3	7	Ball (0.485 dia)	C	
				U	450
			1	C	150
				U	200
		28	Ball (0.485 dia)	C	400
				U	500
1	C		200		
	U		250		
1.50	A-3	7	1	C	600
				U	1200
	A-4	7	1	C	
				U	800

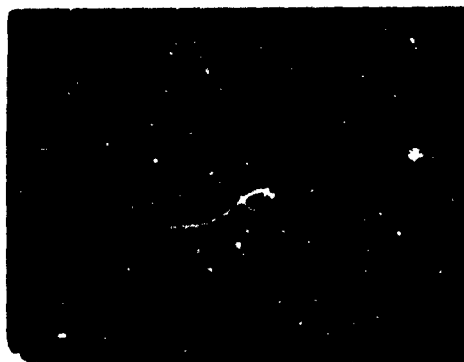


Figure 11. Typical Wave Pattern in 0.25 inch Thick Specimen



Figure 12. Typical Wave Pattern in 0.50 inch Thick Specimen

Table 4. Ultrasonic Test Data

Aggregate	Cure (days)	History (U-unshocked S-shocked)	Diameter (inches)	Thickness (inches)	Wave Speed (in/sec)	Dynamic Modulus (psi)
A-3	7	U	0.75	0.25	111000	2.4
A-3	7	S	0.75	0.25	111000	2.4
A-3	28	S	0.75	0.25	125000	3.0
A-3	7	U	1.50	0.25	122000	2.9
A-3	7	S	1.50	0.25	114000	2.5
A-3*	7	S	1.50	0.25	106000	2.2
A-4	7	U	1.50	0.25	100000	2.1
A-4	7	S	1.50	0.25	114000	2.7
A-3	7	U	0.75	0.50	143000	3.9
A-3	7	S	0.75	0.50	135000	3.5
A-3	28	S	0.75	0.50	152000	4.5
A-3	7	U	1.50	0.50	154000	4.6
A-3	7	S	1.50	0.50	154000	4.6
A-4	7	U	1.50	0.50	154000	4.9
A-4	7	S	1.50	0.50	152000	4.8

* Transducer placed on piece of unmixed cement



Figure 13. Strain Pulse Propagating in an 0.75 inch Diameter Concrete Bar (Ball, 204 in/sec, u, A-3, 28, 20 μ sec/cm, 0.2 m volt/cm.)

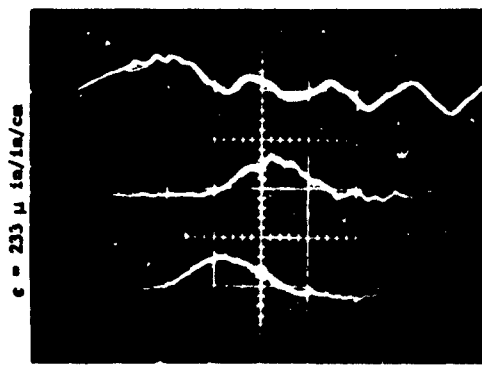


Figure 14. Strain Pulse Propagating in an 0.75 inch Diameter Concrete Bar (1", 195 in/sec, c, A-3, 7, 20 μ sec/cm, 0.5 m volt/cm, lower signals reversed)

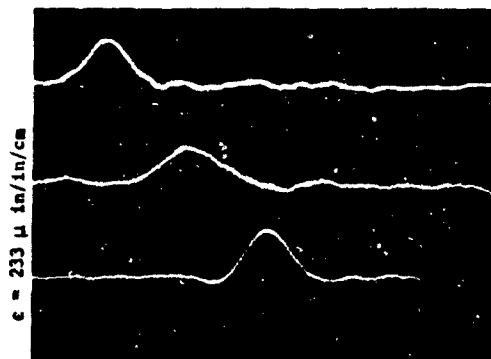


Figure 15. $t = 20 \mu \text{ sec/cm}$
Strain Pulse Propagating in
a 1.50 inch Diameter Concrete
Bar (1", 195 in/sec, C, A-3, 7,
20 $\mu \text{ sec/cm}$, .5 m volt/cm)

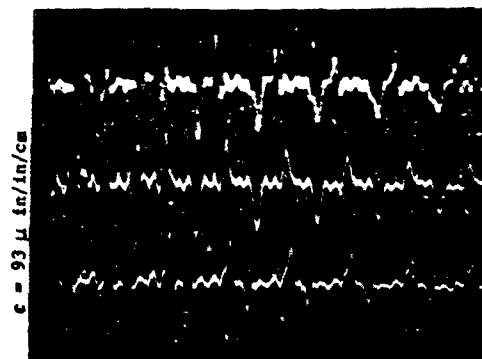


Figure 16. $t = 200 \mu \text{ sec/cm}$
Strain Pulse Attenuation in a
1.50 inch Diameter Concrete Bar
(Ball, 331 in/sec, U, A-4, 7,
200 $\mu \text{ sec/cm}$, .2 m volt/cm)



Figure 17. $t = 50 \mu \text{ sec/cm}$
Effects of an Epoxy
Joint on Pulse Propagation
(1", 444 in/sec, U, A-3, 7,
50 $\mu \text{ sec/cm}$, .5 m volt/cm)



Figure 18. $t = 50 \mu \text{ sec/cm}$
Effects of an Epoxy
Joint on Pulse Propagation
(1", 229 in/sec, C, A-3, 7,
20 $\mu \text{ sec/cm}$, .5 m volt/cm)

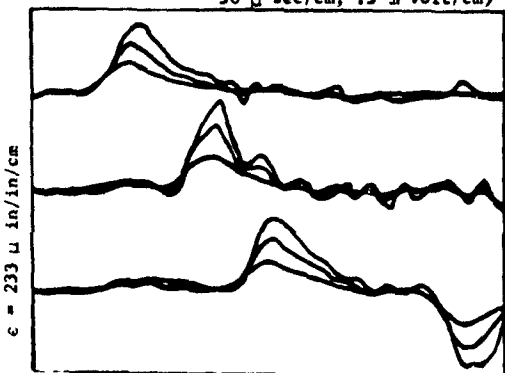


Figure 19. $t = 20 \mu \text{ sec/cm}$
Strain Amplitude as a Function of
Impact Velocity (1.50 inch diameter,
A-3, 7 day cure, 1 inch impactor, .2
m volts/cm, 20 $\mu \text{ sec/cm}$, 0.25 inch
cap, $V_1 = 163 \text{ in/sec}$, $V_2 = 250 \text{ in/sec}$,
 $V_3 = 333 \text{ in/sec}$)

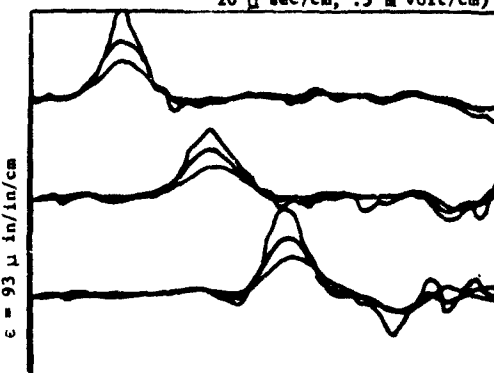


Figure 20. $t = 20 \mu \text{ sec/cm}$
Strain Amplitude as a Function of
Impact Velocity (1.50 diameter,
A-3, 7 day cure, spherical impac-
tor, .2 m volts/cm, 20 $\mu \text{ sec/cm}$,
0.50 inch cap, $V_1 = 200 \text{ in/sec}$, V_2
 $= 333 \text{ in/sec}$, $V_3 = 476 \text{ in/sec}$)

13-16. Details of each test are given in parentheses in the following order: projectile, velocity, end condition (u-uncapped, c-capped), aggregate, cure time, oscilloscope sweep speed, oscilloscope voltage). Steel caps 0.25 inches in thickness were used on several of the bars tested. The diameter of the caps matched the diameter of the bar to which it were attached. All caps were bonded to the bars using Devcon "5 minute" epoxy.

After repeated impacts, the tensile stress waves created weak areas in the bar being tested with fracture or hairline cracks generally noted. When fracture did occur, the specimen was rebonded using Devcon "5 minute" epoxy and the bar was retested. For bars where fracture occurred beyond the third gage station, pulse characteristics were recorded for fast sweep speeds in order to observe the first pulse passage. The information obtained in this manner was found to be equivalent to a bar without a fracture as long as interference did not occur for the incident compressive and reflected tensile pulses.

Pulse propagation characteristics through an epoxy joint between gage stations were also obtained. Some typical data has been included in Figures 17 and 18.

RESULTS AND DISCUSSION

Data obtained from the Dynamic Impact Test series indicate that the velocity required to produce a single tensile fracture is reduced as the impactor length increased. In addition, the influence of a cap at the impacted end of a bar appears to cause tensile failure nearer the distal end of the bar. Also, repeated impacts on previously tested and rebonded specimens tend to produce random fractures.

Results from the ultrasonic tests conducted indicate that thickness of specimens tested is important in establishing wave speed data with higher wave speeds in thicker specimens. Also, wave speeds determined in concrete composed of A-3 and A-4 type aggregates were found to be similar. It was observed that concrete of longer cure time had a slightly higher wave speed; this result occurring due to the increase in modulus with increasing cure time.

In general, pulse propagation speeds determined from bar impact studies were found to be in the range of 118,000 inches per second to 150,000 inches per second and in agreement with results from the ultrasonic tests. Wave shapes were approximately a half sine wave with long rise times, and almost symmetrical about the peak magnitude point.

Observations of the pulses from photographs of fast sweep speeds (20, sec/cm) indicate the pulses propagate with little or no observable attenuation and dispersion and remain elastic in character during initial traverse

along the bar. The absence of attenuation and dispersion did not appear to depend on bar geometry as used in this study and can be noted by comparing Figures 14 and 15.

Previous studies [3] on concrete rod specimens indicate that a solid friction model is representative of the resulting data. However, there is an order of magnitude difference in the impact velocities in that particular study and the study presented here. The author [3] further goes on to say, based upon past dynamic studies on rock specimens that "any material will behave as an elastic solid below a critical stress level, will exhibit attenuation above this level, and will regain its elastic behavior upon saturation of microscopic structural damage." If this situation does indeed occur for concrete then it is possible for impact velocities at or near the tensile failure strength of concrete that a completely elastic behavior may be expected.

Surface strain gage data shows that pulses propagated through a bonded front steel cap are shorter in wave length than pulses generated from impacts on uncapped bars. This result is in agreement with fractures observed in the dynamic impact velocity threshold test series with a shorter pulse producing a tensile fracture nearer the distal end of the bar.

Tests have been conducted in order to determine the effects of increasing impact velocity upon subsequent strain amplitude. Figure 19 presents the effects on a capped 1.50 inch diameter bar for a 1 inch cylindrical projectile with hemispherical nose while Figure 20 presents the effects on an uncapped 1.50 inch diameter bar for a spherical projectile. Both sets of data indicate good reproducibility with approximately a linear relationship between strain amplitude and projectile impact velocity.

Comparison of pulse data on similar bars having different gage lengths (0.13 vs 0.50 inches) showed little observable differences. Cross comparisons between bars instrumented with gages of varying length can thus be used with confidence.

Results from the amplitude attenuation studies for which multiple reflections were observed indicate that a decay in amplitude occurs with progression down the bar while amplitude growth is observed with progression of the reflected tensile pulse toward the impact end. The differences are small and are possibly within the error of the experimental apparatus, however, this observation is noticed on repeated tests of the same bar and also from tests on different bars. Data presented in references [8,9] has also shown this same phenomenon for dynamic impact tests of igneous rock specimens and hypothesized that this effect is due to the release of stored energy in the grains as the tensile wave passes.

CONCLUSIONS

1. Concrete behaves as an elastic solid for stress levels near the tensile failure strength of the material for initial wave passage.
2. Tensile wave speed in concrete is approximately 1.2-1.5 times faster than the compressive wave speed.
3. The compressive wave speed decreases with propagation down the bar while the tensile wave speed increases with propagation towards the loaded end after reflection.
4. The dynamic Young's modulus is similar to the static modulus for stress levels near the tensile failure strength of the concrete, and the dynamic ultimate strength is 1.3 to 1.5 times the static ultimate strength for stress levels near the tensile failure of the concrete.
5. Aggregate size does not significantly affect dynamic properties when the aggregate varies in grain diameter from .5mm to 1.5mm.
6. Dynamic tensile fracture stresses are a function of the projectile momentum and not a function of impact velocity only.

REFERENCES

- [1] D. L. Birkimer and R. Lindemann, "Dynamic Tensile Strength of Concrete Materials," Journal of the American Concrete Institute, Vol. 68, 1971, p. 47.
- [2] D. Watstein, "Effect of Straining Rate on the Compressive Strength and Elastic Properties of Concrete," Journal of the American Concrete Institute, Vol. 24, 1953, p. 729.
- [3] W. Goldsmith, M. Polivka, and T. Yang, "Dynamic Behavior of Concrete," Experimental Mechanics, Vol. 6, 1966, p. 65.
- [4] W. Goldsmith, V. H. Kener, and T. E. Ricketts, "Dynamic Loading of Several Concrete-Like Mixtures," Journal of the Structural Division (ASCE), Vol. 94, 1968, p. 1803.
- [5] K. P. L. OH and I. Finnie, "The Location of Fracture in Brittle Solids-II," International Journal of Fracture Mechanics, Vol. 6, 1970, p. 333.
- [6] Sierakowski, R. L., Nevill, G. E., Ross, C. A., and Jones, E. R., Studies on the Ballistic Impact of Composite Materials, AFATL-TR-69-99, Air Force Armament Laboratory, Eglin Air Force Base, Florida, July 1969.
- [7] Nevill, A. M., "Properties of Concrete," John Wiley and Sons, New York, 1971.
- [8] Goldsmith, W., Austin, C. F., Wang, C. C., and Finnegan, S., "Stress Waves in Igneous Rocks," Journal of Geophysical Research, Vol. 71, No. 8, 1966, p. 2055.
- [9] Goldsmith, W., and Austin, C. F., "Some Dynamic Characteristics of Rocks," Stress Waves in Anelastic Solids, Springer, Berlin, Germany, 1964, p. 237.

DISCUSSION

Voice: ... on dynamic tests of concrete. I recommend to you the summary technical report of Division 2 of the NDRC 1946-47 which has a lot of data. It will be at 1600 feet/sec not 1600 in/second and up. Also, if you look in the engineering index from about 1940 to 1944 you will find a lot of data on the stress waves produced by impact on concrete bars, in this case about 6 in. square and 20 feet long with real life-size aggregate.

Mr. Griner: Were these instrumented tests?

Voice: Yes they were!

Voice: I was in the Laboratory in Raleigh School of Mines in 1940 and right next to my testing machines was the test apparatus for doing this very thing. I'm sure it was written up and reported.

Mr. Griner: One thing I might point out to you is that for these low stress levels i.e. 100 to 700 psi, the dynamic modulus did not change that much but if we went to 5000 psi then it may go up to as much as 1.5 and I think that is what has been reported. The ultimate strengths were slightly higher, even at the low stress levels. Now one thing that I think needs more work in this particular area and that is finding the critical stress level at which fracture occurred. Now my strain gages were at a certain position that I could measure the pulse but of course the fracture didn't occur right at the strain gage so I really couldn't tell exactly what the stress was when it fractured. I think that would be one of the most important parameters.

Mr. O'Hearne: (Martin Marietta) I noticed in statically loading the cylindrical bars it looked as though the loading area was smaller than the cross-sectional area of the bar and I was wondering why the failure didn't occur in the neighborhood of the loading head?

Mr. Griner: Near the pulling end?

Mr. O'Hearne: Right!

Mr. Griner: What we did is we fabricated these particular specimens in molds that were 3/4 inches in diameter and they were split down the middle on both sides and taped together such that we had no water leakage. There were some surface irregularities inside that and as a result it wasn't a completely uniform .75 inches but those pulling ends were exactly .75 inches.

In fact the cylindrical specimen was slightly larger than the pulling end. And like I say the epoxy and so forth was so strong that it did fail near the center near the ends but in most cases if we went to a larger diameter specimen or a higher strength specimen it fractures right on that epoxy joint but it was within the concrete.

PREDICTING PLATE RESPONSE TO BLAST LOADING*

Lt. Col. Robert O. Meitz
and
Lt. Philip B. Aitken-Cade
Air Force Institute of Technology
Wright-Patterson Air Force Base, Ohio 45433

The use of the iso-damage curve as a predictive tool for designers is explored in the context of plastic deformation. Analytical and experimental results available in the literature are used to demonstrate the feasibility of suppressing variations due to geometry and boundary conditions by selecting suitable non-dimensional variables.

INTRODUCTION

The response of structures to various types of dynamic loading, including that due to blast effects, is frequently characterized by plotting curves of constant response using the peak value of load and delivered impulse as coordinates. If the coordinates are suitably scaled by dimensional analysis or other techniques, a single such curve, called an iso-response or iso-damage curve, can be used to predict the behavior of all similar structures, providing the geometry of the structure, any boundary conditions and the pulse shape of the load remain the same. The objective of this study was to examine the feasibility of constructing an iso-damage curve which is valid for differing structural configurations, that is, to lift the restrictions to similar geometry and boundary conditions.

A brief introduction to the concept of iso-damage curves will be followed by a review of selected literature dealing with the plastic deformation of plates which are subjected to dynamic loading. Next, a set of sample iso-damage curves are developed, based on analytical solutions available in the literature. Finally, experimental results for impulsively loaded plates are used to test the validity of the proposed technique.

ISO-DAMAGE CURVES

The concept of iso-damage was originated at Ballistic Research Laboratories, Aberdeen Proving Ground. The fundamental idea is that some specified level of damage to a target may be related to certain quantitative characteristics of the loading imposed on it. Then, if the locus of points representing the specified level of damage is plotted using the load characteristics as coordinates, the resulting curve represents the boundary between regions where damage either

exceeds or is less than the level under consideration. Just as an iso-bar is a line on a map connecting points having equal barometric pressure, so an iso-damage curve is a line connecting points on a graph representing equal levels of damage. Such a plot may be used by a weapon designer to establish parameters required to achieve a desired level of damage to his target. Obviously, this data is equally valuable in assessing the vulnerability of one's own equipment and structures to a postulated threat. Iso-damage theory and the use and construction of iso-damage plots for structures under blast loading were described rather completely by Greenspan [1].

The definition of damage levels will vary with the problem at hand and may be either qualitative or quantitative. For example, collapse of structures, rupture of pressure vessels, or loss of mobility of vehicles are possible qualitative measures; while the occurrence of critical stresses or specified permanent deformation are quantitative in nature.

When considering blast loading as the damage mechanism, a convenient choice of coordinates for the iso-damage plot would be the peak pressure and total impulse per unit area delivered to the target. Other damage mechanisms would lead to different choices of coordinates. Kornhauser [2] has presented a collection of iso-response curves for various impact phenomena which illustrates to some extent the variety of

*A portion of the material reported here was taken from a thesis submitted by the second author to the Air Force Institute of Technology in partial fulfillment of the requirements for the MS degree.

coordinates which may be used.

To make the iso-damage concept more concrete, Figure 1 represents a typical iso-damage curve. The curve may be divided arbitrarily into three regions following the discussion of Lindberg [3]. The three regions may be classified as the impulsive loading realm, region I, the dynamic loading realm, region II, and the quasi-static loading realm, region III. In region I where the curve approaches the vertical asymptote, peak pressure becomes unimportant and the damage level depends mainly on impulse. The impulsive loading is of short duration with respect to the response time of the system under consideration and as the duration approaches zero, the impulse approaches a limit. This limit leads to the value of the impulsive asymptote depicted in Figure 1. This vertical

asymptote indicates a minimum impulse for which a given damage level will occur. For any impulse less than this minimum the damage will be less than the specified damage level regardless of the pressure amplitude. Region II is a region of dynamic loading where the damage level to the system is sensitive to changes in both pressure and impulse. In addition, the time history or "pulse shape" of the loading is important in this region. Region III is the quasi-static loading realm where the curve approaches the horizontal asymptote. The impulse becomes unimportant and the damage depends mainly on the peak pressure. The horizontal asymptote indicates a minimum pressure for which a given damage level will occur. For any pressure below this minimum the damage will be less than the specified damage level, regardless of the level of impulse.

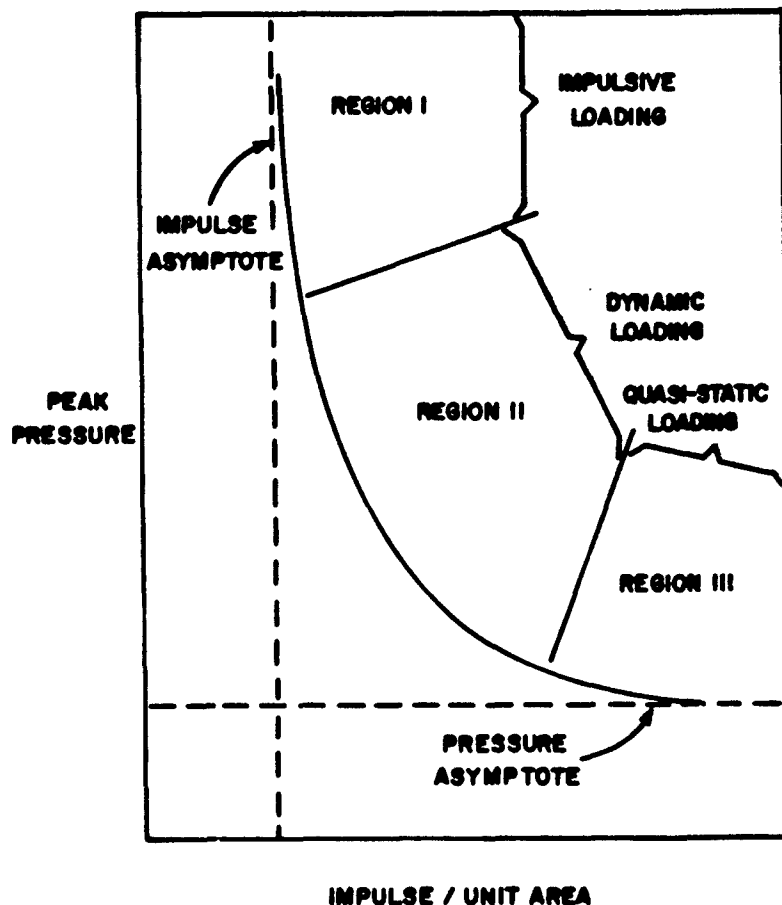


Figure 1 Typical Iso-Damage Curve

DYNAMIC PLASTIC DEFORMATION OF PLATES

Military equipment and structures may be subjected to attack by a variety of weapons employing various damage producing phenomena including fire, impact by projectiles, radiation and high pressure, short duration loads from blast waves. Because of the importance of the last of these and its relative susceptibility to theoretical analysis, there has been considerable interest in the failure modes of simple structures such as beams, plates and shells under blast loading. Since many portions of structures of interest may be modeled as plates, for example, the wing panels of aircraft, armor and various portions of buildings, the present study is limited to considering plate elements.

In the early 1950s studies were being made of the permanent deformation of plates. Hopkins and Prager investigated the load carrying capacities of circular plates. In a paper presented in 1953 [4] they discussed the quasi-static yielding of a plate subjected to a transverse load under conditions of circular symmetry. The plate material was assumed to be non-hardening rigid-plastic and to obey the yield condition and associated flow rule of Tresca. The basic assumptions made by these authors were similar to those of the conventional engineering theory of thin elastic plates [5]. For example, the shearing stress was regarded as small when compared to bending stresses, and the effect of transverse shear strain rate was neglected. A notable feature of this paper was that, within the framework of the incremental theory of plasticity, exact solutions were obtained for problems involving either uniformly distributed or concentrated loads.

The extension of the fundamental analysis from quasi-static problems to dynamic problems was first made by Hopkins and Prager and presented in the Journal of Applied Mathematics and Physics in 1954 [6]. As in their previous paper about the load carrying capacities of thin circular plates, the authors assume a rigid-plastic material that obeys Tresca's yield condition and the associated flow rule. In this paper the same type of analysis is applied to discuss the dynamic behavior of a simply supported circular plate. The deflection equation was obtained for the simply supported plate subjected to a uniformly distributed load which is brought on suddenly and, after being held constant for a certain length of time, is removed suddenly.

The deflection equations of plates under impulsive loading with simply supported or built-in edge conditions have been given by Wang [7] and Wang and Hopkins [8], respectively. Wang adapted the analysis of Hopkins and Prager to discuss the problem of the plastic deformation of a simply supported circular plate under an impulsive load. The impulsive load was supposed to be such that at some instant of time a uniform velocity is imparted to the entire plate,

except at the circumference where the velocity is zero. Subsequently, the plate is subject only to edge forces which effect simple support conditions. The paper by Wang and Hopkins addresses the problem of plastic deformation of a built-in circular plate under an impulsive load. This problem only differs mathematically from the formulation of the simply supported case with respect to the edge conditions of support.

In many of the studies of the permanent deformation of plates attention is confined almost exclusively to the case of circular symmetry. Hopkins [9] extends the theory to a more general concept. He develops a specialization of the general theory of stress and strain rate fields for non-hardening rigid-plastic materials. The physical laws and assumptions invoked in the analysis are those of motion, of plastic flow without fracture at the yield limit and rigidity below the yield limit, and of conservation of mass. The basic assumptions of plastic theory for thin plates are similar to those made in elastic theory, but the effects of transverse shear strain and rotatory inertia are neglected. The field equations involve the stress moments and the middle-surface curvature rates as the generalized stress and strain rates. A detailed study is made of discontinuities in the field quantities since a single plastic regime cannot be expected to provide the complete solution of a given problem. This study is fundamental in the classification of the field equations for the various plastic regimes.

For reasons of mathematical simplicity, for a homogeneous isotropic plate it is customary to use the Tresca yield condition. Mansfield [10] points out that exact solutions for plates satisfying this yield condition are confined mainly to the case of circular symmetry. However, for continuous reinforced concrete plates the Johansen yield criterion is applicable. In the Johansen (or square) yield criterion, yielding occurs when the numerically greater of the principal bending moments attains the absolute value of the fully-plastic bending moment. Mansfield considers the collapse mechanisms of a rigid-plastic plate which obeys this yield condition. He obtains upper bound solutions for a uniformly loaded plate of regular polygonal plan and indicates that the plastic hinge lines radiate regularly from the geometric center of the plate.

A study of the dynamic plastic deformations of simply supported square plates is made by Cox and Morland [11]. Their analysis is given within the framework of thin plate theory. All effects due to elastic strain, work-hardening, and strain rate are neglected. To simplify the analysis, the Johansen yield criterion is adopted as an approximation of Tresca's condition. According to the authors, this approximation is likely to involve an error of about

ten percent in the maximum displacement and time of motion. They show that results obtained for the maximum central displacement and total time of motion for a square plate may be generalized to solve the problem for a regular, n -sided polygonal plate, with n greater than 4. Cox and Morland assume that the velocity field has the features of that described by Mansfield [10]. In other words, they assume that plastic deformation only occurs along the square plate diagonals where hinge lines form, the rest of the plate remains rigid. This is significant deviation from the analysis presented by authors such as Wang, Hopkins, and Prager. These authors assumed that the plastic deformation is such that the plate middle surface is divided into a rigid central circular region together with surrounding alternate annular regions of rigid or plastically deforming material. The number and position of these regions varies with time.

Florence [12] treats the problem of clamped circular rigid-plastic plates under blast loading in a similar manner to that used in [4], [6], [7], and [8]. There are two additional contributions made by Florence. First, he elaborates on the fact that there are two mechanisms of deformation. If a blast load is idealized as an instantaneous rise to some peak pressure followed by a continuous monotonic decay, then mechanism 1 corresponds to peak pressures in excess of the static collapse pressure, but less than twice the static collapse pressure. Mechanism 2 corresponds to peak pressures greater than twice the static collapse pressure. If the deformation occurs by means of mechanism 1, the circular plate will be transformed slowly into a cone with the vertex at the plate center. In mechanism 2, a central region of the plate acquires a uniform velocity. This central region is circular, with a radius which is a function of the magnitude of the peak pressure, the duration of the loading, and the time elapsed subsequent to the loading. The radius of this region finally decreases to zero, after which time the deformation continues as in mechanism 1. Secondly, and of major importance, he shows the dependence of the permanent central deflection on pressure and impulse when the blast loading is taken as a rectangular pulse.

ISO-DAMAGE CURVES FOR PLATES

In this section iso-damage curves will be developed for a circular plate with simply supported edges, a circular plate with clamped edges and a simply supported square plate. The development is based on analytical results given by Hopkins and Prager [6], Florence [12], and Cox and Morland [11]. These solutions were chosen for comparison because all three employed similar plate behavior theory and the same type of loading. Consequently, the only significant differences between the cases considered were in platform and boundary conditions.

In each of the three cases, the usual thin plate assumptions were adopted according to

which the bending stresses and in-plane shearing stresses far exceed the transverse shearing stresses. Although the shear force resulting from the shearing stresses normal to the plate surface was taken into account in the equation of dynamic equilibrium, these stresses were neglected in the yield condition. The effects of rotatory inertia were also neglected. The plate material was assumed to be non-hardening, rigid-plastic and to obey either the Tresca or, for the square plate, Johansen yield condition and associated flow rule. The use of different yield conditions does not cause any difficulty here; when principal bending moments have the same sign, the two criteria are indistinguishable. For each plate configuration, the loading was a uniformly distributed transverse pressure with a rectangular time history.

The collapse behavior of plates generally differs significantly from that of frame structures and beams. When determining the collapse loads of frames, the elements of the frame may be assumed to be rigid-plastic, and have a calculable fully plastic moment. When considering the corresponding behavior of rigid-plastic plates additional complications arise because of the presence of two principal bending moments. Before the total collapse of a plate occurs, the load is resisted by the middle surface forces. For a rigid-plastic plate the total collapse will only occur when the plate is acting as a plastic membrane. It is assumed, however, that the plate is not so thin that the load would be resisted purely by middle surface forces. Therefore, a partial collapse mechanism must be considered.

Partial collapse mechanisms are characterized by the formation of plastic hinge lines. In the case of circular rigid-plastic plates under uniform transverse loading several authors have characterized the partial collapse mechanism by the formation of circular hinge lines. Several such hinge lines may form as concentric circles centered at the geometric center of the plate.

A study of the collapse mechanisms of rigid-plastic plates is given by Mansfield [10]. A variety of shapes, boundary conditions, and loadings are investigated including the case of a square plate under a uniform transverse load. The dynamic loading situation is not considered, but the static collapse pressure is determined. The collapse mechanism for a square plate is theorized to involve the formation of plastic hinge lines along the plate diagonals. This collapse pattern is used in the development of the deflection equations for the simply supported square plate.

When the applied pressure is great enough to produce the partial collapse mechanism, the plate will begin to deform. Upon release of the load, the plate will continue to deform until all of its kinetic energy is absorbed by plastic work. Because elastic effects have been

neglected, the deformation at this time is taken to be the permanent plastic deformation. For simplicity, the maximum transverse displacement of the plate (which occurs at the plate center) was chosen as the quantitative measure of damage received.

After the expression for the final central deflection of a plate is obtained, non-dimensional pressure and impulse characteristic equations may be determined. It is from these equations that the iso-damage curves are constructed.

Considering the preceding discussion, it is necessary to consider the static collapse load for each configuration. For the simply supported circular plate, Hopkins and Prager [4] give

$$P_s = \frac{6M_0}{R^2} \quad (1)$$

where

$$M_0 = \sigma_y h^2$$

is the fully plastic bending moment per unit length, and

P_s is the static collapse pressure

R is the radius of the plate

σ_y is the yield per unit area

$2h$ is the plate thickness

For the clamped circular plate [12],

$$P_s = \frac{6M_0}{r_s^2} \quad (2)$$

where

$$r_s = 0.73R$$

For the square plate [11],

$$P_s = \frac{6M_0}{L^2} \quad (3)$$

where L is the half side length of the square.

Now, consider that the applied pressure is of the magnitude, P , and persists from time, $t = 0$, to $t = t_0$, when the pressure is suddenly reduced again to zero. After release of the load, the plate comes to rest at $t = t_f$.

For $P = P_s$ the plate yields indefinitely slowly and inertia forces do not arise. For $P > P_s$ the dynamic behavior of the plate is found to have a different character according to whether the load is "medium" ($P_s < P < 2P_s$) or "high" ($P > 2P_s$). Consequently, the expressions for final displacement of the plate will differ depending

on the load regime, and each iso-damage curve will consist of two portions which meet at $P = 2P_s$.

Expressions for the deflection of the simply supported circular plate and the square plate are given in [6] and [11] respectively. Although the form of the deflection function obviously must differ for the two cases, the expressions for the central deflection are identical when written in terms of the static collapse pressure rather than using yield stress or yield moment as the strength parameter. Thus, for both plates, the final central deflections are:

$$\text{For } P < 2P_s, \quad W_f = \frac{I^2}{m P_s} \left(1 - \frac{P_s}{P}\right) \quad (4)$$

$$\text{For } P > 2P_s, \quad W_f = \frac{I^2}{2m P_s} \left(\frac{3}{2} - \frac{P_s}{P}\right) \quad (5)$$

where,

$I = P t_0$ is the impulse per unit area, and m is the mass per unit area of the plate.

Florence [12] provides the solution for a clamped circular plate. The resulting expressions are quite complex and require the use of a high speed computer to obtain solutions. Florence has done this and presented the results in the form of a Pressure-Impulse diagram. This diagram has been rescaled to conform with the non-dimensional coordinates used in this study as will be described below.

An observation is made in [10] that if the boundaries are simply supported then the collapse pressure of a regular polygonal plate depends only on the radius of the inscribed circle and the value of the principal bending moment at yielding. Comparing Eq(1) and Eq(3) shows that this relationship also holds in the limiting case of the circular plate. In that case it would be advantageous to define non-dimensional pressure and impulse expressions so that they are independent of shape. This is achieved if the non-dimensional pressure is defined as

$$F = \frac{P}{P_s} \quad (6)$$

and the non-dimensional impulse is defined as

$$I = \frac{I}{\sqrt{m P_s} W_f} \quad (7)$$

Now since P_s is defined uniquely for each of the plates under consideration the expressions for F and I provide a common basis for comparison.

Substituting Eq(4) and Eq(5) into the non-dimensional impulse expression, the following

equations are obtained.

For medium load ($1 < \bar{F} < 2$)

$$\bar{Y} = \sqrt{\frac{\bar{F}}{\bar{F} - 1}} \quad (8)$$

For high load ($\bar{F} > 2$)

$$\bar{Y} = \sqrt{\frac{4\bar{F}}{3\bar{F} - 2}} \quad (9)$$

It is emphasized that these equations are written in terms of the individual plate static collapse pressure as defined by Eq(1) or Eq(3), whichever is applicable. Eq(8) and Eq(9) depend only on \bar{F} and \bar{Y} and are not explicitly dependent on the plate shape, thickness, size, density, or material. It is therefore possible to construct one iso-damage curve for both the square and circular simply supported plates. This iso-damage curve is presented in Figure 2.

The expression used in [12] for the non-dimensional impulse is

$$\bar{I}' = \frac{\bar{I} R}{\sqrt{12 \pi H_0 W_f}}$$

If the clamped circular plate collapse pressure Eq(2), is substituted into the above expression,

the following is obtained:

$$\bar{I}' = \frac{\bar{I}}{\sqrt{1.066 \pi F_s W_f}} = \frac{\bar{I}}{\sqrt{1.066}}$$

Therefore,

$$\bar{I} = 1.032 \bar{I}' \quad (10)$$

The curve presented in [12] may now be rescaled to conform with the coordinates defined by Eq(6) and Eq(7). The rescaled iso-damage curve is plotted in Figure 3, together with that for the simply supported plates.

For a given value of \bar{F} , except in the quasi-static realm, a corresponding value of \bar{Y} for a simply supported plate is very nearly the same as the \bar{Y} for the clamped plate. In the quasi-static realm the curves coincide.

Since the coordinates for points chosen to plot the iso-damage curve of the clamped circular plate were read from a copy of a similar diagram in another report [12], it cannot be expected that the curve is very accurate. However, it is significantly close to the curve for the simply supported plate. It is suggested that Figure 2 is an acceptable iso-damage curve for a square or circular, simply supported or clamped, thin plate subjected to blast loading when that individual plate's collapse pressure is used in the expressions for ordinate and abscissa.

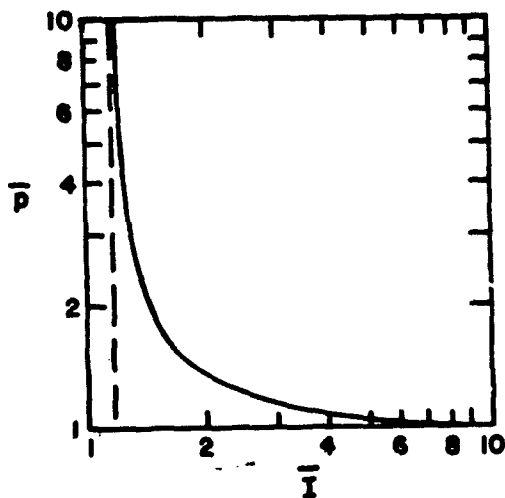


Figure 2 Iso-damage Curve for a Simply Supported Plate

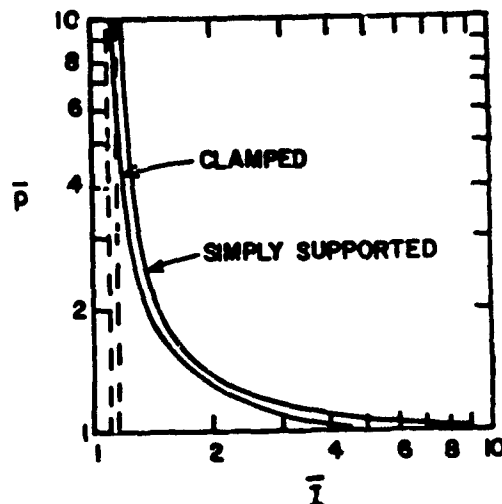


Figure 3 Iso-damage Curves for a Clamped Circular Plate and a Simply Supported Plate

EXPERIMENTAL EVIDENCE

Experimental results relevant to the concepts presented here are not plentiful in the literature; however some supporting data are available for plates subjected to loads in the impulsive region, [13], [14]. Under these conditions, the plate behavior may be conveniently displayed by plotting plate deflection against impulse. Suitable non-dimensional forms of the variables may be selected by considering the equation of the impulse asymptote to the iso-damage curve.

$$I = C$$

where C is some constant. Using Eq(7), this may be rearranged to the following equation,

$$\left[\frac{W_f}{d} \right] = \frac{1}{C^2} \left[\frac{I}{\sqrt{\pi P_s d}} \right]^2 \quad (11)$$

where d is the plate thickness. If the bracketed quantities are used as coordinates, Eq(11) may be represented by a straight line on a logarithmic plot.

Experimental results for simply supported circular plates [13] and fully clamped rectangular plates [14] have been plotted in Figure 4.

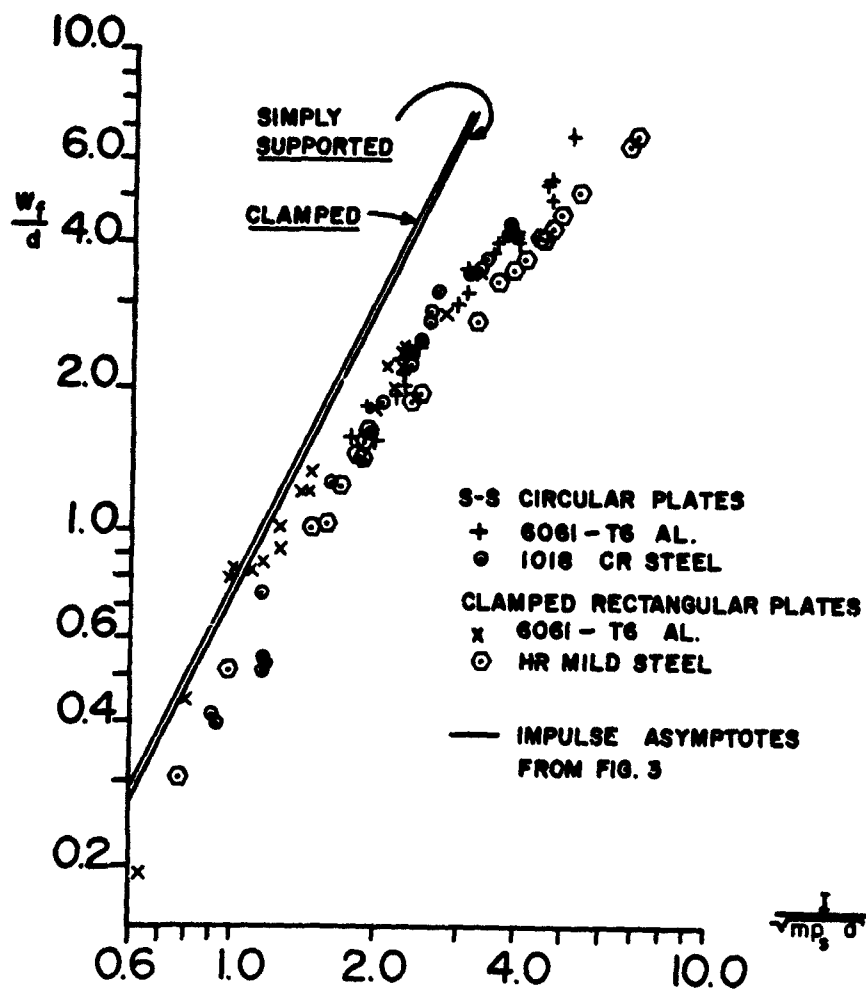


Figure 4 Deflection - Impulse Relation for Impulsive Loading

The static collapse pressure for the circular plates was defined by Eq(1) while that of the rectangular plates was determined using the principle of virtual work and the collapse mechanism suggested in [14]. All the rectangular plates had an aspect ratio of 1.69, for which the collapse pressure is given by Eq(12).

$$P_s = 22.3 \frac{M_0}{L^2} \quad (12)$$

where $2L$ is the length of the plate.

Figure 4 shows very good agreement among the data points for the various combinations of material and plate configuration. The asymptotes to the curves of Figure 3 are also plotted in Figure 4. On this plot the two asymptotes are nearly indistinguishable from one another. The experimentally measured deflections are smaller than the predicted values. Since the theoretical models involved neglect the stiffening effect of membrane forces, this outcome is not surprising.

CONCLUDING REMARKS

These results suggest that iso-damage curves, appropriately scaled on the basis of static collapse pressure, provide a useful means for characterizing the response of plate structures in a relatively compact and convenient form. With proper care and knowledge of static collapse pressures, a designer may be able to use experimental or theoretical results for one configuration to construct reasonable predictions of the behavior of many other proposed structures.

The construction of iso-damage curves in the manner proposed is based on an intuitive feeling that the effects on plate response of geometry and boundary conditions, which come into play in both static and dynamic problems, are relatively invariant with changes in the duration of the loading. On the other hand, effects due to the inertia characteristics account for the major portion of the variation in response as the duration is altered. Just as conventional scaling as employed in [12] suppresses variations due to size, density and choice of material, it is hoped that the scheme adopted here would suppress those due to geometry and boundary conditions. It is hoped that experimental investigators in this field will be encouraged to try the suggested construction using data available to them and thus demonstrate whether or not this approach is also valid for dynamic and quasi-static loading conditions.

REFERENCES

- [1] J. E. Greenspon, "Theoretical Calculation of Iso-damage Characteristics," BRL TR 10, Aberdeen Proving Ground, Maryland, 1970.
- [2] K. Kornhauser, *Structural Effects of Impact*. Spartan Books, Maryland, 1964.
- [3] H. E. Lindberg, et al, "Response of Reentry Vehicle-type Shells to Blast Loads," AF04(694)-655, Norton Air Force Base, California, Ballistic Systems Division, 1965.
- [4] H. G. Hopkins and W. Prager, "The Load Carrying Capacities of Circular Plates," *Journal of the Mechanics and Physics of Solids*, Vol. 2, pp. 1-13, 1953.
- [5] S. Timoshenko and S. Woinowsky-Krieger, *Theory of Plates and Shells*, McGraw-Hill, New York, 1959.
- [6] H. G. Hopkins and W. Prager, "On the Dynamics of Plastic Circular Plates," *Zeitschrift für Angewandte Mathematik und Physik*, Vol. 5, pp. 317-330, 1954.
- [7] A. J. Wang, "The Permanent Deflection of a Plastic Plate under Blast Loading," *Journal of Applied Mechanics*, Vol. 22, pp. 375-376, 1955.
- [8] A. J. Wang and H. G. Hopkins, "On the Plastic Deformation of Built-in Circular Plates under Impulsive Load," *Journal of the Mechanics and Physics of Solids*, Vol. 3, pp. 22-37, 1954.
- [9] H. G. Hopkins, "On the Plastic Theory of Plates," *Proceedings of the Royal Society of London*, Vol. 241, pp. 153-179, 1957.
- [10] E. H. Mansfield, "Studies in Collapse Analysis of Rigid-Plastic Plates with a Square Yield Diagram," *Proceedings of the Royal Society of London*, Vol. 241, pp. 311-338, 1957.
- [11] A. D. Cox and L. W. Morland, "Dynamic Plastic Deformations of Simply Supported Square Plates," *Journal of the Mechanics and Physics of Solids*, Vol. 7, pp. 229-241, 1959.
- [12] A. L. Florence, "Clamped Circular Rigid-Plastic Plates under Blast Loading," *Journal of Applied Mechanics*, Vol. 33, Series E, pp. 256-260, June 1966.
- [13] A. L. Florence, "Circular Plate under a Uniformly Distributed Impulse," *International Journal of Solids and Structures*, Vol. 2, pp. 37-47, 1966.
- [14] Norman, Jones, T. O. Uren and S. A. Tekin, "The Dynamic Plastic Behavior of Fully Clamped Rectangular Plates," *International Journal of Solids and Structures*, Vol. 6, pp. 1499-1512, 1970.